

NISSAN TECHNICAL REVIEW

2022
No.
88



Nissan Intelligent Factory Starting from ARIYA / Next-generation flagship: ARIYA

NISSAN
MOTOR CORPORATION

NISSAN TECHNICAL REVIEW



2022 No. **88**



“NISSAN TECHNICAL REVIEW” WEBSITE

<https://www.nissan-global.com/EN/TECHNICALREVIEW/>

NISSAN TECHNICAL REVIEW 2022 No.88

Contents

Published in September, 2022

◆ Preface

- Preface : Nissan's DNA develops Super evolution "a production system in harmony with Blue Earth" 1
Hideyuki Sakamoto

◆ Special Feature 1 : Nissan Intelligent Factory Starting from ARIYA

1. Nissan Intelligent Factory Starting from ARIYA 7
Hidetoshi Okaguchi
2. Application of Next-Generation Underfloor Process Accommodating Various Powertrains 13
Hiromasa Tsuchikane Atsushi Ugaji Yoshihisa Naito
3. Manufacturing Innovation in a New Motor Line through Digitalization and Internet of Things (IoT) 19
Satoru Iizuka
4. Process Innovation Through the Development of a Simultaneous Body/Bumper Painting System 23
Takeshi Goto Tomoyuki Okamoto Chie Michiura
5. Creation of a Quality Gate through Automated Technology of Appearance and Specification Inspection 29
Teruyuki Ishiwata Mitsuru Hirayama Daisuke Tanaka Takayuki Moriya
Yasuo Yamada Makoto Yamada Takeshi Honda
6. Improvement of the Equipment Operation Rate and Process Capacity by
Implementing Predictive/Preventive Maintenance and Remote Maintenance Technology 37
Katahiro Ogawa Satoru Sakurai Koichi Makino Takuya Tsumoto
Susumu Abe Masayoshi Hayakawa Kazunari Seo Minoru Kono
7. Development of Die-Cast Technology for Realizing Innovative Thin-Walled Light-Weight Cylinder He 43
Yuuta Sugiyama Shinichi Tsuchiya Hiromichi Kume Takahiro Nishi Machi Tabuchi

◆ Special Feature 2 : Next-generation flagship: ARIYA

1. ARIYA: new generation of flagship EV 49
Eiichi Akashi Hikaru Nakajima
2. Development of EV-specific platform CMF-EV for high packaging efficiency 53
Masahiro Oonishi
3. Integrated interface display 57
Tetsu Obata Takashi Eguchi Yasutomo Sasanuma
4. Development of new NissanConnect 61
Toshiro Muramatsu Kazuhiro Funai Masaru Tasaki Shintaroh Murakami Hiroyuki Kamishima
5. High-capacity lithium-ion battery for ARIYA 65
Junji Katamura Kentaro Hata Keisuke Wakabayashi Masanori Takagi Naoto Todoroki
6. Newly developed motor to realize ARIYA's performance 69
Takahito Okubo Hiroki Wada
7. Nissan' s "e-4ORCE" : Proposition for evolution of electric AWDs
— Aiming for a more exhilarating and confident driving experience 73
Hiroyuki Togashi Yutoku Miyagoshi Takeji Katakura

◆ Technical papers

- Study about Workload Reduction by Multiple Modal Interface Using Gaze and Voice Recognition 77
Yusuke Morita Sou Tamura
- The Development of Bearings for the Multi-link Crank Mechanism to Achieve Variable Compression Ratio Engine 85
Katsutoshi Nakamura Katsuya Moteki Satoru Ookuma
- Surrogate Model Development for Prediction of Car Aerodynamics Using Machine Learning 93
Kei Akasaka Fangge Chen Takehito Teraguchi
- A Study on Pitch Characteristic to Reduce Line Trace Deviation in Small Steering Angle 101
Mitsunori Tao Naoya Machida Yutaka Hayashi Ken Nagasao

◆ Technical Awards

- An Approach to Exploring Vehicle Motion to Enhance Ride Quality of Passenger 109
Mitsuhiro Makita Akihiro Matsushita Yoshinori Kusayanagi Masahiro Miura
- Development of driving assistance system in multi-lane highway 117
Yohei Taniguchi Katsuhiko Degawa Seiji Tokunaga Shimpei Nagae Koji Sasaki
- Strength evaluation of CFRP tank based on meso-scopic zooming analysis 119
Shinichiro Takemoto



Nissan's DNA develops Super evolution "a production system in harmony with Blue Earth"

Executive Officer, EVP **Hideyuki Sakamoto**

1. Introduction

Nissan Motor is a car manufacturing company where automotive engineers play a central role in manufacturing cars. Nissan's history began in 1933 with the development and mass production of domestically manufactured automobiles based on the spirit of its founder, Yoshisuke Ayukawa, to "do what others will not do." This positioned Nissan Motor as a company in the early days of the industry; presently, Nissan is a leading player in Japan's modern automobile industry.

The domestic production of automobiles marked the beginning of the evolution of automobile technologies. Since then, Nissan has followed the values and vision of its founder at the company's core and expanded their business internationally through exports and overseas production. Nissan has experienced many waves of challenges, including global social issues such as environmental and air pollution, traffic accidents, oil shocks, fuel economy regulations, and trade friction, among others. However, by using technology created by Nissan's innovative and visionary engineers, the company has continued to successfully overcome new challenges in the industry, even where other companies have faltered. Nissan's storied history is an excellent demonstration of how new innovations in automobiles and manufacturing can be introduced to the market for the first time.

Connected, automated, shared/service, and electric vehicles (EVs)—collectively referred to as the "CASE" areas—and carbon neutrality have been widely covered in the media as once-in-a-century issues for the global automotive industry. The development of future automobiles will aim to realize visions of a technologically advanced future and will rely on the large-scale and high-level development of new technologies that interact with complex social systems. Automotive engineers play a critical role in developing these technologies, and they will continue to do so in the future. The focus of technological development is on the value it offers to customers and society. With this in mind, automotive engineers should fully understand and apply market and technological trends to create the best possible technical solutions that perform key functions for customers and society. These values have been engrained in Nissan's work since its inception and will remain as a guide for the company in the future.

The special feature in this issue of Nissan Technical Review includes technical reports on the best available

solutions to realize new functions and achieve high performance that will resonate with customers and society, demonstrating the value of technological evolution that has been inherited from Nissan's founder to today's engineers.

2. Societal Changes and the Automotive Industry

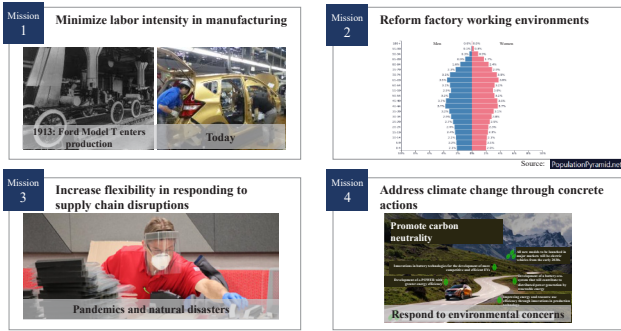
Nissan Motor envisions four missions for car manufacturing and the next generation of the automotive industry.

The first is a shift from a labor-intensive business model. The method of mass production for the Ford Model T was introduced by Ford 100 years ago. It was a revolutionary method and involved many people who worked together to efficiently produce cars. As modernization has progressed, various types of automation have been incorporated into automobile manufacturing processes, but many manually intensive methods are still used presently. However, given the recent shortage of automobile factory workers in Japan and other countries around the world, which has been exacerbated by the COVID-19 pandemic, it is becoming increasingly difficult to ensure work by many people to produce cars. Therefore, it is necessary to move away from the current production model and establish a streamlined automated production system with a reformed working environment.

Secondly, this trend is expected to worsen, given the declining birthrate and aging population, which make it increasingly difficult to provide young people with the advanced training that is necessary for challenging car manufacturing tasks.

Thirdly, additional flexibility in responding to unexpected situations is also needed in production systems. Various factors such as the COVID-19 pandemic, the shortage of semiconductors, and major disruptions in the logistics network have become extremely serious issues that can cause fluctuations in automobile production, making it crucial to develop systems that can deal with manufacturing disruptions. In addition, batteries, e-components, and their raw materials will also face issues with unstable supply in the future, which will undoubtedly cause major fluctuations in production that must be managed.

Finally, the automotive industry should take concrete actions to combat climate change and contribute to achieving carbon neutrality in conjunction with efforts that are currently underway around the world.



Four priorities for the future of automotive manufacturing

How should production activities be developed for the new car of the future with these four conditions met? Cars and their production will become highly sophisticated in the coming years as “Electrified”, “Intelligent”, and “Connected” become the industry standard. Similarly, manufacturing is becoming increasingly demanding as guaranteeing the functionality of various systems becomes more complex. For example, modern manufacturing requires a large amount of software to be installed simultaneously, many sensors to be calibrated, and advanced self-diagnostic systems and fail-safes to be verified, which poses challenges for manufacturing. As an additional layer of complexity, a wide range of customizations is required in car manufacturing, including large batteries with long-range and standard types for EVs, highly automated driving technology that enables hands-off driving, and standard driver assistance systems for automated driving intelligence technologies. Resilient production facilities and technologies to manufacture such complex and advanced vehicles are critical to Nissan's future success.



Meeting the needs of increasingly advanced products

3. Initiatives to Address Climate Change and a Carbon Neutral Life-Cycle

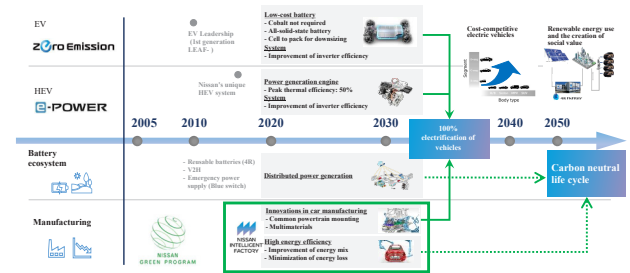
3.1 Nissan Green Program

Countries around the world are now committing to achieving carbon neutrality by 2050 and implementing various policies to tackle climate change.

Nissan has also committed to achieving carbon neutrality by 2050 by electrifying vehicles in major markets in the early 2030s and by promoting innovation in production technology to achieve carbon neutrality in car manufacturing processes. Nissan was among the first companies to take action in reducing CO₂ emissions through the Nissan Green Program starting in 2005. Under the program, the company began the mass production of its first-generation EV, "LEAF," in 2010, offering it to the mainstream market as an EV for daily use. Subsequently, e-POWER was launched with the aim of helping customers feel the joy of driving an EV and

promoting the commercialization of EVs.

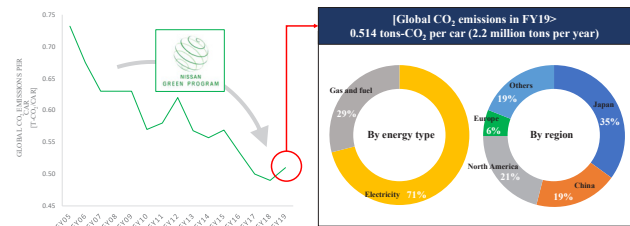
In addition, efforts have been made to reduce CO₂ emissions by reducing the amount of energy used to produce these vehicles. Further innovations will be made in the future to make this a reality.



Initiatives for life-cycle carbon neutrality

Under the Nissan Green Program, the CO₂ emissions from car production were successfully reduced by 30% per car from 2005 to 2019. The current energy used in manufacturing is composed of 71% electricity and 29% gas and fossil fuel. Finding an approach to reduce this gas and fossil fuel usage to 0% will be a priority in the forthcoming years, and future innovations will be invaluable in making carbon-neutral manufacturing and vehicle life-cycles a reality.

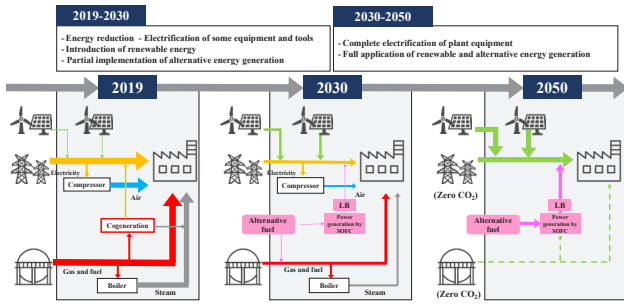
■ Shift from dependence on gas and fossil fuels toward carbon neutrality in production and strengthened responses in Japan, China, and North America



Reduction of CO₂ emissions during production

3.2 Initiatives for Carbon Neutrality in Production

A roadmap to achieving carbon neutrality in Nissan's plants by 2050 has already been determined with ongoing technology development. Current plants operate with electricity and high-pressure air from compressors as power sources, as well as steam, heat, and electricity converted from gas and fossil fuel. Energy consumption is planned to be drastically reduced by 2030. Moreover, solid-oxide fuel cells (SOFCs) using clean alternative fuels will be used to generate carbon-neutral power, expanding the trial of clean energy generation in combination with renewable energy sources, such as solar radiation and wind. All production equipment running in the plants will be electrified by 2050, and all energy sources will be replaced by renewable and clean energy generation.

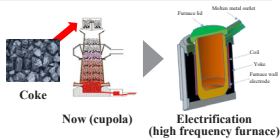


Roadmap for reducing CO₂ emissions from production

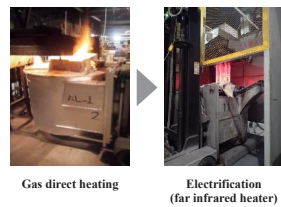
One of the most difficult production processes to electrify is the casting process, especially for carbon steel commonly used for drivetrains, where coke is used to carburize steel while it is melted. Further technological developments are required to use high-frequency furnaces for the electrification of this process. This technology will also be valuable in the efforts to completely electrify the melting process of aluminum alloys commonly used for powertrains. Furthermore, the tools used in factories will also be replaced by electric tools instead of air tools.

It is important to note that the trends in the development of advanced technologies in the energy industry need to be closely monitored, as the future development of new alternative clean fuels capable of directly providing thermal energy as an alternative to conventional fuels (light oil, natural gas, etc.) will require us to pivot our technological development.

Steel casting



Aluminum melting ladle heating



Tool



Ongoing efforts to reduce CO₂ emissions during production through electrification

Relying solely on external sources for clean energy poses challenges to business continuity due to unstable supply and the inability to control costs. Therefore, plans are being developed to test and implement clean energy power generation in Nissan's plants. Carbon-neutral power generation from bioethanol using an SOFC will be tested at the Tochigi Plant with plans to implement this strategy worldwide. Nissan's Sunderland plant in the UK has already begun to use solar and wind power and will further incorporate large-scale clean energy supplies and solar power generation via microgrids in the future.

Alternative fuel and power generation

- Applying the experience of developing SOFCs for automotive to stationary systems
- FY22: Small-scale trial (5 kW or less, 60% efficiency)
- FY24-25: Scale-up trial (30 kW or more, 70% efficiency)



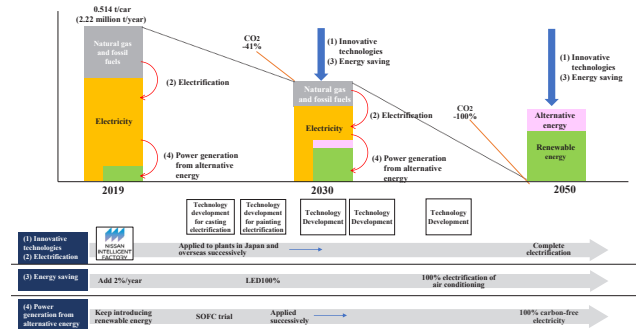
Renewable energy installation



Nissan UK Wind power generation: 6.6 MW
Solar: 5.5 MW
Nissan Mexico Biomass power generation: 2.7 MW
Nissan UK Solar power generation (planned): 20 MW

Alternative fuel and power generation strategies

Nissan is aiming to reduce CO₂ emissions by 41% by 2030 by drastically reducing the energy required to manufacture cars at Nissan's plants and by trialing carbon-neutral power generation strategies. Carbon-neutral power generation and renewable energy procurement will enable 100% carbon neutrality by 2050. The R&D and production technology departments are already collaborating to develop the necessary technologies to achieve this ambitious but critical goal.



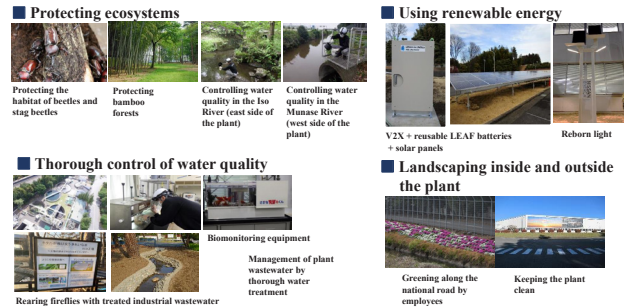
Numerical targets for CO₂ emissions reduction during production

3.3 Approaches to Coexistence between Factories and the Local Environment

Coexistence with the local environment by minimizing environmental impacts is also important for production activities. The area surrounding the Tochigi plant, which implemented the Nissan Intelligent Factory initiative, is full of greenery and a variety of ecosystems. In an attempt to protect the natural environment, environmental dependency was minimized, and load during production was maintained at sustainable levels. Furthermore, the plant acts as an environmentally friendly manufacturing site by protecting the ecosystem, managing water quality, maintaining the landscape, and utilizing renewable energy. For example, the new painting booth at Nissan Intelligent Factory does not use water to collect paint mist. Eliminating wastewater from the painting booth made it possible to eliminate the need for energy for wastewater treatment. Wastewater from other processes is still thoroughly treated to control the water quality. The small stream in the factory that receives treated

wastewater is inhabited by fireflies, which give off beautiful light in the summer.

Minimize environmental dependence and energy demands during production to protect natural environment around the plant



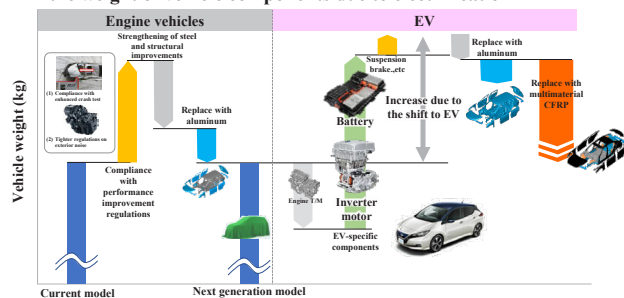
Coexistence with the local environment

3.4 Mass-producible Weight Reduction Technologies Necessary for Electrification

While EVs are becoming increasingly used worldwide, the technologies required for their widespread use extend beyond EV powertrain technologies, such as motors, inverters, battery materials, and other structures, to include critical mass-producible technologies for reducing vehicle weight. EVs are becoming heavier with larger batteries to ensure a longer range, demanding a drastic revision of the vehicle body structure and innovative body weight reduction strategies.

It is common to use ultra-high-tensile materials for parts that require structural strength and aluminum alloys for cover parts to reduce weight; however, the extent to which other materials can be substituted for steel is limited by material strength. The joining of aluminum alloys is conventionally performed with rivets (SPR), which increases the weight of the vehicle in accordance with the number of rivets. To overcome this challenge, welding and innovative technologies are needed for joining different materials, such as aluminum alloys, steel, and resin.

Further weight reduction is needed to meet the need for higher fuel efficiency in engine vehicles. Various factors will increase the weight of vehicle components due to electrification

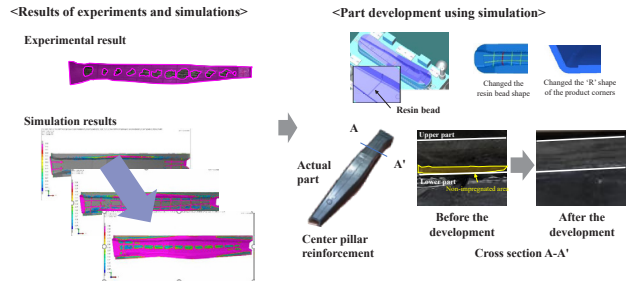


Electrification and vehicle weight

Carbon-fiber-reinforced plastics (CFRPs) have long attracted attention for their potential to reduce the weight of car bodies. Though several decades have passed since CFRPs were first launched, the establishment of mass-production technology has been a perennial issue in terms of cost and cycle time. Furthermore, breakthroughs in the production technology were

insufficient to realize the mass production of CFRPs. However, Nissan introduced a mass-production technology for CFRPs in 2020 through the application of a resin flow simulation, making it feasible to achieve a cycle time of two minutes by applying the compression resin transfer molding (C-RTM) method to mass production. A rate of 2 minutes per car implies that the process can maintain a standard production speed of 30 jobs per hour (30 JPH), revolutionizing mass production for this material.

- Simulation accuracy improved
- Development of parts that satisfy performance requirements by revising the shape of the gate and resin bead using simulation

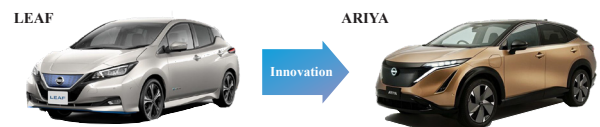


Electrification and vehicle weight

4. ARIYA: A Flagship Vehicle from the Nissan Intelligent Factory

ARIYA features a design that embodies the new Nissan and Nissan Intelligent Mobility, equipped with a lineup of four powertrains to meet a wide range of customer needs, comfortable and responsive driving performance, a new generation of EV powertrains, state-of-the-art driver assistance technologies, and advanced connection technologies.

Nissan's EV innovation began with the first mass-produced EV, "LEAF," in 2010.



- Nissan's first mass-produced EV (since 2010)
- Range of up to 458 km (WLTC mode)
- Nissan's first crossover EV
- Range of up to 610 km (WLTC mode)

	LEAF	ARIYA	
Intelligence	Number of ECUs*: 36	2x Number of ECUs*: 78	*Electrical Control Unit
	Number of CAN** signals: 3,600	2.5x Number of CAN** signals: 9,500	**Controller Area Network
Electrification	Two types of batteries: 60/40 kWh	1.5x Two types of batteries: 91/66 kWh	
	Energy weight ratio (Battery capacity/vehicle weight) 32Wh/kg / 22Wh/kg	1.5x Energy weight ratio (Battery capacity/vehicle weight) 41Wh/kg / 34Wh/kg	

Nissan EV innovation

LEAF has been repeatedly improved during its model life and now has a range of 458 km. In contrast, ARIYA has a range of up to 610 km and has been significantly advanced in terms of electrification and intelligence with twice the number of ECUs installed, 2.5 times the number of signals used for communication and 1.5 times the capacity of the two types of batteries as well as the battery capacity per weight compared to those of LEAF. The four pillars of the Nissan Intelligent Factory were

created to efficiently produce the complex and highly advanced ARIYA. After many years of developing basic and applied technologies, sophisticated product is now being realized.



Four pillars of the Nissan Intelligent Factory

While there have been many challenges and successes in recent years, an innovative automation line has now been completed through the efforts of many Nissan automotive engineers. It was truly a moment of great joy when the line began operating fully automatically, and this happiness and excitement was shared by everyone on-site for this momentous occasion. The Nissan Intelligent Factory will be rolled out globally, with the Tochigi plant as the pilot model.

5. Summary

5.1 Future Challenges in Automobile Manufacturing

While the future remains uncertain, automotive engineers and the broader Nissan team will undoubtedly be able to make further breakthroughs by innovating together. The following are some of the challenges in automobile manufacturing that will need to be tackled in the years to come:

- A new pandemic or friction between the US and China that would wreak havoc on the global supply chain
- Continued efforts are needed to avoid further weight increases in response to electrification, with a requirement for innovative car body weight reduction strategies relating to the use of multi-materials, joining of different materials, and innovative structures, among others
- Market cost impact and increase in risk level due to raw material procurement risk
- Intensifying competition for the acquisition of employees with strong AI and systems skills due to the emergence of new competitors amid a shortage of new talent
- Worsening global hiring environments for automobile production plants

5.2 A Message to Nissan's Automotive Engineers

Hopefully, all the Nissan engineers who are to overcome the challenges of the future will revisit the history and achievements of Nissan's past automotive engineers. These individuals have worked passionately and diligently to develop new technologies with the

perspective of how their hard work and approaches have "paved the way for the times." It is important to understand this history and pass on the lessons from past visionaries to the future.

Although it takes time for a technology to mature, developing the ability to understand its purpose will enable individuals to ask what this technology is useful for, to take action towards achieving future goals, to improve quality, and to promote steady evolution of the tools and products of the industry. These efforts are essential for creating the car of the future through technological innovation alongside a production system that is resilient in the face of change, instability, and new global challenges. Furthermore, we hope that these efforts will contribute to the creation of a human-friendly workplace where people can take pride in their work. Nissan's automotive engineers are responsible for the future of Nissan, and their enthusiasm and efforts will create new ideas that would shape the industry.

Nissan's automotive engineers have always taken action in the spirit of improving and advancing the Japanese automotive industry. The products and new technologies developed by Nissan's automotive engineers have improved people's lives by enabling them to do things they could not or had given up doing before. This technical review will hopefully encourage individuals to take pride in your work, believe in their own abilities, innovate, and continue to change the industry by solving the challenges of the future.

1. Nissan Intelligent Factory Starting from ARIYA

Hidetoshi Okaguchi*

1. Trends in the Automotive Industry

The automotive industry is experiencing a once-in-a-century revolution with rapid changes in vehicle technology related to the connected, autonomous, shared/service, and electric (CASE) areas. These changes have led to the increasing intelligence and electrification of cars, resulting in more advanced vehicles. Thus, it is now necessary to manufacture advanced vehicles with the same quality standards and cost-effectiveness as those of conventional vehicle manufacturing.

In addition to the advances in automotive technologies, the automotive industry is expected to shift in response to a shrinking workforce resulting from declining birthrates and an aging population. This demographic shift will cause the current manufacturing system, which relies on gathering many workers in the same place at one time, to become unsustainable. In conjunction with changes in worker attitudes and critical job skills, these workforce changes will necessitate the creation of workplaces where more individuals can work as well as a shift away from labor-intensive automobile production systems.

Finally, the automotive industry and other industries are facing several major new challenges. With the increasing frequency of pandemics, natural disasters, and problems with semiconductor supply, many industries must become more flexible in response to unexpected situations. Furthermore, there is also a growing sense of international urgency regarding climate change; thus, there is an urgent need to implement concrete measures to achieve carbon neutrality in the automotive industry (Fig. 1).

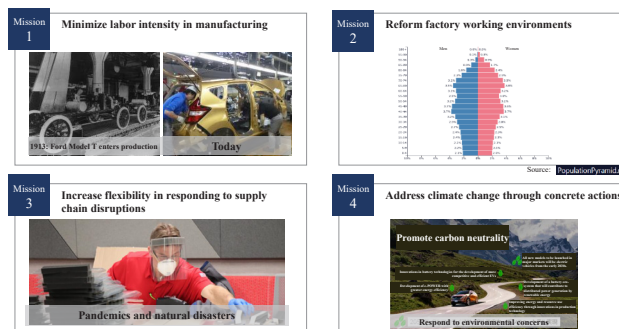


Fig. 1 Trends and priorities in the automotive manufacturing industry

2. Future Direction of Nissan's Production Plants

Nissan Motor's production plants have been modernizing and modifying their production lines under the Nissan Production Way/Alliance Production Way while globalization has accelerated. Since establishment, Nissan has taken advantage of their technology to overcome new challenges. This approach led Nissan to address the environmental impact of automobiles by becoming the first company to mass-produce electric vehicles. The efforts to address industry challenges with new technology have accelerated, leading to the introduction of ARIYA, a flagship Nissan Intelligent Mobility product, at Nissan's production plant.

Flexibility and responsiveness to accelerating industry changes are critical for Nissan's ongoing evolution. With the advancement and diversification of both hardware and software in vehicles alongside the acceleration of intelligence and electrification (Fig. 2), the mainstream vehicle manufacturing process must shift from that of internal combustion engine vehicles to that of electric vehicles. The processes of mounting many components and checking functions that have never been needed before are also necessary for connecting components for autonomous vehicle functions.

*Corporate Vice President **Nissan Product Development Department No.1



Fig. 2 Features of the ARIYA, a Nissan Intelligent Mobility flagship product

However, production plants that rely on human power will not be attractive to workers in a shrinking workforce. Thus, there is a need to eliminate jobs that tend to be avoided, such as those requiring physical effort or repetition of simple tasks, and to provide an attractive workplace environment. Notably, moving away from labor-intensive work will require workers to have skills related to the use of advanced technologies, which will create new opportunities and challenges for employees. Furthermore, unexpected events such as pandemics, natural disasters, and supply chain issues require production sites to respond to temporary changes in production volume and to rearrange the workforce in order to compensate for variable worker availability. This poses an extra burden for both workers and the factory that is unnecessary for normal production, such as having multiple workers learn the same task for redundancy and ensuring that workers have developed necessary skills from their training to allow for redeployment if needed.

On a global scale, initiatives are accelerating internationally to protect the environment, demanding that corporations implement more environmentally friendly initiatives and practices than in the past. Consumer sentiment is also changing to expect companies to proactively address environmental concerns and portray a “green” image through their practices and products.

Given the variety of challenges facing the automotive industry, it is important for the Nissan Intelligent Factory to have the flexibility to respond to changes in the workforce and customer sentiments and to enhance the resilience of the manufacturing process against a variety of challenges. This must be achieved without excessively decreasing profits by minimizing costs that would not have been necessary in normal production processes. It is also critical to ensure that manufacturing quality is not affected by changes made to the production process. Viewing flexibility and resilience against challenges as key features in evolving manufacturing, the Nissan Intelligent Factory introduced equipment and machinery that have been established through the development of basic and applied technologies. These digital technologies were then connected as a single production system operated by highly skilled workers. The Nissan Intelligent Factory is an initiative that will

ensure plant competitiveness and the ability to profitably create Nissan Intelligent Mobility products for decades.

3. Four Pillars of the Nissan Intelligent Factory

The four pillars of the Nissan Intelligent Factory were established based on the background presented in Sections 1 and 2 to define the challenges and objectives to be addressed by the factory (Fig. 3). The Nissan Intelligent Factory consists of the latest technology for each process based on these concepts. The core production technology is supplemented by cross-sectional systems necessary for maintenance and quality control

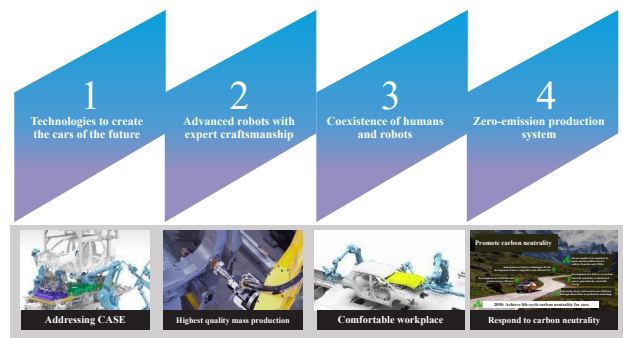


Fig. 3 The four pillars of the Nissan Intelligent Factory

3.1 Technologies to Create the Cars of the Future

In recent years, production plants have been required to adapt in order to keep up with the advancement and electrification of vehicles owing to accelerating changes in the CASE areas. The car of the future, that is, a car with a wide variety of specifications to meet the needs of the growing diversity of users who desire advanced technologies in their products, is represented by Nissan Intelligent Mobility. For example, it is important to have a variety of powertrains to meet the diverse needs of customers; thus, the ARIYA has four powertrain alternatives that allow customers to select between two types of batteries and two types of drive systems. Determining the common and customizable elements of the product structure and designing the product, process, and equipment to minimize the changes required for customizable elements enhance the ability to easily adapt to current and future production changes.

ARIYA is equipped with 78 electrical control units (ECUs) that provide the “intelligence” control for the car, which is more than twice that of the conventional Nissan electric vehicle, LEAF. This advancement required the development of systems for high-speed data communication and expansion of the data-writing process, which can be manufactured at the production plant.

The diversification of available cars leads to the diversification of potential incidents in the process of production, shipping, and quality assurance. The visualization of product quality and equipment abnormality data using digital technologies to accurately

identify these complicated incidents, alongside the development of a system that provides workers with data on all manufacturing equipment, has contributed to seamless production processes. To this end, the following technologies and processes have been integrated into the Nissan Intelligent Factory:

- Batch mounting system for the powertrain (Fig. 4)
- Digital technologies to improve worker learning
- New joining process for dimple welding
- Establishment of electric systems for automobile intelligence
- Automation of the magnet-free field motor winding (Fig. 5)
- Automatic inspection of paint job appearance
- Integrated automatic inspection of specifications and scratches
- Assured quality control using a quality gate
- Equipment failure diagnostic system and tools for predictive and preventive maintenance of equipment

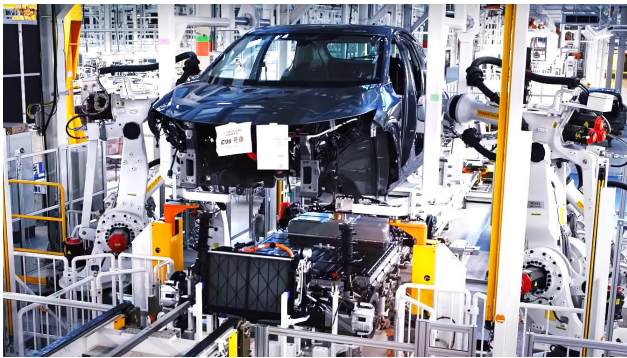


Fig. 4 Batch mounting system for powertrain



Fig. 5 Automation of magnet-free field motor winding

3.2 Advanced Robots with Expert Craftsmanship

Expert craftsmanship refers to work that makes full use of visual, tactile, and auditory perception, based on the accumulated experience and training of a skilled worker. This is an essential element for the production of high-quality cars. Passing on the skills of expert craftsmen to robotic operations and machine control circuits will allow workers to focus only on improving work sites where their skills offer greater added value, conducting inspections of components where perceived

quality is difficult to assess automatically, and performing specialized work regarded as challenging for machines. This combination of robotics and skilled craftsmanship leads to the production of vehicles of the highest quality.

The work of expert craftsmen (Takumi) was repeatedly analyzed to quantify the domains of sensing, information processing, and actuation. In addition to quantification, the process and outcomes of intuitive decisions made by craftsmen using their vast experience were translated into logic. This strategy, in conjunction with development of basic and applied technologies that combine state-of-the-art high-performance sensors, cameras, and image-processing technologies, made it possible for robots to demonstrate expert craftsmanship in assembly and quality inspection work.

Robots can perform precise, repetitive operations and work at a consistent level to achieve quality beyond that of craftsmen in certain areas. Furthermore, if an unexpected event causes a temporary change in production volume, robots can quickly start and stop again without incurring extra costs, which increases their resilience in the face of production changes or disruptions. To this end, technologies for the following processes have been integrated into the Nissan Intelligent Factory:

- Automatic tightening and alignment of suspension links (Fig. 6)
- Automatic headlining assembly
- Automatic cockpit module assembly
- Automatic inspection of painting appearance
- Integrated automatic inspection of specifications and scratches (Fig. 7)



Fig. 6 Automatic tightening and alignment of suspension links



Fig. 7 Integrated automatic inspection of specifications and scratches

3.3 Coexistence of Humans and Robots

Physical and mental stress on workers has been reduced by partially automating tasks that are physically demanding, such as heavy lifting, upward and bending postures, and repetitive work; processes that are stressful but production-critical; and operations that require considerable memory. The Nissan Intelligent Factory environment has been established to reduce the burden on workers by capitalizing on the advantages of automated processing through digitization, data collection, and communication. However, tasks that require manual calibration each time will continue to be carried out by workers as robots are poorly suited to these tasks. Thus, a work environment where humans and robots can coexist has been achieved by optimizing the assignment of tasks to integrate work for which robots are well suited with specialized or rewarding tasks that are performed manually. This combination allows both humans and robots to perform at their best in their respective areas of expertise and creates a more inclusive and encouraging working environment for employees. This integration is well represented in the following processes:

- Batch mounting system for the powertrain
Automatic tightening and alignment of suspension links
Automatic headlining assembly (Fig. 8)



Fig. 8 Automatic headlining assembly

3.4 Zero-emission Production System

Nissan Motor Company has been actively engaged in the company-wide adoption of wind and solar power, cogeneration, and other initiatives as part of the Nissan Green Program.

To achieve carbon neutrality across the entire life cycle of cars—including corporate business activities—by 2050, the company will further increase the use of wind and solar power generation and electrify the power sources for plant equipment by 2030. The company will also work on the adoption of alternative fuels and power generation—such as bioethanol, hydrogen, artificial methane, and solid oxide fuel cells (SOFCs)—and is planning to start a demonstration experiment at its Tochigi plant regarding the use of SOFCs in its production facilities in 2022.

The Nissan Intelligent Factory will contribute to carbon neutrality by electrifying plant equipment as it

adopts innovative technologies, improving the energy efficiency and reducing the material footprint through recycling.

For example, a water-based paint that cures at low temperatures was developed for the new painting process, making it possible to lower the baking temperature from 140°C to 85°C. Consequently, energy use was reduced by 25%, representing a significant contribution to carbon neutrality. The following processes and technologies are related to the goal of achieving carbon neutrality at the Nissan Intelligent Factory:

- Integrated painting of body and bumper (Fig. 9)
- Dry booth for painting
- In-house power generation using alternative fuels.



Fig. 9 Integrated painting of body and bumper

4. Nissan Intelligent Factory Value Proposition

The creation of production lines compatible with the electrification, intelligence, and diversification of automobiles through the integration of advanced robotics with human workers offers the opportunity to create a more inclusive working environment that produces high-quality modern vehicles. Importantly, these production lines are also more adaptable and resilient to the various challenges facing the automotive industry. For example, even when unexpected events such as pandemics or semiconductor supply shortages occur, highly automated processes can be promptly stopped and restarted flexibly to meet the demand without incurring extra costs. This will also contribute to increased business profits by reducing the cost of production through the labor-saving effects of automation and digitalization, as well as the reduction of energy costs through changes in manufacturing processes such as integrated body and bumper painting.

Importantly, the implementation of the Nissan Intelligent Factory will make a significant contribution to achieving carbon neutrality in the automotive industry and will allow plants to evolve in parallel with the ongoing evolution of vehicles and the automotive industry more broadly. Together, the advantages of the Nissan Intelligent Factory will enable automakers to continue their business and evolve to meet customer demands for upcoming decades.

5. Summary

The Nissan Intelligent Factory was first implemented at the Tochigi Plant, where the ARIYA, a flagship Nissan Intelligent Mobility product, is being produced. The Nissan Intelligent Factory concept announced in 2019 was presented at the Tochigi Plant in October 2021 for internal and external individuals for the company, revealing the actual product. This presentation offered a unique opportunity to communicate the value of the Nissan Intelligent Factory, which will contribute to the enhancement of the Nissan Motors brand and customer confidence. The development of manufacturing technology will continue in earnest to keep pace with the rapid evolution of automobile technology and will be implemented in both Japanese and overseas plants as appropriate, in line with facility renewals and the launch of new vehicle models.



Fig. 10 Concept announcement in 2019

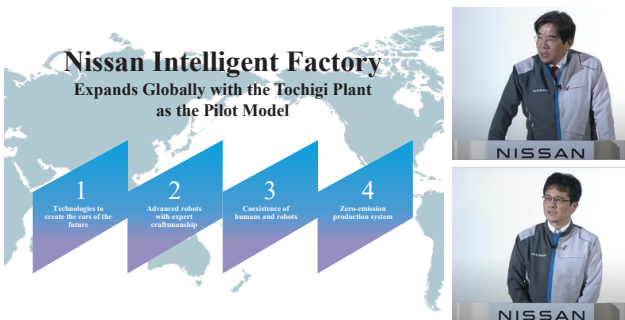


Fig. 11 Presentation at the Tochigi Plant in 2021

Authors



Hidetoshi Okaguchi

2. Application of Next-Generation Underfloor Process Accommodating Various Powertrains

Hiromasa Tsuchikane* Atsushi Ugaji** Yoshihisa Naito***

1. Introduction

As global activities for carbon neutrality have been accelerating, Nissan Motor has been aiming to realize carbon neutrality throughout life cycles, such as by accelerating the implementation of electric vehicles (EVs, e-Power) at an unprecedented level.

Meanwhile, production sites are experiencing prospective reductions in the numbers of highly skilled technicians and workers as the birthrate declines and the population ages in Japan, Europe, and Asia. Therefore, it is urgently necessary for vehicle assembly plants, as labor-intensive facilities, to take measures against this issue (Fig.1).

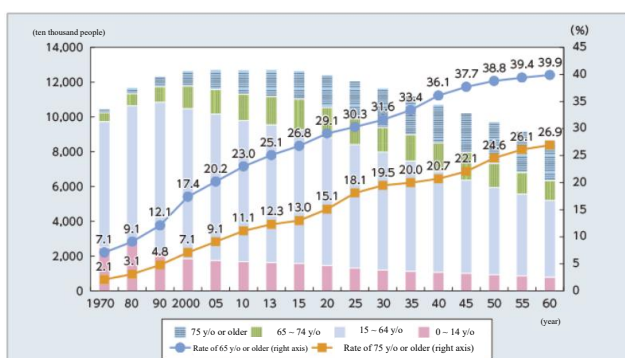


Fig.1 Transition of population by age and population aging rate

As described above, the social environment is currently changing quite rapidly, and vehicles are also changing rapidly with electrification. To respond to this evolution flexibly, the Nissan Intelligent Factory (NIF) at Tochigi Plant applied a next-generation underfloor process, as introduced here by Production Engineering.

2. Process required for next-generation production site

If vehicle electrification, the declining birthrate, and the aging population mentioned above are considered, automotive production sites are required to take two main actions.

2.1 Flexible production process

To realize a decarbonized society, the prevalence of electrified vehicles, which have batteries and motors, such as EVs and e-Power, must increase rapidly (Fig.2). Conventional vehicles, which have internal combustion engines (ICEs), will also be produced for some time.

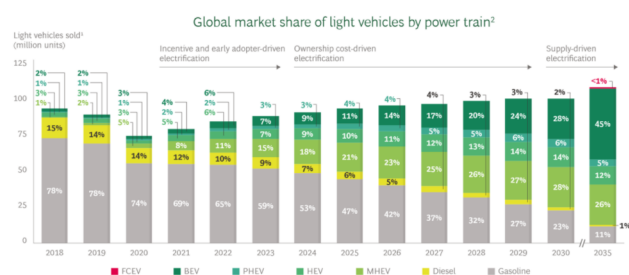




Fig.2 Estimation of electrified new car sales

Thus, production sites are required to operate existing production lines efficiently to produce various old and new powertrains, including EVs, e-Power, and ICEs. However, the arrangements of parts and structures are widely different between EVs and conventional vehicles (Table.1). Thus, various models also have different processes and operations; accordingly, mixed production in an existing production line does not enable workers to perform the same operations in the same process for cyclic operations, resulting in considerable losses of quality and working time.

Table.1 Comparison of structural differences between ICEs and EVs

Vehicle type	Underfloor parts layout	Part count	Parts weight difference	No. of bolts
ICE		16	-	32
EV		8	ICE + 500 kg	52

*Nissan Product Development Department No.1

Particularly for EVs, further technological development and evolution are expected in the future, and the trend of EV structures is fluid; consequently, production sites are required to handle such electrified vehicle structures flexibly. Therefore, in this study, the objective was to achieve efficient and flexible production of various powertrains by utilizing an existing production line and applying a new method.

2.2 Production process accessible to everyone

At present, in vehicle assembly plants, processes for assembling the underfloor parts of vehicles include many operations performed by highly skilled technicians, such as heavy work and elevating work (Fig.3).



Fig.3 Hard elevating work

In addition, the globally declining birthrate and aging population will cause the number of workers to decrease. In order to retain workers, it is necessary to reduce the high-impact operations that workers must perform, such as heavy work and elevating work, through appropriate planning processes that make these tasks accessible to everyone.

Vehicle electrification will also lead to large and heavier batteries, which will increase the number of tightening points (Table.1). Accordingly, underfloor operations, where many elevating actions are concentrated, will impose more burdens on workers than ever, requiring further measures to be taken to improve the work environment. Consequently, in this study, the objective was to realize a production process that is accessible to everyone by reducing overburdened operations for workers.

To achieve these two next-generation processes, the NIF at Tochigi applied two systems: the “Underfloor parts batch-mounting system” and “Suspension link automatic tightening system,” which are introduced in Chapters 3 and 4, respectively.

3. Underfloor part batch-mounting system

As described in the preceding chapter, to realize a production process that is flexible and accessible to everyone, an underfloor parts batch-mounting system was introduced, as reported in this chapter.

3.1 Accommodation to various powertrains

Previously, in multiple processes, dedicated lifters have been used to install powertrain parts, such as engines, transmissions, and large EV batteries in the underfloor areas of vehicles. (Fig. 4 Before). In addition, supports for parts fitted on lifters had to be replaced manually according to the part specifications. Mixed production of ICEs and EVs, which have different components, in such processes caused their work times to differ because of the differences between the operation items (tooling change/mounting operations) in those processes. Then, workers were distributed according to the most time-consuming case, resulting in a loss of waiting in some models.

This time, the process design was revised: the operations affected by differences in the powertrain specifications were moved to sub-lines, the combination of the operations could absorb time differences, and a newly developed pallet system was applied so that the operations of mounting parts assembled in the sub-lines of the vehicle could be integrated into a single process to achieve batch-mounting (Fig.4 After).

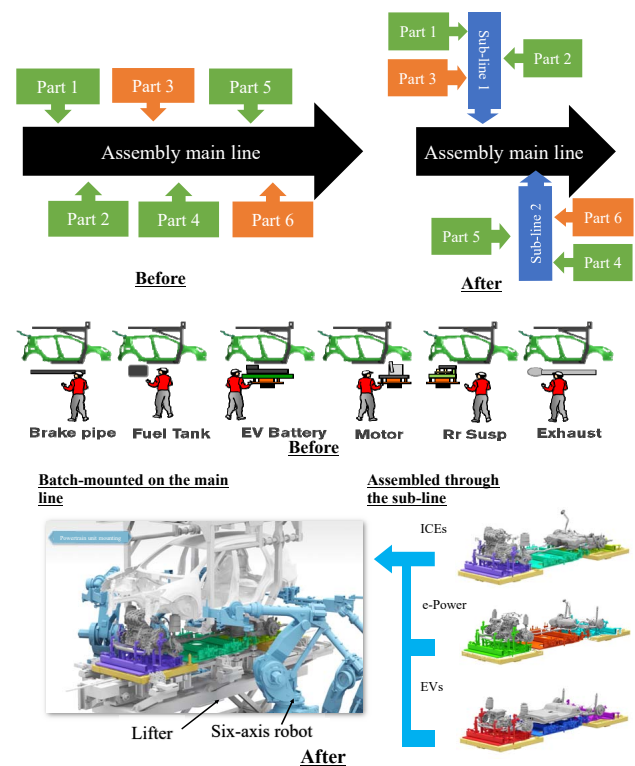


Fig.4 Before and after introducing the underfloor process

In addition, full automation of batch mounting was achieved by measuring the dimensional tolerances of each vehicle between the vehicle body and underfloor parts to develop a logic for automated positioning.

3.1.1 Pallet system

The conventional mounting process employs a method to integrate supports for parts with lifters. Meanwhile, an upper/lower two-layer pallet system was developed in this study (Fig.5).

The lower layer has a fixed shape to function as a conveyor, and the upper layer has a structure exchangeable according to the vehicle model and powertrain as a section touching the vehicle body and parts.

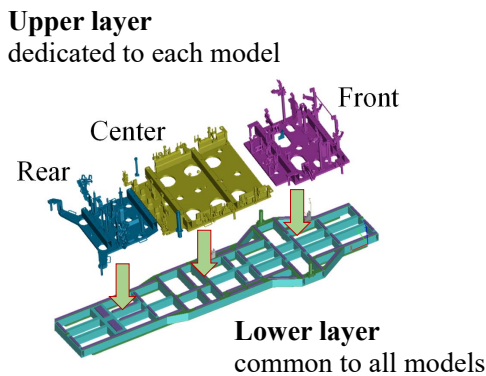


Fig.5 Two-layer pallet

An ordinary pallet system has complicated mechanical adjustment functions to absorb the effects of various accuracy variations of the part supports and parts to be mounted. The functions must be maintained and accurately controlled. In this study, a two-axis robot-type positioning function was provided for the lifter. A method of absorbing the part accuracy variations was adopted, where each upper pallet was aligned with a conveyed vehicle body to simplify the pallet accuracy control.

A system to feed bolts to a tightening robot directly without a pallet as an intermediate was developed to eliminate bolt jigs on the pallet that were previously necessary for feeding bolts to a tightening unit and reducing the pallet cost.

3.1.2 Positioning logic

The rear shock absorbers installed on a vehicle body and rear suspension link arms mounted on the rear pallet cannot be aligned and connected without any adjustment by lifting the latter (Fig.6). Therefore, the position data of a vehicle and the position data of the rear suspension link arms were used to correct both positions, and six-axis robots were employed to position the shock absorbers to achieve alignment.

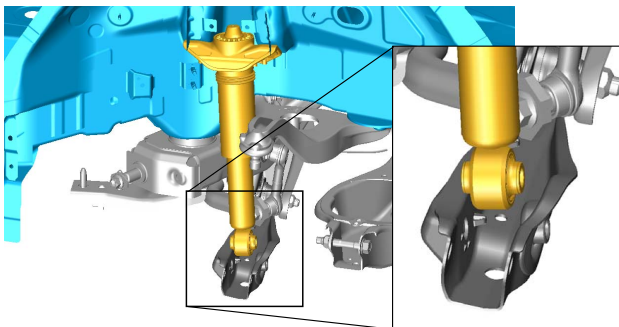


Fig.6 Alignment of rear shock absorbers

Specifically, rear shock absorbers are installed on a vehicle body in the preceding process (Fig.7 [1]). Following this, a vision system is used to measure the assembly accuracy of the rear suspension on the pallet in a sub-line (Fig.7 [2]).

The vision is also utilized to measure the vehicle position (Fig.7 [3]), the measurement error effect is minimized by photographing multiple points, the two-axis robots on the lifter are used to adjust the position of the rear pallet, and the rear suspension is moved to a fitting position (Fig.7 [4]).

The six-axis arm robots hold the rear shock absorbers and correct them to the positions of the rear suspension link arms based on the measured assembly accuracy of the rear suspension (Fig.7 [5]). The lifter moves upward to complete the connection (Fig.7 [6]).

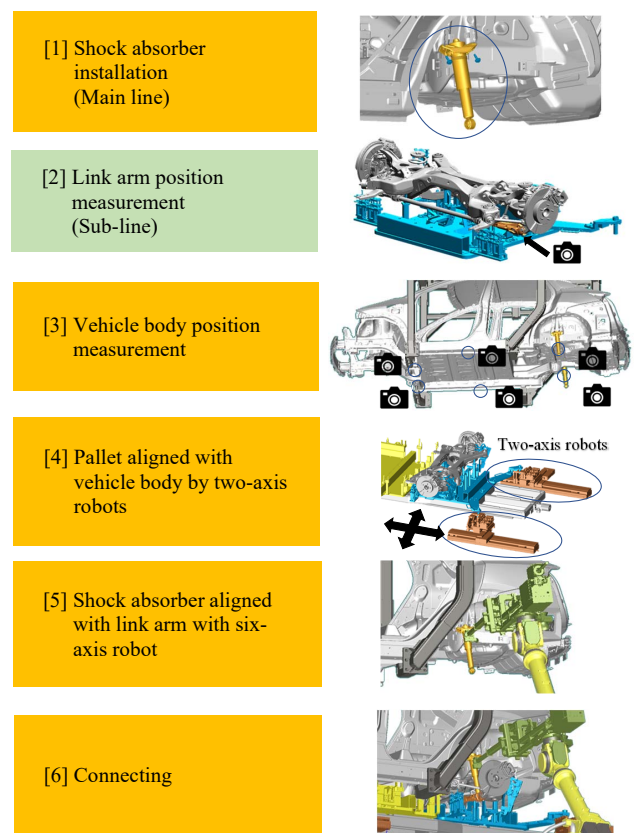


Fig.7 Rear shock absorber alignment process

3.2 Automation of tightening process

In the conventional underfloor process, workers elevate their work for assembly. The parts handled in the underfloor process are important and require reliable tightening; therefore, large and heavy tightening tools were applied. Because bolts differ in size and tightening torque depending on their tightening points, tools are exchanged frequently, resulting in overburdened work. To realize a production process that is accessible to everyone, as mentioned in Section 2 of this chapter, it is necessary to resolve these issues. This process is introduced in the following subsections.

3.2.1 Realization of in-line automatic tightening

To eliminate high-load tightening operations in the underfloor process, tightening automation is promoted. Rounded-tip bolts, which are robust against misalignment and suitable for auto-tightening, were applied. Positioning mechanisms advantageous for auto-tightening were also incorporated into the vehicle parts. In addition, it is necessary to reverse the bolt direction because downward-pointing bolts are conveyed and supplied to the robots because of the structure of the bolt feeder, and they are tightened upward. Accordingly, a unique bolt-reversing system was developed for automatic feeding to reverse each bolt and align them in the tightening direction of the vehicle body. A flexible socket system was employed to change the socket sizes with a single action to tighten different bolts, from M8 to M14.

To place a bolt in an underfloor tightening point, approaching through a narrow gap between obstacles such as a pallet and conveyor for the pallet, a tool more than 1.4 m long was utilized, and a vision system for measuring and correcting the position of a tightening point that ensures accuracy even over a long range was employed. The utilization of these items enabled elimination of the effects of variations in the on-pallet part, mounting, conveyance equipment production, and stoppage accuracies and ensured a bolt position correction accuracy of ± 0.5 mm, leading to the realization of full tightening automation (Fig.8).

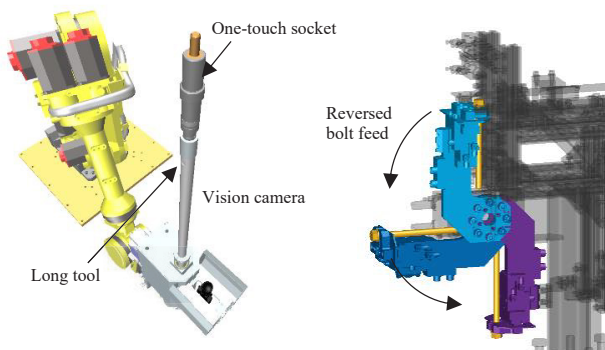


Fig.8 Bolt feeding system and automatic tightening robot

4. Suspension link automatic tightening system

As mentioned above, the issues existing in the underfloor operations of the main line are also present in the sub-lines, so similar activities are performed. As an example, this chapter introduces a system to tighten link bolts in a multi-link suspension unit automatically.

4.1 Link bolt tightening mechanism

A suspension unit consists of a suspension member with a motor unit mounted, axle modules with hubs on which tires rotate, brake rotors, brake clippers, and links that connect the suspension member and axle modules. The links and axle modules as well as the links and suspension member are tightened by bolt-nut systems

that pass through those parts (Fig.9).

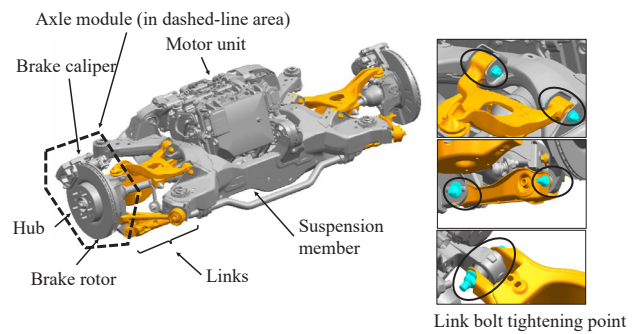


Fig.9 Suspension unit link bolt tightening mechanism

In this link bolt tightening process, similar to an underfloor process, workers had to grab and use different, heavy, high-torque tools for different tightening positions of various models within a single process in the past (Fig.10).



Fig.10 Different tightening tools to be used for different points

Furthermore, as tightening a bolt-nut system requires placing a tightening tool on one side and an anti-spin wrench on the other side, workers had to perform a two-handed operation in which it was required to place a heavy tool in a tightening point with the non-dominant hand.

To automate such physically overburdened two-handed link bolt tightening operations, this equipment applies a new concept regarding the combination of robots and tightening tools.

4.2 Tightening action by two opposite robots

The automatic tightening system consisting of robots and tightening tools has three main issues.

The first issue is the variation of the bolt position caused by the aggregated dimensional accuracies of a conveying trolley, jig, and workpiece. This variation does not allow a robot to play back a taught position or to establish the alignment of a bolt and tightening tool, so that the bolt and nut cannot be rotated.

The second issue is that the different shapes of the link bolt tightening sections include peripheral parts, as

shown in Fig. 9, requiring a tightening tool to approach the required point according to shape and placement.

The third issue is that the use of a dedicated tool whose tightening-reaction support and anti-spin part are designed according to each shape causes the number of tightening tools and robots to increase in proportion to the number of tightening points. In this case, multiple points cannot be tightened from a single location at which a worker can handle the operations; therefore, a larger equipment installation area would be required.

To resolve these issues, the proposed system employs a couple of robots with a vision system and tool-changing mechanisms and placed on both sides of a workpiece to allow them to reproduce worker operations of using both hands to handle general-purpose tools and tighten multiple points (Fig.11).

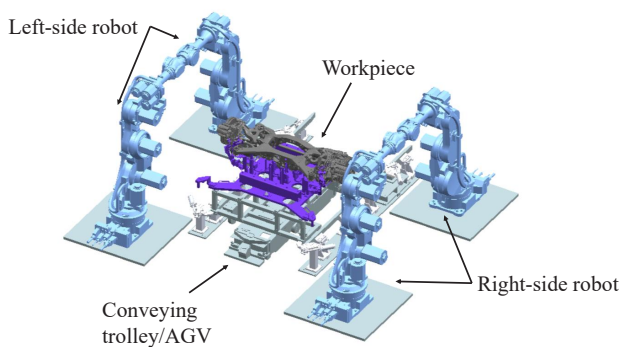


Fig.11 Link bolt tightening with a couple of robots

Firstly, to handle variations in the bolt position, a vision system developed for NIF was applied similarly to the underfloor process, introducing a 3-D position-correcting system composed of low-cost general-purpose equipment. One of the robots has a camera installed, which detects the position of the object workpiece. The detected position data are shared with the other robot so that the two can correct their motions based on the same data and handle bolt misalignment.

Secondly, to adapt to the different shapes of each tightening point and to achieve the function in a minimum area, a system employing two robots to operate generally shaped tools independently for tightening was developed. Each of these robots has one anti-spin wrench and one tightening tool (nut runner) to turn a nut on the tightening side and to control the tightening torque installed. The two robots operate independently to tighten the tightening and anti-spin sides at opposite positions. Because the tightening tools are not dedicated to models or tightening points but have simple general shapes, the same tools can approach multiple points for tightening (Fig.12).

In addition, connecting a robot and tightening tool via a tool-changing mechanism enables one tool to be exchanged for another tool according to the tightening points, which permits four robots and four tools to tighten 10 tightening points in total. In this way, compact equipment in which the numbers of robots and tools

remain less than half the number of tightening points was realized.

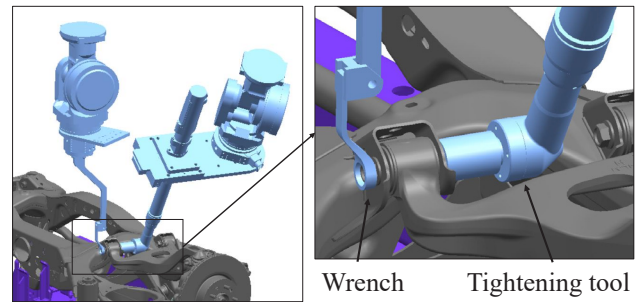


Fig.12 Bolt and nut tightened by two opposite robots

In addition to the resolution of the issues, the work method of a highly skilled technician was incorporated into the robot control to achieve an operating speed equal to that of the worker and the robustness of reliable tool placement.

In bolt-nut opposite tightening, a tool on the tightening side rotates a socket and presses it into a nut simultaneously, which allows the hexagons of the nut and the socket to align with each other and the nut to enter the socket. On the other hand, on the anti-spin side, simply pressing a wrench against a bolt does not enable it to fit the bolt.

To resolve the above issue, focusing on the worker actions performed to fit a wrench into the hexagon of a bolt while turning the wrench on the bolt axis, it was proposed to make a robot reproduce this action. However, if a multi-joint robot reproduces this action, the robot must continually change its entire posture to hold and move the wrench. Because the movable range of a robot is limited in link bolt tightening and the approached spot is small, moving a wrench while changing posture is difficult.

Consequently, a wrench-holding hand whose rotational axis (J6 axis) is aligned with the center of the wrench was designed (Fig.13). This structure enables a robot to turn a wrench without changing its posture and to place the wrench on the bolt quickly and without interfering with the surroundings.

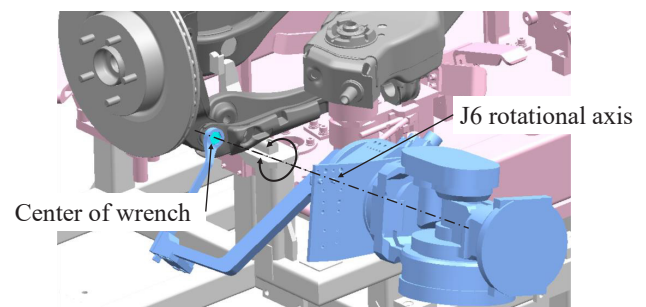


Fig.13 Wrench hand

As mentioned above, this system was realized by combining integrating general-purpose robots, low-cost

vision systems, and simple tightening tools with motions reproducing those of workers.

5. Conclusion

Two production systems were applied in the NIF at Tochigi, realizing a next-generation underfloor process that accommodates various powertrains and suspension units flexibly. In addition, the equipment has separately designed changeable and fixed sections and employs software-controlled robots, enabling hardware modification to be minimized and helping reduce facility investments and the time required to prepare for production of a newly introduced model.

In addition, heavy and elevating work, which is difficult for workers, could be reduced by approximately 15%. Furthermore, the tightening quality ensured by the equipment reduces the physical and mental burdens on workers in important safety-related processes, realizing a production process that is accessible to everyone.

The technology currently applied in the NIF should be developed further to respond rapidly and flexibly to continuously progressing technological innovation and globally and continuously changing social environments. The subsequent challenge will be to distribute the results to the Production Engineering Departments at bases worldwide.

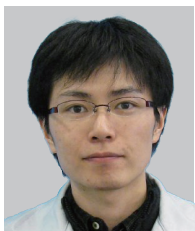
6. References

- 1) Annual Health, Labour and Welfare Report 2014, website of Ministry of Health, Labour and Welfare
- 2) “Why Electric Cars Can’t Come Fast Enough”, Boston Consulting Group, Inc. (April 2021)

Authors



Hiromasa Tsuchikane



Atsushi Ugaji



Yoshihisa Naito

3. Manufacturing Innovation in a New Motor Line through Digitalization and Internet of Things (IoT)

Satoru Iizuka*

1. Introduction

The term digital transformation (DX) is being recognized by individuals as well as production plants. During the recent COVID-19 calamity, whereas manufacturing staff have been required to work at plants, technical staff have been steadily working at home. Therefore, it is essential to know the production status of plants in real time and to support production, even in a telecommuting environment. To realize these objectives, the utilization of digital technologies, such as the Internet of Things, is essential. The powertrain production engineering division, to which the present writer belongs, is promoting activities to eliminate any quality defects, stabilizing quality (not only retaining product quality and production conditions within the control ranges, but also targeting the centers of their standard ranges (the nominal values)), and increasing

the overall equipment effectiveness (OEE), which is an index of production efficiency, to 95%. The new motor line at Tochigi has introduced many digital systems to achieve these targets by exploiting digital technologies (Fig. 1).

This chapter introduces issues that need to be resolved in these systems and provides outlines of the systems.

2. Current situation and issues in application of digital technology

Various issues have been identified to achieve the aforementioned targets, many of which are expected to be resolved by digital technology. This chapter introduces two major issues.

2.1 Stabilization of product quality at high level

Various manufacturers seem to concentrate on the quality control of products, and Nissan also recognizes this aspect as the most important issue. The Quality

Digital technology introduction into new motor assembly line at Tochigi Plant

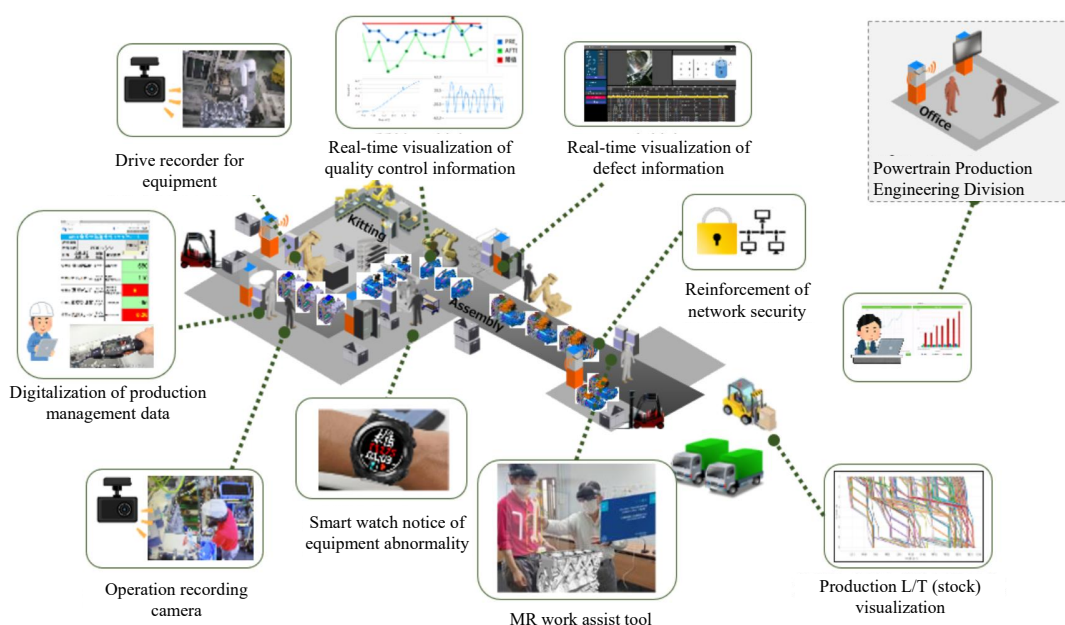


Fig. 1 Digital systems of new motor assembly line

*Powertrain Planning Department

Assurance Depa a leader, the Production Engineering Department, and the Manufacturing Department cooperate in seeking to ensure high quality. Whereas the lineup of products sold by Nissan is shifting from internal combustion engine vehicles to e-power hybrid electric vehicles and electric vehicles, quality control items to be controlled in new model projects are increasing year by year. Manufacturing sites perform quality trend control through daily quick response quality control. However, hundreds of items must be checked manually, causing delays in noticing trend changes and potentially delaying the implementation of appropriate countermeasures. In order to maintain and improve quality, it is important to notice any signs of an impending decrease in quality before the quality trend worsens and to feed this information back to the production conditions of the equipment as soon as possible. How the current daily checks can enable close to real-time control step by step, such as in hours or minutes, is an issue.

2.2 Highly efficient production

Another issue at manufacturing sites is improving production efficiency. If production equipment has a short stop, its recovery work is left to the production site, and the recovery period varies depending on the members and groups at the production site. For highly efficient production, recovery period variations must be minimized. In the current situation, however, the actual ability of each group cannot be determined quantitatively and in a timely manner. In the complicated operations of manufacturing sites, reducing the burden on supervisors and workers to organize the environment for efficient production is an issue.

Another issue is implementing more efficient worker training performed by staff at manufacturing sites. Particularly in new model projects, considerable amounts of time are allowed for training to improve work quality. Further efficiency improvement using only on-the-job training and/or educational content in the form of conventional videos and paper materials is difficult, so the development of a system that enables workers to perform self-learning easily is an issue.

3. Introduction of systems applied to new motor line

This chapter introduces systems applied to the new motor line at Tochigi as countermeasures against the issues mentioned above.

3.1 Real-time data visualization and internally produced agile development

As mentioned in Subsection 2.1 of this chapter, in order to better stabilize product quality, it is necessary to notice any signs of an impending decrease in quality before the quality trend worsens and to feed it back to the production conditions of the equipment as soon as possible. However, when a potential quality defect occurs, a person in charge of Production Engineering uses a USB flash drive to extract necessary data from the production

equipment and utilizes Excel to analyze or visualize changing points. Therefore, action is taken only after a potential defect occurs. To further reduce quality defects and the accompanying errors, it is desirable to detect them before they occur.

Accordingly, the new line introduced a system that collects and visualizes production equipment information in real time. The quality measurement results, as well as the production conditions of the production equipment, which are regarded as factors, are visualized in real time. In addition, if a set threshold is exceeded, a notification is sent to a person in charge to enable this person to notice the condition before a quality defect occurs, accelerating the feedback cycles of quality improvement activities. The technical staff support the site remotely based on that information, even in a telecommuting state.

Such systems have been previously applied in some cases, many of which are based on packaged software. If the standard functions of a package are insufficient, customization is usually performed. Nissan often outsources such customization from an external cooperative company as a form of entrusted development. An issue in this case is the lead time until software development is completed. For outsourcing, a waterfall method is often applied as a development method from the perspective of deliverable assurance, and at least several months can elapse before delivery of the requirements, specification decisions, system development, and testing.

However, manufacturing sites can benefit from a much faster process. If a line has a new potential defect, it is desired to install a necessary sensor immediately that can produce a graph on the next day, even if the graph is not implemented in the system. The conventional system development method cannot handle this task, so that a USB flash drive is used to extract data and Excel is used to draw a graph. When such a system is finished, quality effect factors will have been identified and equipment measures will have already been taken, rendering the system meaningless.

For outsourcing, because an agile method, which does not assure deliverables, is difficult to apply, the new line introduced a system for developing in-house visualization by designating a development team in-house. As a base system, software including collection, accumulation, and data visualization (graphing, etc.) functions was selected. In-house staff can perform customization using this approach, such as creating a screen and changing the data flow. An agile method is applied for development, where the Plan-Do-Check-Action is cycled in a small unit. In the case in which a graph should be shown as soon as possible, similar to the occurrence of a new potential product defect, the first edition with minimum necessary functions is released rapidly and a notification and other functions are added later, enabling the manufacturing sites to be treated immediately and flexibly. Fig. 2 shows an example of an in-house-developed screen. The main functions of this screen are to search for two types of data to be compared and to display the graph. Even the volume of this functional level requires a development period of

approximately three months for outsourcing. However, the period could be shortened to one week by using in-house development.



Fig. 2 Data visualization system screen

3.2 Notification of equipment defect to smart watch

As described in Subsection 2.2, for highly efficient production, the recovery period after a short stop occurs must be minimized. Previously, if a short stop occurred in production equipment, a site worker who noticed the abnormality by looking at an andon or rotating light handled it. For the new line, a system to send a notice to a smart watch (Fig. 3) worn by a site worker in case of an equipment abnormality was developed and introduced. Because a smart watch enables the name of the affected piece of equipment and abnormal contents to be checked, recovery work can be started immediately. In addition, if a worker taking action presses the action start button on the smart watch, other workers can see who is taking action and concentrate on their own work. The introduction effect of the system is estimated to increase the OEE by 2% based on past results. Production lines take action to improve daily and accumulate improvement measures in units of decimal percentage, making a 2% improvement in this system remarkable.

Meanwhile, for this system, the contents of equipment abnormalities and the times of related occurrence/action start/recovery have been accumulated. Nissan exploits these data to analyze differences in action time between work orders or group members to discover improvement points such as working group arrangement, personnel distribution, and work movements (Table 1).

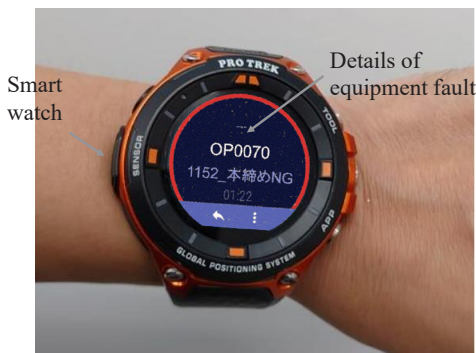


Fig. 3 Smart watch to notice equipment defects

Table 1 Number of abnormality stops and action time by

Working group	Abnormality occurrence times	Average time to start	Remarks
A-group	333	3:29	Average-level instructor, workers
B-group	227	2:20	Highly skilled instructor, workers
C-group	335	3:56	Highly skilled instructor, seasonal workers

In addition, a function to predict short stops of production equipment will be incorporated into this system to shorten recovery periods further in the future.

3.3 Work mastery with mixed reality (MR)

To achieve highly efficient production as described in Subsection 2.2, the period necessary for a supervisor to educate a new worker should be shortened. A new model project experiences several trial lots before the start of mass production. If any changes occur, such as in the design, working order, or work content, education must be performed from the beginning. Hence, education man-hours should be reduced using digital technology to shorten the mastery periods of workers.

For the new line, a work mastery system that exploits MR, a cross reality (xR) technology, was developed. MR goggles are used in the system. A worker wearing these goggles can master a work order and work points through holograms (Fig. 4). Even information such as an assembly point, which is difficult to understand through the existing 2-D information forms such as paper sheets and videos, can be indicated through holograms, enabling anyone to understand the contents easily and thereby reducing the mastery period.

As this system enables workers to study by themselves without supervisor attendance, the number of supervisor man-hours for education can also be reduced. In the new motor line, the numbers of supervisor man-hours for education and worker mastery hours could be reduced by 90% and 50%, respectively.

In addition, after worker training, images from the eyes of the workers are retained as records, which the supervisor can check to determine and feed back whether the worker understood the work correctly, and the mastery level of the worker.

4. Conclusion

Three systems utilizing digital technology were introduced. These were developed not for specific lines, but rather as general-purpose systems, so that they can be deployed globally within Nissan. It is desired to apply these systems to achieve an OEE of 95% with no quality defects and to target nominal values in the future.

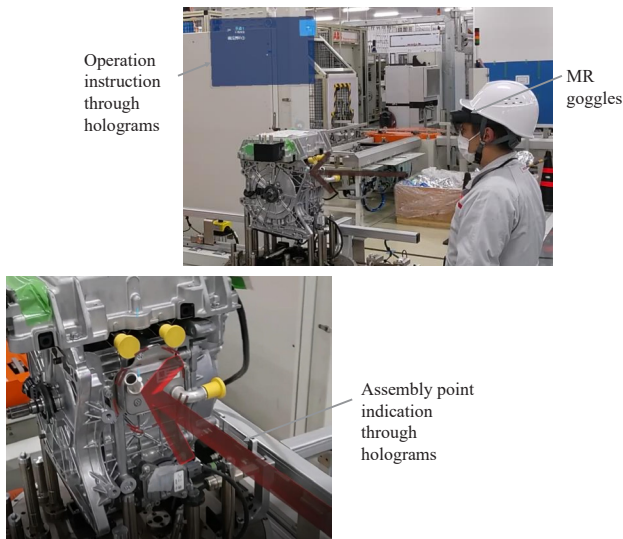


Fig. 4 Mastery work with holograms

Meanwhile, the difficulties of the steps involved in exploiting digital technology increase in the following order: data acquisition, visualization, automatic analysis/prediction, and automatic control. Nissan is at the stage of starting a range of visualization and automatic analyses. Some issues must be overcome for wider implementation of these technologies. One of them is to ensure sufficient human resources. It is said that Japan is behind Western countries and Asian countries such as China, Korea, and Singapore in terms of digitalization. One of the main factors is the shortage of human resources. Although highly skilled people, such as data scientists, must be ensured, people who utilize digital systems, or people at manufacturing sites, will gradually be required to improve their digital literacy.

Using a tablet terminal to conduct start checks, which were previously performed only with paper sheets, causes manufacturing sites to experience significant stress. In a previous incident, a manufacturing site avoided such systems due to the notion that they were difficult to deal with. Nissan has implemented measures to address this issue, including providing educational opportunities and consultation services that can be used by manufacturing-site workers in need. It has also promoted the incorporation of site operations that utilize systems into standard operation sheets.

However, these measures are not sufficient to utilize systems for the maximum effect. For example, the shortage of human resources in maintenance departments needs to be resolved in the future. If a system does not work correctly because of difficulties after the system is introduced, maintenance staff must handle this problem. Although maintenance departments have human resources with digital knowledge and skills, the number is insufficient at present.

As digital technology is a tool, people must fully utilize it to benefit from its advantages. The most important aspect of digital technology application is to employ and fuse this technology into operations at manufacturing sites to enable the manufacturing site to realize its advantages. In addition, to maintain and control the situation, sufficient human resources should be ensured, and training should be implemented along with system development and introduction. Nissan intends to address these issues urgently.

Authors



Satoru Iizuka

4. Process Innovation Through the Development of a Simultaneous Body/Bumper Painting System

Takeshi Goto* Tomoyuki Okamoto** Chie Michiura*

1. Introduction

In 2015, Nissan's main painting plants in Japan became obsolete, 35 years or more after their construction; hence, there was an urgent need to upgrade the facilities.

The painting plant mentioned here is actually a large-scale plant in which a combination of processing steps including pretreatment/electrodeposition processes, a sealing process, an intermediate coat process, a top coat process, and a finishing process is adopted. The cost of upgrading these facilities is expected to exceed 10 billion yen, including the cost of upgrading the buildings. Therefore, upgrading is usually carried out on a 25- to 30-year cycle.

These circumstances led to the commencement of planning for upgrading Nissan's Tochigi Painting Plant, which later developed into what is now known as the Nissan Intelligent Factory initiative (NIF).

The key concepts were established as follows:

- ✓ The production facility should have QCT competitiveness, even after 20 years.
- ✓ Energy-saving facilities shall be established, with the aim of realizing carbon neutrality.
- ✓ Emission of volatile organic compounds (VOCs), substances that pollute the environment, should be regulated.

Plans were formulated considering these target concepts. Integral coating of the body and bumper, which is described in this report, is a novel technology that was developed as a method for realizing the abovementioned target concepts. This technology is introduced forthwith.

2. What is body–bumper integral coating technology?

Body–bumper integral coating technology is technology that enables the simultaneous coating of the metallic vehicle body and the bumper, which is composed of resins. Conventionally, these are produced in separate plants or at separate locations in the same plant. This technology is schematically illustrated in Fig.1.

The main advantages of this new technology are the following rationalization effects stemming from the

integration of two plants:

1. Reduction in initial costs (15%)
2. Reduction in running costs (25%)
3. Reduction in CO₂ emissions (25%)

As detailed in this paper, significant benefits can be obtained from the new method.

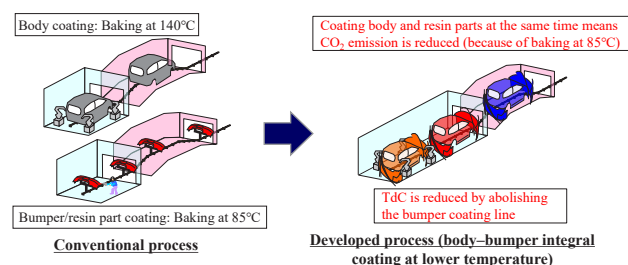


Fig.1 Conceptual diagram of body–bumper integral coating method

Furthermore, producing the body and bumper in the same area completely eradicates the color-matching problem that occurs at the painting site. Therefore, this novel technology can exert a significant effect in terms of improving quality.

3. Development of integral coating

The development of the body–bumper integral coating technology is described in detail in this section. In the conventional, so-called separate coating method, the target materials to be coated are significantly different: metals and resins. To satisfy the coating performance requirements for the coated films, different coating materials are used for each target material. Therefore, different performance requirements are set for the paints for the metallic vehicle body and the resin bumper, and different baking temperatures are used for these coatings. The main difference between the performance requirements is that the paint for the vehicle body needs to be more rigid, i.e., it needs to have a higher strength. Therefore, only materials baked at a high temperature (140°C for 20 min), which ensures that this performance requirement is met, are used. By contrast, the resin paint materials need to be flexible, and the baking process

*Paint and Plastic Engineering Department

**Body Engineering Department

needs to be carried out at a relatively low temperature (85°C) to avoid the resin deformation caused by melting at high temperatures. In other words, the two types of paint have completely different properties (see Table 1 for details).

Table.1 Performance requirements of body and bumper paints

	Common performance criteria	Unique performance criteria	Physical property of coating film
Body coating (140°C)	<ul style="list-style-type: none"> Weather resistance <ul style="list-style-type: none"> -XUVON, natural exposure, etc. Scratch resistance <ul style="list-style-type: none"> - Car washer: wiping with dry cloth, etc. Adhesion property <ul style="list-style-type: none"> - Hot water, humidity resistance, thermal cycle, etc. 	<ul style="list-style-type: none"> Chipping resistance (Surface of steel sheets with low energy absorptency) Window glass adhesion (Bearing capacity against high separation force) 	Coating film that has rigidity and high strength (Bearing capacity against input)
Bumper coating (85°C)	<ul style="list-style-type: none"> Atmospheric deposition resistance <ul style="list-style-type: none"> - Acid rain, bird droppings, pollen, etc. Chemical resistance <ul style="list-style-type: none"> - Gasoline, alkaline substances, wax, etc. Compatibility with indirect materials <ul style="list-style-type: none"> - Double-sided tape, PGF, etc. 	<ul style="list-style-type: none"> Resistance to light collision (Ability to follow the deformation of the resin substrate) Resistance to chipping and cracking at the rear (Ability to follow the deformation caused by stone thrown up by own vehicle) 	Coating film that has flexibility and high elongation rate (Elongation that allows for following the substrate)

Therefore, with the aim of developing a coating that can simultaneously be applied to both the body and the bumper, a material that can be baked at a temperature of 85°C and also satisfies the characteristic performance requirements of both substrate materials was designed (Fig.2).

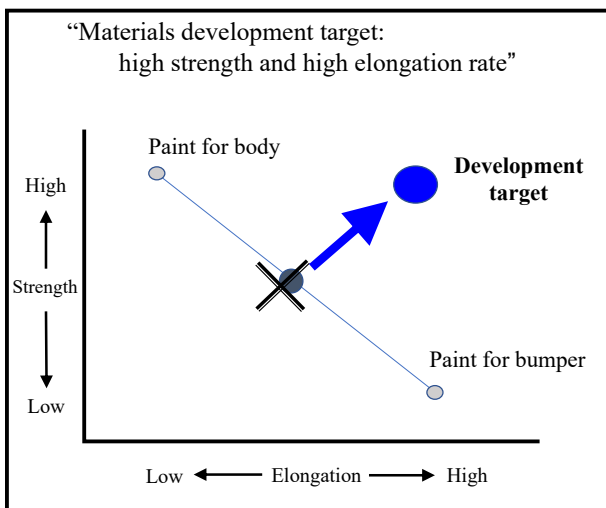


Fig.2 Conceptual diagram showing development target of coating material for both body and bumper

4. Details of material development

If the baking temperature for the body coating is lowered to 140–85°C, the coating film will not possess sufficient strength, a property that is conventionally conferred by thermosetting. Therefore, the development of a material based on a two-pack paint containing isocyanate (NCO), which can be cured even at low temperatures, was set as a goal. At the time of development, no other water-based, low-temperature, 3-wet car coatings had been developed. Therefore, this attempt was a first for this industry.

When designing the material, the fact that two-pack paints are expensive and that it would be necessary to invest in mixing equipment for each paint machine was considered. Thus, although it could be possible to use two-pack paints in the production line for the intermediate

coat (for which there are only a small number of available colors) as well as for the clear coat, two-pack paints are not a viable option for the base coat, because the diversity of available colors would mean that the cost would be prohibitively high.

Therefore, a conventional single-pack paint was used for the base coat. To enable the low-temperature curing of this paint, the method of impregnating NCO from the undercoat (intermediate coat) and topcoat (clear coat), hereafter referred to as the sandwich method, was adopted. In other words, the method of utilizing NCO in layers other than the base coat, which allowed the NCO in the other layers to impregnate the base coat after it had been applied and a film had formed, was invented during this development project (Fig. 3).

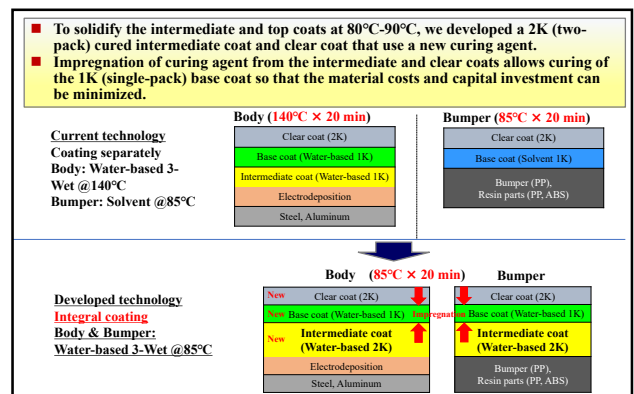


Fig.3 Schematic comparing conventional coating method with the new common material composition (sandwich method)

To obtain a coating film with high strength, flexibility, and elongation, using the sandwich method, the basic composition of the material was selected as detailed in Fig.4.

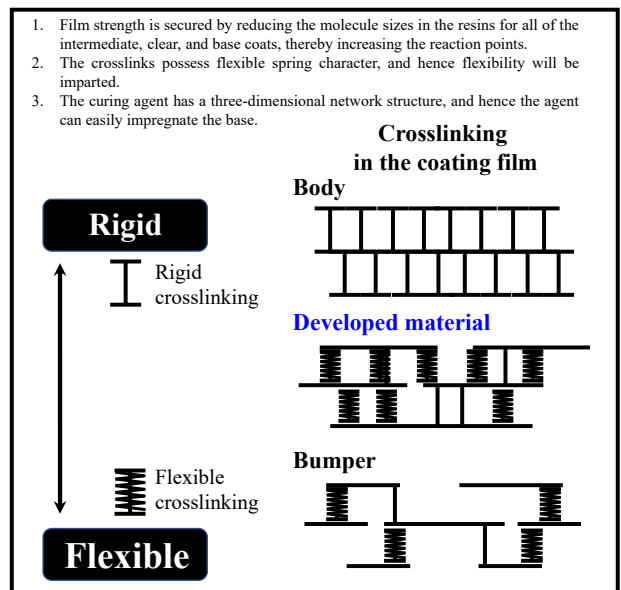


Fig.4 Conceptual diagram of the design of the coating film for the two materials

After fabricating the paint based on the concepts summarized in Fig.4, testing to determine the basic performance of the coated film was carried out; to evaluate the feasibility of its use in an actual production line, the workability was concurrently evaluated.

Conventionally, such evaluations are performed in a certain order. However, the material under development was completely new, and hence, there was a strong possibility that past experience was not applicable. Therefore, the evaluations were conducted concurrently with the aim of minimizing the loss due to rework. While these evaluations were being conducted, the variable factors in the production line, such as the baking temperature, coating thickness, and amount of curing agent, as well as the ranges over which they varied, were identified. In addition, accurate information regarding the margin for the ultimate performance limit (cliff of quality) was obtained to ensure that the developed material would be considerably robust. The relationships between these factors are shown in Fig. 5.

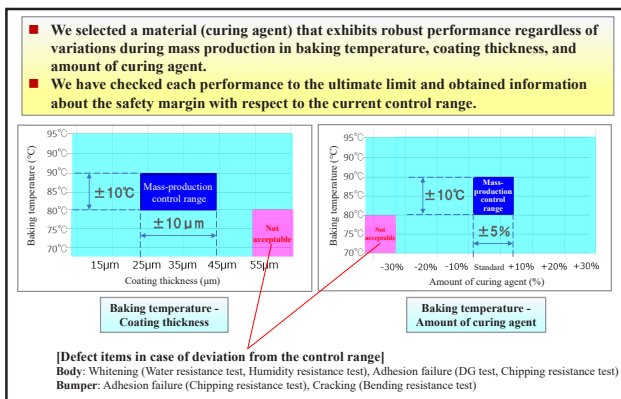


Fig.5 Relationships between baking temperature and coating thickness (left) or amount of curing agent (right)

5. Development of supporting technologies for integral coating

5.1 Development of low-temperature oven for integral coating

To simultaneously bake the resin parts and the vehicle body, which is constructed from steel sheets, the blowout temperature of the drying oven needed to be fixed below the thermal deformation threshold temperature of the resin (95°C). When the blowout temperature was controlled in this manner, problems occurred in certain sections, such as the inner surface of the vehicle body door (Fig.6). Compared to operating the oven with the conventional blowout temperature, more than twice the time was required for the temperature to increase to the specified value in this area (Fig.7). Hence, long machine design were required for the baking and drying oven.

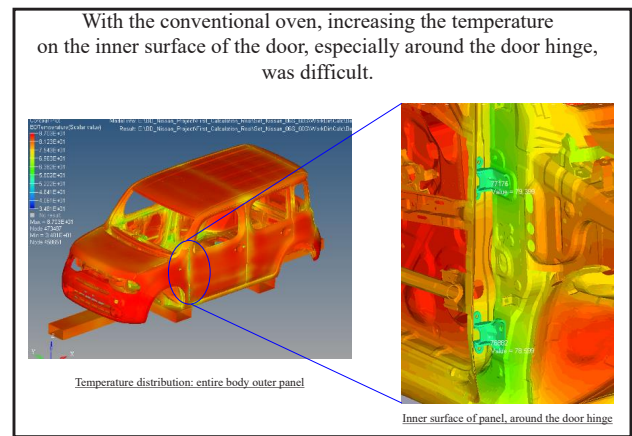


Fig.6 Example of a poorly baked section: around the door hinge of the vehicle body

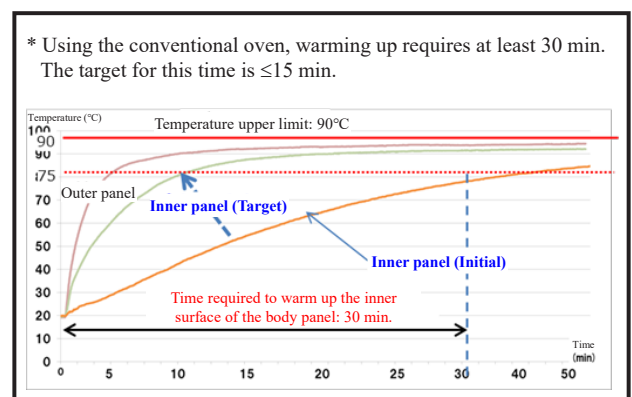


Fig.7 Target and initial (measured) temperature increase curves for the inner surface of the panel

Therefore, to resolve this problem, a flow analysis was conducted using the higher-order total variation diminishing method to calculate the appropriate air flow velocity and volume. Based on the results of this analysis, it was deemed appropriate to design a new nozzle shape for use in the baking oven. Fig.8 shows the results of simulations that visualize the change in temperature of the hot air volume flowing into the vehicle body. In the conventional oven, the hot air failed to reach inside the vehicle body, and heat exchange via convective flow occurred only at the outer surface of the panel. However, when the air flow volume and velocity were increased, hot air entered the vehicle body and convective flow occurred at the inner surface of the panel, as shown in Fig.9. In this manner, it was possible to ensure that, in an actual production line, the target temperature increase curve could be realized, even for the inner surface of the panel.

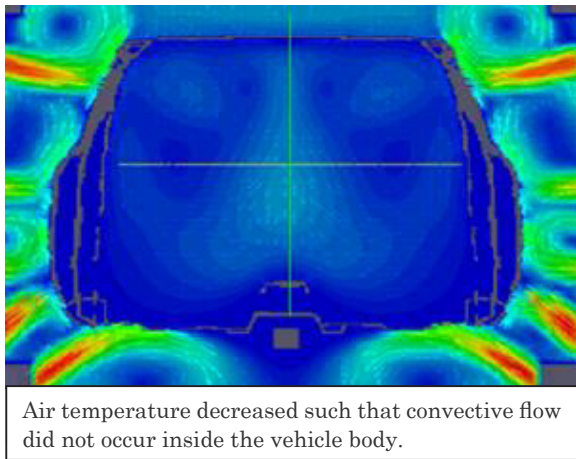


Fig.8 Temperature simulation for the conventional drying oven

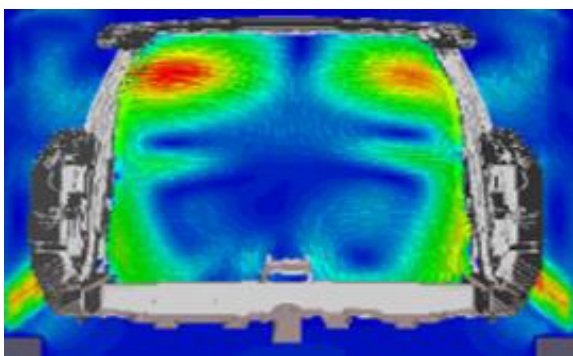


Fig.9 Temperature simulation for the drying oven used for integral coating

5.2 Color matching under integral coating conditions

In automotive coating lines, electrostatic coating is performed to improve the material yield. Because the vehicle body, which is constructed from steel sheets, and the resin parts have different electrical conductivities, it is not possible to obtain the same color for these parts simply by coating them simultaneously.

To solve this problem, all the following conditions need to be the same.

1. Coating environment (temperature, humidity, and downflow air velocity)
2. Paint material
3. Coating conditions (discharge volume, rotation speed, shaping air flow rate, and voltage)
4. Coating locus (distance between objects to be coated, coating pitch, and speed)
5. Coating thickness

In particular, considering point 5, it is important to ensure that the electric conductivity of each workpiece is identical for achieving an equivalent electrostatic coating effect. In other words, the electrical conductivity of all the materials must be the same.

Therefore, in this development project, water-based paints were selected to ensure electrical conductivity, and coating was performed from the grounding point of each part such that the same electrical conductivity would have been achieved regardless of the material. In this manner, it was possible to achieve the same color for

all the materials, leading to an acceptable quality of color matching.

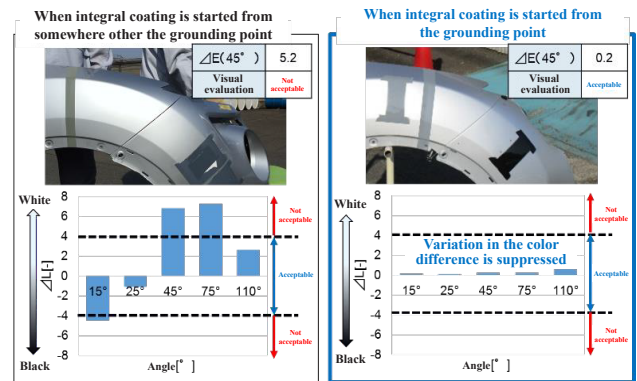


Fig.10 Color as a function of angle: comparison between coating from the grounding point and coating from somewhere other than the grounding point

Even if complete matching of the spectral reflectance is achieved for all the angles, the color of different parts will appear to vary if there is a change in the angle at the interface of the parts.

When using the integral coating method, if this phenomenon occurs at the production site, there will be no room for adjustments because color toning cannot be performed for each material. Therefore, for each part that undergoes color matching, it is important to determine in advance the permissible angle deviation and to conduct surface angle evaluations during the actual color matching evaluation. In this development project, a digital color-matching evaluation system was designed to prevent the occurrence of this problem, as detailed in Fig. 10. The system, used in combination with a 3D scanner, will be used to resolve such problems and prevent their occurrence in the future.

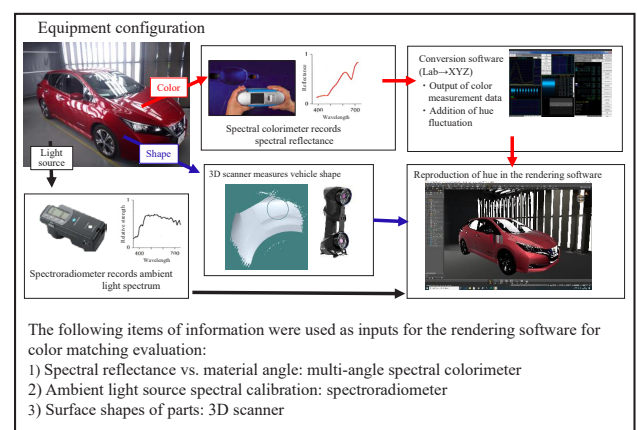


Fig.11 Digital color-matching system

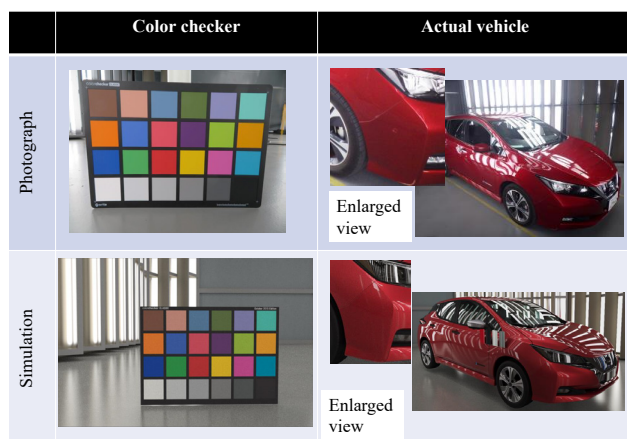


Fig.12 Color tone evaluation: actual photograph vs. Simulation

6. Value and future prospects of integral coating method

By establishing the new body–bumper integral coating technology, 25% reductions in energy consumption and CO₂ emissions, compared to the conventional method, were achieved. Henceforth, this method will be regarded as a new standard method and will increasingly be adopted in newly established production lines and contribute toward the realization of carbon neutrality.

By adopting this technology, it was confirmed that it is possible to abolish the necessity for color matching between the body and bumper of the vehicle, which typically requires long periods of time at the painting site for optimization. Apart from affording the possibility of shorter lead times for the fabrication of new vehicle models and improved stability of quality at launch, this method should lead to the adoption of highly stylish paints (for example, paints with high gradation), which could not be achieved via conventional coating methods. Therefore, it should be possible for manufacturers to offer more attractive colors schemes.

By introducing this novel method, it is also expected that the novel technology can be used to offer customers higher-quality coatings.

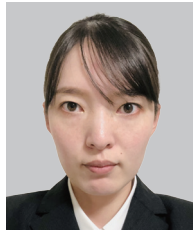
Authors



Takeshi Goto



Tomoyuki Okamoto



Chie Michiura

5. Creation of a Quality Gate through Automated Technology of Appearance and Specification Inspection

Teruyuki Ishiwata* Mitsuru Hirayama* Daisuke Tanaka* Takayuki Moriya**
Yasuo Yamada** Makoto Yamada* Takeshi Honda***

1. Introduction

To produce better cars with high quality, the ideas and knowledge regarding craftsmanship accumulated so far have been organized into the alliance production way (APW). Accordingly, “Synchronization of quality: Thoroughly making goods with quality meeting customers’ expectations through processes” have been designed so that sub-par goods are not accepted, produced, or released publicly.

To achieve this objective, a system of “Necessary quality is defined and assured at a quality assurance stage set in each manufacturing process (from heading to assembly) to complete the assurance within the process” was defined as a quality gate. This chapter will introduce the development of automated inspection technology for achieving quality gates at the Nissan Intelligent Factory (NIF).

2. Process assurance by quality gate

2.1 Necessity of automated inspection by quality gate

Training and maintaining skilled inspectors will become an issue due to the workforce decrease as the birthrate declines and the population ages. Meanwhile, all interior/exterior types and paint colors resulting from the diversification of customer needs must be ensured. To respond to such environmental changes, promoting the automation of inspections is an effective way to produce quality cars. In addition, utilizing inspection data, whose acquisition will be possible with automation, will lead to further prevention of defects.

To promote these aspects, it is necessary to exploit automated inspection technology at a quality gate.

2.2 Expected effects of automated inspections

The following items should be achieved for in-process assurance, promoting automated inspections by quality gates.

- The quality assurance level should be improved through Glass pattern automated inspections. Completely automatic inspections enable stable inspection/judgment abilities to be kept independent of inspector

skills for difficult-to-judge inspections and various specifications.

- Further quality improvement should be attained by exploiting automated inspection data. By controlling automation-provided inspection results for all vehicles sent to the Internet of Things server, a system in which a transition to the next process requires passing quality standards should be established. In addition, exploiting recorded traceable data can lead to early identification of potential defects.

2.3 Application of automated inspection technology

In order to realize automated inspections by quality gates, the following issues at the NIF must be considered: paintwork defects, which greatly affect vehicle design, and specification errors, which ruin customer trust. Here, two application cases will be introduced for 100% assurance inspection equipment.

- In the first case, total assurance of color, clarity, and film thickness in paint processes is achieved (Section 3 of this chapter). Minute paint faults, which can only be detected by experts, become detectable. In addition, 100% measurements of the color, clarity, and film thickness become possible.
- In the second case, assurance of vehicle paintwork secondary defects, glass defects, and specifications, is achieved (Section 4 of this chapter).

Regarding appearance inspections such as those conducted to identify defects on the glass, which are difficult to notice, and inspections of various specifications, stable assurance independent of worker skills can be achieved.

*Production Engineering Research and Development Center
***Paint and Plastic Engineering Department

**Vehicle Quality Engineering Department

3. Paint appearance automated inspection

3.1 System composition and process outline

Multiple robots with inspection/measurement units (Fig. 1) were utilized in the final paint appearance inspection process, and a 100% automated inspection area for bodies and bumpers was established.

The layout is shown in Fig. 2. The upstream side detects paint defects such as dust and seeding, and the downstream side measures color, clarity, and film thickness.

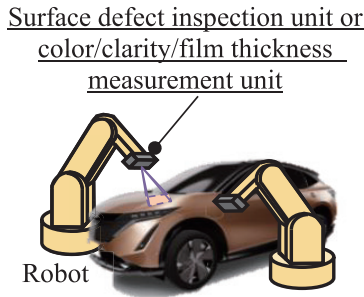


Fig.1 Composition of inspection robot

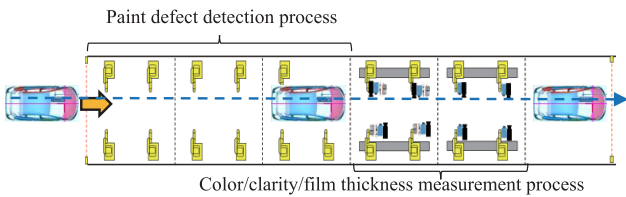


Fig.2 Layout of 100% paint appearance automated inspection area

3.2 Detection of paint defects

<Conventional technologies and issues>

Some widely used paint defect inspection units employ fringe projection-type image recognition techniques. As the fringe projection is moved, multiple images are captured by the camera. Then, highlighting the difference between the maximum and minimum brightness images enables the detection of micro-sized unevenness defects (Fig. 3^{*1}).

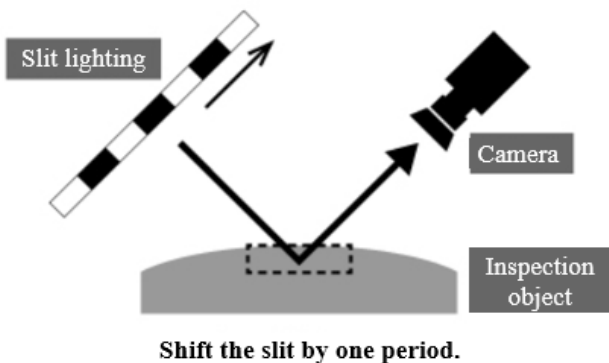


Fig.3 Fringe projection-type image recognition technique

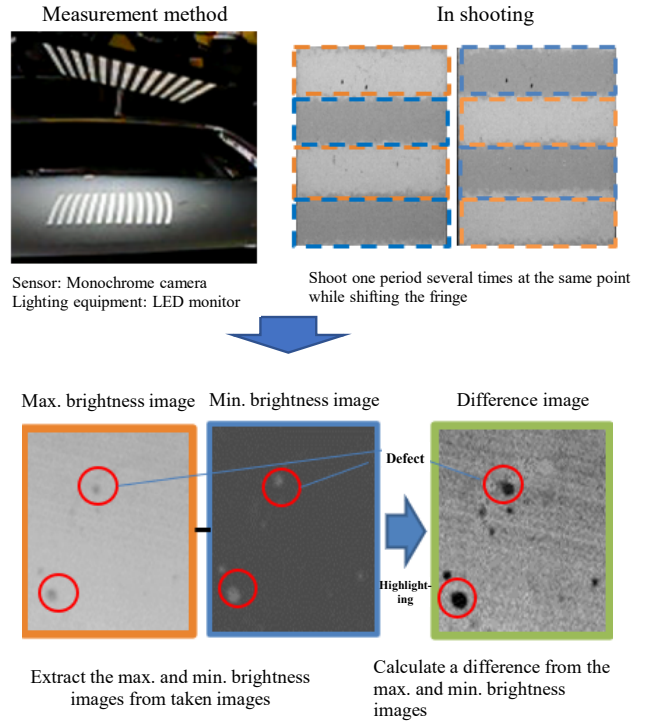


Fig.3 Fringe projection-type image recognition technique

The issue of fringe projection-type image recognition technology is that detection rates vary depending on the brightness levels (L-value) of paint colors.

<Issue-resolving-method details>

To eliminate the detection rate differences due to paint color differences (differences in paint color brightness (L-value)), camera-side gain adjustment by paint color (Table 1) was applied to stabilize the highlighting treatment.

Consequently, even paint defects at a level of 0.3 mm and slight denting crater defects, which could be detected only by humans previously, became automatically detectable (Fig.4, Fig.5).

Table.1 Performance requirements of body and bumper paints

Paint color	Brightness (L-value)	Gain set value								
		1	1.5	2	2.5	3	3.5	4	5	6
K23 (silver)	126	85	100	100	100	60	10	15	10	10
QAB (white)	107	70	100	100	100	80	15	0	5	0
EAU (orange)	83	70	75	100	100	100	75	60	20	0
RBK (blue)	56	70	80	100	100	100	100	100	65	40
NAH (red)	40	65	60	100	100	100	100	100	100	70
KH3 (black)	5	70	75	100	100	100	100	100	100	70

Defect type	Dirt	Popping	Crater	Thinner splash	Water splash
Defect shape	0.5 mm 	0.5 mm 	1.0 mm 	0.5 mm 	0.5 mm
Defect observation photo					

Fig.4 List of detectable paint defects

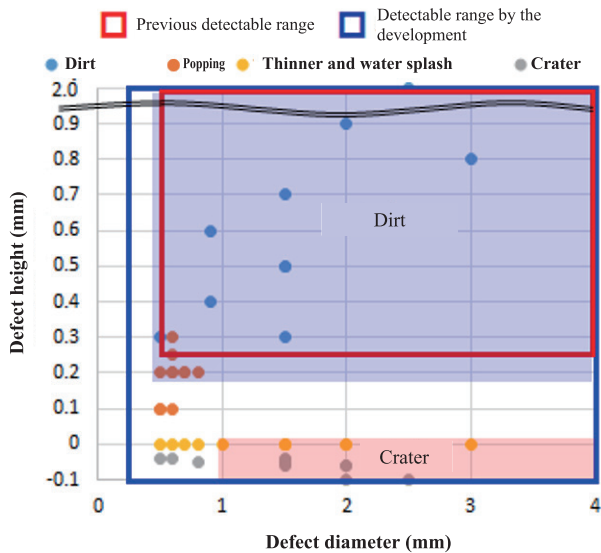


Fig.5 Difference in detectable defective shape between conventional and new systems

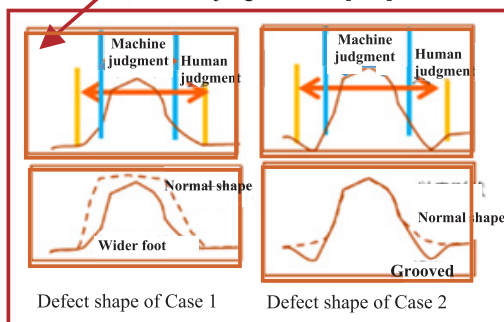
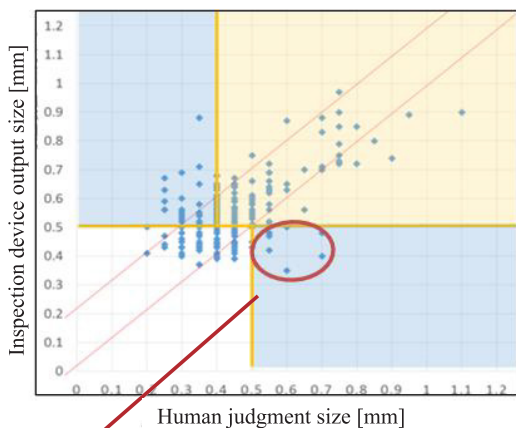
In addition, for defective dirt shapes as in the two cases mentioned below, a range recognized as a defect by a person becomes so wide that the size judged by an inspector device becomes narrower than the size measured by a human.

Case 1: A clear-layer swell makes its foot wider.

Case 2: A defect is surrounded by a groove.

To prevent the defect judgment size from narrowing, a logic in which both composite images and raw images (close to human vision) were used for judgment was added, leading to a narrower deviation from human vision (Fig.6).

<Before the countermeasure logic was added>



Judgment logic added

<After the countermeasure logic was added>

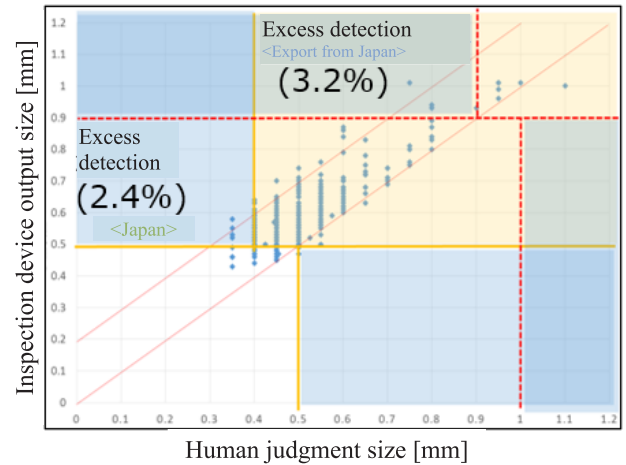


Fig.6 Difference in judgment sizes of special defect shapes between inspection equipment and a human and the effects of implementing a countermeasure

In addition, placing an imaging unit on the robot and changing the fringe direction in the monitor to prevent character lines on the vehicle surface from making the fringe unclear (Fig.7) enabled 98% of the outer surface to be detected even if the vehicle body shape was complicated. Inspecting 562 areas per vehicle and checking 11 resultant images per area for any defect yielded 6,182 imaging times per vehicle.

Detectable:

Character line and fringe pattern in parallel



Undetectable:

Character line and fringe pattern at right angles



Fig.7 Fringe image differences due to combinations of character line and fringe pattern

Based on the above, a previous detection rate of 95%–100% was achieved.

3.3 Measurements of color, clarity, and film thickness

<Conventional technologies and issues>

In previous color, clarity, and film thickness measurements, it was necessary to bring the head of a measuring instrument into contact with the vehicle surface to be measured, and a person adjusted the position of the measuring head. To automate the position adjustment in a contact state, it is necessary to control

the position accuracy of the measuring head with respect to the surface to enable measurement within 1 mm. Therefore, the stop position accuracy of a robot having a measuring head must be improved.

This issue has made it difficult to realize 100% automated measurements in automotive production lines.

<Issue-resolving-method details>

By utilizing a vision system, high-accuracy positioning by a robot and 100% automated inspections were achieved.

3.4 System features

In this system, if either

- ① Incomplete correction completion registration for a defect detected by paint defect inspection equipment occurs or
- ② The color, clarity, or film thickness measurement results do not satisfy quality standards,

then the vehicle will not be conveyed to the next process. This control system was established to realize in-process assurance.

3.5 Advantages

The effect of establishing automated dust inspection is that a four-person inspection of man-hours is not required and that the stable inspection execution causes the shipment quality assurance level to increase. The quality data of all vehicles measured in the final paint process by this system and the database of various in-production conditions monitored by the painting equipment can minimize the time required for potential for potential defects to be identified. and help establish equipment conditions to maintain a more stable quality level (source measurement).

4. Integrated automated inspections (specifications and defect inspections)

4.1 System composition and outline

This equipment performs two types of inspections: specification inspection and defect inspection. Specification inspection utilizes information from the production management system to determine whether object parts were installed according to the instructions. Then, the defect inspection assesses not only the painted surfaces, but also the glass surfaces. Because these inspections are performed in the same stage, the robots have lights and vision sensors separately installed for specification inspection and defect inspection (Fig.8, Fig.9).

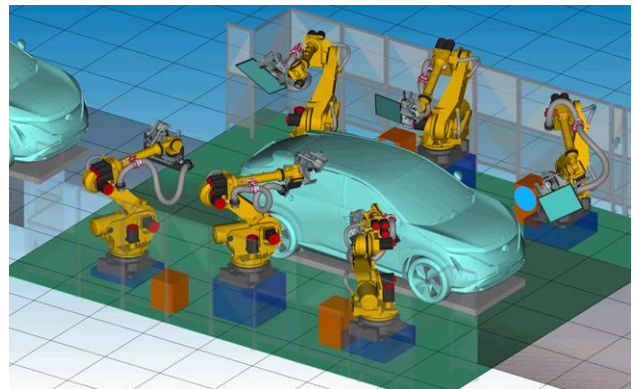


Fig.8 Layout of robots in the inspection stage



Fig.9 Actual inspection scene

4.2 Specification inspection

<Conventional technologies and issues>

(1) Paint color judgment

A judgment method utilizing Euclidean distances (color differences) in the L*a*b* color space is available for image processing in color specification inspection. Vehicle paint colors, however, include similar colors such as solid white and pearl white, whose differences cannot be recognized without placing them side by side and whose distance, as described above, is close. In addition, the relation between a light and an inspection surface may cause the reflection rate to vary, resulting in overlapped distributions and leading to misjudgment, which is recognized as an issue (Fig. 10).

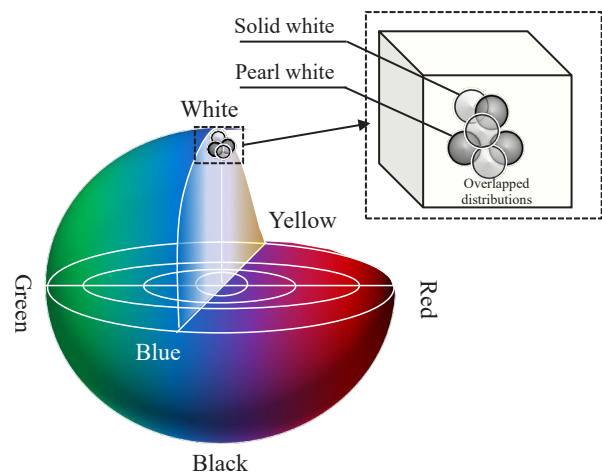


Fig.10 L*a*b* color space

(2) Ensuring judgment accuracy for various inspection objects and surface conditions

In the object inspections performed by this equipment, existence/absence, shape, position, posture, and color are applied to pass-fail judgment. Every judgment other than color is based on the outline of the part from image processing. However, the light reflection rates of parts with different surface conditions, such as painted, mirror-finished, unpainted, and glass surfaces, vary, so that some lighting methods may cause the outline of a part to disappear. An inspection object part and a background of the same color cause no difference in contrast, leading to the disappearance of the outline. The combination of multiple lights and vision sensors can serve as a countermeasure to overcome this issue. This countermeasure, however, causes the number of attachments to a robot to increase, making the avoidance of interference with other robots an issue and causing posture changes to require so long that a target cycle time cannot be achieved.

<Issue-resolving-method details>

(1) Paint color judgment

Lights are placed at positions such that they provide indirect lighting so that the reflection rate can be controlled, and the parameters of the lights and vision sensors can be automatically switched by color group based on information from the production management system. In addition, the detection area is selected so that its position is hardly affected by the reflection rate and two positions of an inspection object part and an adjacent part can be within the vision, and a judgment logic is utilized in which the color-space distances between the two positions described above are compared. Consequently, 100% judgment accuracy can be achieved. Additionally, because inspections can be performed without providing a judgment logic and threshold for each paint color, maintainability is also greatly improved.

(2) Ensuring the judgment accuracy for various inspection objects and surface conditions

With an understanding of the equipment objects, inspection types and part characteristics, scattered light from indirect lighting was utilized for painted and mirror-finished parts to control the reflection intensity, and regular reflection light from a ring lighting device was utilized for unpainted parts and on-glass printed letters to increase the reflection intensity. For slight differences in the reflection rate between parts, the optimal reflection intensity is ensured by providing a sliding mechanism for a lighting device and controlling its illuminating position. The sliding mechanism can also store the lighting section during non-shooting to achieve a small hand section. This approach minimizes the effect on the cycle time (Fig.11).

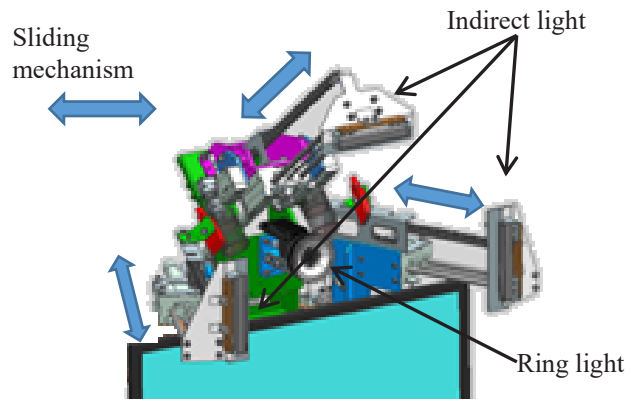


Fig.11 Components of the hand section (lights and vision sensors)

In addition, while minimizing unexpected background appearances within an image, contrast difference is ensured by switching not only the parameters of the lights and vision sensors automatically for each paint color and part, but also the imaging postures. Consequently, a defective-goods outflow rate of 0% and a fine-goods detection error rate of 0.001% or less were achieved (Fig.12).

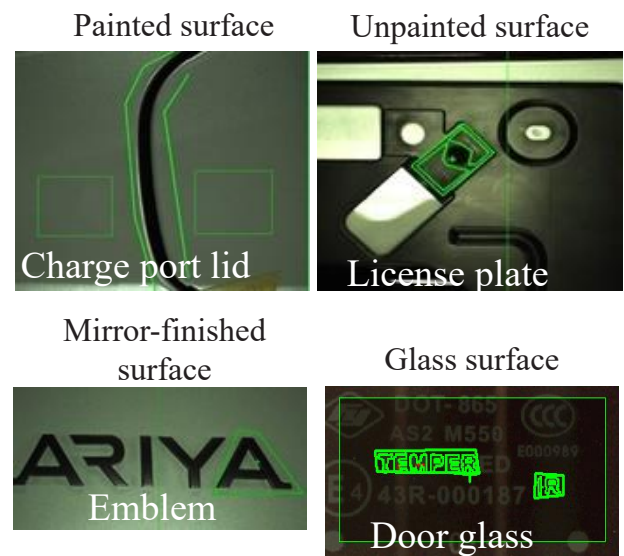


Fig.12 Examples of detection images by surface condition

4.3 Defect inspection

<Conventional technologies and issues>

(1) Defect detection

This equipment employs the same fringe projection-type defect detection sensors utilized for paint inspection, as mentioned above. Most scratches, which are the inspection items, have long and narrow shapes with widths of 0.1 mm or less and have characteristics completely different from those of paint defects. In addition, it is necessary to detect defects even when there is a difference in the light reflection rate between the painted surface and glass surface.

(2) Detection error control

In defect detection, a defect is determined by extracting an area from the image where the pixel brightness suddenly changes. Because the inspection is performed in the final assembly process, in contrast to inspection only for painted bodies, the edges of the installed parts, on-glass identification paint, printed patterns, hot wires, dirt, and/or wiping marks made during work exist (Fig.13). These elements may cause sudden changes in brightness and may be detected as defects by mistake; therefore, this issue must be controlled.

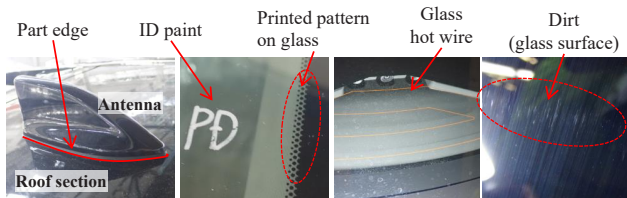


Fig.13 Examples of detection error factors

<Issue-resolving-method details>

(1) Defect detection

The characteristics of the defects that can occur on a vehicle and tuning the fringe width/cycle of lighting, number of imaging times, imaging parameters, and others factors for each of the painted surfaces and glass surfaces enabled clearer defect images to be obtained (Fig.14).

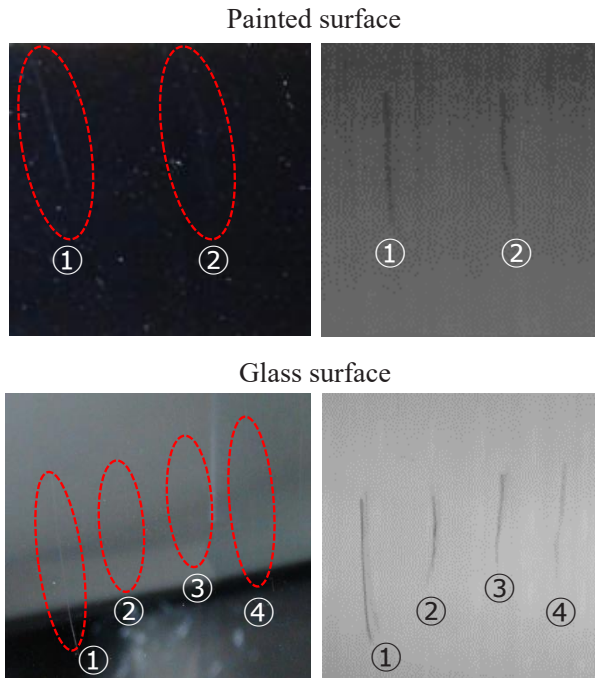


Fig. 14 Images of imitated defect detection on painted surfaces and glass surfaces (left: Camera images; right: Processed images)

(2) Detection error control

To control misdetection caused by part edges, on-glass patterns, hot wires, and other factors, a logic is proposed in which defect misdetection is prevented by using image

processing to extract areas based on the characteristics (patterns) of such items and automatically masking them (Fig.15).

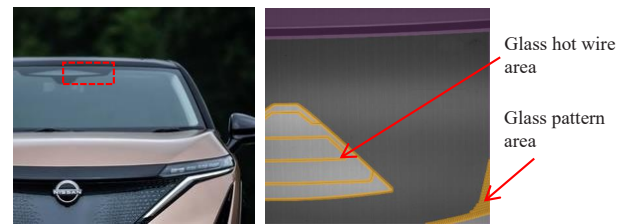


Fig.15 Auto-masked areas (solid in yellow)

It is difficult for the current defect judgment method to handle dirt or wiping marks (distinction between dirt and defects), which occur in random positions and do not have unique characteristics such as shapes, leading to potential misdetection. This issue can be addressed by considering a new method.

In addition, the inspection results (Fig.16), including those of the specification inspection, are stored simultaneously and accumulated.

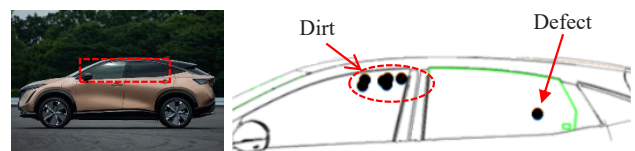


Fig.16 Example of defect inspection results

4.4 Advantages

This equipment enabled the automation of the following inspections based on certain criteria independent of inspector skill in an assembly line for the mixed production of various vehicle models and specifications: complicated specification inspection and defect inspection for painted surfaces and glass surfaces with minute and various characteristics. This approach provides a more stable and higher quality assurance level than the previous visual inspections and will contribute to achieving in-process assurance, preventing potentially defective vehicles from being released to customers. This method also provides a worker-friendly environment in which further quality defects do not occur and are prevented by utilizing accumulated inspection data to identify defect causes and to design processes for fewer defects.

5. Conclusion

This report introduced the concept of a quality gate and the technical development cases of automated inspections to improve the quality assurance level of the quality gate.

At present, the aim is to promote automation of inspections within manufacturing processes. In the future, the objectives the plan to be expanded the range to complete vehicle inspection processes and to promote

the application of automated inspections to the entire assurance process.

These achievements would contribute to improving the brand value of Nissan by improving vehicle quality through high quality assurance level and promoting quality improvement based on inspection results to deliver high-quality products that meet customer expectations.

[References]

*1) x3Projects Co., Ltd.:

Surface inspection equipment, utility model registration number 3197766, (2015)

Authors



Teruyuki Ishiwata



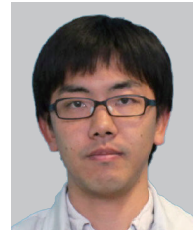
Mitsuru Hirayama



Daisuke Tanaka



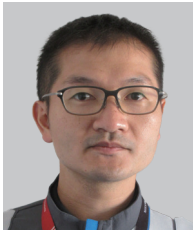
Takayuki Moriya



Yasuo Yamada



Makoto Yamada



Takeshi Honda

6. Improvement of the Equipment Operation Rate and Process Capacity by Implementing Predictive/Preventive Maintenance and Remote Maintenance Technology

Katahiro Ogawa* Satoru Sakurai** Koichi Makino** Takuya Tsumoto***
Susumu Abe*** Masayoshi Hayakawa* Kazunari Seo* Minoru Kono*

1. Introduction

Nissan Motor must stably manufacture vehicles of high functionality and high quality, such as the ARIYA, to deliver them to customers on time. For this purpose, advanced equipment with multiple functions and high performance were introduced into the Nissan Intelligent Factory (NIF). However, there are also a lot of aged equipment at plants. Consequently, the level of maintenance required for smooth production is higher than ever.

The maintenance department has stated the following three principles for some time in order to improve quality, cost, and time (QCT): “allow no equipment failure”; “allow no failure recurrence”; and “fix a failure immediately.” Under these three principles, the maintenance operations has been managed with a large number of skilled maintenance staff. However, the staff structure of the maintenance department has changed. One reason is that as the number of skilled maintenance staff have decreased, it has become impossible to continue the maintenance operations that have heavily relied on their skills and intuition. Another reason is that as the total number of maintenance staff members tends to decrease, it becomes more difficult to handle both sudden equipment failures and regular inspections, which are normal tasks.

In order to resolve these issues, the Maintenance Department of Nissan Motor is promoting various work innovations with digital technology, such as the latest Internet of Things (IoT). As one such innovation, this report introduces the predictive/preventive maintenance and remote maintenance applied to NIF.

2. Predictive/preventive maintenance

As a middle- and long-term strategy for addressing the goals of “allow no equipment failure” and “allow no failure recurrence,” which are two of the three Nissan Motor maintenance principles mentioned in the previous chapter, Nissan Motor has stated a target value, “zero major breakdown (MBD) originating in equipment in FY30.”

An investigation of the equipment failure history revealed that three vehicle plants in Japan (Tochigi, Kyushu, and Oppama) had 371 MBDs that could delay vehicle deliveries over the past five years, and 132 of these cases (34%, and the greatest portion) were caused by equipment defects that were difficult to find through regular inspections. In other words, it implies that conventional Time Based Maintenance is not sufficient to eliminate MBDs, and Condition Based Maintenance (CBM) is necessary.

Accordingly, Nissan Motor decided to exploit IoT technology to introduce a predictive/preventive maintenance system that constantly monitors data indicating equipment defects. This chapter introduces important elemental technologies comprising this predictive/preventive maintenance system.

2.1 Measurement technology

In order to monitor production equipment conditions continuously, it is necessary to measure and collect data indicating equipment defects constantly. “Data indicating equipment defects” can be classified into the following two types: data originally monitored by production equipment itself for controlling the equipment and/or quality control, and data acquired by sensors retrofitted into production equipment, which were not originally monitored by the production equipment. Whereas the cost of acquiring the former data is low, acquiring the latter data requires costs related to the following devices and their installation: [1] sensors for measuring specific physical quantities, [2] amplifiers for amplifying weak signals from sensors, [3] devices for converting analog data from amplifiers into digital data, [4] devices for transmitting digitally converted data into wired/wireless networks, and [5] network wiring for wired transmission. Installation of [1]–[5] at hundreds of in-plant locations needs high cost and long construction period, resulting in the difficulty in increasing a number of equipment monitored. In addition, even for installing a measurement sensor in a movable point of equipment, the necessity of wiring for data transmission may compel such sensor installation to be abandoned.

Accordingly, Nissan Motor jointly developed a “diagnosis sensor HUB” with Fuji Electric Co., Ltd. to

*Plant Maintenance Engineering Department **Powertrain Production Engineering Department
***Production Engineering Reserch and Development

reduce the installation cost of the retrofit sensor significantly and to measure the movable points easily (Fig.1). The device has the following built-in components: [1] a three-axis vibration sensor, [2] an amplifier, [3] an analog/digital converter, and [4] a wireless data transmission system. It also has a four-channel external input terminal and can be connected to various measuring sensors to realize wireless communication of various measurement data at low cost. Furthermore, the dimensions of the diagnosis sensor HUB can be as small as 10 cm × 10 cm × 3 cm, enabling it to be installed easily even in complicated, quickly moving production equipment such as a robot (Fig. 1).

The NIF has 189 diagnosis sensor HUBs installed for constant production robot monitoring. Three-axis 800 Hz vibration data per cycle are transmitted to an IoT network via the field storage system introduced in Subsection 2.2, and the predictive/preventive maintenance platform introduced in Subsection 2.3 diagnoses the data automatically and constantly to identify any abnormalities.



(Source: Website of Fuji Electric Co., Ltd.)

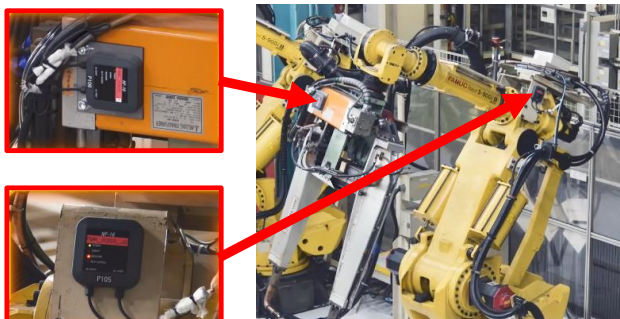


Fig.1 Diagnosis sensor HUB installed into a vehicle-body robot

2.2 Data collection and utilized technology

Nissan Motor declares “collect once, use many” as a concept and is promoting the in-house standardization of data communication standards and data structures so that a huge amount of data acquired from production lines can easily be used for not only predictive/preventive maintenance, but also various purposes such as quality monitoring and tracing.

As a unified data communication standard, Nissan Motor selected OPC Unified Architecture (OPC-UA), which is spreading in Europe, where Industry 4.0 is advanced. However, a lot of production equipment and measurement sensors are not yet compatible with OPC-UA; therefore, it is necessary to convert data acquired from production equipment and data measured

by retrofit sensors into data compatible with the OPC-UA standard before they are sent to IoT networks. Accordingly, Nissan Motor developed field storage, which is a tool for converting data of various structures acquired from production equipment into data compatible with the OPC-UA standard. The field storage converts data received from production equipment so that they become compatible with the OPC-UA standard. The converted data are transmitted to the predictive/preventive maintenance platform explained in Subsection 2.3 and/or the database for the quality control system (Fig.2).

Nissan Motor deploys the same type of production equipment in many plants. On the predictive/preventive maintenance platform, in order to apply the same diagnosis logic programs to the same type of equipment at multiple plants, data acquired from the same type of equipment must be stored in a database having a common data structure at all plants. Accordingly, Nissan Motor prepared a standardized data structure called “data model”. “Field storage” converts data so that they conform to the data model. Thus, data acquired from the same type of equipment can be transmitted to and accumulated in the predictive/preventive maintenance platform through the common data structure and the common communication standard at every plant.

At present in NIF, 32,464 types of data are constantly stored in the database for the predictive/preventive maintenance of 1,229 pieces of equipment. As the number of pieces of equipment requiring predictive/preventive maintenance increases in the future, the number of data types will increase as well.



Fig.2 Field storage

2.3 Systemization technology

As mentioned at the beginning of Section 2 in this chapter, Nissan Motor must implement predictive/preventive maintenance over all bases rapidly to achieve “zero major breakdown (MBD) originating in equipment in FY30” and monitor the operation conditions in the future. As a predictive/preventive maintenance platform for this purpose, Nissan Motor has developed “MASTER CBM”.

The greatest feature of MASTER CBM is that one platform has the following three main functions implemented as a single package: [1] a diagnosis logic

preparation function, [2] an online automated diagnosis function, and [3] a diagnosis result dashboard function.

The diagnosis logic preparation function of [1] enables diagnosis logic to be prepared in a non-programming development environment (Fig.3). For the NIF, 29 types of diagnostic logic were prepared. The prepared diagnosis logics can also be shared with all plant of Nissan Motor through the diagnosis model management system developed in this study, and the operation status can be monitored remotely.

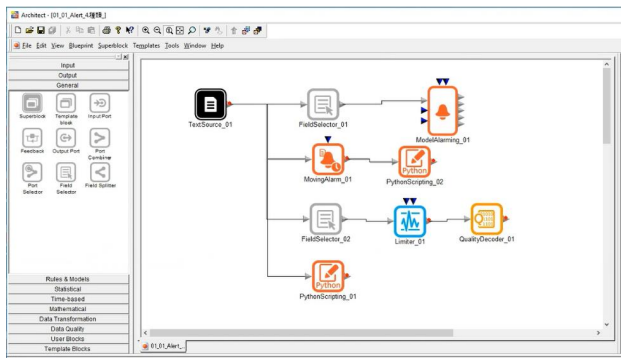


Fig.3 Non-programming diagnosis logic development environment

The online automated diagnosis function of [2] is a function that executes automatically the diagnosis logic created by [1] to judge the data measured and transmitted constantly. Considering the market, few systems have both functions to develop diagnosis logics and functions to auto-diagnose online. Nissan Motor did not prepare these functions in separate systems, but rather intended to use both functions on the same platform. This MASTER CBM has both functions implemented. The results of auto-diagnosing measured data for every cycle are indicated in the plant layout view in real time.

The diagnosis result dashboard function of [3] indicates the equipment that a diagnosis logic judges abnormal with a flashing red indicator (Fig.4). Clicking the red indicator repeatedly enables the following four layers to be drilled down and finally leads to the equipment component causing an alarm: a) in-building layout, b) line layout, c) stage layout, and d) sensor layout (Fig.4). It also has a function to indicate an error point similar to the layout view if a defect occurs in a measurement function itself, such as a sensor. In addition, it can indicate measured raw data as well as the abnormality judging thresholds and feature quantities (statistical values, etc.) used in diagnosis logics at any time scale (Fig.5).

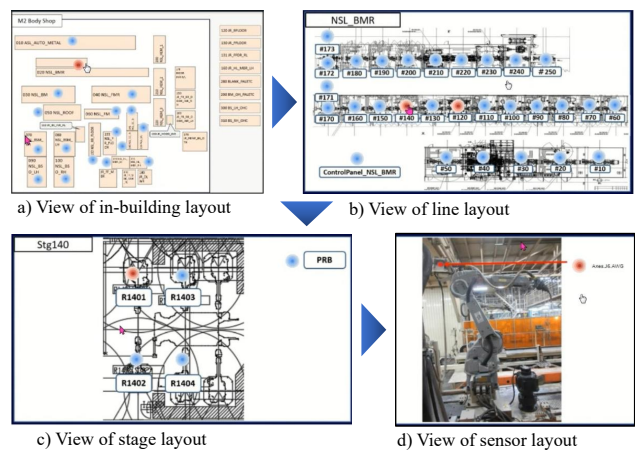


Fig.4 Drilled-down dashboard

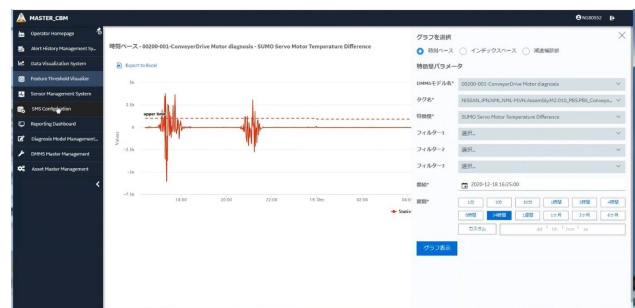


Fig.5 Data indication

Furthermore, for one of the three maintenance principles, “allow no failure recurrence,” MASTER CBM has a function to attribute each measured datum for which a diagnosis logic gave an alarm to the investigation results of the object equipment as a part of the function of [3]. It is desired to enable more accurate estimation of failure points and equipment stop times using measured data from this information in the future.

2.4 Diagnosis logic development

The hardware aspects, such as devices and systems, were explained in Subsections 2.1–2.3. Another important factor is the diagnosis logic in the software, which Nissan Motor has also made an effort to develop.

In the diagnosis logic development, after the object equipment is selected, failure mode and effects analysis (FMEA) is performed to extract parts to be deteriorated and their failure modes based on the components, working mechanisms, and defect history information of the equipment. Then, the optimal maintenance method is selected based on the degree of influence, occurrence frequencies, detectability, and data to be measured, judgment methods and other factors are examined for failure modes that require constant monitoring.

For data to be measured, physical quantities likely to indicate abnormality are selected mainly from electric current, torque, vibration, pressure, flow rate, size, temperature, etc. The pretreatment, feature quantity settings, and criteria of data necessary for detecting abnormality are tentatively fixed by investigating actual data variations in the normal state. The raw values and/

or waveforms of the measured data can be used for judgment as they are in some cases; however, processing is required in most cases. Pretreatment such as noise elimination through a band-pass filter is performed, and the data are processed into feature quantities, such as mean values per cycle or per unit time, medians, maximum/minimum values, and deviations, and verifications are repeated whether methods such as upper/lower limit diagnosis, guard band diagnosis, frequency analysis, and trend analysis can be used to judge the status as normal/cautious (signs of abnormality)/abnormal.

Among these physical quantities, pretreatments, feature quantities, and judgment methods, the optimal combination must be selected, and the most important key point is the setting of certain thresholds for normal/cautious/abnormal levels. Threshold is an important factor in determining the diagnosis accuracy. An improper threshold causes an incorrect report, where a normal state is misjudged abnormal, or, on the contrary, report loss, where even an abnormal state cannot be judged abnormal and an alarm report is missed, leading to a state in which it is impossible to attempt to prevent abnormality.

The difficulty levels in the threshold settings were roughly classified into three types. The first is a case in which the absolute value of an abnormal judgment threshold is predetermined based on standards, equipment specifications, and other factors, so that the threshold can easily be set.

In the second case, although no threshold is determined based on standards etc., the correlation between a change in the measured data and the equipment deterioration condition is clear. If many samples of data during equipment abnormality exist, thresholds can be tentatively set by comparing the data in an abnormal state with data in a normal state (Fig.6). However, data in an abnormal state do not exist in many cases. In such cases, thresholds are tentatively set by statistically processing the data in a normal state. In any case, the thresholds must be verified by each equipment unit and/or section, which requires considerable time and effort. In addition, abnormal data samples are fundamentally few, therefore, thresholds must be continuously fine-tuned, and the occurrence statuses of incorrect reports and report losses must be monitored even after thresholds are tentatively set.

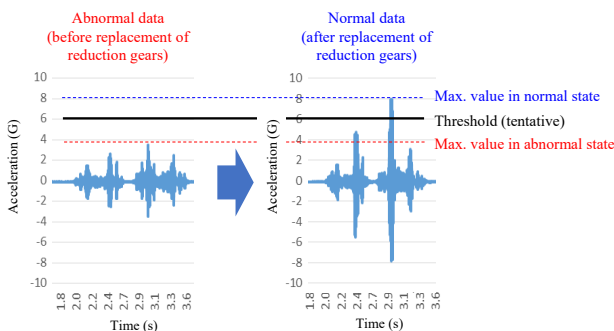


Fig.6 Vibration data before and after replacement of abnormal robot reduction gears

In the third case, the correlation between a change in the measured data and the equipment deterioration condition is unknown. Because such measured data change irregularly, quantification of the change is difficult. For such cases, Nissan Motor fully utilized a statistical method to develop diagnosis logics and constructed a diagnosis logic as an example in which many feature quantities were extracted from the waveforms of the measured data to digitalize the waveform changes (Fig.7). However, this case also requires reviewing feature quantities, thresholds, and other aspects based on a huge amount of abnormality data in order to construct a diagnostic logic with high judgment accuracy, and the actual equipment deterioration levels must be regularly investigated to accumulate information about the correlation with changes in measured data. Nissan Motor will use big data to be accumulated by the predictive/preventive maintenance platform explained in Subsection 2.3 of this chapter to improve the diagnosis accuracy continuously in the future.

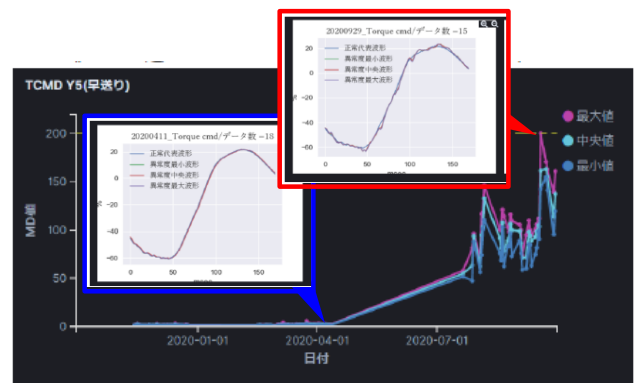


Fig.7 Digitalization of linear-axis torque waveform in machining center

2.5 Technology for visualizing tool exchange schedules

Next, the technology for visualizing tool exchange schedules in the powertrain machining line is introduced.

To prevent a stop, stop factors must be predicted, so that product quality information (measured values, trends), machining condition information (machining times, cutting tool use counts), and equipment status information (main shaft vibration values, cutting fluid flow rate/pressure, etc.) can be collected to monitor the status. Here, the technology for visualizing tool exchange schedules will be explained.

For the exchanges of cutting tools used in machining lines, Nissan Motor previously utilized signal towers and in-line large-sized displays to indicate tool exchange notices to provide information to in-line operators (Fig.8). Therefore, actions were taken each time a tool was exchanged. If multiple pieces of equipment required tool exchanges, delayed actions could cause equipment stop loss.

The system developed in this study collects information

from tool counters on the equipment in real time, which permits tool exchange hours on a particular day to be predicted (Fig.9). The visualization of tool exchange schedules enables minimization of equipment stop loss caused by exchanging tools through the batch exchanges of multiple tools and/or operator relief actions.

The system explained here is a small part of the IoT system. System updates should be promoted to minimize the production loss by the managing equipment for predictive/preventive maintenance and visualization of the line operation status.

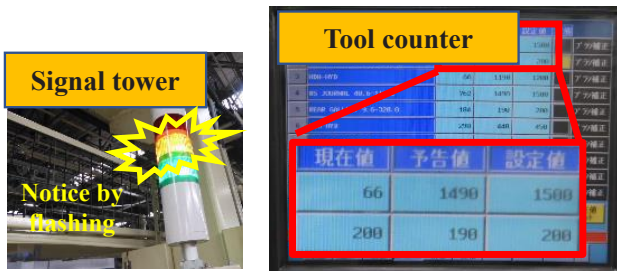


Fig.8 Existing tool exchange notice

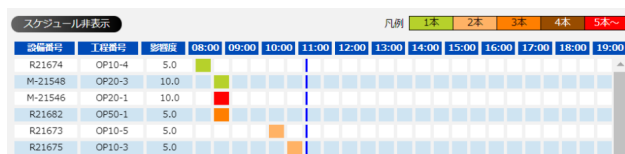


Fig.9 IoT tool exchange schedule screen

3. Remote maintenance

In order to realize the last of the three maintenance principles defined by Nissan Motor, “fix a failure immediately,” in an environment in which the number of skilled maintenance staff members is decreasing, Nissan Motor established a centralized monitoring room in the NIF to which skilled maintenance staff members were assigned and introduced a remote maintenance system in which digital tools are used to connect the centralized monitoring room and maintenance sites.

In the background, as the result of analyzing the previous MBDs, the main factors in long recovery periods include “insufficient grasp of the situation and analysis of factors” and “recovery work errors”, which are related to “insufficient investigation time” and “insufficient knowledge/skill of maintenance staff”. The objective of introducing remote maintenance is to resolve these two factors.

The centralized monitoring room had 27 large monitors for displaying the equipment operation monitors, predictive/preventive maintenance platform, and images of production site cameras (243 units) for skilled maintenance staff to grasp the operation status of the plant (Fig.10). This approach enabled skilled maintenance staff to identify production equipment abnormalities in real time. In addition, the centralized monitoring room

contained information such as maintenance manuals, equipment design drawings, and descriptions of previous problems aggregated in an integrated fashion. This system ensures that after an equipment abnormality occurs, skilled maintenance staff can understand the situation and analyze the factors until the site maintenance staff reach the site.



Fig.10 Centralized monitoring room

As digital tools for connecting in real time between skilled maintenance staff in the centralized monitoring room and all site maintenance staff, 64 sets of wearable cameras, headsets, and tablet terminals were provided, enabling skilled maintenance staff and site maintenance staff to share site images, communicate by voice, and share maintenance manuals and other information in real time, providing a system to compensate for the insufficient knowledge of site maintenance staff (Fig.11).

This remote maintenance system with a centralized monitoring room can expect to reduce the failure recovery period by an average of 30%.

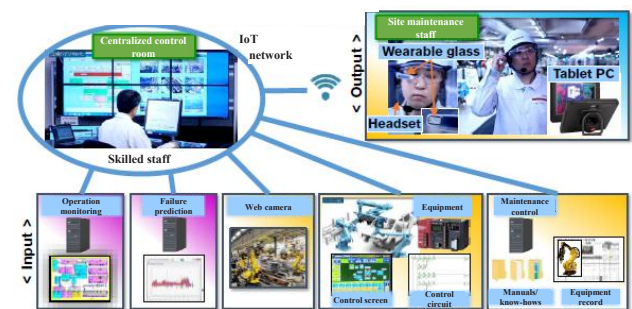


Fig.11 Remote maintenance

4. Conclusion

This report described the ability of the NIF to deliver high quality vehicles to customers on time by using digital technologies to establish predictive/preventive maintenance and remote maintenance systems to reduce equipment stop frequencies and hours in a strict environment in which the number of skilled maintenance staff is decreasing, and advanced maintenance skills are required due to the appearance of advanced equipment and equipment aging.

Nissan Motor will introduce the systems described in this report into all production bases worldwide. In addition, the remaining life prediction and automated troubleshooting assistance of production equipment will be achieved by learning data to be accumulated in the future. Moreover, trouble-proof equipment with high quality will be designed by feeding back knowledge to accumulate in production equipment design. As a result, the targets of the NIF are to minimize the equipment stop frequencies and recovery time, and to deliver advanced quality vehicles to customers worldwide with no delay. Working style diversification and extension of the scope of workers (working-style reforms) in an aging society with a declining birthrate should be advanced by promoting digitalization and innovating into maintenance operations with lower reliance on individual skills.

Authors



Katahiro Ogawa



Satoru Sakurai



Koichi Makino



Takuya Tsumoto



Susumu Abe



Masayoshi Hayakawa



Kazunari Seo



Minoru Kono

7. Development of Die-Cast Technology for Realizing Innovative Thin-Walled Light-Weight Cylinder Head

Yuuta Sugiyama* Shinichi Tsuchiya** Hiromichi Kume*
Takahiro Nishi** Machi Tabuchi**

1. Introduction

Global-scale activities for the reduction of CO₂ emissions are being conducted at an accelerating rate. In Japan, the declaration of aiming to achieve carbon neutrality (a decarbonized society) by 2050 was presented at the 203rd extraordinary Diet session in October 2020. The automotive industry is required to reduce CO₂ emissions by increasing production of electrified vehicles as well as by achieving more efficient conventional internal combustion engines and lighter vehicle weights. It must reduce CO₂ emissions from production plants, or vehicle production processes.

To achieve more efficient combustion in internal combustion engines, a higher compression ratio in the engine cylinder by a supercharger is required. To realize this characteristic, a high cooling performance for exhaust ports is necessary, so that the internal cooling circuit spreading through an engine cylinder head must be thinner and more minute. Therefore, the structure of a water jacket in a cylindrical head is complex. Simultaneously, a thin-walled cylinder head is required for vehicle weight reduction to achieve better fuel economy. The development of a die-cast method that can balance these two issues at a high level is urgently needed (Fig.1).

Also regarding production processes, a cylinder head raw material is produced through an aluminum die-cast method called a “low-pressure die-cast method,” where a considerable amount of energy is used in processes for melting aluminum and heat treatment processes for controlling strength. Consequently, these processes are the third highest CO₂ emitting processes, following the paint and iron processes, among the production processes of Nissan Motor as of 2019. Therefore, CO₂ emission reduction of the entire process is urgently needed. Towards this objective, a new cylinder head production line was developed along with the development and global deployment of new-generation variable compression ratio gasoline engines.

This report will explain the details of the vacuum low-pressure die-cast (V-LPDC) process and related technologies developed for the compatibility of a complex

minute internal cooling structure and thin-walled products.

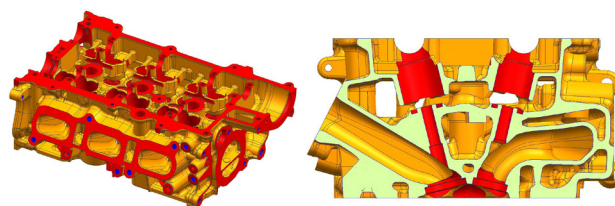


Fig.1 Cylinder head

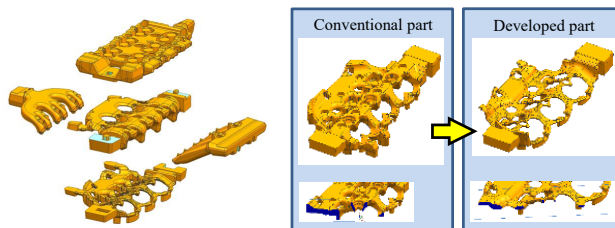


Fig.2 Core

2. Outline of alliance standard line

To achieve thin-walled lightweight cylinder heads, the required technologies were integrated and standardized as the “alliance standard line.”

To improve engine competitiveness, a cylinder head is an important functional part because it manages intake air, combustion, and exhaust. In order to realize these functions, an aluminum die-cast process, which produces cylinder heads, uses dies and cores, which form internal hollow areas (Fig.2) and pours melted aluminum into the dies to form a part.

To manufacture complex cooling paths, integrated parts, and thin-walled shapes with high quality, a new method and various types of automation for minimizing variations were incorporated into the alliance standard line.

The flow of this process is shown in Fig.3. Above all, the main new technologies for thin-wall applications are the vacuum low-pressure die-cast method, inorganic cores, rotary heat-treatment furnaces, and automated inspections with computerized tomography (CT). In these

*Manufacturing and Engineering Department No.2

**Materials Process Engineering Department

processes, one piece is fed at a time, and error/defect occurrence is eliminated by improving the automation level from manufacturing to transport.

From the perspective of CO2 reduction, the application of inorganic cores, Independent melting furnace for each casting machine, and rotary heat treatment furnaces contributes to carbon neutrality.

Improvement of the worker environment was also taken into account. A conventional foundry is dark, foul-smelling, and dirty due to smoke, tar, and dust and also requires considerable handwork, which cannot be regarded as a good factory from an environmental perspective. This new line employs technologies such as inorganic cores to improve the above aspects remarkably.

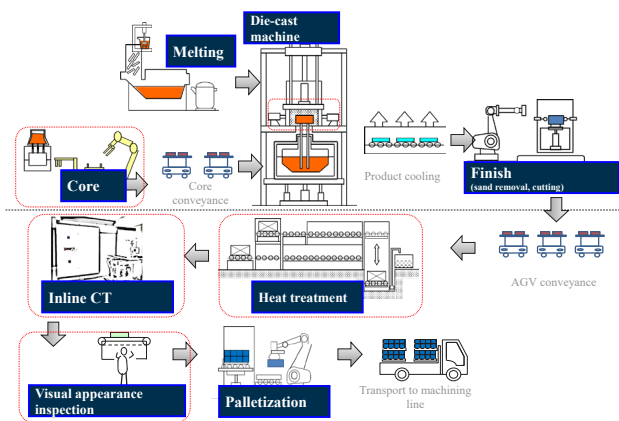


Fig.3 Process flow (outline)

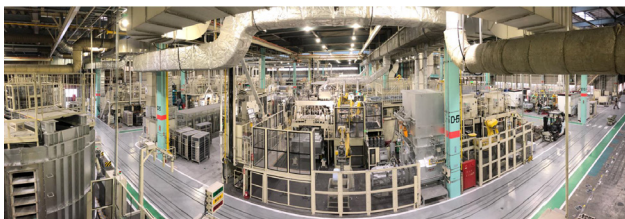


Fig.4 Layout (air view)

3. Development contents

3.1 V-LPDC method

The main technology for realizing an innovative thin-walled cylinder head is the V-LPDC method.

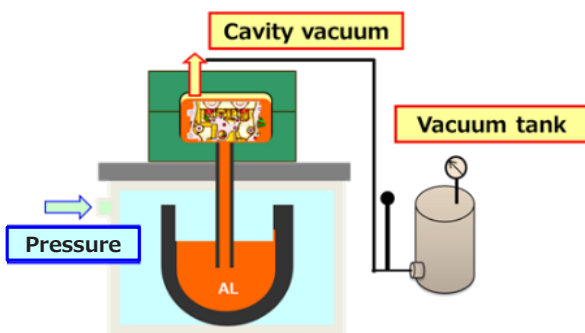


Fig.5 V-LPDC method

As shown in Fig.5, in a cylinder head die cast, the shape is cast by pouring melted aluminum into a cavity in the die to replace the air with aluminum. Then, the air exits structurally through gaps between the parting line of the die. To prevent the liquid aluminum from flowing, the back pressure in the air exit points must be decreased. If the walls are made as thin as possible, this back pressure causes the aluminum to solidify before the air is replaced with aluminum, and a product shape defect occurs. Therefore, technology is necessary to remove the air from between the die parting line to reduce the back pressure (Fig.6).

In this case, balancing the aluminum feeding pressure and pressure inside of cavity is important. Accordingly, a sensor was used to monitor the pressure inside of cavity constantly (Fig.7), and a thermocouple was used to acquire the data of the aluminum flow inside of cavity. Using die-cast computer-aided engineering (CAE) (Fig.8) and these data to set the optimal suction conditions, technology that allows cylinder head die-casting with a minimum wall thickness of 2 mm was developed. In mass production, a weight approximately 4% lighter than that in the conventional model was achieved, while the engine strength requirements were taken into account.

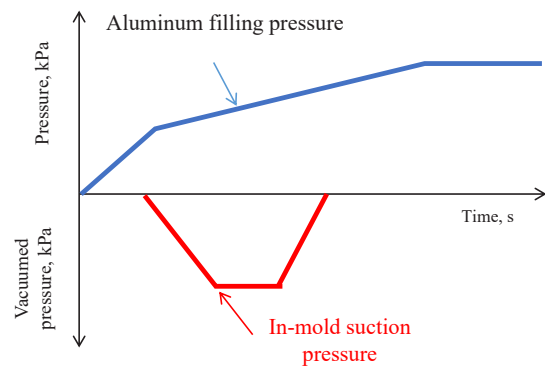


Fig.6 In-die suction conditions

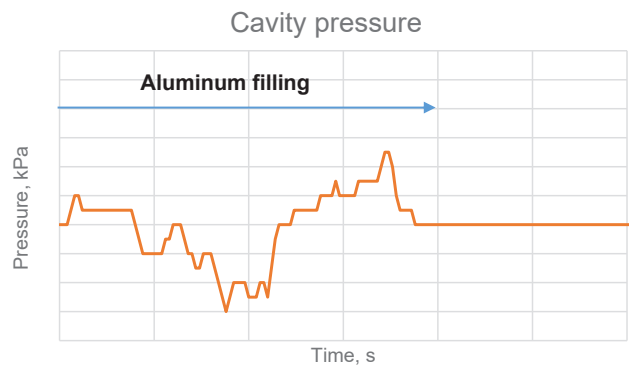


Fig.7 Cavity pressure

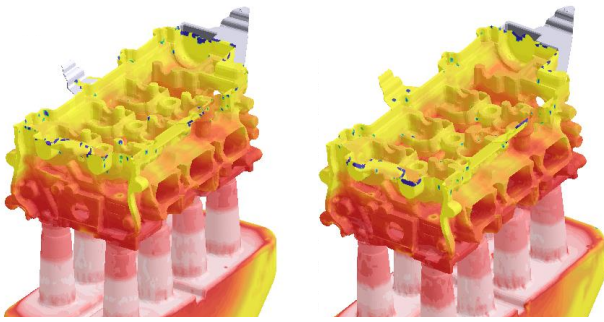


Fig.8 Die-cast CAE

In addition, this vacuum low-pressure die-cast method has an issue in which the shell mold method or a core method using a conventional organic bond causes the suction paths to be blocked by smoke generated during die-casting and/or tar accumulated on the die. Consequently, the V-LPDC method employs the inorganic core technique, in which no smoke or tar is generated (Fig.9). This method uses a liquid glass-based inorganic binder for core making. In this study, the alliance standard line employed these technologies to combine the vacuum low-pressure die-cast method and inorganic cores to realize the mass production of thin-walled lightweight cylinder heads.



Fig.9 Core

3.2 Full automation of core and die-cast processes

As mentioned above, to reduce variations in quality, improve the work environment, etc., the processes of melting, core making, die-casting, finishing, and conveyance in this line were automated as much as possible.

For core making, in order to automate the inorganic core making method fully, the following issues existed: natural sand hardening in the shooting head, handling in a soft state just after shooting, and burring finish by the robot.

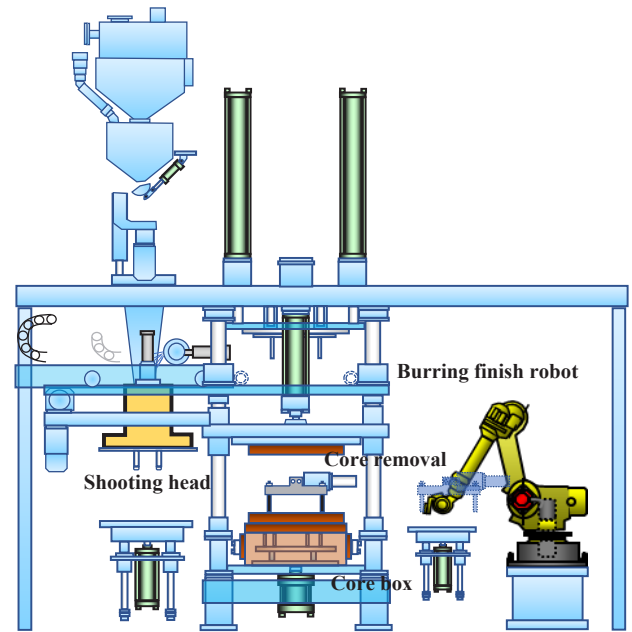


Fig.10 Inorganic core making machine

Inorganic core making (Fig.10) is a method in which mixed sand is hardened by removing water. Therefore, changes in the temperature and humidity of the atmosphere around the core making machine affect the hardening speed of the sand in the shooting head. The inside of the shooting head was water-cooled to prevent the sand in the shooting head from drying. However, a change in the dew point due to temperature and/or humidity causes the water to condense inside and outside the shooting head; hence, too much water is supplied to the sand, degrading the core quality. Therefore, the following dew-condensation preventive measures were taken: measuring the temperature and humidity around the shooting head constantly, calculating and monitoring the dew point constantly, and controlling the temperature of the coolant.

Because an inorganic core is soft immediately after being molded, grasping it is difficult. The cores were handled by scooping them up from underneath, removal from the mold, and loading on the conveyance rack (Fig.11). This approach permitted soft cores to be automatically handled immediately after being molded, without breaking.

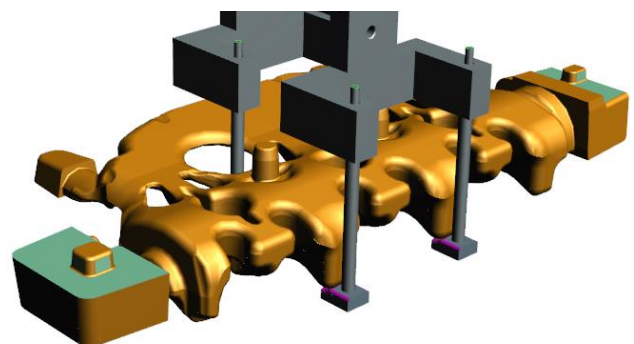


Fig.11 Core grasping tool

A robot is used to burring-finish a core after it is molded. However, owing to the fragility of an inorganic core and its thinness, the core is easily broken during burring-finishing. Accordingly, measures against core breakage are taken by revising the positioning block shape according to the core on the support during burring-finishing and clearance settings to minimize core movement during burring-finishing.

The finished cores are loaded onto the conveyance rack, which is towed by an automated conveyance vehicle (Fig.12) and conveyed to the core inspection area. If a floor condition causes even a small impact to be applied to a core being conveyed, the core can break easily; hence, springs are placed under the conveyance rack and absorb impacts, enabling thin and fragile cores to be auto-conveyed even across an uneven floor.



Fig.12 Automated core conveyance vehicle

The die-cast process uses a robot to automate the work of putting the cores in a die and removing a product from a die.

Because cores are fragile and thin, there are concerns about dropped sand particles causing sand-inclusion defects and die-casting with a broken core placed in a die causing core breakage. These defects were minimized by designing the core print to the optimal shape to handle and grasp the part (Fig.13). A robot was also used to automate the work of air blowing to remove any sand particles after the cores were placed to allow core placement in the die without breakage, and any residual sand particles on the die surface after core placement were removed, which allowed the die-cast process to be automated (Fig.14).

An automated inspection method with CT is applied to inspect hollows composed by cores and assures all complicated and minute internal shapes.

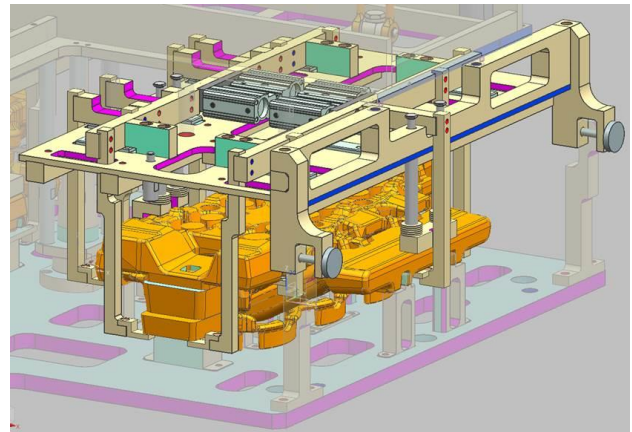


Fig.13 Core placement jig

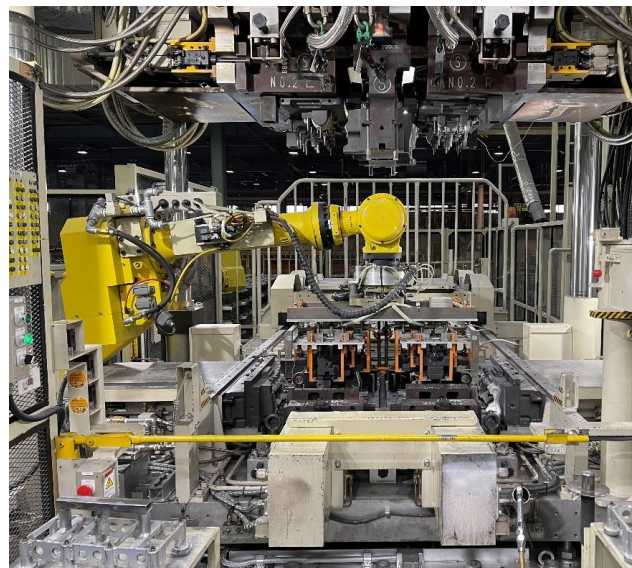


Fig.14 Photograph of die-cast machine during core placement

3.3 Energy loss reduction in melting and heat treatment processes

In the aluminum die-casting process, melting and heat treatment processes account for 35% of CO₂ emissions. As activities for carbon neutrality are being conducted at an accelerating rate, designing production equipment considering energy savings leading to CO₂ reduction is required. This line also employs small modularized equipment and superior heat efficiency to achieve energy savings. The relevant processes are introduced below:

<Melting process>

A conventional melting process is a system in which a large melting furnace with a melting capacity of 3–4 ton/h is placed in each plant, and a forklift with a ladle is used to convey and distribute liquid aluminum to many low-pressure die-cast machines in order. The melting furnace is so large that the molten metal must be maintained with a burner regardless of its operation level, which causes energy loss and safety risks in molten metal conveyance/distribution. This line employed a system in which a small melting furnace with a minimum necessary capacity for one low-pressure die-cast machine (Fig.15) was placed next to each low-pressure die-cast machine, and a robot was used to distribute the molten metal to the holding furnace of the low-pressure die-cast machine. Workers must simply put the aluminum ingot in place; hence, process automation from material feeding to melting/molten metal distribution, which is difficult for a conventional large furnace, is realized. This automation eliminates the risk associated with workers conveying molten metal, thereby improving safety and the environment. In addition, the melting furnace can be stopped according to the operation level of the low-pressure die-cast machine, reducing energy loss.



Fig.15 Appearance of Independent melting furnace for each casting machine

<Heat treatment process>

Cylinder head die-casting involves a heat treatment process to improve the mechanical properties of the products. Conventionally, a continuous-type heat treatment furnace is applied, and similar to the melting process mentioned above, several large heat treatment furnaces are placed in each plant; a stainless-steel basket, called a heat treatment basket, is filled with workpieces; and the basket is conveyed through a solution treatment process (approximately 500°C), water quenching process (approximately 80°C), and aging process (approximately 200°C). The basket used for conveyance in this continuous-type heat treatment furnace is approximately twice the weight of the workpiece. The workpieces and basket used for conveyance are heated to similar temperatures, causing the heat loss to be enormous. At a low operation level, as the number of workpieces filling the basket decreases, a lower heat efficiency is inevitable. The

basket is also deformed by repeated heating and rapid quenching; thus, periodic maintenance is essential. To resolve these issues, a rotary-type rotation heat-treatment furnace (Fig.16) was applied. All processes from workpiece feeding to taking-out were automated using a robot to handle workpieces between processes (solution treatment, water quenching, aging, and air cooling). By feeding workpieces one by one, it is possible to reduce the variation in residual stress inside the product that occurs in the heat treatment process, which contributes to the thin wall thickness of the product. Its production capacity was set to a small module equivalent to two low-pressure die-cast machines.

Heat treatment without baskets eliminated heat loss, and thus the heat efficiency was improved by approximately 44%. The application of the small module enabled the operation to be turned on and off according to the operation level, greatly reducing the energy loss.



Fig.16 Heat treatment furnace appearance

4. Conclusion

A new die-cast technique called the V-LPDC method was developed and applied to a new project, which contributed to a cylinder-head product weight reduction of 4%. In addition, the new alliance standard line, which realizes more attractive products, could be established as a production plant line, whose application to actual production reduced CO2 emissions by 24%.

By continuing further development as well as spreading these technologies globally to maximize their effect, die-cast technologies will provide highly functional and high-quality parts in the future to deliver attractive products to customers.

Authors



Yuuta Sugiyama



Shinichi Tsuchiya



Hiromichi Kume



Takahiro Nishi



Machi Tabuchi

Next-generation flagship: ARIYA

1. ARIYA: new generation of flagship EV

Eiichi Akashi* Hikaru Nakajima**

1. Introduction

Nissan Motor Co., Ltd. commenced mass production of EVs in 2010, globally ahead of all other companies. Based on over 10 years of market experience, Nissan has developed a new generation of EV: the ARIYA (Fig. 1). ARIYA embodies the new Nissan Automotive and Nissan Intelligent Mobility with the aim of being “a new generation of flagship EV that feels like the car of the future.” With ARIYA, Nissan’s goal is “to provide customers a blissful experience that only an EV can deliver.”



Fig.1 ARIYA

2. Toward a new generation of flagship EV

ARIYA was developed to satisfy customers through integration of the latest technologies while fully utilizing the features of an EV. To simultaneously realize many values in ARIYA, new technological elements were developed and their integration was achieved at a high level using innovative system technology.

To start with, an innovative package was introduced through a new EV-specific platform to realize a spacious and noiseless interior, sufficient driving range, and stylish design. The infotainment technologies were revolutionized to offer abundant services and amazing usability, along with integrated vehicle control technologies to achieve high-power and stable driving

performance. In addition, ProPILOT 2.0 was enhanced and a new remote-auto-park function was introduced.

The advancement of each of these technologies is explained in detail in the next chapter and brief explanations are provided below.

3. Innovative packaging with EV-specific platform

In most conventional EVs, the platform designs are based on internal combustion engine (ICE) vehicles. As such, they do not fully benefit from the features of small powertrains that are unique to EVs. To overcome this problem, a new EV-specific package was developed through a high-level combination of an EV-specific powertrain and mounting technologies to increase the interior space, reduce overhang at the front, widen the wheel base, reduce the minimum turning radius, achieve more stable control, improve driving comfort, extend the driving range, and achieve a quieter interior.

The means of achieving these individual aims are often conflicting. Hence, technological development of complex systems was achieved by integrating the following high-level elements.

3.1 Basic structure, interior space, and styling

To increase the height of the interior space, a holistic review of the underfloor structure was performed for battery storage. It was determined that the cross members be embedded in the structure such that the necessary battery capacity (explained later) is secured while providing temperature control system without

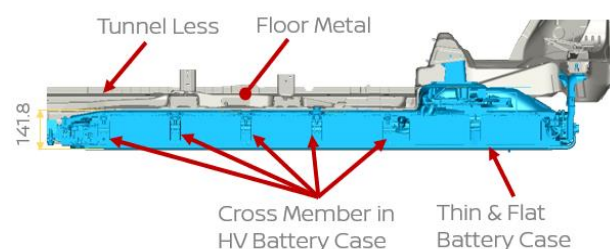


Fig.2 Subfloor structure

*Corporate Vice President **Nissan Product Development Department No.1

compromising the strength and rigidity of the vehicle body (Fig. 2). The new structure enabled development of a body-integrated battery package with high rigidity, which allowed the mounting of an ultrathin large-capacity battery. Furthermore, the torsional rigidity of the entire vehicle body was improved by connecting the high-rigidity package to the front and rear parts of the body. Because the center of gravity was lowered by the subfloor position of the battery with the weight distribution being 50:50 between the front and rear of the vehicle, handling and ride comfort were optimized simultaneously.

Based on the reduced size of the power train, an air-conditioning system (HVAC) was placed in the motor room instead of the inside of the cabin. Because HVACs have large internal spaces in their structures, when placed in a motor room, they act as shock absorbers in the event of a crash. This enabled increasing the interior space while maintaining crash performance standards (Fig. 3). The additional interior space was used to increase the tire turning angle and thereby achieve a minimum turning radius equivalent to that of a B-segment car, despite the large cabin space of that of a D-segment car.

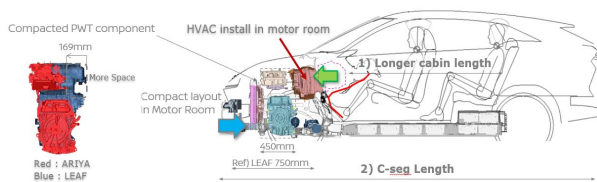


Fig.3 Layout of powertrain and HVAC

The interior cabin length was maximized by introducing an electric center console and minimizing the installment panel. The front and rear leg rooms were expanded owing to the flattened floor. This platform enabled increasing the effective length of the cabin interior to that of the D-segment level, whereas the overall body length was in the C-segment. Because of this platform, a short overhang and long wheelbase layout was possible for realization of a radical yet attractive design. The revolutionary interior and appearance are the major attractions of ARIYA that were enabled by the new EV-specific platform.

3.2 Long driving range

To motivate more customers to purchase ARIYA and to increase EV usage, the basic performance of the EV including driving range, battery charge performance, power consumption for heating/cooling, and usability in real situations must be more advanced.

In particular, advancements were made to reduce the general driving resistance and air resistance, which is the major cause of driving resistance, in addition to enhancing quick charging performance that is critical to highway driving in summer, heating performance, and battery low-temperature tolerance in winter.

3.2.1 Battery capacity

The driving ranges were set to B6- and B9-grade cars to allow a breadth of selection according to customer usage. The B6 grade is targeted for daily use, including commuting and shopping, whereas the B9 grade is targeted for weekend leisure activities, such as golf and camping. The battery capacities required for the expected driving ranges were estimated from data obtained during technological development, as explained below, and determined to be 66 and 91 kWh for the B6 and B9 grades, respectively.

3.2.2 Reduced air resistance

To reduce the air-resistance coefficient (Cd value), the roof shape was streamlined and an air curtain (a type of duct) was placed over the front mask to control airflow. In addition, a flat and full undercover was placed underfloor to control airflow (Fig. 4). Thus, the Cd value was reduced to 0.3 or less, which is outstanding aerodynamic performance for an SUV.

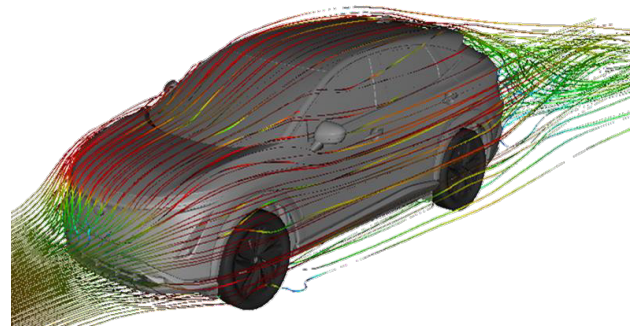


Fig.4 Air flow

3.2.3 Quick charging performance

Considering the quick charging conditions at the parking bays of highways, quick charging performance of 30 min was achieved for recovery from 10 to 80%. Charging speed is strongly dependent on the internal temperature of the battery. Therefore, a liquid battery temperature-control system was developed to achieve stable charging performance using thin batteries without the effects of air temperature and driving mode (Fig. 5). Based on expected future requirements, the allowable input power of the on-board charging device was set to 130 kW during development.

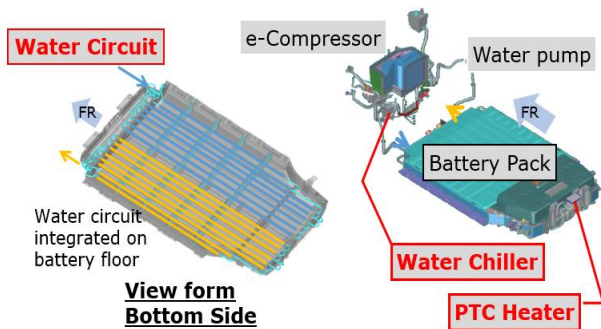


Fig.5 Temperature control system

3.2.4 Heating performance

Next to driving the most energy consumed by an EV is for heating in winter, when the air temperature difference between the inside and outside is larger than that in summer. Hence, efforts were made to increase driving range in winter by adopting highly efficient heat pump system to reduce energy consumption.

3.3 Quietness

EVs do not generate engine noise. The main sources of noise in an EV are the road noise between the road and tires, wind noise during high-speed driving, and motor noise. Road noise was reduced by using special tires containing noise-absorption materials, adapting double antivibration subframes, and thoroughly strengthening the rigidities of the body frame members. Wind noise was reduced by eliminating uneven surfaces and gaps to avoid generating turbulence. External noise was reduced by adapting sound-insulation glasses. At low speeds, when the load noise is small, a slight rotational motion or radial vibration of motor may be noticeable. A newly-developed motor with excellent vibrational properties at low speeds enables realization of a quiet interior space that is appropriate for a flagship EV. (*)

4. Innovative infotainment technologies

When using conventional on-board operation display devices and connected systems, the operations and display become complicated with increasing numbers of services and functions, and the menu selections become wider and deeper. The addition of new functions in complicated systems is time consuming, which makes it difficult to provide timely services. To overcome this challenge and minimize driver distraction, a new input system with high operability was introduced in ARIYA to allow the integrated use of two large displays comprising an IVI panel and a meter panel while reducing the operational hierarchy. Additionally, a new interface was developed for easy operation of the display device, where the two display panels could be used together via swipe actions (Fig. 6). Furthermore, a human-machine interface ("HMI") with high usability was realized through a voice recognition system that allows control of NAVI or air conditioning settings.



Fig.6 Display swipe

To ensure flexibility and rapid development of the connected service system underpinning these functions, the service server was separated from the system server and key function-integrating software was developed in-house. Simultaneously, firmware-over-the-air (FOTA) technology was introduced to update the on-board firmware wirelessly to enable continued offering of abundant services in a user-friendly and timely supply.

5. e-4ORCE: Innovation for integrated vehicle control

The highly desired 4WD was installed in ARIYA to offer additional value beyond ordinary 4WD functionality by integrating vehicle and powertrain controls. High-level integration of the following two advanced technologies was achieved in ARIYA. Namely, 4WD control technology used in GTR and ATTESA that controls torque distribution between the front and rear axles in accordance with driving conditions, and the motor-torque control technology used in LEAF for fast and high-precision control of the motor torque in milliseconds. This combination enables stable vehicle behavior under a variety of road conditions (snow, ice, rain, and dry), thereby providing a confident driving experience to customers.

The two motors placed at the front and back seamlessly produce flexible torque distribution between the front and rear by integrating driving information, such as acceleration, yaw rate, tire slip recognition, and conventional driving-force control. Vehicle behaviors can be controlled with high precision by integrating brake control of the four wheels to optimize the load weight on each wheel. For example, winding roads can be navigated smoothly by independent control of the front and rear torque. At the entrance of a curve, more torque is allocated to the rear, similar to an Front engine and Rear drive vehicle, to improve the turn-in ability. In the middle of the curve, the torque is distributed in a 50:50 ratio between the front and rear to maintain smooth movement. At the curve exit, more torque is allocated to the front, similar to an Front engine and Front drive vehicle (Fig. 7). In addition, the front and rear distributions of the regenerative brakes were optimized by the motors to provide a smooth and comfortable ride. Hence, e-4ORCE is an outstanding system that offers driver secure feel, comfort, and pleasure, in addition to excellent acceleration performance.

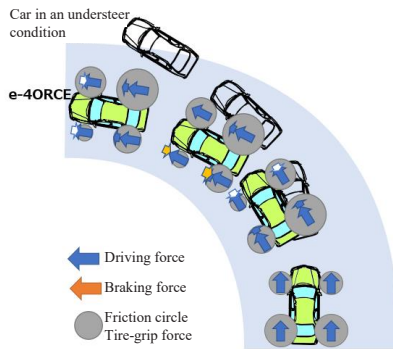


Fig.7 Operation of e-4ORCE

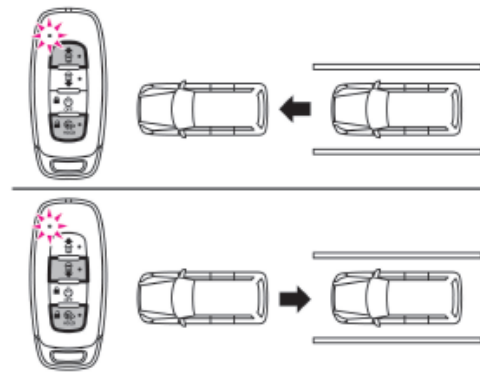


Fig.8 Remote Auto Park

6. ProPILOT 2.0: Remote Auto Park

ProPILOT 2.0, which is installed in Skyline, has garnered much praise as a novel human-vehicle relationship that offers convenience, secure feel and comfort, along with being a “buddy” or “partner.” Its functions were further enhanced and the vehicle location accuracy was increased using signals from the quasi-zenith satellite system.

In the past, there were system limitations in determining the current lane of the car on multilane highways. When using quasi-zenith satellite signals, the driving lanes can be precisely located by detecting vehicle positions within an accuracy of 50 cm. This significantly increases navigation accuracy, thus enabling smooth and accurate guidance for selecting and changing driving lanes at highway junctions. To further assist customer driving, a new technology called Remote Auto Park (RAP) was made available. Using this function, ARIYA can be remotely navigated forward and backward using a designated remote-control key (Fig. 8). Hence, it is possible to park ARIYA in a narrow space by first moving it forward using the RAP function for securing enough space to open the doors.

7. Summary

Although ARIYA is a C-segment SUV, the newly developed innovative system technologies offer enough interior space as a roomy D-segment vehicle and noiseless comfort as an E-segment vehicle, which is appropriate for a flagship EV. The maximum driving range of ARIYA was 610 km in the WLTC mode. ARIYA offers user-friendly infotainment and abundant services through an integrated interface display and a connected service system that allows flexible information manipulation. Owing to e-4ORCE, ARIYA has outstanding drivability for all occasions, from normal driving to snowy conditions. The following chapters discuss several technological challenges that were not explained in this chapter.

ARIYA is equipped with the latest technologies of Nissan and is a icon of Nissan Intelligent Mobility. ARIYA is the next-generation flagship EV that represents the cars of the future. Nissan wishes that our passion will resonate with all users of ARIYA

Authors



Eiichi Akashi



Hikaru Nakajima

*: Where required by law, the EV may be additionally equipped with an alert system that generates the necessary sounds and signals so that pedestrians can detect and recognize the vehicle.

Next-generation flagship: ARIYA

2. Development of EV-specific platform CMF-EV for high packaging efficiency

Masahiro Oonishi*

1. Introduction

The Nissan LEAF, which is a full-scale mass-produced EV released in 2010, has been accepted by customers for its high reliability, safety features, and comfortable driving experience that is typically offered by EVs. LEAF has pioneered the widespread use of EVs.

The high reliability and safety features developed for LEAF have been inherited and further advanced in the newly developed EV-specific platform (CMF-EV) for ARIYA. The target issues of vehicle packaging, driving range, and driving performance have been set to “exceed the expectations of our customers.”

This chapter describes the key points for realizing a large interior space, mounting a large-capacity battery, and achieving high driving performance.

2. Current situation of EV packaging

Our customers’ expectations for EV packaging can largely be classified under the following two features:

- [1] Interior space that is large in the front-rear direction owing to the compact powertrain
- [2] Completely flat interior floor from eliminating the exhaust system and propeller shaft

However, developing an EV that meets both expectations is more difficult than the customers can imagine.

A comparison of the overall vehicle length and effective interior length (distance from the accelerator pedal to hip point of a passenger in the rear seat, which is a representative index of the interior roominess in the front-rear direction) in different commercially available SUVs is shown in Fig. 1. It is seen that the benchmark lines of SUV EVs are inferior in terms of packaging efficiency in the front-rear direction compared to SUV ICE vehicles. If an EV is mounted with a high-capacity and high-voltage battery to secure sufficient driving range, the vehicle mass may increase significantly. Therefore, compared to ICE vehicles, the required crush stroke is higher for damage control during low-speed collisions and for securing passenger and high-voltage safeties during high-speed collisions, thereby offsetting the greater space allowed by the compact drive system.

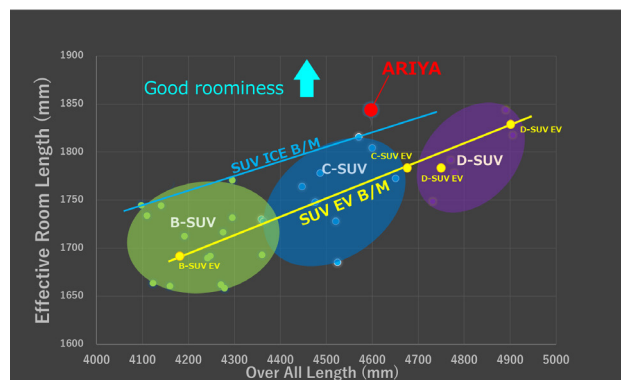


Fig.1 Comparison of overall vehicle and effective interior lengths between SUVs

In LEAF, it was not possible to meet the customers’ demand for a completely flat floor because the brake pipe, cooling water pipe, and high-voltage wiring harness were placed within the center tunnel.

3. Evolution of the novel EV-specific platform CMF-EV

The CMF-EV adopted in ARIYA has a breakthrough feature, wherein the air-conditioning unit is mounted in the motor room and has a higher packaging density owing to functional integration. Thus, both a completely flat floor and space efficiency (in the front-rear direction) exceeding those of the top benchmarked SUV ICE vehicles were realized (Figs. 1 and 2).



Fig.2 Realization of high space efficiency and completely flat floor

*Nissan Product Development Department No.1

The aforementioned functional integration were included under the premise of stiffness of the vehicle body frame structure from the beginning of the planning stage. Consequently, precise maneuvering performance, comfortable riding experience, and mass reduction, which are the expectations of the customers from an EV, have been realized simultaneously.

4. Layout of the air-conditioning unit in the motor room

The realization methods are described in more detail from this section forward. The position of the air-conditioning unit, which was previously situated in the instrument panel of the cabin, was relocated to the motor room to realize a thin instrument panel. This change was introduced during the world premiere of ARIYA and has been well known since then.

However, changing only the mounting position of the unit hardly contributes to improving the ratio of effective interior to overall vehicle length (i.e., packaging efficiency in the front-rear direction). This is attributed to the fact that as the interior space is elongated, the motor room housing the air-conditioning unit must also be extended.

The breakthrough realized in ARIYA is that in addition to the positional change of the air-conditioning unit, measures are provided to the structure so that the air-conditioning unit absorbs energy on impact. As shown in Fig. 3, the air-conditioning unit was previously mounted at the rear side of the dash panel (i.e., in a non-crushable zone). If the air-conditioning unit is relocated to the motor room and crush stroke is maintained, extending the motor room is necessary to accommodate the front-rear length of the air-conditioning unit (Fig. 4).

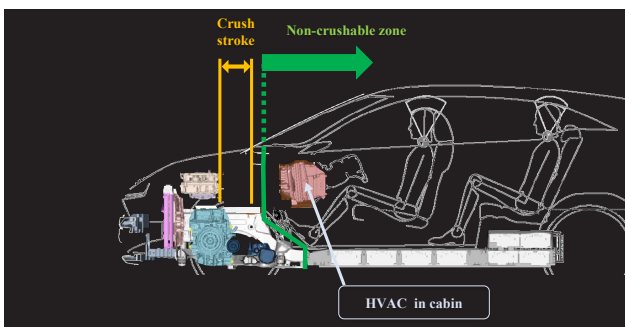


Fig.3 Relationship between previous air-conditioning unit placement and crush space

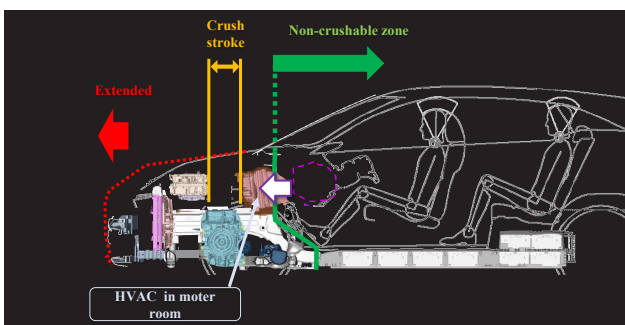


Fig.4 Relocation of the air-conditioning unit and extension of the motor room

For the CMF-EV adopted in ARIYA, the air-conditioning unit was built to be crushed so that the necessary crush stroke could be secured, and the front-rear length of the motor room was shortened (Fig. 5). The air-conditioning unit primarily comprises a heat exchanger, refrigerant pipes, blower fan, and duct. Because the components other than the heat exchanger and blower fan motor are made of resin or have hollow shapes, there is some allowance for crushing. Therefore, the Force-Stroke characteristic for collision was assigned to the air-conditioning unit when developing ARIYA by assuming that the air-conditioning unit body will be crushed to approximately 200 mm during a full-frontal collision. Of the air-conditioning unit components, the air PTC heater, which requires high voltage, was placed within the cabin (non-crushable zone) in consideration of high-voltage safety during collision.

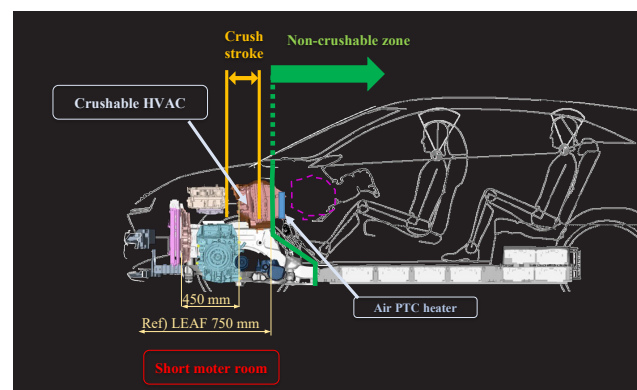


Fig.5 Crush space assuming crushing of the air-conditioning unit

A method for predictably crushing the air-conditioning unit during a frontal collision is described herein. Fig. 6 shows the layout diagram of the CMF-EV motor room. The air conditioning unit is mounted on the rearmost side of the motor room. The upper powertrain unit, which is an assembly of the battery charger, junction box, and DC-DC converter, is mounted on the front side.

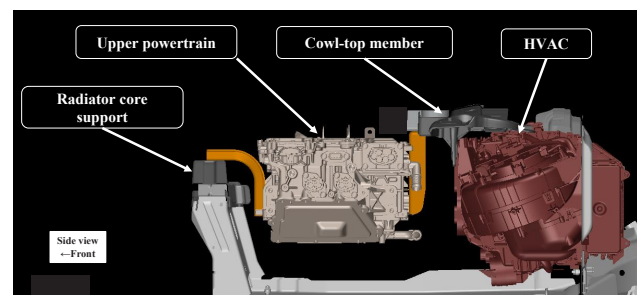


Fig.6 Layout of the motor room

During a frontal collision, the upper powertrain unit starts retracting from the intermediate stage of the collision event, and the maximum amount of retraction occurs at approximately the same time as when the air-conditioning unit is completely crushed. To achieve predictable crushing of the air-conditioning unit under various types of collisions, it is desirable for the upper powertrain unit to retract while maintaining the initial

mounting angle (seen from the side view of the upper powertrain unit). The following measures were implemented to help control motion.

- [1] Connect the front side of the upper powertrain unit to the vehicle body frame structure to stabilize the retraction motion during collision
- [2] Detach the rear fixing bracket when the upper powertrain unit retracts to ensure that the retraction is not obstructed

As a structure that realizes the first measure above, the radiator core support member connected to the front side member was affixed to the front side of the upper powertrain unit. In addition, the allowable bracket deformation amount and deformation modes were specified.

To realize the second measure, a slit was introduced at the bolt fastening portion of the rear fixing point to enable the bracket to slide and come away only upon retraction input due to collision (Fig. 7). To ensure both secure fixation during normal driving and sliding during collision, the bracket stiffness, surface treatment, dimensional accuracy, and fastening torque are strictly controlled. By implementing the aforementioned measures, the space of the air-conditioning unit was utilized as a crushable zone. Thus, sufficient crush stroke was secured while realizing “large interior space in the front-rear direction owing to the compact powertrain”, as expected by the customers.

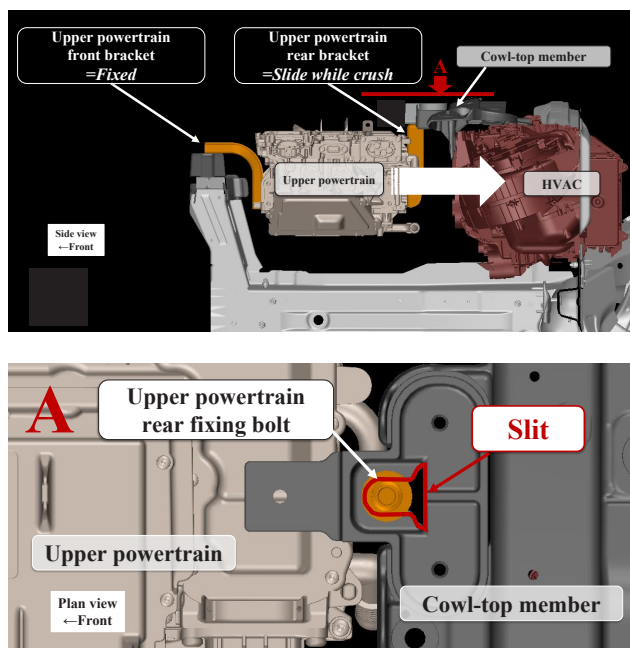


Fig.7 Unit behavior during frontal collision and slit structure at the fastening point

5. Space saving through functional integration and vehicle body stiffness

To mount a high-capacity battery, increase the cabin space, and realize a flat floor and high driving performance, functions were integrated to increase packaging density. Two major case examples are presented here.

The first is a cowl-top member that integrates the upper powertrain unit fixtures, air-conditioning unit

fixtures, and strut tower bar. Previously, the upper powertrain unit was mounted on the member connecting the side members, and the air-conditioning unit was mounted on the steering member in the cabin, as shown in Fig. 8. An additional strut tower bar was added separately in vehicles requiring greater maneuverability.

In the CMF-EV, the functions of fixing the upper powertrain and air-conditioning units as well as the strut tower bar are integrated into a new cowl-top member made of aluminum. Thus, the space and mass necessary for the fixtures were reduced while increasing the structural stiffness around the strut tower (Fig. 8).

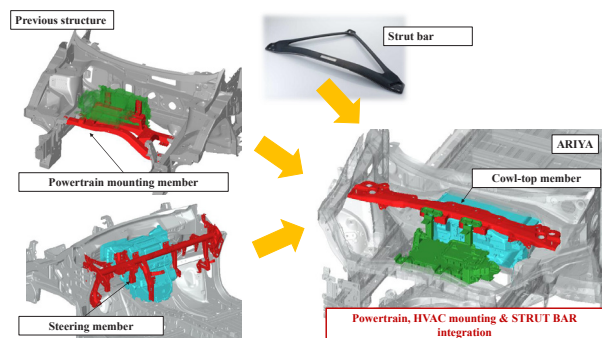


Fig.8 Functional integration using the cowl-top member

The second is a multifunctional frame for the high-voltage battery. Previously, the main functions of the high-voltage battery frame were to support the battery body and protect it from inputs, such as collisions and interference with road surfaces. While more details are described later in the chapter on development of the high-voltage battery, the CMF-EV uses aluminum extruded material for the battery frame. Using this manufacturing method, a water jacket for battery temperature control and a cooling water pipe connected to the rear motor inverter (for 4WD) were integrated in the cross section of the frame (Fig. 9).

Additionally, the high-voltage wiring harness connected to the rear motor inverter was changed to a bus bar and rerouted within the high-voltage battery pack, and the brake pipe was rerouted in the gap between the battery pack and side sill. Thus, removal of the tunnel was realized; additionally, a “completely flat interior floor from eliminating the exhaust system and propeller shaft” was realized in accordance with customer expectations from an EV.

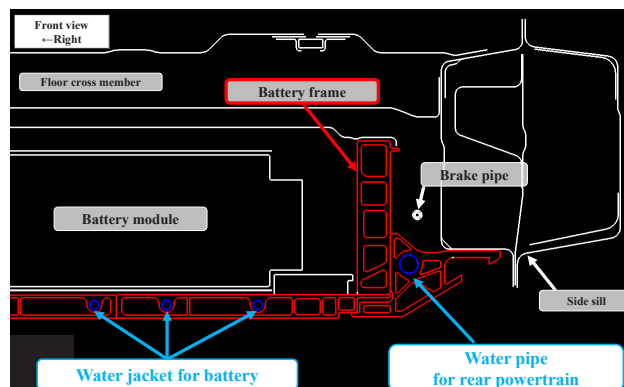


Fig.9 Integration of water pipe with high-voltage battery frame

The high-voltage battery frame is one of the main structural components, and its connections with the vehicle body frame structure and suspension members were strengthened. As shown in Fig. 10, the hot-stamped materials of the vehicle body floor (cross members of the floor and high-voltage battery) were rearranged in an alternating configuration in the front-rear direction. The cross members of the high-voltage battery are connected to the vehicle body side sill via the side frame and side rail. This construction helps protect the high-voltage battery during side collisions and increases the stiffness of the vehicle body frame structure.

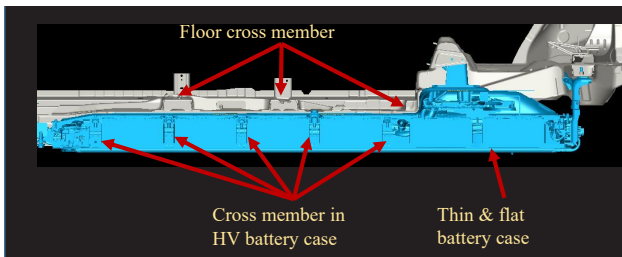


Fig.10 Positional relationship between vehicle body floor and high-voltage battery frame

The high-voltage battery frame was connected with both the rear fastening point of the front suspension member and the front fastening point of the rear suspension member via suspension pin stays. Thus, the lateral stiffness of the suspension member fastening point was increased and steering responsiveness was improved (Fig. 11). By utilizing the high-voltage battery frame as the main structural component, the cross-sectional area of the vehicle body cross member was reduced and a flat floor was realized; additionally, a vehicle body stiffness approximately 1.9 times higher than previous C-segment SUVs was secured. Thus, a low flat floor and dynamic performance, such as ride comfort performance, were realized simultaneously.

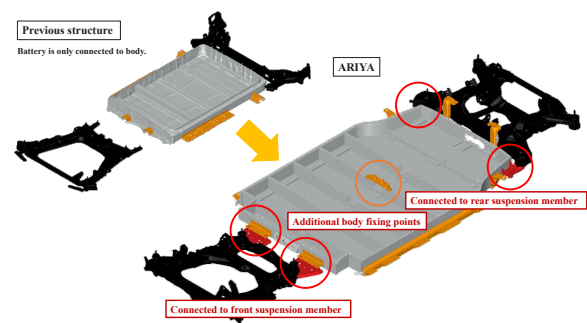


Fig.11 Strengthening connection between suspension and high-voltage battery

6. Summary

The CMF-EV adopted in ARIYA was developed for potential use in Renault vehicles. Renault's core development members, who are permanently stationed in the office at the Nissan Technical Center (Atsugi City, Kanagawa Prefecture), exchanged ideas with us on various technical issues and attended thorough discussions to formulate technical solutions and select the best options during the developmental activities.

During the development stage, the environment surrounding EVs changed drastically on a daily basis. However, there were no changes in our initial target of inheriting and furthering the high reliability and safety developed for LEAF as well as the target "exceed the expectations of our customers further" for vehicle packaging, driving range, and driving performance.

Although not mentioned in this chapter, we succeeded in evolving the ARIYA'S performance from LEAF in terms of the driving range, charging performance, and resistance to capacity decline of the high-voltage battery under actual driving scenarios, such as when using the air conditioner or under varying temperature conditions. In addition, we improved the driving experience unique to EVs (through e-4ORCE) as well as convenience using connectivity. Based on the developmental activities, we are confident that ARIYA will be a popular choice for customers not only as an EV but also as an automobile. We are looking forward to contributing to a more sustainable mobility by attracting and encouraging a wide variety of customers who have previously hesitated in purchasing EVs.

Authors



Masahiro Oonishi

Next-generation flagship: ARIYA

3. Integrated interface display

Tetsu Obata* Takashi Eguchi* Yasutomo Sasanuma*

In recent years, smartphones have become daily tools for handling information and the volume of onboard infotainment information has increased steadily with changes in usage mode and user experience (UX). Further, with the advancements in driver-assistance technologies, the types of information, including sensing information from the surroundings and system conditions, have been changing. To reduce the burden of driving operations under such changes in the information environment, a new human-machine interface (HMI) was developed for easy access to the required information.

This chapter describes new technologies installed in ARIYA, namely an “integrated display package for combined visibility and operability” to support easy access to information and a “structured graphical user interface (GUI) for easy and intuitive handling of a large variety of content.”

1. Interface for combined visibility and operability

Various approaches have been considered for the integration of the infotainment and meter displays into a single information display area. During the development of ARIYA, the dead angle of the steering wheel was considered for determining the display location and its features (Fig. 1).



Fig.1 Integrated interface display

Meter information required for driving is displayed in front of the driver at a convenient distance for clear

visibility, whereas the infotainment information is displayed at a distance conducive to high operability and within easy reach of the driver (Fig. 2). These two information panels are placed adjacent because the human visual field is approximately 1.5 times wider horizontally than vertically, and eye movements are easier in the horizontal direction (Fig. 3).

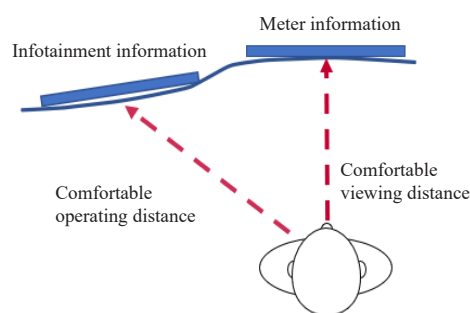


Fig.2 Layout of the information display

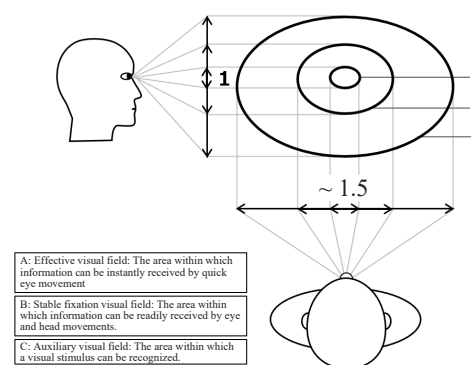


Fig.3 Characteristics of the human visual field

The panels were placed along an S-shaped curved surface, which was in harmony with the futuristic design of the cockpit interior (Fig. 4). The S-shaped display was manufactured as follows. First, a cover glass with multiple curvatures was fabricated via 3D hot forming technology (Fig. 5). Then, a flat liquid-crystal glass was bonded to the cover glass without distortion through optical bonding technology (Fig. 6).

*Connected Car and Services Engineering Department



Infotainment display Meter display
Fig.4 S-shaped display harmonized with the interior

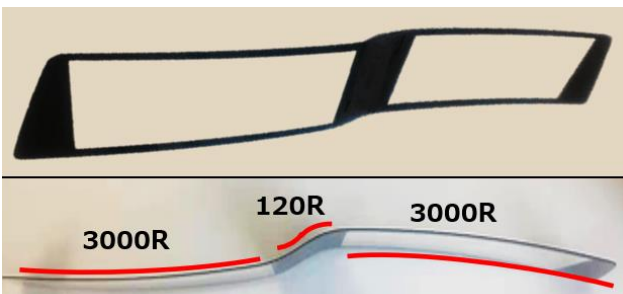


Fig.5 S-shaped cover glass

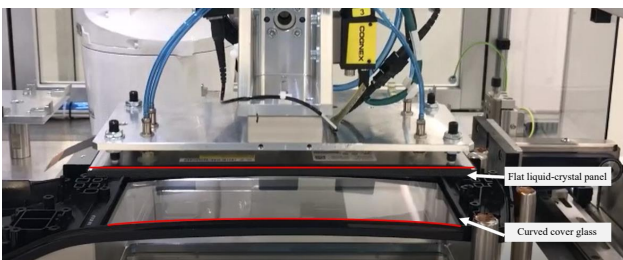


Fig.6 Bonding of curved cover glass

2. Simple and intuitive GUI

2.1 Infotainment information

Because humans have limited ability for processing increasing volumes of information, the number and positions of the displayed menu items were analyzed. The widget sizes (Fig. 7) and tile menus (Fig. 8) were enlarged and their numbers were optimized based on the recognizability and operability of the functions.

The arrangement of the menu items was optimized based on an evaluation of the ease of menu selection as a function of the number of menu items for different age groups. It was observed that short-term memory of a user decreased as the number of menu items increased. A 4-column \times 2-row configuration with a total of eight menu items showed a correct answer rate of over 90% irrespective of age group and was thus selected as the optimum configuration (Fig. 9).

In addition to basic operability, the display configuration allows customers to personalize a variety of

content to their tastes and needs. The tile menu can be intuitively rearranged using drag-and-drop operations (Fig. 10).



Fig.7 Home widgets



Fig.8 Eight-tile menu

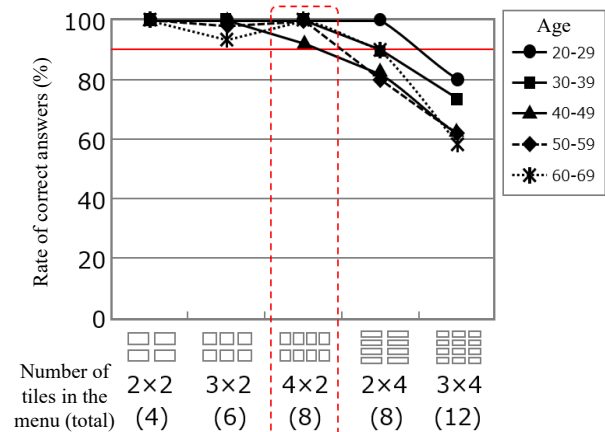


Fig.9 Ease of menu selection as a function of the number of menu items



Fig.10 Customization of home widgets

2.2 Meter information

The meter display consists of three basic zones (Fig. 11) and uses a simple mode, where the volume of information in each zone is restricted such that the desired information can be found easily. For example, the power gauge, instantaneous speed, and drivable distance

are digitally displayed in separate zones, thereby allowing easy confirmation of the conditions of the vehicle (Fig. 12).



Fig.11 Conventional meter display

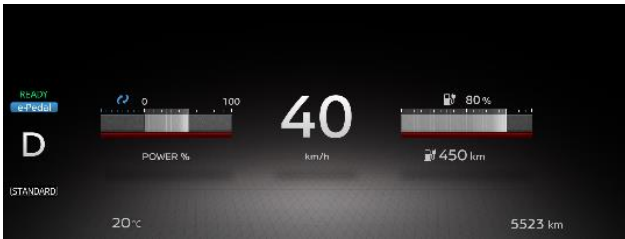


Fig.12 New simple-mode display adopted in ARIYA

2.3 Information communication between the displays

The infotainment and meter displays were synchronized via Ethernet communication and information could be transferred between the two displays instantly using intuitive swipe actions (Fig. 13). This function supports various usage modes, such as moving a map to the meter display while a passenger enjoys other content on the infotainment display.

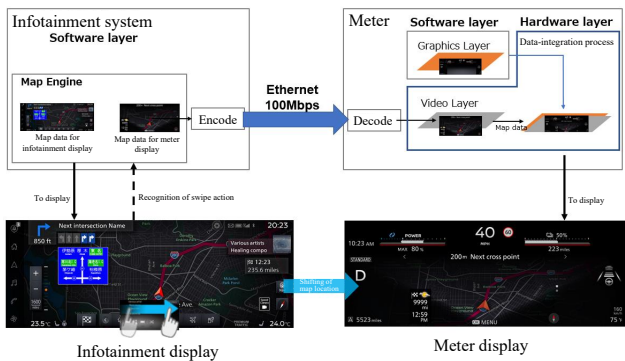


Fig.13 Information transfer between the two displays via Ethernet

2.4 User experience (UX) with emotional value

To provide emotional value to the customer along with high operability of the basic functions, new functions and interactive systems were developed with high interactivity and spatiality. Voice-animation expressions were used for voice recognition because of the excellent interactivity to enhance information recognition (Fig. 14). Home widgets offer new UXs, such as comfortable and enjoyable operations, by providing adequate space to tile menus and icons with parallax effects (Fig. 15).



Fig.14 Voice interaction display



Fig.15 Home screen with parallax effects

3. Summary

ARIYA has been equipped with an “integrated display package for combined visibility and operability” to enable easy access to information and a “structured GUI easy and intuitive handling of a large variety of content.” In addition, ARIYA offers great emotional value to customers through various applications and animations. In the future, the cockpit HMI can be further developed into a drive concierge.

Authors



Tetsu Obata



Takashi Eguchi



Yasutomo Sasanuma

Next-generation flagship: ARIYA

4. Development of new NissanConnect

Toshiro Muramatsu* Kazuhiro Funai** Masaru Tasaki**
Shintaroh Murakami* Hiroyuki Kamishima**

1. Introduction

Connected services, which connect the mobile phone network to the navigation system to provide a wide range of services, were started in the late 1990s. Nearly a quarter century has passed since Nissan launched its “NissanConnect (formerly COMPASSLINK and CARWINGS)”.

Owing to technological evolution in recent years accompanied by the widespread use of the Internet, connecting “things”, such as automobiles and household electrical appliances, to the Internet for better utilization (Internet of Things, IoT) has become popular. In 2019, Nissan updated its connected car system to the NissanConnect service, which provides new experiences to customers by connecting the vehicle and customer terminal seamlessly. The number of users of the NissanConnect service has increased rapidly (Fig. 1). The technologies developed through the dedicated efforts of the NissanConnect development team have been fully adopted in ARIYA to provide new and exciting experiences to customers.

This chapter describes the strengthened NissanConnect platform and the new voice recognition technology developed for the platform.

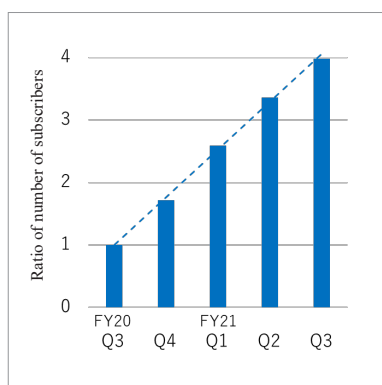


Fig.1 Increase of NissanConnect subscribers

2. NissanConnect system

An overview of the NissanConnect system is shown in Fig. 2. The vehicle is equipped with an in-vehicle infotainment (IVI) system comprising a display and graphical user interface (GUI) as well as a telematics control unit (TCU), which communicates with the cloud. Connections to the other electronic control units (ECUs) and sensors of the vehicle are via LAN. The TCU communicates with the cloud using a mobile phone network. The cloud system is accessible by call centers and third-party information providers that offer services and information to users. In addition, a dedicated app on a user’s smartphone collaborates with the cloud system. The IVI, display, IVC, cloud system, and apps comprise the NissanConnect platform.

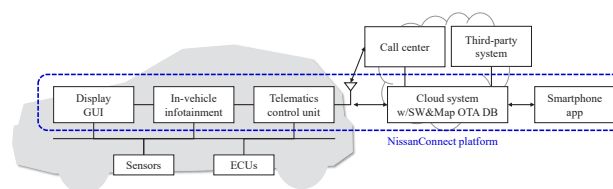


Fig.2 Overview of NissanConnect system

The cloud system consists of three main components: vehicle connection/vehicle information management, service logic/provision management, and software/map over-the-air (OTA) distribution management. The core parts of these components are common globally; hence, global deployment can be achieved quickly. The components may have portions that meet the unique needs of different regions. The system requires both robustness to provide stable service and flexibility to adapt to changing customer requests and peripheral IoTs. To realize these requirements, joint development was conducted with Microsoft Corporation to develop components requiring greater robustness (vehicle connection/vehicle information management and software/map OTA distribution management). In-house development was conducted for the service logic/provision

*Connected Car and Services Engineering Department

**Connected Technology Development and Service Operation Department

management, which requires higher flexibility, for efficiency.

Fig. 3 shows the sequential overview of various services provided by this platform. For example, for the remote function that enables vehicle operation from an app, the user input to the app is used as the trigger to establish a communication path between the cloud server and TCU; subsequently, the commands are sent to the TCU. The TCU operates the vehicle according to the received command and sends the results to the app via the cloud system. In addition, for services that coordinate with third-party information when the vehicle is traveling, user input to the IVI is used as the trigger to convert the cloud system to a proxy, which subsequently connects to the third-party system for service provision. Hence, numerous services can be provided by configuring the functions on the NissanConnect platform.

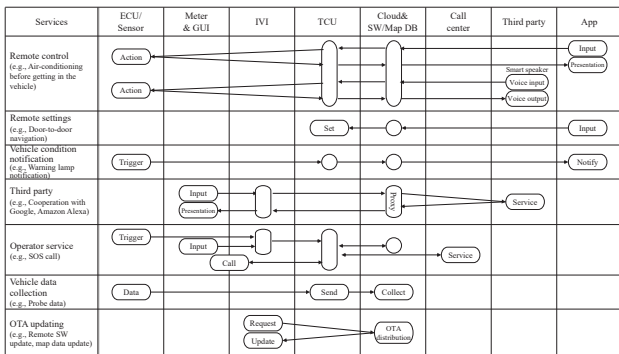


Fig.3 Overview of the NissanConnect service sequence

3. Voice recognition technology supporting CCS

Voice recognition technology is a method to reduce the burden of operating an in-vehicle device when driving. To date, the mainstream voice recognition method has been a standalone method, where a voice recognition engine is installed in the in-vehicle device. For ARIYA, we developed a dictionary database used exclusively by Nissan in addition to the standalone method. The off-board method was adopted for the dictionary database; thus, the database resides on a network configured on the platform. The off-board method was adopted because it is capable of accurately understanding the daily utterances used while driving and the intentions of such utterances.

Natural language speech is acquired using a microphone, processed via voice signal processing in the in-vehicle device, and further processed in the following order. Phoneme recognition, word/sentence recognition, and intention estimation (Fig. 4).

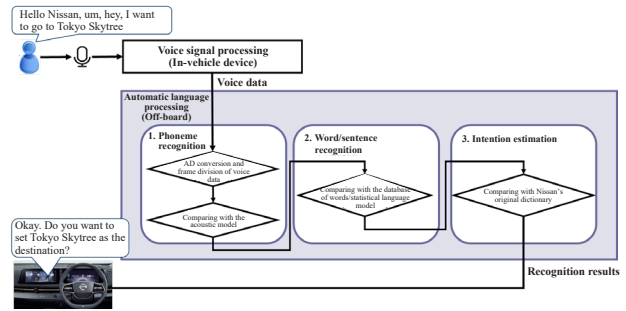


Fig.4 Flow of natural language recognition processing

3.1 Phoneme recognition

The voice signal acquired by the microphone undergoes AD conversion and is sequentially divided into frames of equal lengths. Then, each frame undergoes frequency spectrum analysis to obtain the acoustic features. Subsequently, phonemes are recognized by comparison of the obtained acoustic features with the acoustic model, which is created by statistical processing of human voice.

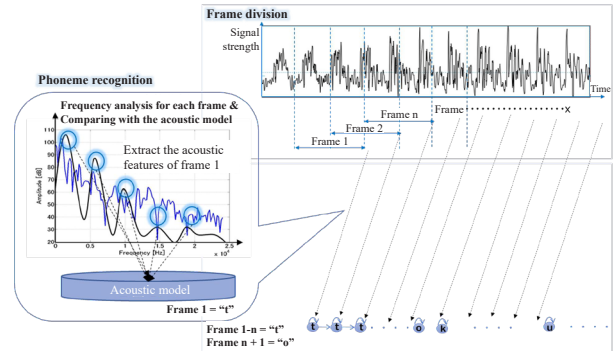


Fig.5 Phoneme recognition

3.2 Word/sentence recognition

Comparing the chronological connections of phonemes with the database of words, the words in the voice signal are obtained. In addition, a statistical language model in the form of parameters obtained by learning the probability of shifting from one word to another is used for comparison when selecting the final candidate for “the most probable word combination result.” For example, given the input “I want to go to tou . . . kyou skytree,” it is possible to recognize an accurate sentence “I want to go to Tokyo Skytree.”

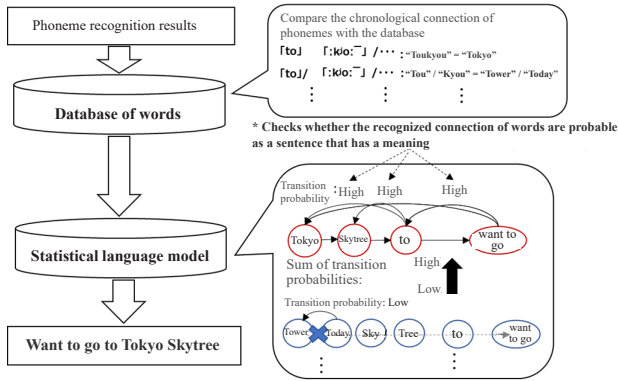


Fig.6 Word/sentence recognition

3.3 Intention estimation

To estimate the intention of an utterance made during driving, it is necessary to process and remove unnecessary words (e.g., “Um...,” “Hey”) and extract only the necessary words (e.g., Tokyo Skytree + want to go). In addition, synonyms of “want to go to” (e.g., “go to,” “set the destination at”) need to be recognized. There may also be cases where the uttered sentences are not grammatically correct. To separate these factors and secure sufficient intention estimation performance in the driving environment, Nissan’s original dictionary database was developed. The database contains learned data from approximately 3,000 utterance patterns collected in actual driving environments. Using this dictionary database and narrowing the database to only the necessary words allowed a voice recognition rate achievement of approximately 85% for ARIYA compared to approximately 70% for systems manufactured by other companies.



Fig.7 Intention estimation

4. Summary

We are at the beginning of an era wherein automobiles have become a part of the Internet, and we are creating new value using the NissanConnect platform. The voice recognition technology described herein has the potential to offer new experiences, such as dialog-type services, including the virtual personal assistant (VPA). Once again, we deeply consider the meaning and significance of our principles “What is important is the value for the customer,” “Is there competitiveness in that subject?” and “Only the customer knows the correct answer” to actively develop leading services for the future.

Authors



Toshiro Muramatsu



Kazuhiro Funai



Masaru Tasaki



Shintaroh Murakami



Hiroyuki Kamishima

5. High-capacity lithium-ion battery for ARIYA

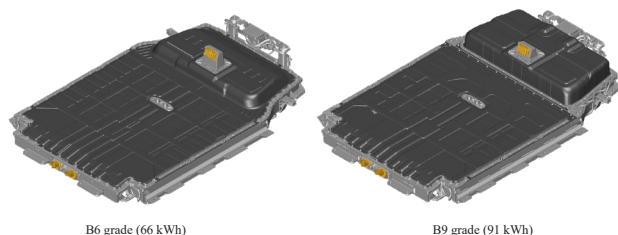
Junji Katamura* Kentaro Hatta* Keisuke Wakabayashi*
Masanori Takagi* Naoto Todoroki*

1. Introduction

Electric vehicles (EVs) have been deployed globally in recent years, and there is demand for a longer driving range. The driving range depends primarily on battery performance. Therefore, it is important to increase the amount of energy within specified battery size, it is important to increase the energy density per unit volume. A newly developed EV-specific platform is adopted in ARIYA to realize a flat and large interior space; thus, the requirement for the battery layout design is to fit within a limited space.

On the other hand, from the viewpoint of improving convenience, there is a high demand for quick charging performance to ensure that a greater amount of energy can be stored in a short period of time. To meet these demands, a temperature control system that appropriately controls battery temperature is essential. However, the battery temperature control system significantly lowers the volume efficiency of the battery pack, and the control system has a large impact, particularly in the thickness (height) direction.

The newly developed battery pack has improved energy density per battery pack thickness (approximately 2.3 times that compared to the LEAF E+), even though it is equipped with a temperature control system. Consequently, top level volume energy density and quick charging performance (for EVs) have been realized while improving interior comfort. This article describes the development of the high-capacity lithium-ion battery mounted in ARIYA.



B6 grade (66 kWh)

B9 grade (91 kWh)

2. Technology for low and flat floor in the cabin

As mentioned above, the newly developed EV-specific platform was adopted in ARIYA to realize a flat and large interior space. This required designing a thin and flat battery structure. The main technologies developed newly for this requirement are described herein.

2.1 Thin cooling mechanism

Typically, a temperature control system that uses LLC (Long life coolant) is adopted in battery EVs (BEVs). In this system, a plate is placed at the bottom of the battery pack. The LLC is cooled using a chiller, heated using a heater, and supplied to the plate to control battery temperature.

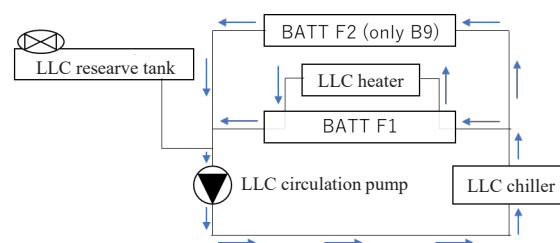


Fig.1 Diagram of the battery temperature control system

To uniformly cool/heat the battery modules arranged within the battery, the LLC must be supplied uniformly across the entire of the lower plate. However, the space within the battery must be watertight and separate from the LLC flow channels. Therefore, three structures, namely the lower plate, LLC flow channel mechanism, and protection cover, are necessary, as shown in Fig. 2. In ARIYA, these structures are integrated to realize a thin battery pack (Fig. 3).

*Powertrain and EV Energy Storage Technology Department

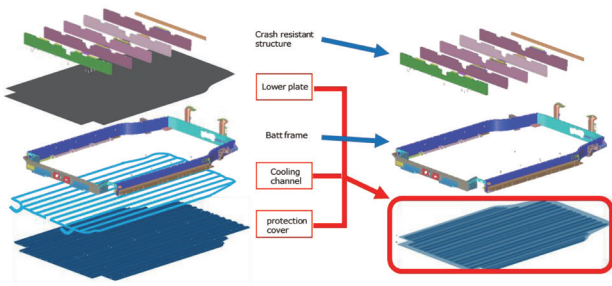


Fig.2 Battery cooling structure of other companies

Fig.3 ARIYA cooling structure

side to increase the heat-insulating property and cooling efficiency (Fig. 5).

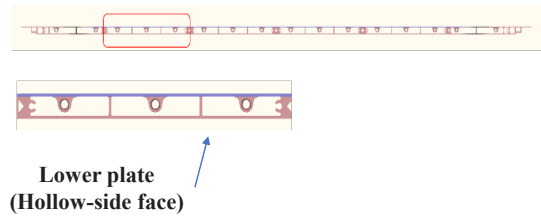


Fig.5 LLC flow channel cross section

2.2 Battery floor manufactured by aluminum extrusion

Aluminum extrusion method was adopted to manufacture the battery casing to integrate its lower plate, LLC flow channel mechanism, and protection cover. A cross-sectional structure was established such that the LLC flowed inside the extruded lower plate. In this manner, the lower plate and cooling plate were integrated to realize a cooling mechanism with reduced thickness (Fig. 4).

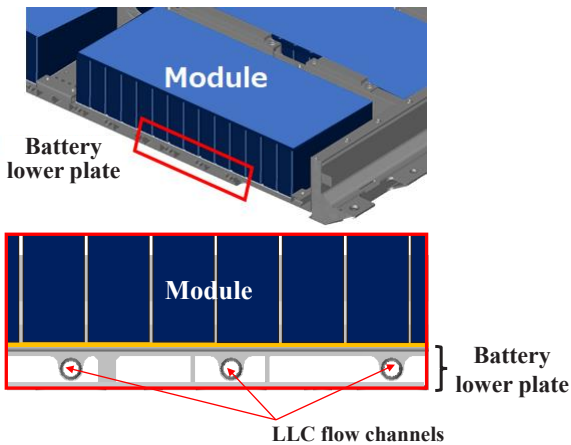
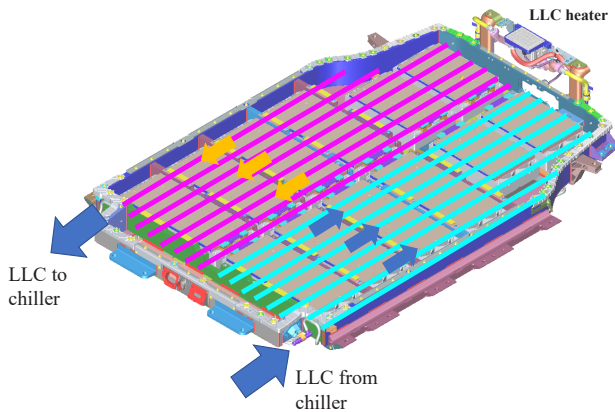


Fig.4 cross section of battery lower plate with LLC flow channels

The cross section in which the LLC flows is structured such that the flow channel is in contact with the upper plate on which the battery module is mounted. A hollow space is formed between the flow channel and lower plate

To realize a thin and flat battery layout design, the battery modules are arranged in a thin and wide layout (Fig. 6). Therefore, the space between the battery pack peripheral frame and battery modules is narrow, which results in very little crush allowance during collisions. To solve this problem, multiple cross members are placed within the battery pack to realize high resistance against impact.

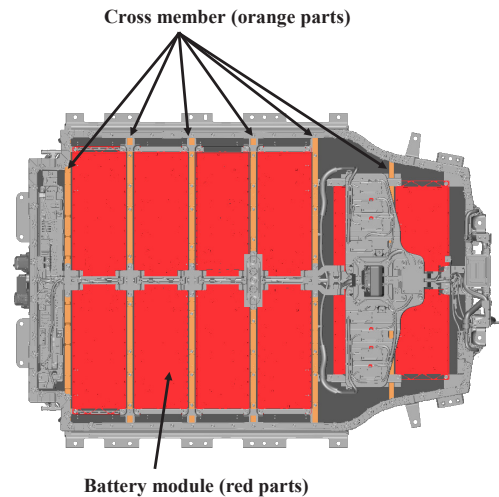


Fig.6 ARIYA battery layout

3. Balanced evolution of the trade-off performance

Although our previous battery development activities were based on balancing high-level performances, we have improved the balance further in ARIYA. The main battery performances that provided value to customers were compared among ARIYA, LEAF, and other existing technologies; the comparison results are summarized in Table 1. Balanced evolution of the battery performance was realized in ARIYA, which is a trade-off relationship. The representative items are described here.

Table 1 Comparison with existing technologies

Value for our customers	Battery performance	Natural heat dissipation (LEAF)	Temperature control by fluid (Existing technology)	Thin temperature controlling mechanism (ARIYA)
Interior space	Battery pack thickness	BASE	△	○
Driving range	Energy	BASE	×	○
	Mass	BASE	×	△
Price	Number of components	BASE	×	△
	Structure expansibility	BASE	←	○
Convenience	Consecutive charging	BASE	⊙	⊙
	Low-temperature charging	BASE	⊙	○

3.1 Convenience improvement

The thin cooling mechanism described in the previous section was instrumental in realizing a flat and large interior space unique to EV-specific platforms. Additionally, it helped realize quick charging performances in various types of environments. Fig. 7 shows the amount of energy stored in 30 min of quick charging at ambient temperatures of 40°C and -5°C. It was possible to achieve excellent and quick battery charging performance in ARIYA under various types of environments by appropriately controlling the battery temperature (heating during winters and cooling during summers).

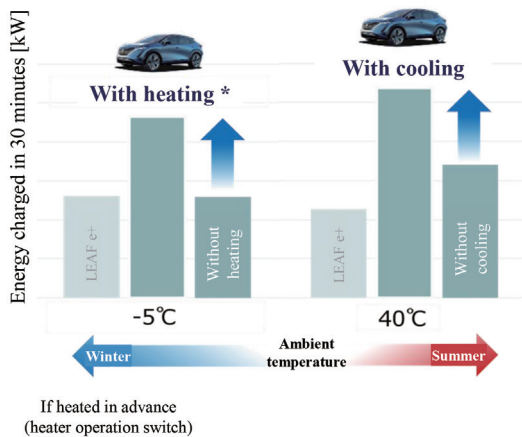


Fig.7 Quick charging performance

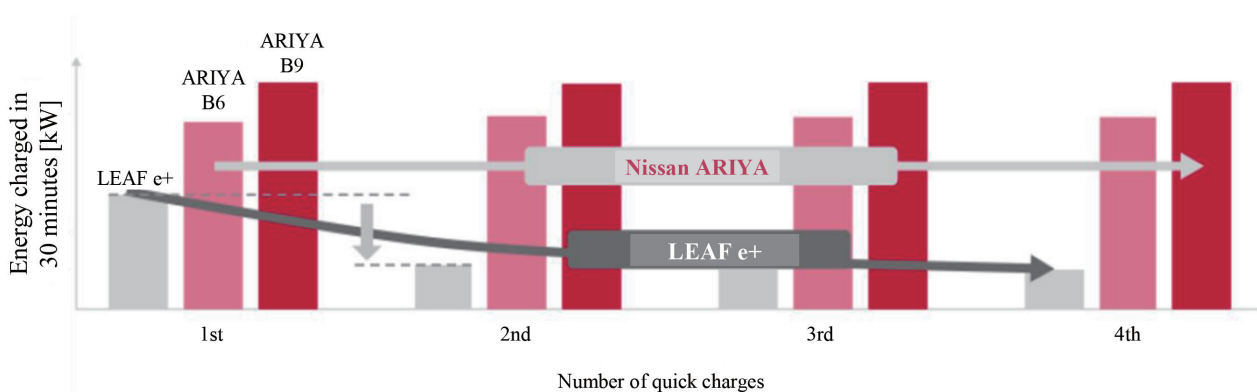


Fig.8 Transition in the amount of energy charged with repeated high-speed traveling and quick charging

Fig. 8 shows the quick charging performances of Nissan EVs assuming a situation where the vehicles are driven for long durations and mainly on highways, with repeated high-speed traveling and quick charging. In LEAF E+, the battery temperature increased with the number of quick charges, and the charging speed tended to decline from the second quick charge onward. However, the battery temperature is controlled appropriately in ARIYA; therefore, the charging speed did not decline even with repeated high-speed traveling and quick charging, thereby enabling comfortable long-distance driving.

3.2 Battery structure for high expansibility and fewer components

The battery floor structure fabricated by aluminum extrusion enables a thinner battery and realizes high expansibility to various types of vehicle specifications. Because the battery casing is extruded in the front-rear direction of the vehicle body, simply changing the extrusion length enables the application of the battery casing in vehicles with different wheelbases. Thus, the number of specifications was reduced. Even in the two-story-structured B9 grade (91 kWh battery specification, in contrast to the one-story-structured B6 grade (66 kWh)), where the battery modules are arranged in the space below the rear seat to obtain high energy capacity, the basic structure of the first-story portion can be standardized (Fig. 9). As noted previously, integrating the lower plate and LLC plate of the battery casing enables an approximately 60 % reduction in the number of components. These technologies can promote high competitiveness.

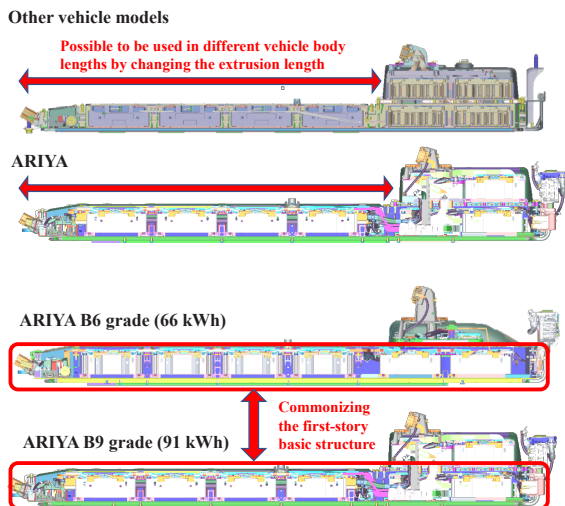


Fig.9 High expansibility to other vehicle models

4. Summary

The battery mounted in ARIYA has a newly developed thin structure and is equipped with a temperature control system. Thus, a flat and large interior space that is unique to EV-specific platforms was realized. Moreover, improved energy density per volume as well as high quick charging performances under various types of environments were realized.

To promote the widespread use of EVs, we will continue to improve the chemistry of lithium-ion batteries while maintaining their high performance and reliability, improve the energy density, and develop batteries with greater competitiveness.

Authors



Junji Katamura



Kentaro Hatta



Keisuke Wakabayashi



Masanori Takagi



Naoto Todoroki

Next-generation flagship: ARIYA

6. Newly developed motor to realize ARIYA's performance

Takahito Okubo* Hiroki Wada**

1. Introduction

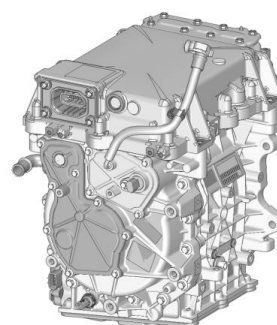
One of the concepts realized in ARIYA is providing the feeling of being in a lounge. The key points of the lounge concept are ensuring a high level of quietude as well as smooth acceleration and deceleration without abrupt shocks, in addition to the design and quality of the interior, such as the seats. This chapter describes how these requirements were met. The main focus here is on the motor, which has been completely redesigned for ARIYA.

2. Overview of the newly designed motor

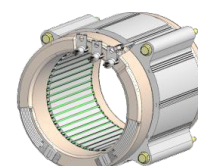
In ARIYA, EESM^{*2} was adopted instead of the IPM (SM)^{*1}, which was adopted in LEAF, NOTE, and SERENA E-POWER. Although the EESM is similar to the IPM in that three-phase AC is supplied to the stator by PWM control, the EESM does not use permanent magnets in the rotor and instead uses electromagnets operated by DC. Thus, appropriate amounts of current can be selected for the rotor and stator based on the driving load, thereby leading to improved efficiency as well as reduced vibration and noise. However, the heat generated increases owing to the supply of electric current to the rotor, and securing torque responsiveness is an issue (as described in the next section).

An expanded view of the EESM used in ARIYA is shown in Fig. 1. For comparison and reference, a similar view of the IPM of LEAF is shown. An eight-pole rotor structure is adopted in the EESM in ARIYA. The DC generated in the PEB^{*3} is supplied to the rotors via a brush system. The amounts of DC for the rotor and three-phase AC for the stator are calculated in the PEB according to the torque instruction values based on the driving force requirements. The current values are controlled such that an optimum combination can be achieved. Direct oil cooling is used to cool the motor.

ARIYA

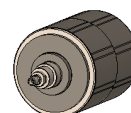


Rotor assembly

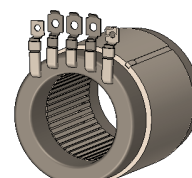


Stator assembly

LEAF



Rotor assembly



Stator assembly

Fig.1 Motors used in ARIYA and LEAF

*Powertrain and EV Engineering Division

**Powertrain and EV Electrical Technology Department

3. Value realized by ARIYA's motor

3.1 Realizing quietness

Compared with combustion engine and hybrid vehicles, there is no generation of engine noise in a BEV^{*4}. Therefore, the road and wind noises are more prominent. Moreover, there are instances where high-frequency noise generated by the motor and inverter are issues that are never observed in combustion engine vehicles. In ARIYA, several measures are implemented in the vehicle body to suppress the road and wind noises heard by passengers. Further, measures are provided to suppress the high-frequency noise generated by the motor. By implementing these measures, the overall quietness was improved.

The high-frequency noise generated by the motor, whose main component is the electromagnetic excitation force, changes according to the torque and number of revolutions. The magnetic force of the rotor is constant in an IPM; therefore, the torque is controlled only by the current supplied to the stator. Thus, the electromagnetic excitation force is proportional to the supplied current. However, in the motor used in ARIYA, the current is controlled for both the stator and rotor, the electromagnetic excitation force is reduced, particularly in the low-torque area. Further, a higher level of quietness is realized in scenarios where the driving force requirement is not large, such as during gentle acceleration and cruising (Fig. 2).

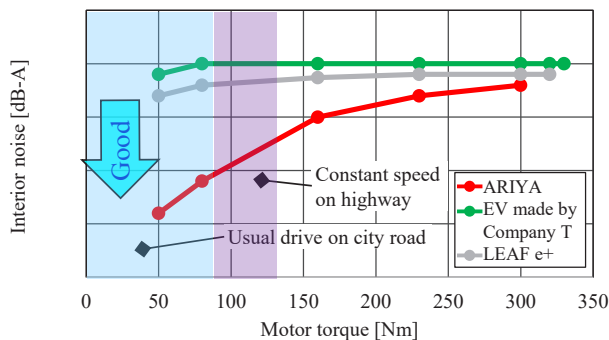


Fig.2 Comparison of interior noise

3.2 Improving electrical energy consumption

The induction voltage generated between the rotor and stator in the IPM increases with the increase in the number of revolutions. In such cases, the output is usually secured in the high-revolution regime by measures, such as field-weakening control; however, this may simultaneously worsen the efficiency. Owing to a similar mechanism as that for high-frequency noise, the magnetic force is constant for the IPM. Therefore, the magnitudes of the induction voltage and field-weakening current are determined uniquely according to the torque and number of revolutions. In ARIYA's motor, the magnetic force of the rotor can be changed by changing the supplied current. Accordingly, the rotor and stator currents are controlled such that the induction voltage is

suppressed while the required torque is exerted. Thus, the decline in efficiency is reduced even when driving at high speeds (Fig. 3).

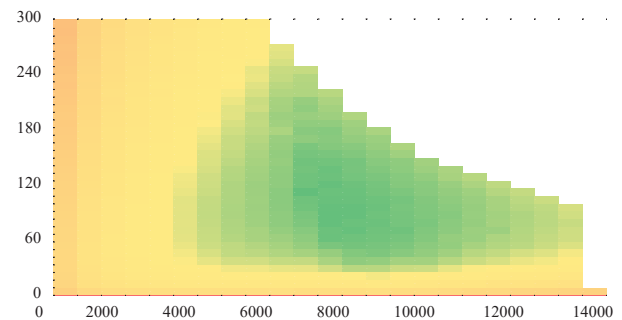


Fig.3 Efficiency

4. Characteristics of ARIYA's motor

4.1 Structure of the wound rotor

EESM, as the name suggests, is structured to supply DC to the rotor that acts as an electromagnet. Therefore, the rotor has a wire-wound structure. The rotor developed for ARIYA has eight wire-wound poles. Renault, which is Nissan's alliance group, has adopted an EESM in ZOE that has four wire-wound poles. To obtain higher outputs, the rotor volume was increased and the number of poles was increased to eight to secure the necessary electromagnetic force and torque responsiveness.

Moreover, the number of revolutions is higher in ARIYA. To realize this feature, the aforementioned measures have been implemented for increasing the output and additional measures are provided in the rotor structure. The cross section of the rotor and a magnified view of a portion of the cross section are shown in Fig. 4. After winding the wire on each of the eight rotor poles, wedge-shaped slots were inserted between the poles to suppress wound-wire deformations due to centrifugal forces. Therefore, the stability of the wound wire shape is crucial. When commencing the motor production process for ARIYA at the Nissan Intelligent Factory, a fully automatic wire-winding machine capable of winding eight rotors at once was introduced to ensure sufficient production capacity. In addition, collaboration was undertaken with the Production Engineering Division to realize uniform and stable wire-winding shape between rotors.

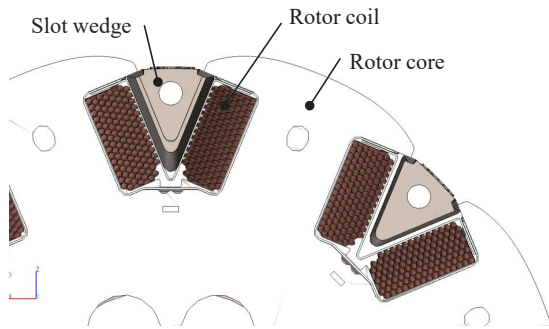
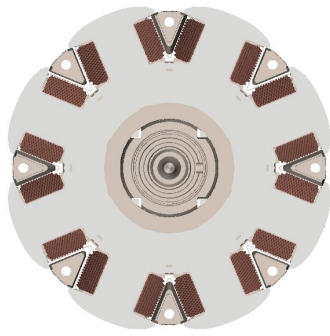


Fig.4 Structure of the wound rotor

4.2 Improved cooling performance via oil cooling

Because the EESM is structured to supply electrical current to the rotor that acts as an electromagnet, the heat generated by the rotor is high. Therefore, a direct oil-cooling method was adopted in ARIYA. The configuration of the oil-cooling circuit is shown in Fig. 5. The oil that accumulates in the oil pan below the motor is pumped using an electric pump, transferred through the channels in the motor casing, and sprayed over the stator and rotor. For the stator, oil is supplied from the outer periphery primarily to cool the core. For the rotor, the supplied oil cools the front and rear coil end portions, and oil is simultaneously supplied to the bearings and oil seals to ensure lubrication.

The oil circulates only inside the motor, and the generated heat is discharged to the water-cooling circuit of the vehicle side through a heat exchanger attached to the side of the motor. The discharge quantity of the oil pump can be varied according to the temperatures of the stator and rotor. Thus, the electrical power consumed by the pump is suppressed.

Additionally, the oil is used to cool the high-voltage components. Therefore, oil that can achieve stable performance from very low to high temperatures while ensuring electrical insulation performance was selected. In addition, a maintenance-free system that requires no replacement or replenishing of the oil is realized.

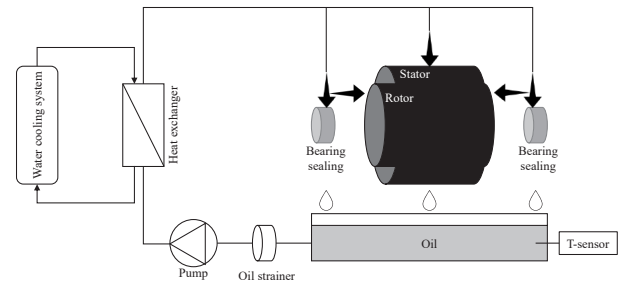


Fig.5 Oil-cooling circuit of the motor

5. Summary

Electric drive technology is rapidly evolving along with the acceleration of electrification trends. In addition to IPMs, which have been widely used previously, an EESM has been developed for ARIYA with sufficient performance and mass-production quality. Thus, we are now able to provide the technology most suited for meeting customer demands regarding vehicle performance. Furthermore, we are able to reduce the cost and supply risks of rare-earth materials.

In future, we intend to further utilize the characteristics of EESMs. For example, in vehicles that have drive motors at both the front and rear ends, during low loads (e.g., when cruising), the electric current supply to the stator/rotor can be turned off for one of the motors to effectively improve electrical energy consumption.

Terminology

- *1 IPM (SM): Interior permanent magnet synchronous motor, which is an embedded-magnet-type synchronous motor.
- *2 EESM: Electrically excited synchronous motor, which is an external-field-type synchronous motor.
- *3 PEB: Power electric box that mainly integrates the inverter function with the peripheral circuits and power source branching function.
- *4 BEV: Battery electric vehicle, which is an electric vehicle driven primarily by the energy stored in an externally charged battery.

Authors



Takahito Okubo



Hiroki Wada

Next-generation flagship: ARIYA

7. Nissan's "e-4ORCE" : Proposition for evolution of electric AWDs

— Aiming for a more exhilarating and confident driving experience

Hiroyuki Togashi* Yutoku Miyagoshi** Takeji Katakura***

1. Introduction to "e-4ORCE"

Starting from ARIYA, Nissan will be adopting "e-4ORCE," which is a novel technology for controlling electric all-wheel drives (AWDs). The "e" in "e-4ORCE" indicates the electric drive of EVs. Whereas, the "4ORCE" (read as 'force'), which combines the physical power and energy with the "4" of four-wheel drives, indicates the will to control the power or force of the tires of four-wheelers.

In recent years, electric AWDs mounted with two high-power motors, one each at the front and rear, have been increasingly adopted by companies to meet the demands for higher vehicle dynamics and environmental performance. Compared to previous mechanical AWDs, Nissan considers that electric AWDs have very high technological potential because of their "good acceleration" and "high ultimate performance levels", and because they can achieve better vehicular motion "quality" even in daily usage environments. The "e-4ORCE" technology is an attempt to unleash the potential of electric AWDs and improve the quality of vehicular motion. This section describes the "e-4ORCE" technology.

2. Overview of the "e-4ORCE" technology

The previous AWD system, which was mounted with combustion engines, realized power generation at the combustion engine and its mechanical distribution to the front and rear wheels via the connected propeller shaft (Fig. 2). Therefore, there may be mechanical delays when transferring power and mechanical limits to the resolution of power distribution. Unlike electric motors, it is difficult for combustion engines to control their outputs with high responsiveness. Therefore, it is difficult to achieve total driving force control of the order of 0.1 s.

The basic configuration of "e-4ORCE" is an electric AWD. As electric AWDs are mounted with independent electric motors at the front and rear (Fig. 1), it is possible to distribute driving force to the front and rear tires with high responsiveness and accuracy. The technological aim of "e-4ORCE" is to realize the full potential of electric

AWDs to ensure that drivers feel secure when operating the vehicle regardless of the environment, and the vehicle posture can be controlled such that all passengers can feel comfortable.

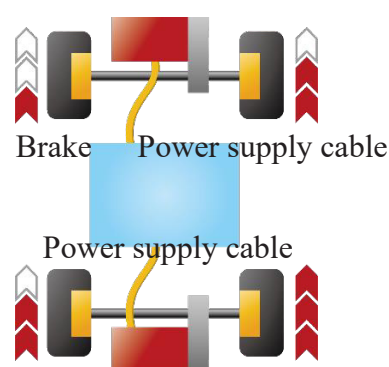


Fig.1 Diagram of e-4ORCE AWD system

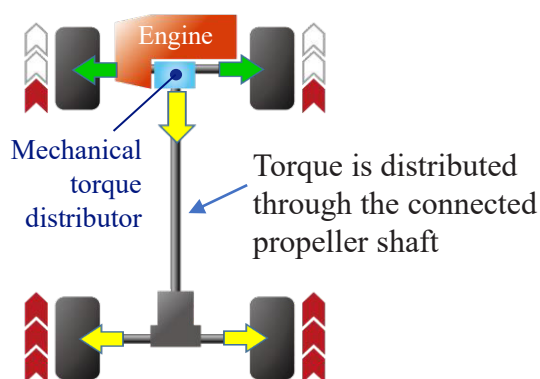


Fig.2 Diagram of previous AWD system

When a vehicle body is supported by four wheels, the load applied to each wheel changes constantly owing to the road surface and vehicular conditions. Additionally, the frictional force limit of each tire changes according to the load on the wheel (Fig. 3). The key criterion here is to achieve control such that the load is distributed to all tires, with good balance including some margin, and within the limits of the tires.

*Vehicle Performance Engineering Department & Powertrain and EV Performance Engineering Department

**AD/ADAS and Chassis Control System Engineering Department

***Powertrain and EV Performance Engineering Department



Fig.3 Tire friction circle and resultant force

In front-wheel drive vehicles, the turning and acceleration/deceleration functions are integrated at the front tires; thus, there is little room for margin. In four-wheel drive vehicles, the turning and acceleration/deceleration functions are optimally shared between the front and rear wheels (Fig. 4) to achieve stability by preventing each tire from exceeding its limit. In the ultimate limiting behavior, the load is distributed such that the maximum value (edge of the friction circle) of each tire is optimally used.

Below the limiting behavior, load distribution is controlled loosely yet carefully within the limits of each tire. Thus, smooth and easy-to-manuever vehicle motions that are impossible in mechanical AWDs can be realized. In addition, the left/right brakes are controlled according to the situation, and the braking force is utilized in situations other than deceleration to improve turning performance.

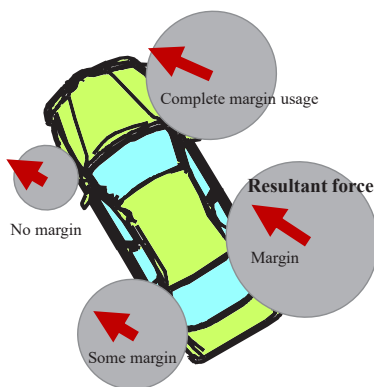


Fig.4 Relationship between the friction circle and resultant force of the four wheels

These technologies have been created and developed by crossbreeding, combining, and further advancing the technological and empirical genes developed by Nissan over the years. These technologies include the AWD technologies, such as the Advanced Total Traction Engineering System for All Electronic-Torque Split (ATTESA E-TS) 4WD system, Intelligent 4 × 4 system, and knowledge gained for electric drive control through LEAF and E-POWER (Fig. 5).

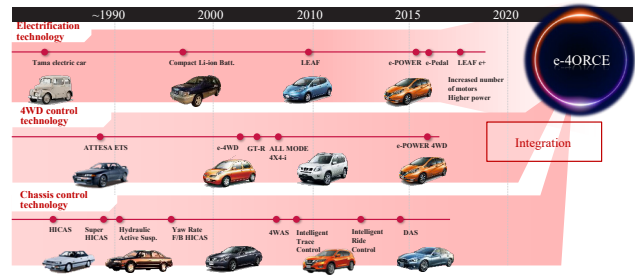


Fig.5 History of e-4ORCE

3. Customer experience offered by "e-4ORCE"

— An exhilarating and confident driving experience —

Given the premise of an electric AWD configuration, the target of "e-4ORCE" is to fully unleash the high potential of the electric motor of a vehicle to a level that has never been achieved by conventional combustion engine vehicles or electric AWDs manufactured by other companies. This includes excellence in handling maneuverability; sense of security regardless of the type of road surface; and comfortable riding experience for all passengers.

3.1 Excellence in handling performance

In general, accelerating a vehicle along a curve causes the vehicle to deviate outward with respect to the normal line of travel. Therefore, the driver must operate the steering wheel further or decrease the speed (understeer). This phenomenon occurs because a portion of the limit value of the friction circle determined by the load on the wheel is used for acceleration, which weakens the turning force. In accordance with the road surface and driving conditions, the "e-4ORCE" technology distributes the driving force to the front and rear wheels so that optimal tire gripping is achieved based on the fluctuating loads on the wheels. In normal driving mode, the front/rear torque distribution is close to 50:50. Moreover, the distribution is changed automatically to an optimal ratio within the range of 0:100 to 100:0 without driver effort based on the road surface and driving conditions. In addition, curve turning performance is improved during deceleration by combined control of regenerative braking by the front-rear motor and the hydraulic brakes of the four wheels (Fig. 6).

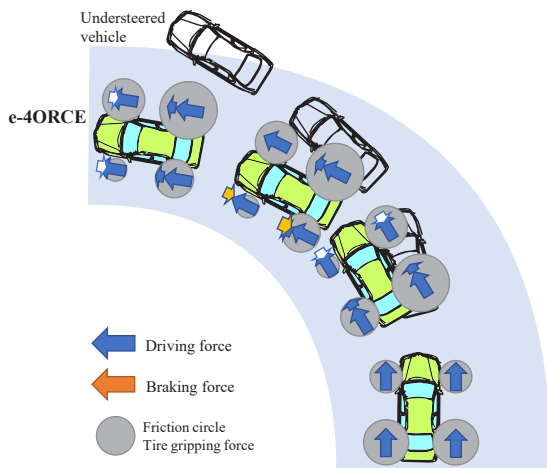


Fig.6 Comparison between e-4ORCE and understeering

This sophisticated control exerts its effects, particularly when turning a curve. Because the vehicular motion is guided by the steering operation of the driver, it is expected that steering correction can be minimized. We hope that the drivers can enjoy a smooth and highly stable driving experience enabled by the “e-4ORCE” technology.

3.2 Sense of security on various road surfaces

The technologies for independently controlling the front/rear motors and brake control developed by Nissan over the years enable excellent driving performance even on constantly changing and slippery road surfaces with snow, compacted snow, ice, ruts, or wetness.

Fig. 7 shows the turning acceleration stability data as a case example of achieving a sense of security. This data graphically compares fluctuations in the steer characteristic when pressing the accelerator for 4 seconds up to full throttle after stabilizing the turning condition to a constant 40R at a vehicle speed of 25 kph. The steer characteristic is an index of the degree of further steering required to align the vehicle with the travel line when the vehicle deviates outward from the target line. If the road surface is covered by snow, the frictional force will be low and surface will be uneven. Therefore, the size of the friction circle fluctuates constantly, and the travel line may deviate both outward and inward; thus, stabilizing the steering condition will not be easy. Even on such snowy road surfaces, ARIYA’s “e-4ORCE” causes very little fluctuation in the steer characteristic, thereby enabling stable driving. Compared to the AWD SUVs of competitors that have high-power motors (green and blue lines in Fig. 7), the fluctuation in steer characteristic was approximately 1/9 for ARIYA. Moreover, the fluctuation achieved was small and approximately 1/3 when compared with the top benchmarked AWD SUV mounted with a conventional combustion engine (orange line).

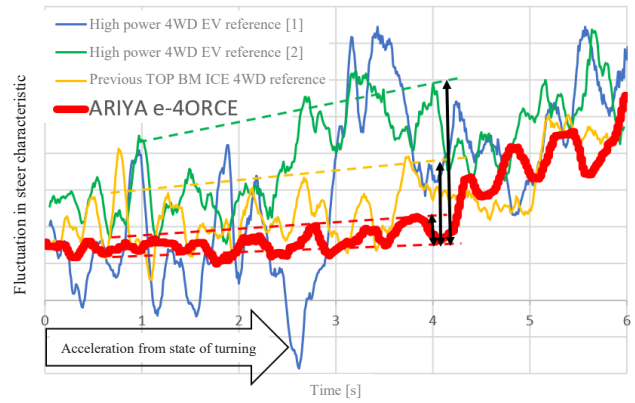


Fig.7 Turning acceleration performance on a snowy surface

A high level of sense of security can be experienced through this high stability, regardless of the situation, road surface, and driver. In addition, this reliability may bring joy to skilled drivers when driving on snowy and frozen road surfaces during winter.

3.3 Comfortable riding experience for all passengers

Control of the regenerative brakes by the motor also contributes to a comfortable riding experience. Even if the vehicle is an EV, applying regenerative brakes to front-wheel drive vehicles can cause a substantial tilting feeling to the passengers because only the front motor is used when braking; thus, the rear of the vehicle is raised when decelerating (referred to as pitch behavior) (Fig. 8).

In the “e-4ORCE” technology, the regenerative brake of the rear motor is used in addition to that of the front motor. Thus, there will be lesser vibration even when the road is congested, thereby resulting in a comfortable riding experience. When accelerating and decelerating, fluctuations in the vehicle posture are suppressed by the optimal control of the motor (right side of Fig. 8). Because the vibrations of the vehicle body are minimized, a smooth and comfortable riding experience is available to both the driver and passengers in other seats.

(Adopted for the first time in NOTE E-POWER 4WD)

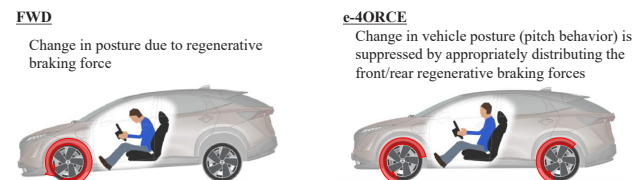


Fig.8 Tilting of the vehicle

4. Summary

The principle behind the development of “e-4ORCE” was to allow the system to achieve control naturally such that the driver would not notice the operation of the system. It is expected that anyone riding in a vehicle equipped with “e-4ORCE” technology for the first time would feel that the vehicle can be maneuvered naturally

and comfortably without great effort.

For our long-time customers who have continued to choose Nissan vehicles, we hope that the "Nissan way" can occasionally be felt when driving the vehicle. We hope that the "Nissan way, but redefined" can be felt by our customers. The "e-4ORCE" technology was developed with the aim that our customers will find it indispensable in their vehicles once they have experienced it and that they would become used to the sense of security it provides.

Because ARIYA provides stable steering operation with very little fluctuation in the steer characteristic, the vehicle can be handled confidently, even though it has the power equivalent to a sports car. Moreover, the "e-4ORCE" technology has potential for further development to enable enhanced performance for sports cars.

References

N. Nakata, Special Feature 2: Evolving e-POWER "2. System Characteristics and Future Development", Nissan Technical Review, No. 88 (2020)

R. Hiraku, E. Sakagami, T. Katakura, Special Feature 2: Evolving e-POWER "6. Value-Adding Electric All Wheel Drive (AWD) Technology," Nissan Technical Review, No. 88 (2020)

Nissan Motor Co., Ltd., "Intelligent Trace Control," Nissan Global Site, https://www.nissan-global.com/JP/TECHNOLOGY/OVERVIEW/cornering_stability_assist.html

Authors



Hiroyuki Togashi



Yutoku Miyagoshi



Takeji Katakura

Study about Workload Reduction by Multiple Modal Interface Using Gaze and Voice Recognition

Yusuke Morita* Sou Tamura*

Abstract Our aim is to improve an HMI that reduces the workload by distributing the different resources (visual / auditory / verbal / spatial etc...) related with human's recognition. In this study, the effect on the driver's workload is clarified by comparing two types of operations: the current voice operation as single modal, and operation using gaze pointing and voice command as multimodal. With regard to gaze and voice control, there are 2 use cases that are more effective than the current voice operation. It was confirmed by subjective evaluation (NASA-TLX) and objective evaluation (Prediction Error) at the driving simulator tests.

1. Introduction

Over recent years, the demands for vehicle safety and comfort have increased. In addition, vehicles are being mounted with increasingly new functions such as autonomous driving, parking assistance, and providing information using connected services. Owing to these trends, the operational workload related to setting, adjusting, and checking functions is increasing. Single-modal interfaces such as touch selection (visually searching the position before touching the position) and voice input (command utterance) are typically used for operations in current vehicles.

In the case of touch selection, for example, a hierarchical structure is generally adopted because the display area is limited. The user must recognize and understand the operation logic and order beforehand to determine the types of functions available at each location. In the case of voice input, the desired operation can be determined directly. However, there are often difficulties when using voice inputs for commands that accompany selection; this is because the workload will be high when uttering the necessary commands (such as the name of the device to be operated) followed by the specific choices (such as "right-front side" or "lowermost").

To reduce the workload in these single-modal operations, the authors focused on multimodal operation based on the multiple resource theory.¹⁾ According to Wickens et al., multiple resources are used according to the type of information when a mental workload, including cognition and response, is imposed to execute an action. In theory, it is considered that a set of three dichotomies of information processing resources are present in humans. The first includes "perception" and

"response," which represent the input and output of information; the second consists of "visual" and "auditory," which are modalities; and the third includes "spatial" and "verbal," which are forms of expressing information. In addition, "visual" is further divided into "focal vision" and "ambient vision." Using different levels in each of these four dimensions instead of focusing on just one resource is considered to contribute toward reducing the workload. Moreover, based on this theory, it has been reported that the workload will be reduced on dispersing the workload across multiple resources.²⁾ In automobiles, voice operation using voice recognition technology is being employed to reduce the workload. However, in this method, only the "verbal" resource of the information expressing form (third dimension) is utilized. The authors hypothesized that it may be possible to reduce the driver workload by dispersing the resources into "spatial" and "verbal," if the spatial information at which the driver is gazing is utilized by employing gaze detection technology, which has evolved over recent years.

Therefore, this study focused on the visual recognition that is regularly performed during driving. In conjunction with voice recognition, multimodal operating commands using gaze pointing and voice commands were created to disperse the workload on the resources, with the aim of reducing the workload in the overall operation. When utilizing the visual recognition activity as the trigger for an operation (for example, using gaze pointing and voice commands to view a navigation map that is off-scale and make corrections or employing an auxiliary monitor to visualize a direction that cannot be seen), monitoring the gaze pointing information of the driver can be valuable for estimating the operation target. Using this method, the authors assumed that the driver can directly give

*Interior and Exterior Engineering Department

commands even if the operation target is not indicated, thus reducing the workload (Figure 1).

Among the multimodal interfaces, those utilizing gaze pointing and voice commands, in particular, have been studied previously.³⁾⁴⁾ However, these studies were limited to general information devices, and the operation of the devices in these works was different from that of in-vehicle devices, because the precondition for in-vehicle devices is that the devices will be used while the driver is always alert to the surroundings. Furthermore, in a study related to in-vehicle devices,⁵⁾ the workload reduction effect was not clearly indicated.

Therefore, this study focused on the operations triggered by visual recognition activities. Operation by voice commands only was compared with operation by gaze pointing and voice commands in order to evaluate the effects of the multimodal interface.

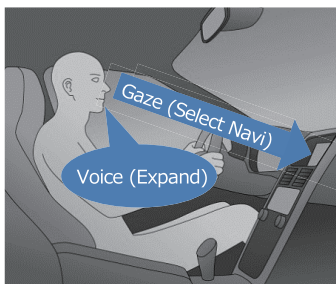


Fig.1 Navi operation by gaze and voice

2. Multimodal interface using gaze pointing and voice commands

2.1 Outline

To evaluate the effect of detecting the gaze of the driver and using it for operation together with voice recognition, this approach was compared with the current operation, i.e., that based on voice recognition alone (single-modal operation). The details are presented in Figure 2. The driver behaviors and thoughts are provided on the left, while the input timing and details for different interfaces are presented on the right for comparison.

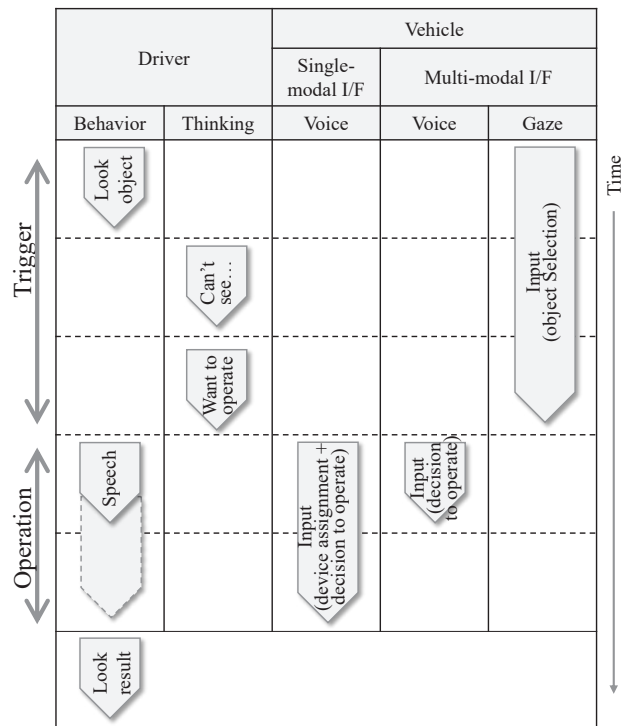


Fig.2 Comparison with single and multi modal operation

According to Figure 2, when the driver attempts to view an object, moves the line of sight, and becomes aware that “it is impossible to see,” a desire to resolve the feeling of discontent will arise.

In the case of voice recognition, the driver will give commands by uttering the device name or direction and the operation command. By contrast, in the case of the operation using gaze pointing and voice commands, the operation target device or direction can be estimated based on the gaze detection function of the vehicle system when visual recognition, which serves as the trigger, is performed by the driver. In this method, the driver does not need to select the target and can perform the operation by uttering simple commands such as “camera” or “expand” as the input. Therefore, compared with the operation using voice commands only, the driver only needs to utter simple words, and supplemental information such as that regarding direction and position is unnecessary.

2.2 Target operation

As described above, the tasks that can realize operational workload reduction by using gaze pointing have a common pattern. Specifically, the information obtained from gaze pointing is utilized as the trigger to proceed with the operation. Considering this pattern, the case in which devices with the same name exist (example: right camera/left camera/rear camera) in a vehicle, and the case in which multiple devices may react to the same command word (example: “expand” of the electronic mirror image/“expand” of the map), the three following case examples were established as the tasks:

(i) Map expansion:

If two or more maps are presented on a large screen

that extends from the meter cluster to the center cluster (which is increasingly adopted in vehicles in recent years) or if the maps are shown on multiple screens, a command of “type of map+details of operation” is needed for voice recognition to operate a certain map. By contrast, in the case of operation commands using gaze pointing and voice commands, the map can be operated directly without selecting it verbally. In this study, a map expansion operation was utilized as the target task.

(ii) Electronic room mirror image expansion:

In this study, the image expansion operation of the rear-view camera served as the target task, assuming that the vehicle or vehicle model at the rear side needs to be checked in a scene where the vehicle at the rear is tailgating (a social problem in recent years), multiple vehicles are traveling in a group, etc. In the case of voice operation, the vehicle will not be able to recognize what device the command is intended for if only “expand” is uttered. By contrast, in the operation by gaze pointing and voice command, the input of the expansion command will be complete simply by uttering “expand” after looking at the mirror. In this study, considering the field of view of the rear-view mirror when an image is expanded, the expanded image is partially overlaid (Figure 3).

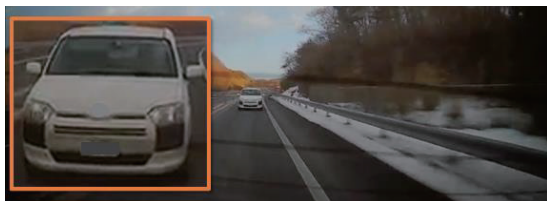


Fig.3 Sample picture of expand view

(iii) Checking the side camera images:

When initiating the camera that assists in viewing the blind spot in a vehicle equipped with multiple cameras, the vehicle will not be able to recognize which camera to start up if only “camera” is uttered. In particular, when passing another vehicle on a narrow road (Figure 4), contact with the wall or the oncoming vehicle must be avoided. Therefore, various types of information must be obtained, judgments must be made, and the vehicle must be operated within a short period of time, which may cause impatience. In the case of operation by gaze pointing and voice command, the operation target device can be estimated based on the gaze pointing direction, and thus, the input for starting up will be complete simply by uttering “camera.”

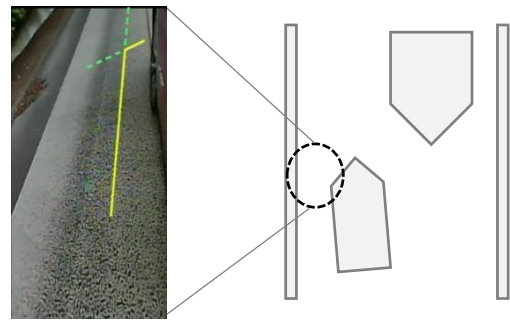


Fig.4 Passing scene

Operation by voice command alone and operation by both gaze pointing and voice command for the abovementioned three scenes were compared. The results are summarized in Table 1.

Table1 Comparison with control of “voice” and “gaze & voice”

Task	Voice	Gaze & Voice
i) Map expansion	(After checking the map once) <ul style="list-style-type: none"> • Expand the center map • Expand the navigation map on center • Expand the IVI map 	(After checking the map once) <ul style="list-style-type: none"> • Expand
ii) eMirror expansion	(After checking the mirror once) <ul style="list-style-type: none"> • Expand the eMirror • Expand the room mirror • Expand the back mirror 	(After checking the mirror once) <ul style="list-style-type: none"> • Expand
iii) Side camera pop-up	(After checking front left) <ul style="list-style-type: none"> • Left side camera • Left camera • Left hand side camera 	(After checking front left) <ul style="list-style-type: none"> • Camera

In operations (i)–(iii), the driver always visually confirms the device (i, ii) or the attention direction (iii) to check the situation before executing the operation. By having the system estimate the intention of the driver from the gaze pointing direction, it was assumed that the voice command workload concerning the device and direction could be reduced.

3. Evaluation test

3.1 Evaluation system

An outline of the system used to evaluate the load reduction for the operations set in Subsection 2.2 is depicted in Figure 5. The system comprises an infrared (IR) camera, a microphone, a personal computer (PC) that processes the data from them, and a display employed as an output device.

The face images obtained by the IR camera were analyzed using a PC. Based on the gaze pointing information of the driver and the mockup layout information from the camera, the data of “which device/area the driver is looking at” were created (Figure 6). Smart Eye CDK v.0.9.0, manufactured by Smart Eye® AB, was used as the gaze detection system, including the camera. In addition, the voice information obtained from the microphone was processed using a voice recognition

system and converted into text data. Google Cloud™ Speech-to-Text API was utilized as the voice recognition system.

In the operation command processing, the gaze point information and voice command information were integrated, and the image to be output was determined.

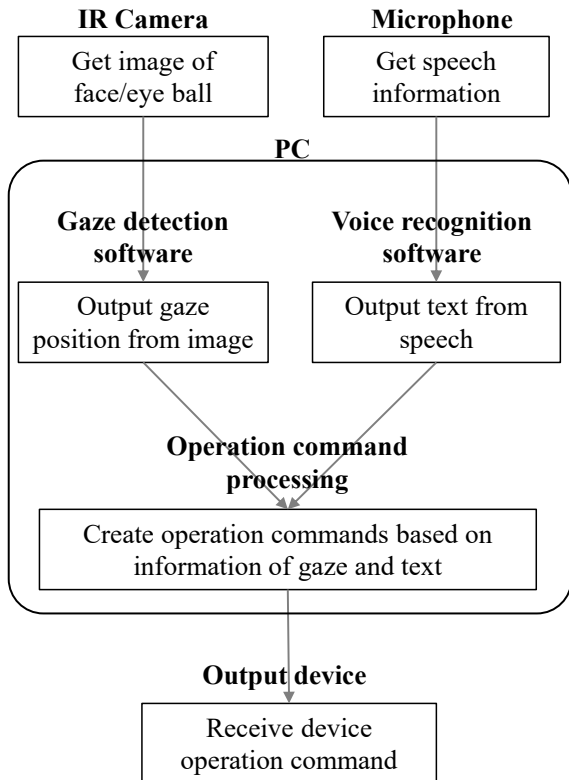


Fig.5 System outline and function flow

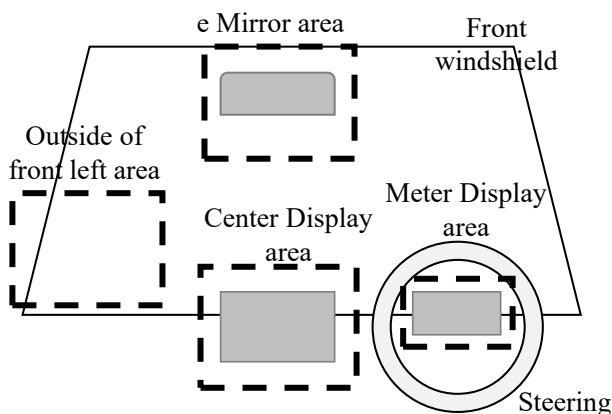


Fig.6 Image of recognizable area



Fig7. Test condition of Driving Simulator

An 11-inch liquid-crystal display (center layout)+8-inch liquid-crystal display (meter layout)+7-inch liquid-crystal display (room mirror layout) were used as the on-board devices which show results .

The tests, including the driving tasks, were conducted using a driving simulator manufactured by Mitsubishi Precision Co., Ltd. The evaluation scene is illustrated in Figure 7.

3.2 Evaluation method

NASA-TLX,⁶⁾ which has been adopted in previous studies, was employed for the subjective evaluation. In addition, for comparisons using quantitative values, the prediction error of the steering angle was utilized. The prediction error of the steering angle is the basis for calculating the steering entropy,⁷⁾ which represents the smoothness of the steering operation of the driver.

The prediction error of the steering angle was derived by a time-series calculation using the difference with past data. The prediction error, and, therefore, the difference, will be larger if sudden steering is necessary. The distribution of the values will be wider and the peak value will be lower if the driver is preoccupied with tasks apart from driving, such as looking aside or becoming absorbed in thought.

Tests were conducted using seven men and women who had their driver's licenses. Their ages ranged from 20 to 69 years. After the drivers underwent sufficient training for each operation, the tests were conducted three times, and the results were evaluated each time the driving test was conducted. The driving and operating conditions are listed in Table 2.

Table2 Test condition

Task	Scene	Speed
i) Map expansion	Highway	100km/h
ii) eMirror expansion	Highway	100km/h
iii) Side camera pop-up	City road	30km/h

The conditions for driving on the highway were as follows. Individually driving in the center lane of a highway section (i.e., with no other vehicle and no lane changing) with a continuous gentle curve (minimum radius of approximately 1,000 m). Half of the curve consisted of a right-hand curve, whereas the other half consisted of a left-hand curve. Therefore, it is considered that there was no bias in the curve conditions. The conditions for driving on the city road were as follows: driving on a road (with a width of approximately 5 m) that has no center line while avoiding a car parked on the passenger side.

For both driving on the highway and on city roads, tests were conducted with the following three patterns: no load (driving operation alone, without any other task), operation by voice command, and operation by gaze pointing and voice command. Considering the order effect, the tests were conducted in a random order for each participant.

The experiments performed in this study were examined and approved by the Ethics Committee of Nissan Motor Co., Ltd. The tests were conducted after obtaining informed consent from the participants.

3.3 Subjective evaluation results

The results of the subjective evaluation by the NASA-TLX are presented in Figure 8. To assess whether the workload reduction by using gaze pointing and voice commands, as compared to that when using voice commands alone, was significant, the evaluation results of each modality of target tasks (i)–(iii) were paired. The probability associated with the student's paired t-test (with a two-tailed distribution) was calculated to derive the p-value.

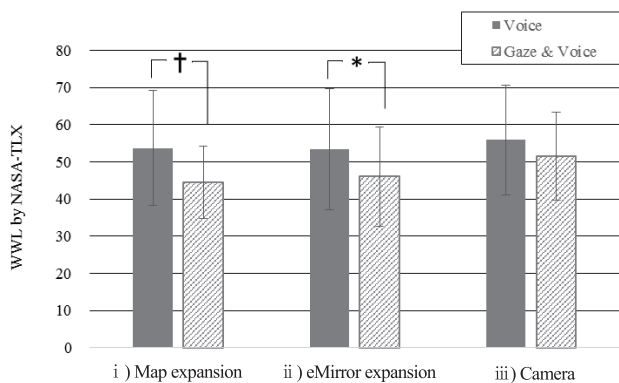


Fig.8 Result of NASA-TLX (* $p < 0.05$, † $p < 0.1$)

Compared to the voice command operation, the weighted workload (WWL) score for the operation by gaze pointing and voice command was statistically significant for (i) map expansion and of low statistical significance for (ii) mirror expansion. The results suggest that, on incorporating gaze pointing, the workload is decreased, as compared to that with the current voice command input.

On the other hand, the camera starting operation method does not have a statistically significant effect.

The results under the current test conditions merely suggest a trend of load reduction.

The initiation of camera operation while passing another vehicle on a narrow road was analyzed based on the aforementioned four dimensions of the multiple resource theory.¹⁾ It was assumed that the driver first had to check the clearance between the vehicle and surrounding obstacles. Therefore, it was necessary for the driver to concentrate on the “focal vision” resource among the focal and ambient visions (dimension 4) and then operate the vehicle to avoid contact with the surrounding obstacles. Thus, the driver was required to concentrate on the “response” resource among perception and response (dimension 1). In addition, both the voice command operation and the operation using gaze pointing and voice commands use the “focal vision” (checking the device) and “response” (operating the device) resources, leading to interference. Therefore, if focal vision is used frequently and if the driving operation workload is high, there is little difference between the voice command operation and the operation using both gaze pointing and voice commands. Furthermore, people with low driving skills may be more affected by the driving operation when passing another vehicle on a narrow road, which may also affect the results.

On the other hand, when driving on a highway, the driver workload is assumed to be relatively low because the vehicle remains in the same lane. Therefore, there were likely sufficient resources to naturally perform activities such as looking at the map or in the mirror, and uttering simple commands also probably reduced the workload.

3.4 Quantitative evaluation results

Examples of the frequency distributions of the prediction error in the steering angle, calculated as quantitative evaluation values of a participant (a female in her 20s), are shown in Figures 9–11. The time elapsed from giving instructions to start the task to its completion was approximately 10 s. Therefore, data for 10 s from the start of the task were used for the evaluation. For α in Figure 9–11, the 90th percentile value of the no-load distribution was used to represent the differences in driving characteristics among individuals.⁸⁾

As mentioned above, in the frequency distribution, the sharpness near the center will increase if the driving is smoother. In the current example, the peak gradually decreases and the distribution spreads out in the order of “no load” → “operation by gaze pointing and voice command” → “operation by voice command,” which suggests that the deviation in steering becomes larger and sudden operations increase in this order.

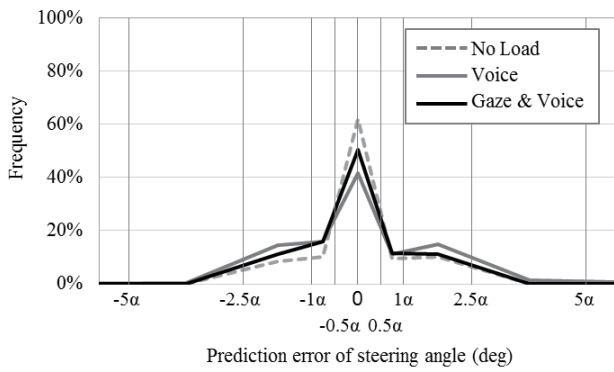


Fig.9 Frequency distribution (Example "Map expansion")

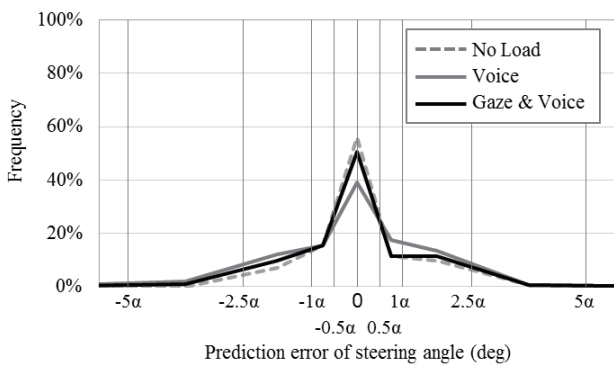


Fig.10 Frequency distribution (Example "eMirror expansion")

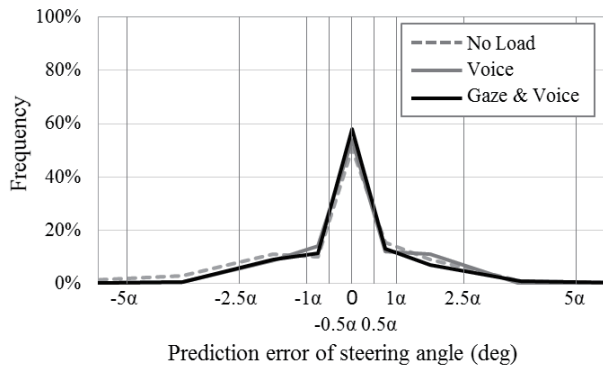


Fig.11 Frequency distribution (Example "Camera")

To understand the overall trend of the participants, the 90th percentile values, α , of the frequency distributions of the steering angle prediction errors were compared. A graph of the comparison results is depicted in Figure 12. Similar to the subjective evaluation described in Subsection 3.3, a t-test was conducted to compare the different cases.

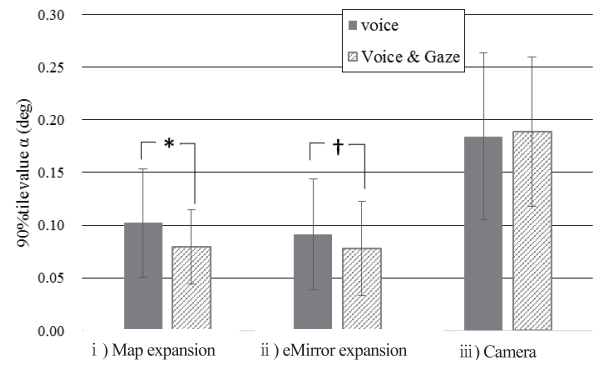


Fig.12 Comparison of α value (* $p<0.05$, † $p<0.1$)

Similar to the subjective evaluation, there exists a statistically significant difference or a trend of statistical significance for (i) map expansion and (ii) mirror expansion. Therefore, the workload reduction was also expressed quantitatively.

For (iii) camera start up, the α value (which shows that the prediction error in the steering angle is large) tends to be larger than those for (i) and (ii). This result suggests that the driver workload is high for (iii), which is a trend similar to that obtained in the subjective evaluation. No significant difference is observed between the two surgical modalities with increasing visual recognition load. This trend is in line with the subjective evaluation results; thus, the trend is considered reasonable.

4. Summary

In this study, a multimodal interface using gaze pointing and voice commands was investigated, focusing on the operations triggered by visual recognition activities. This approach was compared with the conventional voice command operation to evaluate the effects of the multimodal interface. The evaluation confirmed that the workload could be reduced, as compared to that during operation using voice commands alone (single modality).

However, operation by gaze pointing may be difficult in some situations depending on the driving environment or task. Therefore, it is considered that operation by gaze pointing will not completely replace other operation methods such as voice command operations and steering switches. Nevertheless, it would be appropriate to design the settings such that both operation methods are available and that the user can choose the one that is most convenient.

In addition, as described above, the driver workload will be higher if information is concentrated on a certain resource ("focal vision" and "response" in this study), making it more difficult for the driver to respond in the same manner as that during low workloads. For situations where the driver drives on a narrow road and the workload is high, as in the test conditions of this study, it may be necessary to devise an appropriate

method such as automatically showing the necessary camera image.

In future studies, the test candidates will be expanded beyond the three tasks used in this study, with the aim of extracting and realizing tasks with stronger influences. Evaluations must also be conducted under actual driving environments, and it is necessary to assess whether the trend remains the same.

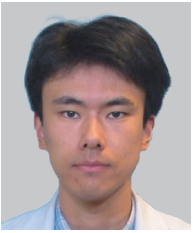
References

- 1) Christopher Wickens: Multiple Resources and Mental Workload, *Human Factors*, Vol.50, No.3, p.449-455, (2008)
- 2) Takahiro Iwata, Tetsuo Yamabe, Tatsuo Nakajima: Workload Evaluation of Information Cognition in a Multi-Task Environment, *IPSJ SIG Technical Report*, Vol.2009-UBI-22, No.8, (2009)
- 3) Tomoya Okada, Daisuke Sakamoto, Tetsuo Ono: Method of Presenting Translations When Reading English Language by Combining Gaze Pointing and Voice Information, *Interaction Papers 2019, IPSJ Symposium*, p.747-751, (2019)
- 4) Chihiro Nakagawa, Toshikazu Matsubara, Martin J. Durst: Proposal and Implementation of the Web Browsing Interface That Combines Gaze Pointing Information and Voice Information, *Proceedings of the 78th National Convention of IPSJ*, p.369-370, (2016)
- 5) Abdul Rafey Aftab: Multimodal Driver Interaction with Gesture, Gaze and Speech, *ICMI '19*, p.487-492, (2019)
- 6) Shigeru Haga, Naoki Mizukami: Japanese Version of NASA Task Load Index: Sensitivity of Its Workload Score to Difficulty of Three Different Laboratory Tasks, *Japanese Journal of Ergonomics*, Vol.32, No.2, p.71-79 (1996)
- 7) Okihiko Nakayama, Tooru Futami, Tomokazu Nakamura, Erwin R. Boer: Development of a Steering Entropy Method for Evaluating Driver Workload, *Proceedings of the JSAE Annual Congress*, No.45-99, p.5-8 (1999)
- 8) Toshiyuki Ito, Okihiko Nakayama, Erwin R. Boer: Establishment of JAMA's Safety Guideline for In-vehicle Information System and Study of a Steering Entropy Method for Evaluating Driver Workload, *IATSS Review*, Vol.26, No.4, p.243-250, (2001)

Source

公益社団法人自動車技術会
自動車技術会論文集
Vol.51, No.5. 文献番号:20204473

Authors



Yusuke Morita



Sou Tamura

The Development of Bearings for the Multi-link Crank Mechanism to Achieve Variable Compression Ratio Engine

Katsutoshi Nakamura* Katsuya Moteki** Satoru Ookuma*

Abstract To achieve variable compression ratio, the multi-link system which has secondary merit as good quietness performance and low mechanical loss was selected. Under these circumstances, it was very important how to design the journal bearings and bushes which is added as important elements to constitute the multi-link system. In this paper, it is described that how to design the journal bearings and bushes for multi-link system based on each peculiar load characteristic and sliding characteristic. At that time, each dynamic characteristic and cooling effect by the engine oil by the added oil feeding path was considered.

1. Introduction

In 2018, the manufacturing of a mass-production type variable compression ratio engine was commenced. The variable compression ratio mechanism used in this type of engine can alter the compression ratio according to the driving scene to achieve both low fuel consumption and high output, which are contradictory characteristics. Among the various variable compression ratio mechanisms proposed through previous research, the multi-link system adopted in this engine exhibits unique value-adding characteristics such as quietness and friction loss suppression, in addition to the main function of altering the compression ratio.⁽¹⁾ Bearing elements are important functional components that constitute the multi-link system, which realizes the abovementioned features. Regarding the bearing elements, this study focused on improving the load capacity according to the peculiar load characteristics and slide characteristics and also on the foreign matter discharging effect and cooling effect on feeding engine oil to the sliding portions. As a result of this research, functional reliability of the bearings was ensured, without impairing the additional values of this mechanism.

At the same time, the friction loss equivalent for engines with the conventional mechanism was realized, even though the number of bearing elements with small shaft diameters was increased.

2. Development concept

Due to the lever structure of a multi-link system, the load input to the bearing elements described herein tends to be larger than the load input to bearings with the

conventional mechanism. Accordingly, it was necessary to ensure a high load capacity and to supply lubricating oil actively to the sliding portions. However, implementing the usual countermeasures such as increasing the shaft diameter hinders the size reduction of the link components, which is necessary to ensure the mountability of the engine. Satisfying these contradictory requirements was considered in this research.

3. Components of multi-link mechanism and bearing elements

3.1 Components of multi-link mechanism

The components of the variable compression ratio (VCR) system, presupposing the use of a multi-link system, are presented in Figure 1. Compared to the conventional mechanism (Figure 2), which comprises a piston, connecting rod, and crank shaft, the VCR system uses a multi-link crank mechanism that consists of the connection of an upper link, a lower link, and a control link (hereinafter referred to as U-Link, L-Link, and C-Link, respectively), which are utilized instead of the connecting rod. Below the crank shaft, the C-Link big end is connected to the control shaft eccentric journal and fixed using the bearing cap. This control shaft is connected to the actuator link (referred to as an A-Link in this report) via the connecting portion, and the A-Link is connected to the actuator (referred to as an ACTR in this paper) installed on the side of the engine.

*Powertrain and EV Mechanical system Technology Department

**Powertrain and EV Advanced Technology Department

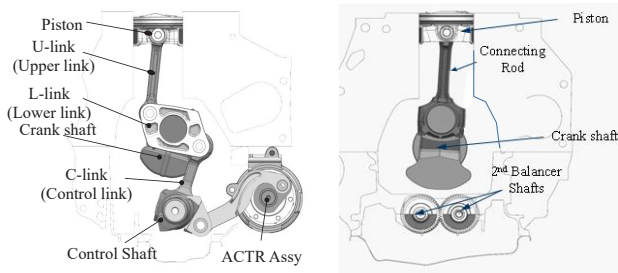


Fig. 1 Components of VCR system

Fig. 2 Components of conventional

3.2 Components of bearing elements in the multi-link mechanism

In the multi-link mechanism, bearing elements are established to form connections between the aforementioned piston, links, and shafts. The components of the bearings are illustrated in Figure 3. The bearing elements for this mechanism are at the following locations. There are five types of bearing element unique to this mechanism: the U-pin bush, which connects the U-Link and the upper pin press-fitted into the L-Link; the L-Link bearing, which connects the L-Link and the crank pin; the C-pin bush, which connects the control pin press-fitted into the L-Link and the C-Link; the C-Link big end bearing, which connects the C-Link and the control shaft eccentric journal; and the control shaft bearing, which connects the control shaft main journal and the bearing cap. In addition, there are two types of bearing element that are identical to those in the conventional mechanism: the main bearings that connect the crank shaft main journal and the bearing cap, as well as the piston bush.

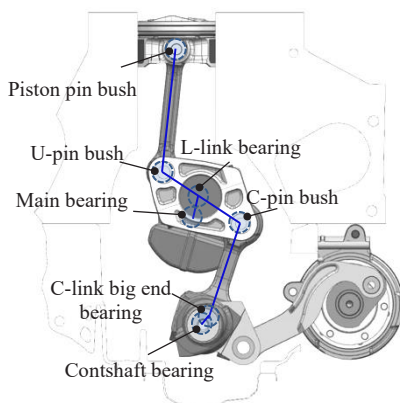


Fig. 3 Bearing components of Multi-link system

4. Designing bearing elements

The aforementioned bearing elements were designed considering their individual load characteristics and usage environments. The appearance, main dimensions, load properties, and sliding properties of each bearing are listed in Tables 1 and 2. The L-Link bearing and main bearing function are the rotating bearings (same as the bearings for the conventional mechanism). On the other

hand, the U-pin bush, C-pin bush, and C-Link big end bearing (which were newly established for the multi-link mechanism) as well as the piston pin bush (equivalent to the conventional mechanism) function as the oscillating bearing. For the clearance in diameter, all bearings have almost the same clearance as the general main bearings and connecting rod bearings.

Table1. Specification of bearings No.1

	L-Link bearing		Main bearing
	Upper	Lower	
Diameter(mm)	42		52
Width(mm)	25		17
Width of groove(mm)	-		3.15
The rate of increase of load	1.9		1.9
Sliding property	Rotating		Rotating
	U-pin bush	C-pin bush	
Diameter(mm)	23	21	
Width(mm)	16.6	18.5	
Width of groove(mm)	2.29	2.29	
The rate of increase of load	1	0.9	
Sliding property	Oscillating	Oscillating	

Table2. Specification of bearings No.2

	C-Link big end bearing	Controlshaft bearing
Diameter(mm)	35	40
Width(mm)	17	17
Width of groove(mm)	2.58	3.15
The rate of increase of load	0.9	0.9
Sliding property	Oscillating	Non-sliding

4.1 Designing L-Link bearing

Three issues arose when designing the L-Link bearing. The first issue originates from the characteristic structure of the L-Link. As described by Tanabe,⁽²⁾ compared to the conventional structure, the L-Link has a wider structure in the engine shaft direction than the connecting rod and it also has a slit structure at the center, which covers half of the overall width. Therefore, in the conventional mechanism, the main pressure-receiving area has lower rigidity than the connecting rod (refer to Figure 4). In addition, the shape of the L-Link is asymmetrical with respect to the center of the L-Link bearing for the U-pin and C-pin sides (refer to Figure 5). Owing to the above-discussed characteristics, the housing side (link side) tends to slip relative to the bearing side during service. The second issue is that the input load increases by up to $(L2+L4)/L2 = 1.9$ times due to the lever structure of the link mechanism, as shown in Figure 6. The third and final issue is that the inertia load, which tends to increase at high engine speeds, is input in the direction of the plain bearing mating surface, as shown in Figure 7. For this

bearing, the cylinder pressure load direction was established to be almost the same as the L-Link bolt axis direction (inclined at 90° with respect to the plain bearing mating surface). However, owing to the oscillating operation of the L-Link, an inertial load is generated during service at approximately 90° with respect to the cylinder pressure load direction. Consequently, this input of the inertial load acts in the mating surface direction, which has a low load capacity. In this research, the following countermeasures were implemented to overcome the three issues described above and secure the bearing function. To address the first issue, i.e., the relative slipping at the bearing back, the shaft diameter was reduced as compared to that of the connecting rod bearing in the conventional mechanism. In addition, as the L-Link width was increased, compared to that of the connecting rod bearing in the conventional mechanism, the bearing width was increased. Using these methods, the total adhesion at the bearing back was increased by a factor of approximately 1.5. The equation for calculating the total adhesion and the specifications of the bearings are listed in Table 3. On increasing the adhesion to the L-Link inner diameter surface, followability was improved. Thus, it was possible to address the issue of relative slipping. In addition, the shape and arrangement of the claw structure at the mating surface were determined. As a result of the above countermeasures, the increased input load (the second issue) was leveled to the average surface pressure, equivalent to that of the connecting rod bearing in the conventional mechanism. Furthermore, to address the third issue, the inertia load in the direction of the bearing mating surface and the height of the relief portion of the crush relief shape was reduced, compared to the height for the general connecting rod bearing, to address to this issue by securing the pressure-receiving area (refer to Figure 8).

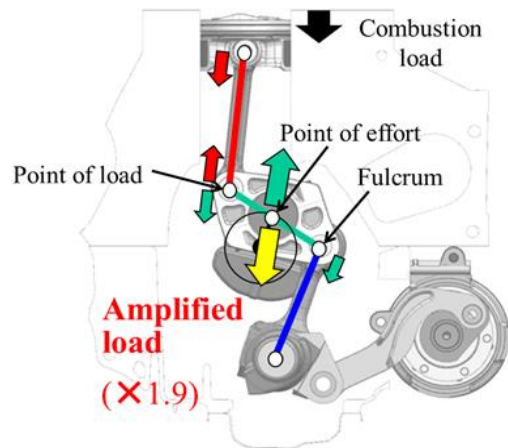


Fig. 6 Principle of lever by multi-link

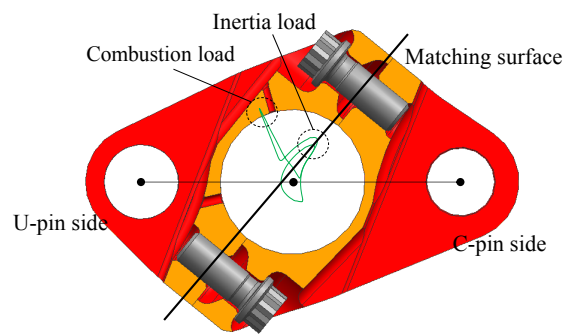


Fig. 7 Load of L-Link bearing

Table3. Specification of L-link(conrod) bearing

	Multi link	Conventional
D(mm)	45	47
t(mm)	1.5	1.5
L(mm)	25	16
Fr ratio※	1.56	1

$$\text{Total adhesion : } Fr = 2(1-t/D)(t/D) \sigma_B L D \pi (\text{N})$$

σ_B : Stress in bearing circumferential direction

※ Fr ratio = Fr value of each model / Fr value of conventional

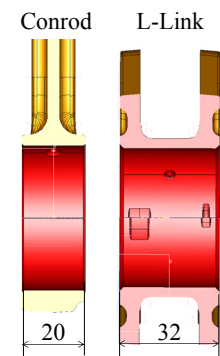
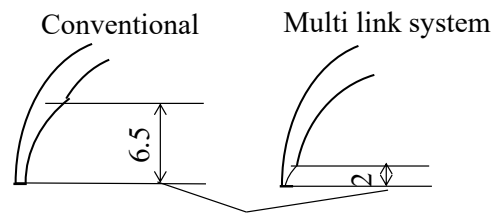


Fig. 4 Width of L-Link



Height of crush relief

Fig. 8 The height of crush relief

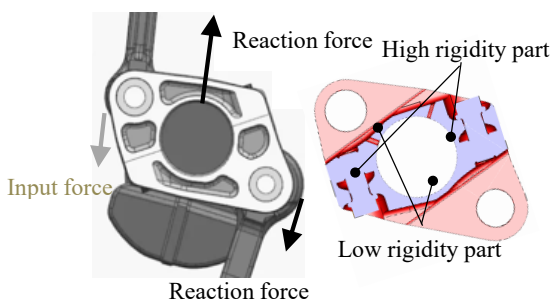


Fig. 5 Mechanical asymmetry of L-Link

4.2 Designing main bearing

As previously reported,⁽³⁾ the load input into the crank shaft main bearing increases by $(L2+L4)/L2 = 1.9$ times due to the lever structure of the multi-link mechanism, similar to the aforementioned L-Link bearing (refer to Figure 6). However, this lever structure also increases the piston stroke. Therefore, the crank radius can be reduced by approximately 50%, as compared to that in

the conventional mechanism; thus, the opening deformation of the crank shaft can be reduced (refer to Figure 9). The results of these advantages and disadvantages are presented in Figure 10. Owing to the multi-link mechanism, the tendency of uneven contact at the bearing is significantly mitigated. Consequently, the load capacity of the bearing is improved, and thus, the bearing lubrication property is improved, although the maximum load is increased to approximately twice that in the conventional mechanism. The effect of the local surface pressure reduction is depicted in Figure 11. This effect is shown as the elastohydrodynamic lubrication (EHL) results of EXCITE™ Power Unit, which is a multi-body dynamics analysis software. It is evident from the results that the local surface pressure decreases, even compared to engines with smaller outputs.

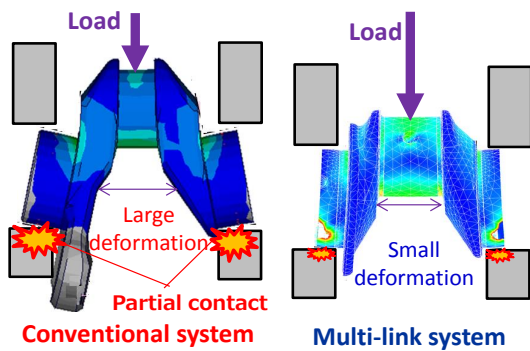


Fig. 9 Comparison of bending deformation

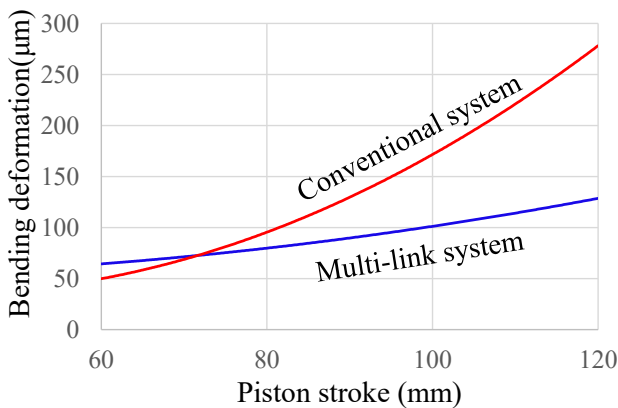


Fig. 10 Bending deformation of crankshaft

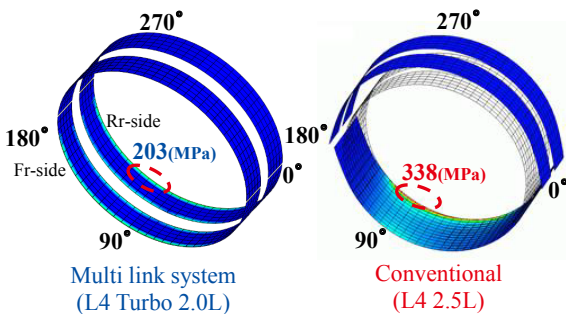


Fig. 11 Local pressure of main bearing

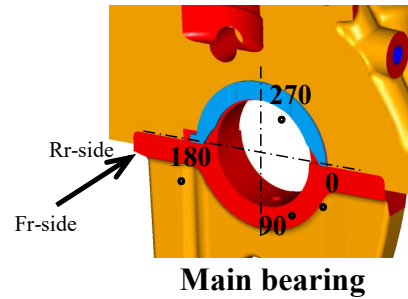


Fig. 12 Positional relation of main bearing

4.3 Designing C-Link big end bearing, U-pin bush, and C-pin bush

The C-Link big end bearing, U-pin bush, and C-pin bush, which are the three elements newly established as the bearing elements for the multi-link mechanism, are all used in the oscillating conditions (identical to the piston pin bush). Figure 13 shows the PV values for each bearing element. The PV value represents the abrasion of the sliding portion, which is a problem in oscillating bearings. For each bearing element, the PV value is higher than that of the piston pin bush with the conventional mechanism. Therefore, as in the case of the piston pin bush, the copper-alloy bush material intended for high surface pressures, which features excellent abrasion resistance, was adopted for each bearing element. Another problem with these bearing elements is that, because their sliding is based on oscillation, the oil flow in the circumferential direction of the bearing, which is induced especially via continuous one-way sliding, is weak compared to that in the bearings used under rotating conditions. Therefore, these bearing elements tend to accumulate contaminants, which degrade the cooling performance of the lubricating oil at the sliding surface; this, in turn, may increase the risk of seizures. To address this problem, a groove structure was established on the bearing surface for the entire circumference. In this manner, the oil flow shortage in the bearing circumferential direction is compensated for by the oil flow in the bearing width direction (refer to Table 1). In addition, oil passages leading to the sliding surface were established in the components (refer to Figure 14). Thus, oil passages that induce the supply and discharge of oil were established. However, there was a concern regarding the effect of the increase in the surface pressure due to the decrease in the pressure-receiving area, resulting from the establishment of the groove along the entire circumference. Therefore, this effect was assessed through EHL calculations, as well as by using analyses and actual measurements of the temperature at the sliding portion. First, EHL calculations were performed for the C-Link big end bearing for the cases with and without the groove along the entire circumference. These calculations considered the deformation of the housing portion under a combustion pressure load, and the results are presented in Figures 15 and 16. Owing to the deformation of the housing, the center of the bearing width has a larger oil film thickness than the edges; thus, it is not the main load-bearing

portion. Therefore, it can be concluded that the function of the pressure-receiving area is limited for the center portion. This suggests that the pressure-receiving function of the bearing will not be impaired even if an oil groove is established at the center of the bearing width. The results of the evaluations of the effects of establishing an oil passage obtained using actual equipment are presented in Figure 17. The temperature of the sliding portion was measured, and the results indicate that the temperature decreases. Therefore, the actual measurements indicate a temperature reduction effect caused by establishing the oil passages as well as the oil groove along the entire circumference. Consequently, the effect of improving the function of the bearing is confirmed via both analytical results and actual measurements. The U-pin bush and C-pin bush were also evaluated in the same manner. Examples of the EHL calculations for the U-pin bush and C-pin bush are presented in Figures 18, 19, 21, and 22. Similar to the results for the C-Link big end bearing, these results confirm that the pressure-receiving function will not be impaired on establishing the oil groove along the entire circumference. It is also evident that the temperature decreases in the sliding portion. Furthermore, it is considered that the establishment of the oil passages as well as the oil groove along the entire bush circumference contributes toward the constant supply of oil to the sliding portion, which is similar to the results for the C-Link big end bearing (refer to Figures 20 and 23). Meanwhile, hydrogen-free diamond like carbon (DLC) material was adopted as the surface coating film for the U-pin and C-pin shaft portions (the shaft side) to withstand high PV value condition. In this manner, the μ value was decreased and the hardness was increased at the sliding portion, such that the seizure resistance performance and abrasion resistance performance were improved.

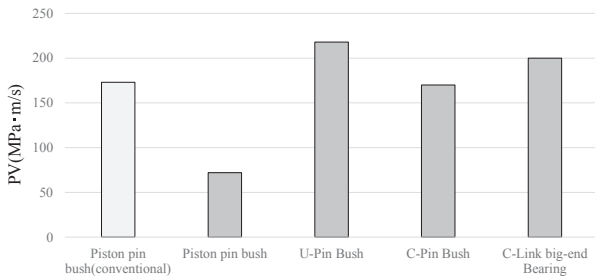


Fig. 13 PV value of bearings for multi-link

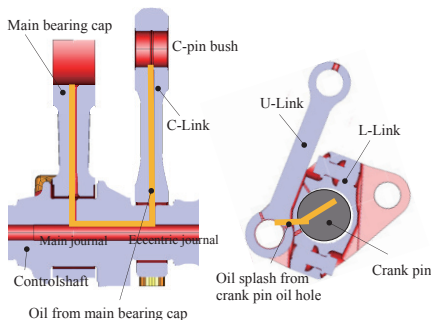


Fig. 14 Oil passage to bearings

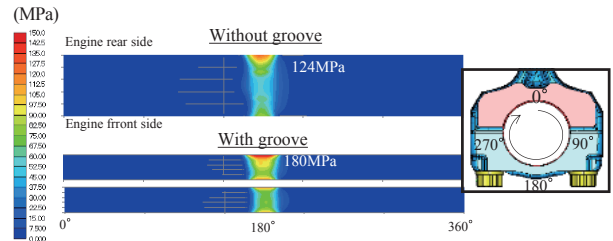


Fig. 15 Local pressure of C-link big end bearing

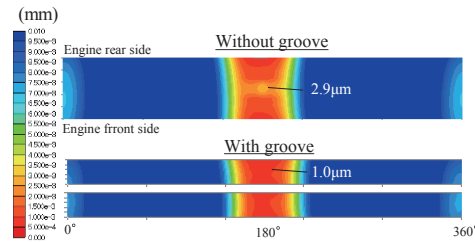


Fig. 16 Oil film thickness of C-link big end bearing

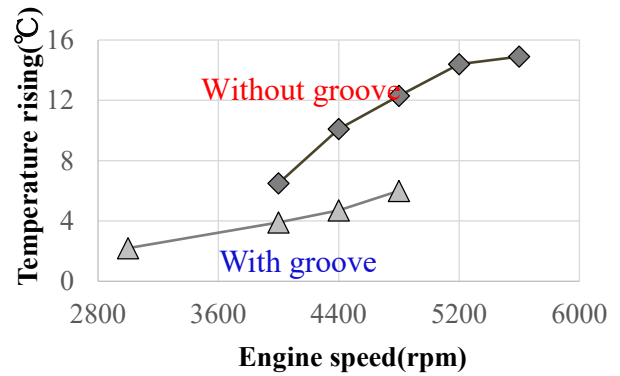


Fig. 17 Thermal measurements of C-link big end bearing

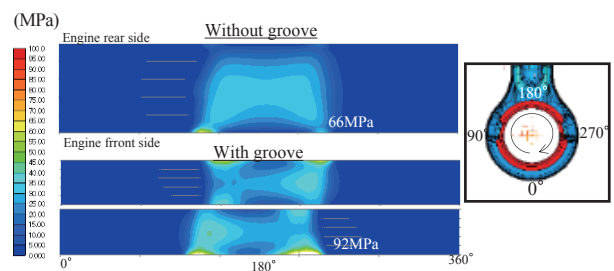


Fig. 18 Local pressure of U-pin bush

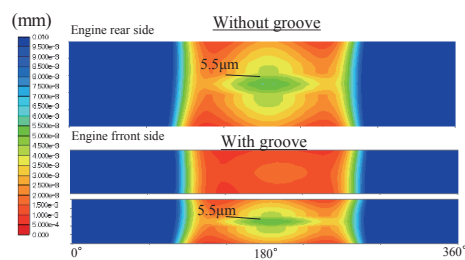


Fig. 19 Oil film thickness of U-pin bush

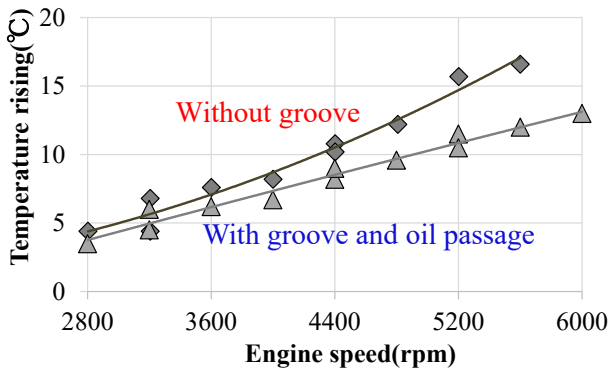


Fig. 20 Thermal measurements of U-pin bush

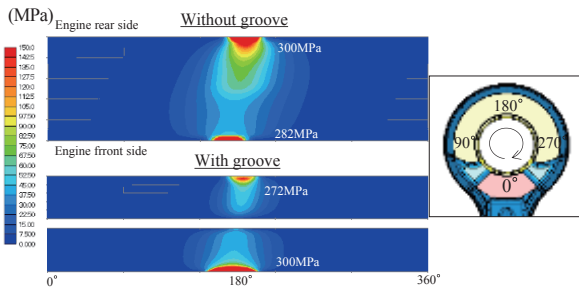


Fig. 21 Local pressure of C-pin bush

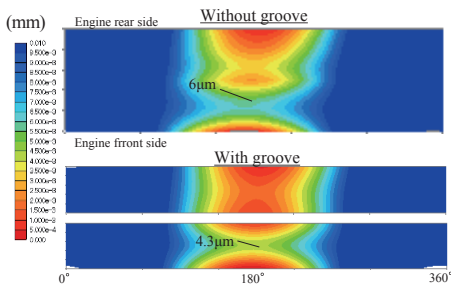


Fig. 22 Oil film thickness of C-pin bush

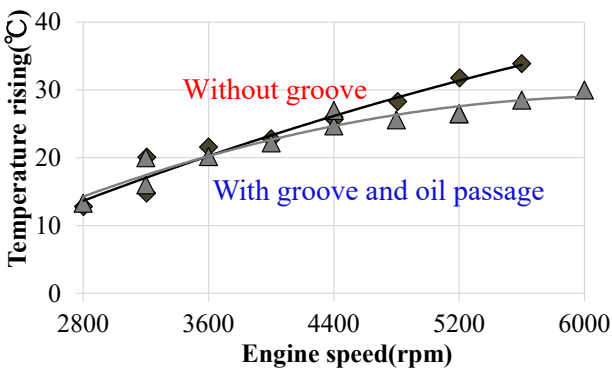


Fig. 23 Thermal measurements of C-pin bush

4.4 Designing control shaft bearing

Compared to the aforementioned oscillating bearing elements, the control shaft bearing is used in the non-sliding case where no rotating motion or oscillating motion occurs, except for when the compression ratio is changed. Owing to this characteristic, the flow of

lubricating oil owing to the sliding motion cannot be expected for this bearing. Therefore, there are concerns that the abrasion will increase due to direct contact. To address this problem, an oil groove was established for the entire circumference, as in the case of the aforementioned oscillating bearings, to ensure lubrication via oil flow in the bearing width direction. In addition, because the flexural rigidity of the control shaft is significantly higher than that of the crank shaft, the tendency of uneven contact at the bearing can be mitigated significantly, as compared to that at the main bearing of the crank shaft. For the bearing material, the copper-alloy bush material intended for high surface pressures, which was used for the oscillating bearing elements, was adopted at this location to ensure adequate abrasion resistance.

4.5 Designing piston pin bush

Compared to the conventional mechanism, the multi-link mechanism tends to have a lower PV value at the piston pin bush (refer to Figure 24). This is attributed to the decrease in the sliding velocity of the piston pin bush, which occurs because the U-Link (corresponding to the connecting rod in the conventional engine), connected directly below the piston, maintains a vertical orientation compared to conventional connecting rod when the piston is lowered during after top dead center (ATDC), the expansion stroke during which the combustion load is received (refer to Figure 25). This tendency suggests the ease of reducing the piston pin diameter when designing the piston for the multi-link mechanism. Therefore, when considered together with the side thrust force reduction effect of this mechanism, this tendency also suggests the possibility of reducing the piston size and mass.

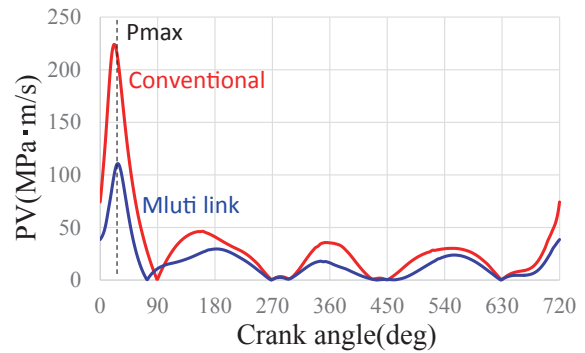


Fig. 24 PV of piston pin bush

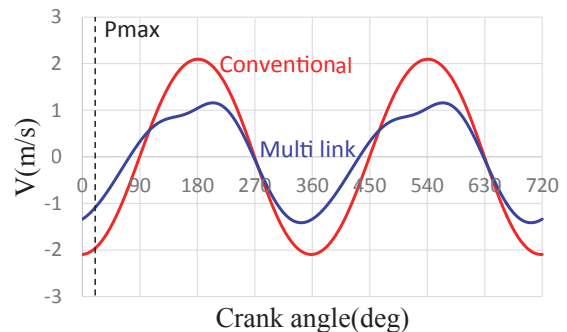


Fig. 25 Sliding velocity of piston pin bush

5. Organizing characteristics of bearing elements of multi-link mechanism

The bearing elements of the multi-link mechanism can be classified into three groups according to the usage environment and characteristics of each bearing. The L-Link bearing and main bearing, classified under group 1 in Figure 26, are required to function as the rotating bearing, similar to the connecting rod bearing and main bearing in the conventional mechanism. Meanwhile, the input load increases by up to 1.9 times due to the lever structure of the multi-link mechanism. To accommodate this increased load, the width of the L-Link bearing was increased as a countermeasure against the relative slipping at the bearing back, which was likely to occur because of the mechanism and structure. The countermeasure also led to a reduction in the surface pressure. The functional reliability of the main bearing was ensured by increasing the rigidity of the crank shaft to prevent uneven contact. The C-Link big end bearing, U-pin bush, and C-pin bush, classified into group 2, are bearing elements that were newly established for the multi-link mechanism. These bearing elements function as oscillating bearings, similar to the piston pin bush in the conventional mechanism. However, with regard to the PV value, an index that represents abrasion (refer to Figure 13), these bearing elements tend to have larger PV values than the piston pin bush. This tendency leads to a degradation in the seizure resistance. Therefore, to improve the seizure resistance performance, oil passages were established to draw engine oil into the sliding portion. In addition, a groove structure was established on the bearing itself along the entire circumference, to ensure that the cooling effect and foreign matter discharging effect are enforced and that the seizure resistance performance is secured. The oil groove established for the entire circumference was arranged at the center of the bearing width, which is not the main area subjected to the load. Thus, it was possible to achieve the cooling function and foreign matter discharge function without impairing the load capacity. The control shaft bearing, classified into group 3, often functions as a non-sliding bearing. For this location, an oil groove was established along the entire circumference, in the same manner as in group 2, to realize the foreign matter discharging function. In addition, the tendency of uneven contact was significantly suppressed by the control shaft, which had high flexural rigidity. The bush material was adopted as the bearing material, in the same manner as in group 2, to ensure adequate abrasion resistance performance. Although the specific countermeasures against the increasing load and decreasing oil flow (caused by an inability to supply sufficient oil) may be different for each group, the functional reliability of each group was secured by establishing oil passages to secure oil flow in the bearing width direction, while preventing increases in the component sizes and ensuring the load capacity at the bearing by focusing on the rigidity characteristics.

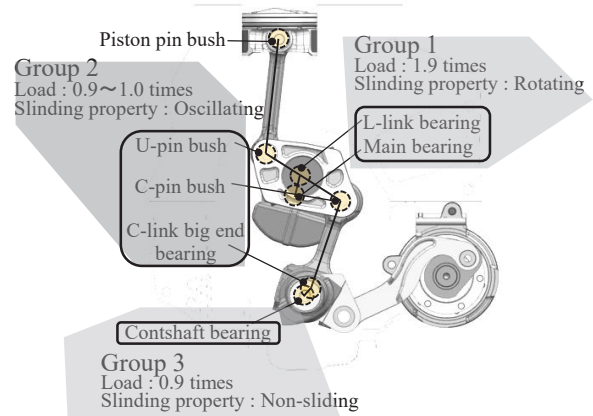


Fig. 26 The grouping of bearings

6. Evaluation of friction loss

Bearing elements have been newly added to the multi-link mechanism, which would increase friction loss. However, each of the added bearing elements was used in the oscillating operation, and they all had small diameters. Therefore, the increase in friction loss was limited. By contrast, owing to the reduction in the piston thrust force in the multi-link mechanism, caused by the vertical orientation of the U-Link during ATDC, and because it was possible to reduce the crank shaft diameter via the aforementioned correspondence, it was possible to reduce the friction loss, as compared to that in naturally aspirated engines with the same displacement, as shown in Figure 27.

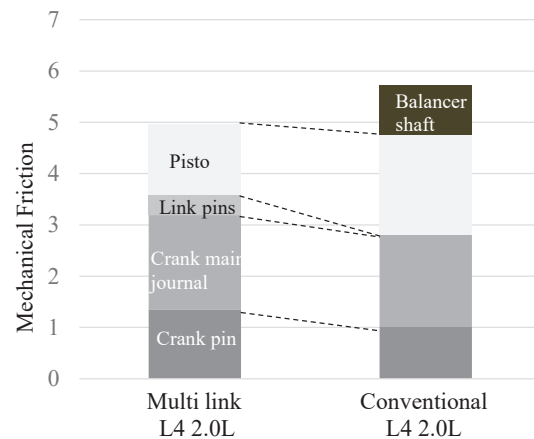


Fig. 27 Comparison of mechanical friction

7. Conclusion

The conclusions of this work are listed below.

It was possible to ensure the functional reliability of each bearing of a multi-link mechanism by implementing the following countermeasures according to the characteristics of each bearing.

- With respect to the bearings around the crank shaft, which are present in the conventional mechanism, the

load applied to the bearings will increase owing to the lever structure. However, it is possible to accommodate to the tendency of internal rotation and the local increase in the surface pressure by increasing the rigidity of the bearing itself or that of the component parts, such as the crank shaft.

- Regarding the oscillating bearings and non-sliding bearings that were newly established for the multi-link mechanism, the copper-alloy bush material, intended for high surface pressures, was adopted for improving the abrasion resistance performance.

- Due to the high hardness of the above material, there was a tendency for degradation in the seizure resistance performance owing to foreign matter. In addition, because the shaft rotation was limited, the oil flow was also limited, resulting in degradation in the foreign matter discharging performance. As a countermeasure for these problems, grooves were established along the entire bearing circumference and oil passages to ensure an oil supply path to the grooves; this also increased the oil flow in the bearing width direction.

Acknowledgements

For this research and development, we received significant support from the “Strategic Development of Energy Use Rationalization Technology,” a NEDO commissioned project. The authors would like to thank everyone who helped us with our research.

References

- (1) Katsuya Moteki: A study of a Variable Compression Ratio System with a Multi-Link Mechanism, SAE Paper 2003-01-0921, (2003).
- (2) Takashi Tanabe: The Structure of the Multi-link Parts for the Variable Compression Ratio Engine VC-T That Aims at Leveling the Bearing Surface Pressure, Proceedings of the 2018 JSAE Annual Congress (Spring), 20185421, (2018)
- (3) Katsutoshi Nakamura: The Development of the Multi-link Crank Mechanism for the Variable Compression Ratio Engine VC-T Utilizing the Dynamic Behavior Analysis, Proceedings of the 2018 JSAE Annual Congress (Spring), 20185420, (2018)

Source

公益社団法人自動車技術会
自動車技術会論文集
Vol.51, No.4 文献番号:20204316

Authors



Katsutoshi Nakamura



Katsuya Moteki



Satoru Ookuma

Surrogate Model Development for Prediction of Car Aerodynamics Using Machine Learning

Kei Akasaka* Fangge Chen** Takehito Teraguchi**

Abstract In the evaluation of car aerodynamics, Computational Fluid Dynamics (CFD) are frequently used as well as a wind-tunnel. However, the CFD simulations consume a lot of resources and time. In this study, a surrogate model using machine learning was developed to reduce the amount of resource and time needed for CFD. In the proposed model, the relation between car shapes and CFD results was learned for rapid prediction of pressure, velocity, and coefficient of drag for aerodynamics. In this paper, we introduce the proposed model, the training dataset, the accuracy, and the computational time.

1. Introduction

In recent years, it has become necessary to further reduce aerodynamic drag in order to improve the fuel efficiency competitiveness of cars and comply with new environmental regulations. Computational fluid dynamics (CFD) is often used as well as wind tunnel experiments to evaluate the aerodynamic performance of cars^(1,2). However, CFD requires a significant amount of time and resources. In particular, the resources required to perform CFD computations are increasing every year owing to the necessity of pre-calculations prior to experiments, the increase in the number of evaluation specifications, and the demand for improved calculation accuracies. Therefore, this study attempted to develop a surrogate model that estimates the CFD results (flow velocity, pressure, and drag coefficient C_D) using machine learning method, by learning the relationships between the car shape and the quantities evaluated using CFD. Using this approach, aerodynamic analyses can be replaced with the surrogate model, such that the amount of CFD computations and time consumption, as well as the corresponding costs, can be reduced. This paper outlines the proposed method, the dataset, and the validation results.*Received on November 10, 2020. Presented at the Technical Sessions of the Autumn Congress of the Society of Automotive Engineers of Japan on October 23, 2020.

2. Machine learning model

2.1 Previous Studies & Related Studies

Several studies similar to the present investigation have been reported. For instance, Umetani et al.⁽³⁾

constructed a machine learning model to learn and estimate the quantified features and characteristics evaluated via CFD (flow velocity, pressure, and C_D) for the car shape by using the Gaussian process to estimate the C_D values and flow fields of the cars. They trained the model with approximately 800 examples of car shapes and CFD results. They reported that the C_D and flow field estimation results matched the CFD calculation results, which served as reference information for our research. However, it is difficult to learn complex shapes of actual cars using their method. Specifically, this method uses a polyhedron called “PolyCube” and projects the constituent points of the PolyCube onto a car shape within a range in which the topology does not vary. The coordinates and heights of each projected constituent point are used as features. It is necessary to prepare a PolyCube with a topology similar to the shape of the car to be learned. However, it is difficult to use the same PolyCube for all car shapes because actual shapes have different topologies; for instance, minivans, hatchbacks, and sedans have 1-, 2-, and 3-BOX topologies, respectively. Hence, a PolyCube suitable for each car model needs to be prepared for individual learning, which requires time and effort. In addition, the actual cars have complicated shapes such as engine room parts, tires, floor components, and door mirrors, and it is difficult to prepare a PolyCube with a topology that can express such complicated shape elements. Therefore, the results obtained by Umetani et al. can only be applied to relatively simple car shapes.

By contrast, Guo et al.⁽⁴⁾ used a distance function that represents the distance from an object as input data and constructed a machine learning model that estimates two- and three-dimensional flow fields (corresponding to the flow velocity vector and pressure) based on a convolutional neural network (CNN)⁽⁵⁾. Because the

*Integrated CAE · PLM Department

**Nissan Research Center Mobility & AI Laboratory

distance function can be applied to complicated shapes and can also be extended to three dimensions relatively easily, the model structure proposed by Guo et al. was adopted for the flow field (i.e., flow velocity and pressure) estimation.

However, because C_D cannot be estimated using the model of Guo et al., a separate surrogate model for estimating C_D is required. Therefore, we proposed a surrogate model that estimates $C_D^{(6)}$ based on the input of voxel data. Because the estimation accuracy of C_D is satisfactory, the surrogate model structure of C_D was adopted in this study as well.

In related studies, a single model that can learn both the flow field and C_D has not been proposed thus far. Therefore, in this research, two different machine learning models based on related studies were developed to estimate the flow field and C_D .

2.2 Outline of estimation model for estimating flow field

The basic configuration of the flow field estimation model adopts the network structure proposed by Guo et al., as shown in Fig. 1. This model consists of an encoder and a decoder connected by a fully connected layer. When applying the model practically, such as in this study, it is necessary to increase the size of the distance function to be input according to the degree of complexity of the shape. In addition, the intermediate layers between the encoder and decoder need to be multilayered to improve the estimation performance. However, the use of multilayered intermediate layers easily causes gradient disappearance or gradient explosion problems during training, making it difficult to proceed with training. Therefore, to solve the gradient disappearance and explosion problems, in this study, residual blocks⁽⁷⁾ were used instead of the fully connected layer in the model structure of Guo et al. The model proposed herein is illustrated in Figs. 2 and 3. This model inputs a distance function and outputs (a) the three components of the flow velocity vector and (b) the pressure. For the encoder and decoder, batch normalization⁽⁸⁾ and instance normalization⁽⁹⁾ are used to suppress the disappearance of the gradient.

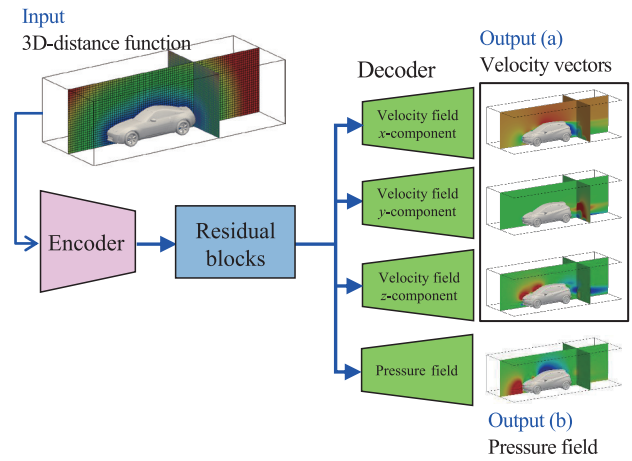


Fig.2 Structure of proposed model for flow field estimation

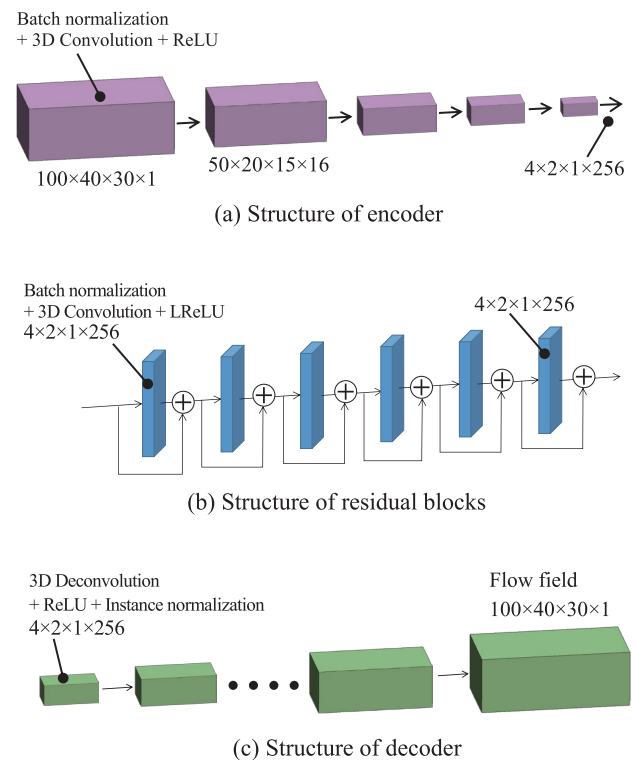


Fig.3 Details of encoder, residual blocks and decoder of proposed model for flow field estimation

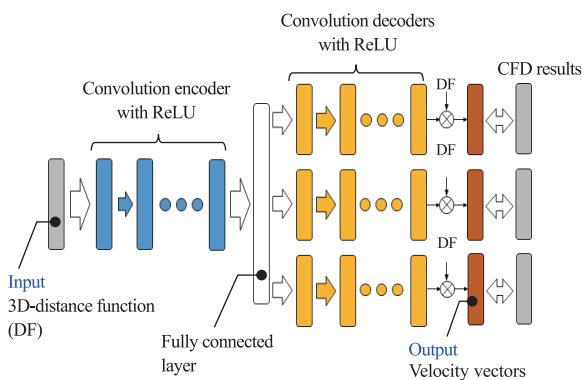


Fig.1 CNN structure of prediction model for flow field proposed by Guo⁽⁴⁾

2.3 Outline of estimation model for estimating C_D

The estimation model for estimating C_D is described in this section. We previously proposed an estimation model that estimates C_D based on the input of voxel data⁽⁶⁾. Although the model is based on Voxnet, proposed by Maturana⁽¹⁰⁾, global average pooling, instead of a fully connected layer, is used according to the research of Lin et al.⁽¹¹⁾ to reduce the amount of calculation when converting the intermediate layer into one dimension. Because the estimation accuracy of C_D is satisfactory, the estimation model structure based on our previous study was adopted in this study as well.

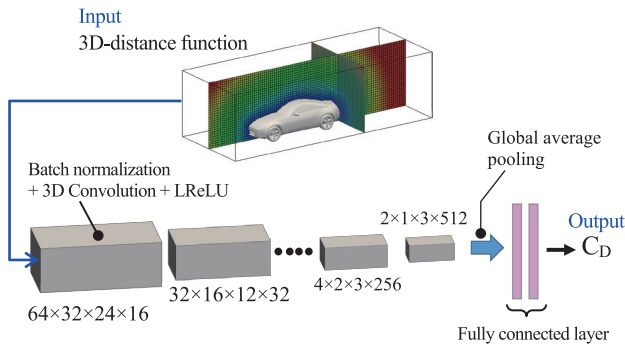


Fig.4 Structure of proposed model for coefficient of aerodynamic drag (C_D) estimation

However, in terms of convenience, it is desirable to avoid the use of different input data when estimating the flow field and C_D . Therefore, the input data for the C_D estimation model are converted from the voxel into the distance function to unify the flow field and C_D estimation model input data into the distance function. The network structure in which the input data are unified into a distance function is shown in Fig. 4.

2.4 Distance function and hyper-parameters

First, the distance function to be input into the estimation model can be described as follows. The distance field of the three-dimensional distance function used in this study is illustrated in Fig. 5. The colors indicate the distances from the car shape at each grid point. The distance function was created as follows. A bounding box was set around the car shape, and orthogonal equal-interval grid points were arranged in the bounding box. The shortest distance from the car shape was calculated for each grid point to create the relevant distance field. The sizes of the bounding boxes, grid pitches, and numbers of grids are provided in Table 1. For the distance function used to predict C_D , a smaller grid pitch is employed to ensure that even a slight shape change can be captured.

The optimizers, loss functions, and hyper-parameters used in this study are listed in Table 2.

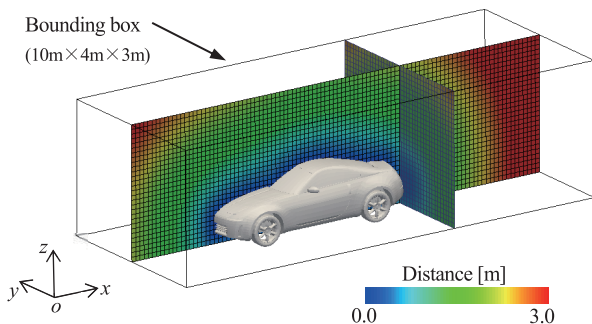


Fig.5 3-dimensional distance function around car shape

Table 1 Parameter of distance function

	Flow field prediction	C_D prediction
Bounding box	10.0m×4.0m×3.0m	6.4m×3.2m×2.4m
Grid pitch	0.10m	0.05m
Num. of grids	100×40×30	128×64×48
	120,000	393,216

Table 2 Optimizer, loss function and hyper-parameters

	Flow field prediction	C_D prediction
Optimizer	Adam	Adam
Loss function	Mean absolute error	Mean absolute error
Learning rate	10^{-3}	10^{-4}
Epoch	5,000	2,000
Batch size	16	16

3. Dataset and validation results

3.1 Dataset

The dataset is shown in Fig. 6. One case includes six pieces of information: the distance function, three components of the flow velocity vector, pressure, and C_D value. Only the distance function is input into the estimation models, and the flow fields and C_D value are the outputs of the models respectively. Training was performed such that these outputs matched the flow velocity, pressure, and C_D value of the training case. For this study, 1,123 cases were prepared and divided in a ratio of 10:1 into training and testing datasets. The datasets included six types of cars: sedans, coupes, SUVs, hatchbacks, pickup trucks, and light cars. The proportions of car types included in the training and test datasets were approximately the same. The flow velocity vectors, pressures, and C_D values used for training and test were calculated using commercial CFD software. The calculations were performed under straight running conditions at a car speed of 33.3 m/s and Reynolds number of 1.0×10^7 . Because a grid unrelated to the distance function was used in the CFD calculations, the CFD calculation results were mapped to the grid for the distance function.

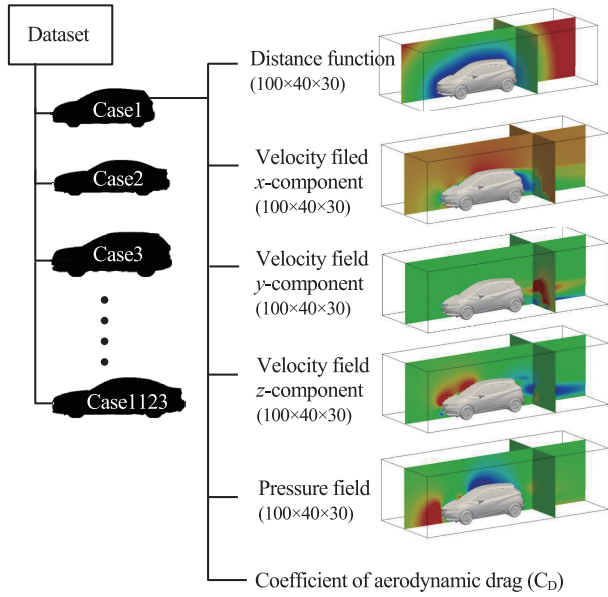


Fig.6 Distance function, flow fields and aerodynamic drag (C_D) in dataset

In addition, because the distance function and CFD results are dimensional information, normalization was performed before using them for learning and testing in this study.

A NVIDIA DGX-1™ (1 GPU) was used as a computational resource for learning, and Tensorflow 2.0 was employed as a library for machine learning. The time required for learning the flow field was approximately 4 days, whereas the time for learning C_D was approximately 0.5 days. In addition, by calculating the number of epochs shown in Table 2, it was confirmed that the values of the final loss function of the three components of the velocity vector, pressure, and C_D value are reduced to the extent shown in Table 3.

Table 3 Errors of loss functions in velocity vectors, pressure and C_D at last epoch of proposed model

Velocity vectors	Pressure	C _D
0.003~0.005	0.002	0.001

3.2 Flow field validation results

Next, the flow field estimated by this method was considered as follows. Each test case had a flow velocity vector of 120,000 points (100 × 40 × 30). The mean error of those 120,000 points was considered using the mean absolute error (MAE) shown in equation (1):

$$MAE = \frac{1}{n} \sum_{i=1}^n |a_i - y_i| \quad (1)$$

where a_i and y_i represent the CFD results and the estimation results of the proposed model, respectively. In addition, n represents the number of grid points, which was 120,000 in this case.

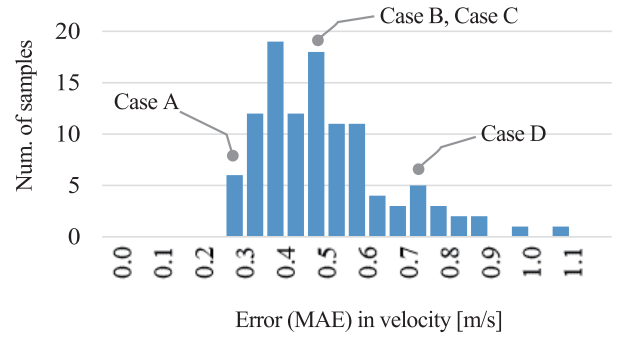


Fig.7 Histogram of mean absolute error in x-component of velocity vector on test cases

The mean absolute error (MAE) of the x-direction component of the velocity vector is presented in Fig. 7. The mean error of the x-component is 0.2–1.1 m/s, which is within the error range of the car speed wind (0.6%–3.3%). In addition, the mean errors of the y- and z-components were smaller than that of the x-component.

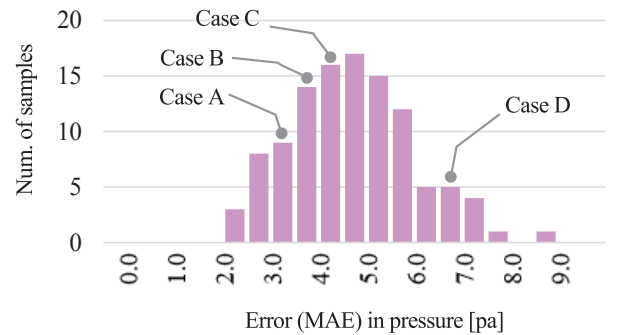


Fig.8 Histogram of mean absolute error in pressure on test cases

The MAE results for the pressure estimated by the proposed model and evaluated at 120,000 points in the same manner as the velocity vector are presented as a histogram in Fig. 8. The MAE of the pressure is 2.0–9.0 Pa, which is within the error range of approximately 0.3%–1.3% of the dynamic pressure based on the car speed wind. There were no significant differences in the error tendencies among the car types in terms of both velocity and pressure.

The pressure and velocity magnitude distributions obtained from the CFD calculations and proposed model are compared in Figs. 9 and 10, respectively. Cases A–D are typical examples of the test cases, and the velocity and pressure errors in each case are shown in Fig. 7 and Fig. 8, respectively. In both Fig. 9 and Fig. 10, the upper rows show the CFD calculation results, whereas the lower rows indicate the estimation results of the proposed model to be compared for each case.

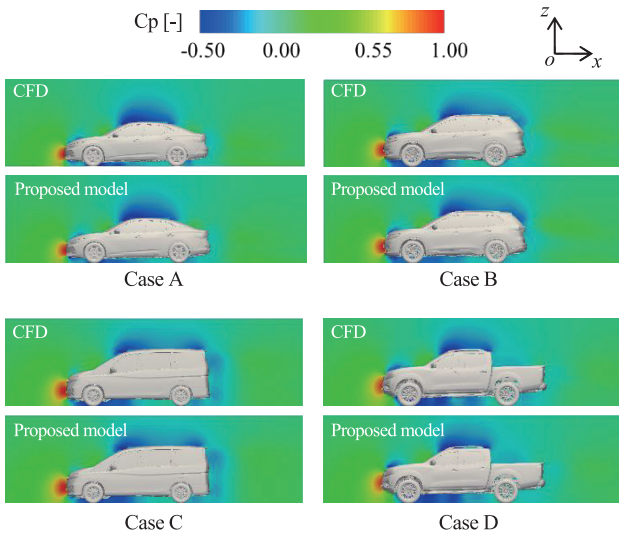


Fig.9 Comparison of pressure between CFD and proposed model in central cross-section

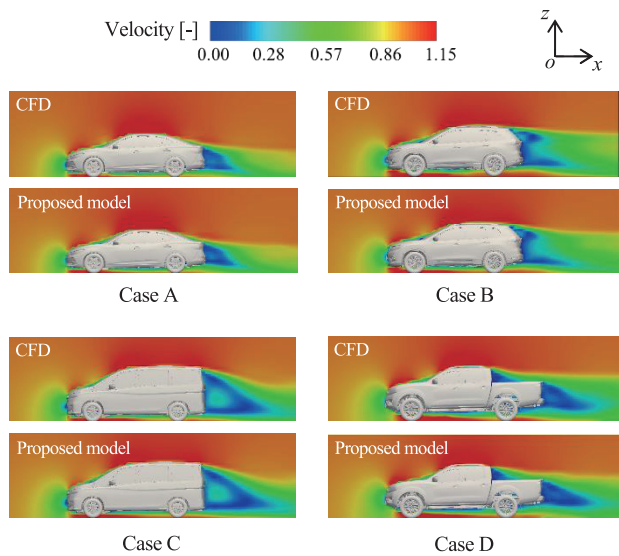


Fig.10 Comparison of velocity magnitude between CFD and proposed model in central cross-section

The pressure distribution at the central cross-section of the car is shown in Fig. 9, where the pressure is converted into a dimensionless value by using the dynamic pressure. In each case, the pressure distribution estimated by the proposed model reproduces the tendency of the CFD results.

The velocity magnitudes in the central cross-section of the car are shown in Fig. 10. The velocity was made dimensionless by using the car speed. The proposed model qualitatively reproduces the CFD results in terms of the size of the rear stream region behind the car and the tendency of the velocity magnitude, which are important, especially in aerodynamic evaluations.

According to the comparison results shown in Fig. 9 and Fig. 10, it was confirmed that the proposed model can reproduce not only the qualitative tendency of the flow field even in case D, in which the error between pressure and velocity is relatively large, but also the characteristics of the flow fields of different car types.

3.3 Effect of the residual blocks

The network structure proposed by Guo et al., in which a fully connected layer was adopted for the connection between the encoder and decoder, and the network structure proposed in this study, in which residual blocks were adopted instead of a fully connected layer, are compared in this section. The velocity magnitudes at the central cross-section of the car are shown in Fig. 11. The results of the CFD calculations and training using the residual blocks are presented in Figs. 11 (a) and (b), respectively. Here, the results of the proposed model are similar to the CFD calculation results. By contrast, in the results of training using the fully connected layer, shown in Fig. 11 (c), the tendency of the velocity magnitude is different from that in the CFD results. Owing to the gradient explosion, the weight optimization failed during training, and the value of the loss function of the velocity vector was 0.1. This value is larger than that of the loss function of the proposed method, as shown in Table 3, and it did not decrease even when the number of epochs was increased. According to these results, the residual blocks were considered to be effective.

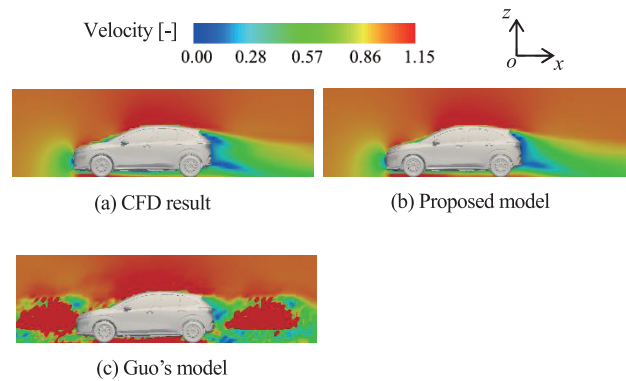


Fig.11 Comparison of velocity magnitude between Guo's model and proposed model in central cross-section

3.4 C_D validation results

The errors in the C_D values estimated using the proposed model are depicted in Fig. 12; the errors obtained in the training and testing cases are shown in (a) and (b), respectively. Table 4 shows the results of evaluating the error using the mean absolute percentage error (MAPE), described in equation (2), and the standard deviation:

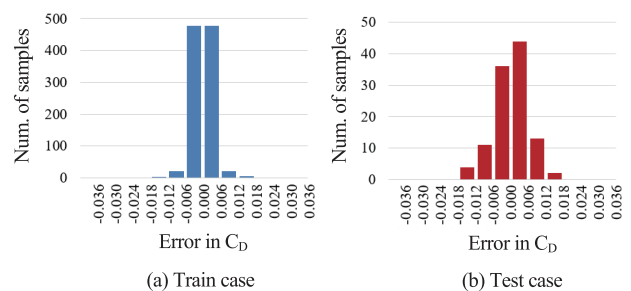


Fig.12 Histograms of error in C_D

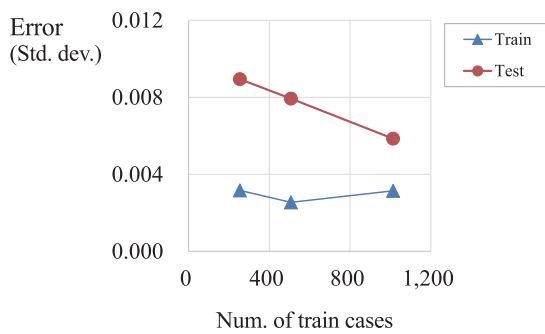
Table 4 Error in C_D of train and test

	(a) Train case	(b) Test case
Std. deviation	0.002	0.006
MAPE	0.5%	1.4%

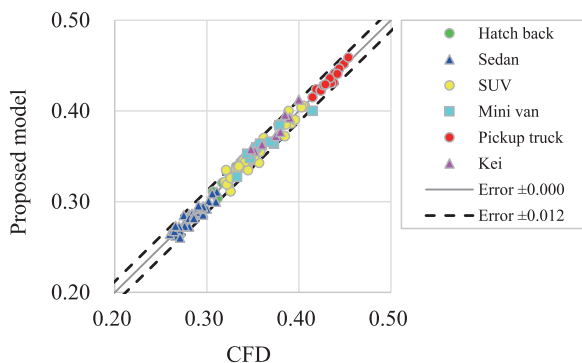
$$MAPE = \frac{100}{n} \sum_{i=1}^n \frac{|a_i - y_i|}{a_i} \quad (2)$$

In equation (2), a_i and y_i represent the CFD result and the estimation result of the proposed model, respectively, and n represents the number of training cases or the number of testing cases.

Because the standard deviation and MAPE of the training case (a) shown in Fig. 12 and Table 4 are sufficiently small, it is evident that the dataset has been trained appropriately. For the testing case (b), however, the error is larger than that for the training case, and there exists a problem with the generalization performance.


Fig.13 Error history in C_D with increase of train cases

The error trend with an increase in training cases is shown in Fig. 13. The horizontal axis represents the number of training cases, and the vertical axis represents the error (standard deviation). As the number of training cases increases, the error of the testing cases decreases. Therefore, it is considered effective to increase the number of training cases in order to improve the generalization performance.


Fig.14 Comparison of coefficient of aerodynamic drag (C_D) between CFD and proposed model

The C_D values and CFD results of the test cases estimated by the proposed model are compared using a scatter plot, as shown in Fig. 14. The vertical axis represents the C_D values estimated by the proposed model, and the horizontal axis represents the values calculated using CFD. The testing case includes six car types, and the C_D values estimated by the proposed model for each car type are generally within ± 0.012 of the CFD results.

In the initial phase of car development, aerodynamic evaluation is performed on multiple car design proposals; however, various car shapes have been proposed, and C_D also varies considerably more than the error of the proposed model. Therefore, in the initial phase, the proposed model can be used to evaluate the superiority or inferiority of C_D for each proposed design, and it is expected that the frequency of CFD usage and the amount of calculations can be reduced.

3.5 Estimated time required for machine learning model

The times required to predict the velocity, pressure, and C_D in Case A described above when using the proposed model are shown in Table 5 and compared with the times required when the commercial CFD software is used.

Table 5 Comparison of computational time between CFD and proposed model

Proposed model		CFD	
Distance function	11.4 min.	Mesh generation	4.0 H
Prediction of velocity, pressure and C_D	0.1 min.	Flow calculation	20.0 H
Sum.	11.5 min.	Sum.	24.0 H

In the case of CFD, approximately 24 h was required for mesh preparation and flow calculation⁽¹⁾. This calculation time was recorded when using Intel® Xeon® (approximately 80 million meshes and 256 CPU cores). For the proposed model, a notebook PC (CPU: Intel® Core-i5™) was used to compute the distance function; this required approximately 11 minutes, whereas the predictions of the velocity, pressure, and C_D only required 3 seconds. Therefore, the proposed model is deemed useful for checking the qualitative flow field and C_D for various shape designs within a short period of time.

4. Summary and conclusion

In this study, a practical surrogate model that can predict the flow field and C_D around a car with a complicated three-dimensional shape was developed.

- 1 We developed a model using residual blocks, instead of the fully connected layers used in the network structure of Guo et al., to effectively avoid gradient explosion and accurately predict the flow field around the car shape.
- 2 It was confirmed that the flow field estimated by the proposed model could qualitatively reproduce the

CFD results.

- 3 The error (MAPE) in the C_D value estimated by the proposed model was 1.4%.
- 4 The proposed model is a useful surrogate model that can replace CFD because the flow fields and C_D values for various shape designs can be estimated within a significantly short period of time. Using the proposed model, it is expected that the resources required for aerodynamic analyses can be reduced considerably.

References

- (1) K. Akasaka, et al.: Simultaneous Estimation of Aerodynamic and Thermal Performances Using CFD, Proceedings of SAE Seminar, No.96-05, pp.11–14 (2005).
- (2) M. Arai, et al.: Development of the Aerodynamics of the New Nissan Murano, SAE Technical Paper, 2015-01-1542 (2015).
- (3) N. Umetani, et al.: Learning Three-Dimensional Flow for Interactive Aerodynamic Design, ACM Trans. Graph., Vol. 37, No. 4, Article 89 (2018).
- (4) A. Guo, et al: Convolutional Neural Networks for Steady Flow Approximation, Proceedings of the 22nd ACM SIGKDD International Conference on Knowledge Discovery and Data Mining, pp.481–490 (2016).
- (5) Y. LeCun, et al.: Gradient-based learning applied to document recognition, Proceedings of the IEEE, 86(11), pp.2278–2324 (1998).
- (6) K. Akasaka, et al.: Development of A Tool for Interactive Prediction of Car Drag Coefficient Using Machine Learning, at The 34th Annual Conference of the Japanese Society for Artificial Intelligence, 206-GS-13-02 (2020).
- (7) K. He, et al: Deep residual learning for image recognition, Proceedings of the IEEE conference on computer vision and pattern recognition, pp. 770-778 (2016).
- (8) Ioffe, et al.: Batch normalization: Accelerating deep network training by reducing internal covariate shift, arXiv preprint arXiv:1502.03167 (2015).
- (9) Ulyanov, et al. :Instance normalization: The missing ingredient for fast stylization, arXiv preprint arXiv:1607.08022 (2016).
- (10) D. Maturana, et al.: VoxNet: A 3D Convolutional Neural Network for real-time object recognition, IEEE/RSJ International Conference on Intelligent Robots and Systems (IROS), Hamburg, pp. 922-928 (2015).
- (11) M. Lin, et al.: Network in network, arXiv:1312.4400 (2013).

Source

公益社団法人自動車技術会
自動車技術会論文集
Vol.52, No.3 文献番号:20214248

Authors



Kei Akasaka



Fangge Chen



Takehito Teraguchi

A Study on Pitch Characteristic to Reduce Line Trace Deviation in Small Steering Angle

Mitsunori Tao* Naoya Machida** Yutaka Hayashi*** Ken Nagasao****

Abstract When driving along a straight roadway, a driver regularly makes minute steering adjustments in order to maintain the vehicle's position within the driving lane. In the research of the previous report, the quantitative relationship of several steering characteristics in this scenario was clarified for accurate line tracing. However, it was found that the deviation of the tracing line by trials was not small at the same time. This paper clarifies one of the factors of the deviation and its improvement by adding minute pitching motion to the vehicle in proportion to the steering angle.

1. Introduction

For the daily driving scenarios encountered by typical drivers, most driving is performed along straight trajectories, including operations performed for fine adjustments in the travel path with small steering angles. According to our survey conducted in Europe and Japan, steering with angles of 5° or less, which is considered as minute steering, accounts for more than half (51.1%) of all steering across all vehicle speed ranges and approximately 80% (79.6%) in zones with higher speed limits of 80 km/h or more, which is supported by some data. The traceability of a target driving line with such small steering angles is an important aspect of performance that is frequently encountered by many drivers; however, its mechanism has not been fully clarified thus far. Therefore, at actual development sites, there are many cases where the development of this ability relies on tuning an actual vehicle.

With regard to this issue, our previous paper¹⁾ clarified the quantitative relationships between the steering force and yaw characteristics with respect to line traceability; this was achieved by quantitatively determining the dead zone of the driver in the minute steering angle range and the dead band of the yaw characteristics of the vehicle and then analyzing the relationship between the evaluated line traceability defined in the study and the two dead zones. However, a new issue was also observed: the line trace deviations of the drivers varied considerably between trials.

In this study, considering that one of the causes of this variation in the line tracing deviations originates from the steering mechanism of the driver within the minute steering angle range, it was hypothesized that the

variations can be reduced by adding a certain amount of pitch motion to the steering angle in order to reduce variations. This hypothesis was verified using a driving simulator, and the quantitative effect of the variation reduction was extracted. Following our previous work, which clarified the vehicle characteristics that enable drivers to drive accurately, on average, along a target driving line, this research focused on the vehicle characteristics that enable accurate driving with little variations between trials.

To explain this research, an outline of our previous work and the variation in the line trace deviations, which is the subject of the present study, is first provided. Next, the driver steering mechanism, which is considered to cause variations in the minute steering angle range and also defined as a hypothesis in the previous work, will be described; the reasons for choosing the pitch as the vehicle behavior to be added to reduce variations are also explained. Subsequently, the quantitative pitch characteristics that can reduce the variation in the line trace deviations based on the driver sensitivity characteristics (related to the pitch motion obtained from experiments) are hypothesized, and the results of the experimental verification are reported.

In this study, two experiments were conducted with 25 male drivers in their 20s and 50s who drove their cars on a daily basis. The tests were examined and approved by the Experimentation Ethics Committee of Nissan Motor Co., Ltd., and informed consent was obtained from the test participants.

2. Outline of and issues in our previous study

In our previous study, an evaluation course was established, consisting of an R1200 curve and its

*Nissan Research Center Mobility & AI Laboratory **Powertrain and EV Performance Engineering Department

Customer Performance and Test Engineering Methodology Innovation Department *Vehicle Performance Engineering Department

relaxation section; this required a steering input of approximately 5° from a straight line at a constant speed of 80 km/h, as shown in Fig. 1, and the drivers drove along the course with the target line. The actual deviations in the travel trajectories during driving were defined as “line trace deviations,” whose mechanism was clarified.

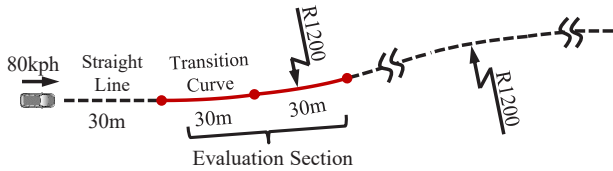


Fig.1 Evaluation Course

As shown in Fig. 2, the line trace deviations can be accurately indicated using two types of characteristics: the steering reaction force characteristics, which are highly sensitive to the minimum steering angle that the driver recognizes as “steering input to the vehicle,” and the “yaw-rate dead band” characteristic (shown in Figs. 3 and 4), which is highly sensitive to the steering angle generating the minimum yaw rate of $0.21^\circ/s$ that enables the driver to sense that “the vehicle has moved.” This was clarified through the driver-vehicle model hypothesis and the simulator-based verification conducted by the evaluators. The verification results are shown in Fig. 5. For the specifications at the front of the graph, indicating significant steering forces and large yaw-rate dead bands, the line trace deviation is negative, causing the vehicle to move outward with respect to the target line. Conversely, under the specifications for weak forces and small dead zones, the vehicle moves inward. Therefore, the target line can be traced accurately by setting the steering force and dead band along the thick broken line.

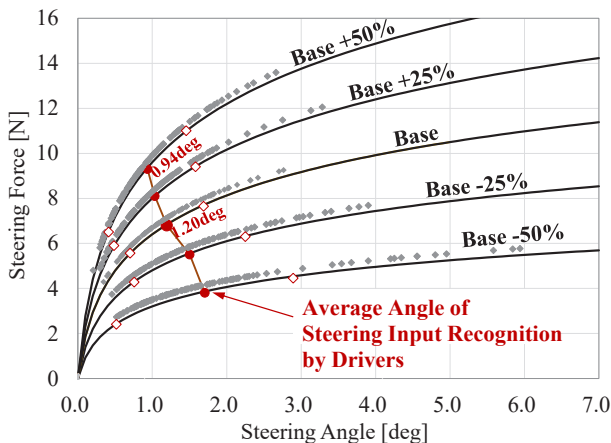


Fig.2 Steering Force & Driver's Input Recognition Angle

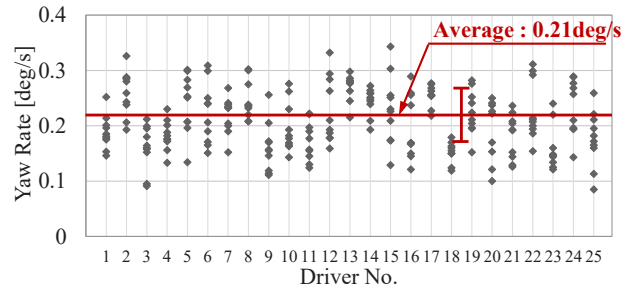


Fig.3 Driver's Yaw-Rate Sensitivity Experimental Result

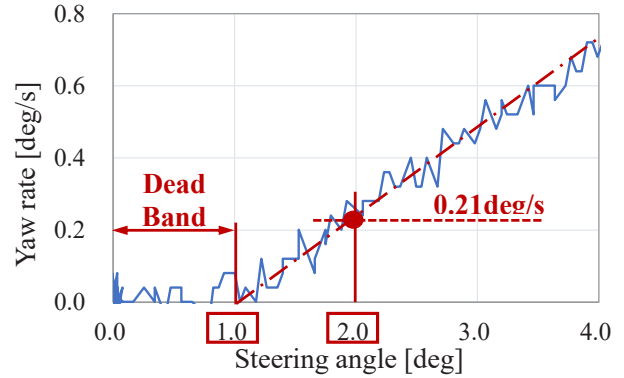


Fig.4 Yaw-Rate Characteristic in Small Steering Angle

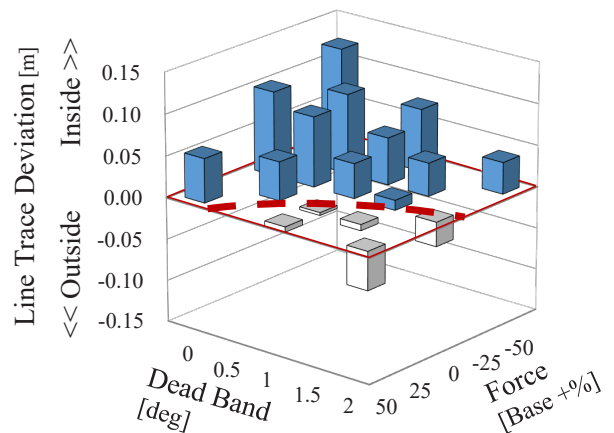


Fig.5 Experimental Result of Line Trace Deviation

However, as a new issue, it was confirmed that the line trace deviations varied considerably between the trials performed by individual drivers. The line trace deviations for a certain driver across six trials under the specifications of a steering reaction force of +25% and a yaw-rate dead band of 1° , which allow the average of the line trace deviations of 25 drivers to be almost zero, are shown in Fig. 6. On average, they appear to coincide with the thick, dashed target line; however, certain variations exist.

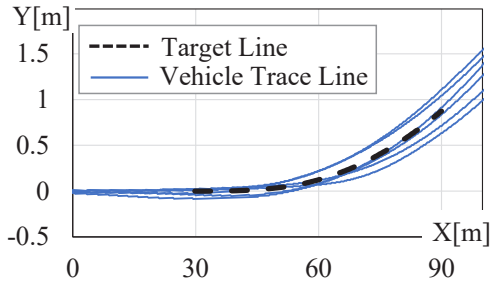


Fig.6 Line Trace Deviation by a Driver

The variations in the line trace deviations of 25 drivers based on their respective standard deviations under the same specifications are depicted in Fig. 7, with the average value of 0.047 m. This average is not sufficiently small, even compared with the fluctuation in the line trace deviations under the different specifications defined for the average value of all the trials by all the drivers, as shown in Fig. 5.

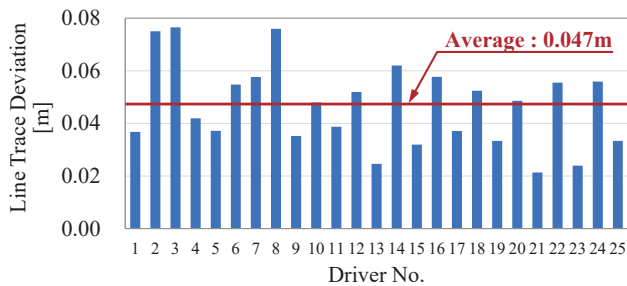


Fig.7 Average of Line Trace Deviation by 25 Drivers

Following our previous work, which clarified the vehicle characteristics that enable drivers to drive accurately, on average, along a target driving line, this research focused on the vehicle characteristics that enable accurate driving with little variations between trials.

3. Causes of variation in line trace deviations and reduction measures

3.1 Steering mechanism for minute steering angles and variation in line trace deviations

Various factors can be considered as the causes of the variation in the line trace deviations for each trial of a driver, such as differences in the line of sight, how the steering wheel is held, or the degree of concentration when driving. This work focused on the steering mechanisms of the drivers with minute steering angles, as hypothesized in the previous work, and conducted a detailed analysis.

As shown in Fig. 8, when steering from straight running toward the target line, the driver first recognizes that the steering input to the vehicle is commenced at a steering angle of approximately 1° based on the steering reaction force information. Therefore, by setting a dead

band in the yaw rate such that the vehicle can initiate the yaw movement simultaneously, the vehicle movement that matches the feeling of the driver can be realized. As a result, on an average, the line trace deviations are reduced. However, the driver can only sense the movement due to this yaw rate as visual information when the value exceeds 0.21°/s and the steering angle reaches approximately 2°. In other words, in the section where the steering angle is 1°–2°, it can be considered that the driver is performing blind steering without obtaining feedback regarding vehicle movement in the visual sense and relying solely on the information from the steering reaction force.

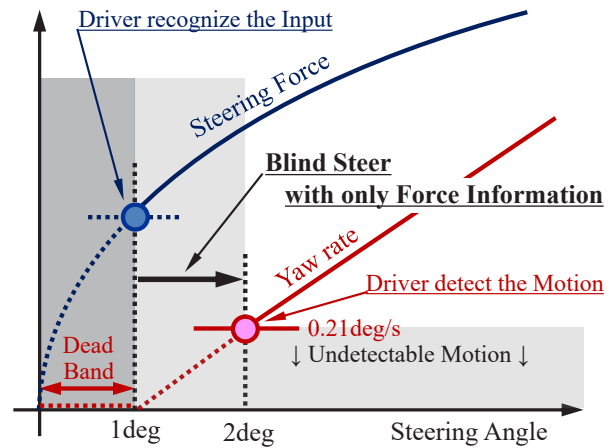


Fig.8 Driver's Steering Process in Small Steering Angle

It is clear that visual feedback is one of the most important types of information for stable and accurate driving, and it is conceivable that even a small steering angle range, such as 1°–2°, has an unexpectedly large influence on stable and accurate driving. In particular, with regard to the line traceability at minute steering angles of less than 5°, as in this case, the effect is considerably large and likely one of the major factors in the variation of the line trace deviations.

Therefore, visual information is fed back to the driver, indicating that the vehicle begins to move in the yaw direction at a steering angle of approximately 1°, which the driver can recognize as a steering input. When movement increases with the steering angle, the driver will be able to steer in a more accurate and stable manner; consequently, variations in the line trace deviations will be reduced.

3.2 Vehicle behaviors for providing visual information to drivers

As mentioned earlier, the yaw movement itself does not enable the driver to sense that the vehicle responds to the steering and begins to move in the yaw direction; this is because a yaw rate of 0.21°/s or higher is required for the driver to detect movement in the yaw direction. By contrast, if a higher yaw rate threshold for the driver to sense vehicle start movement is set, the yaw-direction movement of the vehicle may become excessive and the vehicle will not travel accurately along the originally

targeted driving line.

In this study, based on the vehicle movements in the six translational and rotational motion directions, the movement to convey to the driver as visual information on behalf of the yaw movement of the vehicle that the vehicle is responding immediately after the start of the yaw movement was examined. First, the roll, pitch, and bounce motions were selected as candidates, excluding the plane motions in the front-back and left-right directions, which directly affect the travel trace of the vehicle, such as the yaw-direction motion. Subsequently, referring to previous studies²⁾ where human sensitivity was investigated, the motion in the pitch direction, to which it was reported that humans have the same high visual sensitivity as the yaw-direction motion, was finally selected.

In previous literature^{3), 4)}, it was reported that the feeling of steering, or the equivalent characteristics, could be improved by imparting a downward pitch to the vehicle during steering, as compared to the cases where no pitch motion was provided or an upward pitch was provided. Therefore, in this study, downward pitch motion was imparted to the vehicle during steering.

4. Hypothesis for reducing variations in line trace deviations using vehicle pitch motion

4.1 Experiments on driver sensitivity to pitch motion

To determine the minimum pitch motion that a driver can detect, a sensitivity experiment was conducted using a driving simulator. The experimental setup is depicted in Fig. 9. When a constant downward pitch was provided to the vehicle, the drivers were instructed to gaze at the front view of the screen and to press the switch at hand the moment they sensed the pitch movement. A total of eight experiments with different pitch rates, ranging from an extremely low pitch rate of 0.0125°/s to a relatively high pitch rate of 0.3°/s, were conducted five times each, and the pitch angles sensed by the drivers were recorded for each trial.



Fig.9 Pitch Sensitivity Experimental Scene

The measurement results are presented in Fig. 10. The experimentally specified pitch rates (eight specifications) are provided on the horizontal axis, whereas the pitch angles sensed by the driver at each pitch rate are denoted on the vertical axis. The measurement data obtained from the 25 experimental evaluators (drivers) are indicated by the dots, and the average values are connected by the solid line. For the highest pitch rate of 0.3°/s, the results of the push-button switch operation

and the evaluation comments confirmed that all the drivers could feel the pitch movement as soon as it was initiated; therefore, the data in Fig. 10 can be considered as the operational time differences of the drivers between the moment at which the pitch rate of 0.3°/s was generated and the time at which the button was pressed by the individual drivers. The average value (0.51 s) of the operation times for all the drivers was subtracted from all the experimental data for correction.

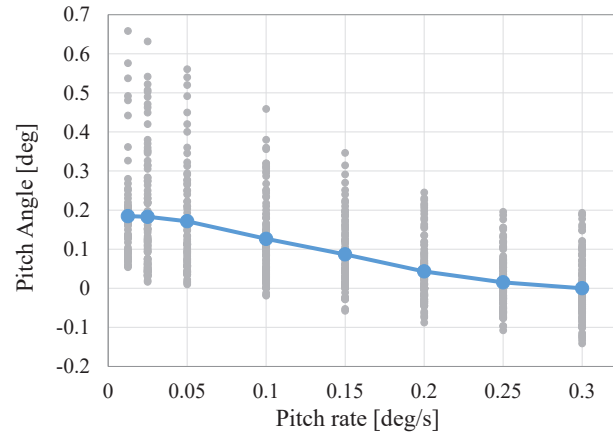


Fig.10 Driver's Sensitivity for Pitch Motion

At low angular velocities with pitch rates of 0.05°/s or less, all the drivers sensed the movement at a pitch angle of 0.15°–0.2° (refer to the left side of the graph); the drivers could not sense pitch rates lower than 0.05°/s and the movement was detected for the first time by the size of the integrated pitch angle. By contrast, at a high pitch rate of 0.3°/s, the drivers sensed the movement with almost no pitch angle (see the right side of the graph), which is likely because the drivers could detect the speed at this pitch rate, as described above. The central region between these two regions is considered as the section where the drivers could sense the pitch rate and the pitch angle as a whole; hence, the sensitivity graph presents a downward-sloping line connecting the two regions. Next, using this sensitivity line, the pitch motion that enables drivers to sense the initiation of yaw motion was hypothesized.

4.2 Hypothesis of pitch characteristics to reduce variation in line trace deviations

The pitch characteristics were hypothesized based on the pitch motion required for drivers to recognize a steering input and sense the vehicle response near a steering angle of 1° (at which the yaw motion commences and increases). Although various generated pitch motion patterns can be considered, such as steering angle proportionality, steering wheel angle rate proportionality, and the addition of non-linearity to each, this study aimed to verify the mechanism in the simplest possible manner and selected the pitch angle (downward) proportional to the steering angle, shown in Fig. 11, to formulate a hypothesis of the required proportionality constant. In addition, the experimental results of our

previous research confirmed that drivers steer at an angular velocity of approximately $3^\circ/s$ in the target scene; hence, this steering wheel angle rate was added to the prerequisites.

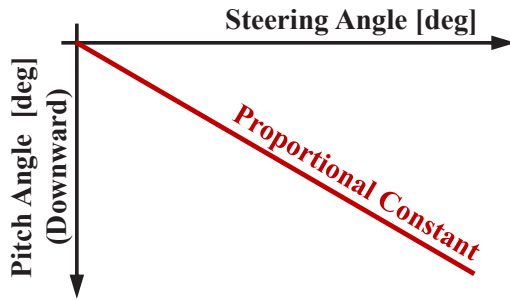


Fig.11 Pitch Characteristics for Driver's Information

$$\theta_{pitch} = K \times \theta_{steer} \quad (1)$$

$$\dot{\theta}_{pitch} = K \times \dot{\theta}_{steer} = 3K \quad (2)$$

θ_{pitch} : Pitch Angle (Downward) [deg]

θ_{steer} : Steering Wheel Angle [deg]

K : Proportional Constant

$\dot{\theta}_{pitch}$: Pitch Angle Rate (Downward) [deg/s]

$\dot{\theta}_{steer}$: Steering Wheel Angle Rate [deg/s]

Based on the driver sensitivity line for the pitch motion (Fig. 10), obtained through the experiment, and the pitch characteristics during steering, defined in equations (1) and (2), the proportionality constant K , which enables drivers to sense the pitch motion at a steering angle of 1° , was obtained. A graph of the pitch rates and pitch angles generated at a steering angle of 1° when K was changed from 0 to 0.08 in 0.02 increments, with respect to the driver sensitivity line for the pitch motion, is shown in Fig. 12.

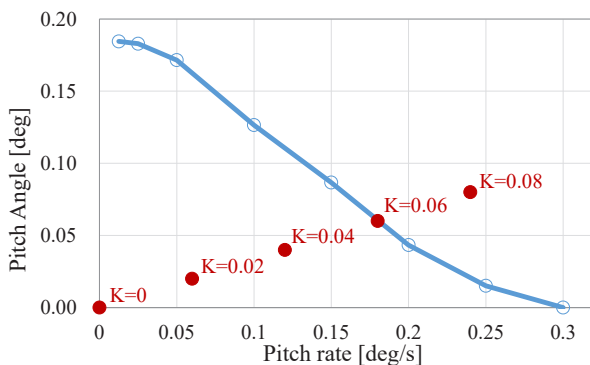


Fig.12 Pitch Motion by each "K" at Steering Angle 1deg

When K is 0.04 or less, the pitch motion generated at the steering angle of 1° does not reach the driver sensitivity line, indicating that this setting does not enable the driver to sense the pitch motion at a steering

angle of 1° . However, when $K = 0.08$, the pitch motion has already considerably exceeded the driver sensitivity line at a steering angle of 1° ; thus, it is considered that the driver can sense the motion before the steering angle reaches 1° . When $K = 0.06$, the pitch motion almost falls on the driver sensitivity line. In other words, this value of K enables the driver to sense the pitch motion at a steering angle of 1° .

$$\theta_{pitch} = 0.06 \times \theta_{steer} \quad (3)$$

As shown in equation (3), which uses the pitch angle and steering angle, the visual information (pitch motion) enables the driver to recognize a steering input and sense the vehicle response near a steering angle of 1° (at which the yaw motion of the vehicle commences and increases). Therefore, it is assumed that the variation in the steering angles and the line trace deviations can be reduced by adding visual feedback in the minute steering angle range, wherein the drivers were deemed to have performed blind steering. The abovementioned hypothesis was verified as discussed in the following section.

5. Verification of hypothesis

The hypothesis was verified using the model of a certain C-segment vehicle and the driving simulator that reproduced the evaluation course shown in Fig. 1, as in our previous research. The outline, method, and results of the experiment are as follows.

5.1. Overview of vehicle model and simulator used in experiments

The main parameters of the vehicle model used in the experiment are listed in Table 1.

Table 1 Vehicle Model Parameter

Parameter	unit	Value
Vehicle Mass	kg	1670
Vehicle Yaw Inertia	kgm^2	2600
Vehicle Pitch Inertia	kgm^2	2300
Height of C.G.	m	535
Front axle~C.G.	m	1.08
Rear axle~C.G.	m	1.62
Front Cornering Power	kN/rad	62.5
Rear Cornering Power	kN/rad	95.5
Steering Gear Ratio	-	15.0

An external view of the driving simulator used in the experiment is provided in Fig. 13. This simulator is equipped with a cabin with a hexapod mounted on slide rails (motion range of 22×6 m) and 64 linear motors that drive the hexapod with high precision; thus, this simulator can reproduce the actual vehicle motions under many scenarios.⁵⁾

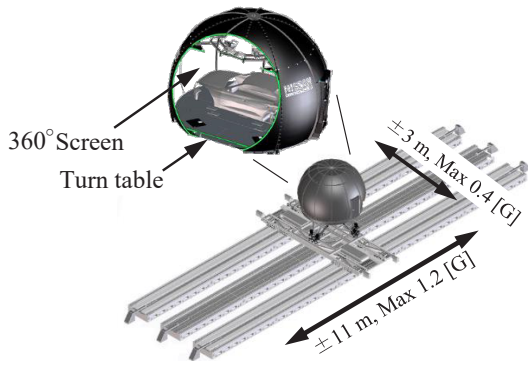


Fig.13 Driving Simulator

Next, the accuracy of this simulator was verified as follows. The actual data measured using the C-segment vehicle and simulator for the dependence of the steering force and yaw rate on the steering angle are presented in Fig. 14; notably, both exhibit high reproducibility.

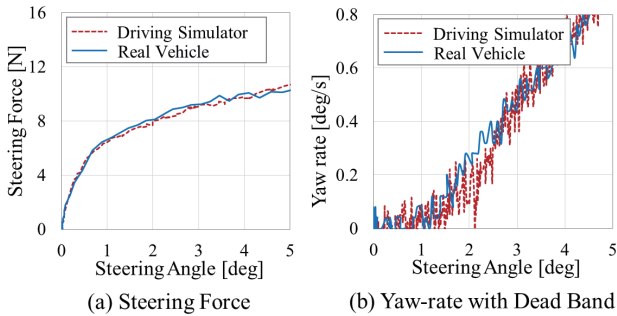


Fig.14 Driving Simulator Accuracy Confirmation

5.2 Experimental method

The experiment was conducted using the same 25 drivers as in the pitch rate sensitivity experiment. The vehicle speed was fixed to 80 km/h, and the drivers were instructed to operate the steering wheel to solely drive the vehicle along the center of the lane. With regard to the experimental specifications, the yaw-rate dead band and steering reaction force were set to 1° and the standard +25%, respectively, which afforded the smallest average value (almost zero) of the line trace deviations for all trials in our previous research. Furthermore, K of the pitch angle to the steering angle was changed five steps from 0 to 0.08 in increments of 0.02. For each step, the experiments were conducted by performing a total of 30 randomly arranged trials, with three right steering and three left steering experiments. The steering angle and the line trace deviations were measured.

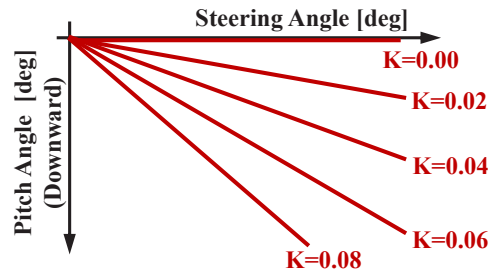


Fig.15 Pitch Characteristics

5.3 Experimental results

The measured line trace deviations for a certain driver with respect to different values of K of the pitch are presented in Fig. 16. The right-turn data were mirror-compensated in the left-turn direction. The variation in the line trace deviation from the target line decreases as K increases. In addition, the numerical values in each graph, which represent the calculated line trace deviations, quantitatively confirm the tendency of the variations.

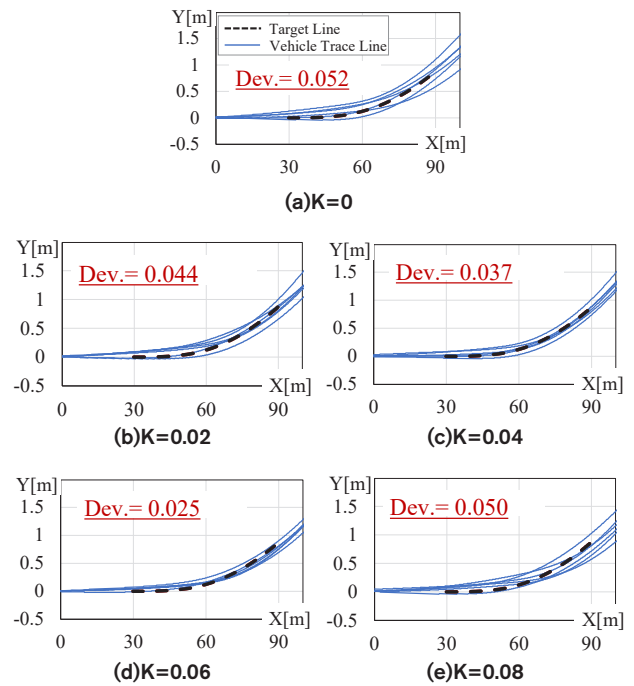


Fig.16 Line Trace Experimental Result

The variations in the line trace deviations under different pitch specifications, calculated from the measurement results of the travel trajectories of 25 drivers, are depicted in Fig. 17, with the horizontal axis representing K. It is evident that the variation in the line trace deviations tends to decrease as K increases. The thick solid line, which connects the average values obtained under the different specifications, indicates that the deviation is the smallest at K = 0.06 and then increases again at K = 0.08. Thus, the hypothesis established in this study was verified. Further, when K =

0.06 was added, the variation in the line trace deviations could be reduced by approximately 33%, as compared to that in the case where no pitch motion was added.

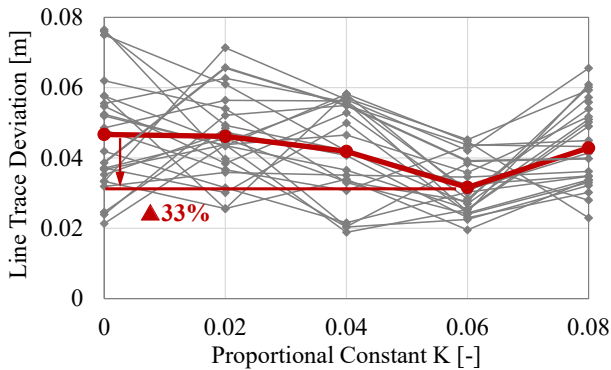


Fig.17 Line Trace Deviation Experimental Result

Subsequently, the change in the line trace deviation with increasing K was evaluated. There was no significant difference between the deviations for $K = 0$ and $K = 0.02$, because $K = 0$ does not generate any pitch motion; furthermore, even when $K = 0.02$, the driver cannot detect the movement before the steering angle reaches approximately 3° and the yaw movement is near 2° . Hence, it is likely that no visual information was provided within the blind steering section of 1° – 2° . Similarly, when $K = 0.04$, the driver can detect the pitch movement at a steering angle of approximately 1.5° ; therefore, even if it is not possible to completely cover the blind section, as in the case of $K = 0.06$, it is possible to provide visual information to the driver for approximately half of this section, thereby reducing the variation to a certain extent. However, when $K = 0.08$, it is conceivable that the pitch motion was detected by the driver before the steering angle reached approximately 1° . Generally, when the driver recognized the steering input and the vehicle actually commenced the yaw movement, there was an increase in the variation, as compared to that in the case of $K = 0.06$; this was attributed to the additional visual information that hindered accurate operation by the driver.

Finally, the effect of pitch motion on the average value of the line trace deviations was studied. In this study, the purpose of adding the pitch motion was to reduce the variation in the line trace deviations by providing drivers with visual information regarding the pitch motion, in addition to the steering reaction force information, on which drivers relied at the start of vehicle movement. Therefore, it is considered that the pitch motion required for this purpose does not affect the average value of the line trace deviations. The average values of the line trace deviations for the 25 drivers who participated in this study are shown in Fig. 18. It is confirmed that the addition of the pitch motion does not significantly alter the values.

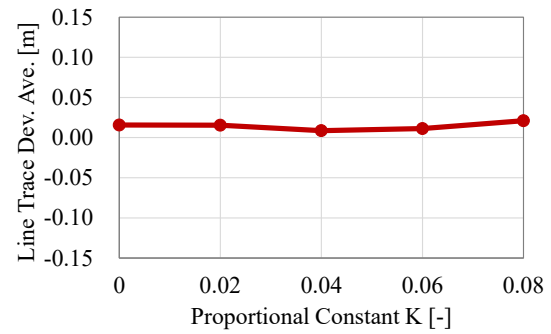


Fig.18 Line Trace Deviation Average Experimental Result

6. Summary and conclusion

Considering that one of the causes of the variation in the line trace deviations originates from the blind steering section in the minute steering angle range, it was confirmed that this variation can be reduced by adding a certain amount of pitch motion as visual information within the blind steering section.

Based on investigations of driver sensitivity to the pitch motion, the appropriate amount of pitch motion to be added was hypothesized and experimentally verified, and the quantitative effect of reducing the variation in the line trace deviations was extracted. In addition to the vehicle characteristics that enable drivers to drive appropriately, on average, in the minute steering angle range, which were clarified in our previous research, the other characteristics necessary for accurate driving were identified.

References

- (1) Mitsunori Tao et al., "A Clarification of Relationship of Steering Force and Yaw Characteristics to Line Traceability in Small Steering Angle", Transactions of the Society of Automotive Engineers of Japan Vol.51 No.3 pp.428-433 (2020)
- (2) Katsuhiko Fukui et al., "Technology for Improving Roll Feeling Based on Visual Characteristics", Transactions of the Society of Automotive Engineers of Japan Vol.40 No.5 pp.1185-1190 (2009)
- (3) Hideki Sakai et al., "Damping Force Control That Emphasizes Transient Turning Sensation", Transactions of the Society of Automotive Engineers of Japan Vol.43 No.3 pp.709-716 (2012)
- (4) Makoto Yamakado, "Study on 3-Dimensional Ideal Body Behavior by EV's Precise Braking and Driving Force Control", Journal of the Japan Society of Precision Engineering Vol.84 No.9 pp.765-768 (2018)
- (5) Masayuki Imamura et al., "Development of High-Performance Driving Simulator", Nissan Technical Review (Dynamic Performance Technology) No.83 pp.60-65 (2018)

Source

公益社団法人自動車技術会

自動車技術会論文集

Vol.52, No.2 文献番号:20214137

Authors



Mitsunori Tao



Naoya Machida



Yutaka Hayashi



Ken Nagasao

An Approach to Exploring Vehicle Motion to Enhance Ride Quality of Passenger

Mitsuhiro Makita* Akihiro Matsushita**
Yoshinori Kusayanagi*** Masahiro Miura***

Abstract A passenger's passive motion, as a result of the vehicle's motion, impacts ride quality. So, we built the methodology to explore desirable passenger body motion, under a fixed driving task, by employing inverse dynamics analysis based on optimal control. First, we embedded a passenger body model in a vehicle model using a set formula. Next, we developed a soft sensor model so that acceleration and jerk could be integrated into the cost function for minimizing by optimal control. Then, inverse dynamics simulation was becoming executable to derive vehicle motion meets to the aiming passenger's passive motion. Designing passenger motion will lead to the understanding of human perception on vehicle.

1. Introduction

This study aimed to establish a method for analyzing the effects of vehicle dynamics on non-driving passengers from the perspective of ride quality. With regard to ride quality, ride comfort is normally considered, which is affected by the vehicle motion in the direction perpendicular to the road surface. In the future, when autonomous driving becomes common, driving tasks will be conducted independently from that of humans. Therefore, to create a comfortable moving space, the vehicle dynamics in the direction parallel to the road surface will also be an important research subject.

The body of a passenger is moved by an inertial force that is generated by the acceleration of the vehicle. Therefore, the passenger may experience some discomfort due to the body movement. Although the application of an inertial force to the body of the driver, which is the result of his or her own driving style, might be a positive experience for some drivers, this force is usually a cause of discomfort for passengers. Hence, body movement must be restrained by the seat and a restraint device if high-acceleration motion, such as emergency evasion, is necessary. However, within the range of normal driving, it is desirable to enhance ride quality by devising the vehicle motion such that the effect of the inertia force on the passengers is reduced.

In this regard, it is important to determine how vehicle dynamics should be perceived to enhance the ride quality of passengers. The main factors related to vehicle acceleration are <path> and <speed>. Therefore, it is possible to mitigate the inertial load acting on the passenger by driving the vehicle along an appropriate path. As autonomous driving technology is becoming

increasingly advanced, setting the travel path is important for controlling vehicle dynamics. Research has focused on generating travel paths while considering the motion perception of the driver⁽¹⁾ and also on setting travel paths that can reduce the occurrence of car sickness among passengers, which can degrade the ride quality.⁽²⁾

As a research approach that focuses on passenger behavior, the use of a model that represents the behaviors of the bodies of passengers can be considered. In cases where the vehicle motion is known, a method for analyzing the behavior of passengers has been proposed,⁽³⁾ and the impacts of the travel path have been investigated.⁽⁴⁾

Previous value-creating research includes analyses of the timing of the inertial force application to the bodies of passengers and its effects on the autonomous posture control of passengers;⁽⁵⁾ the creation of the vehicle acceleration that stimulates the motion perception of passengers, enables passengers to recognize vehicle motion, and assists passengers in preparing their posture for motion has also been evaluated.⁽⁶⁾ The approach of focusing on the senses and body movement mechanisms, including car sickness, is gaining importance as the understanding of humans has become increasingly advanced.

Considering the aforementioned preceding research, the establishment of a method for exploring vehicle behaviors that suppress the body behavior of passengers and the amount of accompanying motion perception under an assumed travel scene can be expected. Therefore, to respond to such expectations in this study, the research that the authors have been conducting—the exploration of vehicle motion that optimizes the evaluation values set by applying optimal control—was designated as an inverse vehicle dynamics analysis method,⁽⁷⁾ and the scope of this method was

*Nissan Research Center Mobility & AI Laboratory **Customer Performance and Test Engineering Methodology Innovation Department
***AD/ADAS and Chassis Control System Engineering Department

expanded to include passengers.

If optimal control is employed, it is possible to “derive the desired vehicle motion and the control inputs for its realization by converting the matter into deriving the minimum value of the evaluation function.” In other words, “the characteristics of vehicle motion that can enhance ride quality can be extracted using the evaluation function by using various values that are considered to have impact on ride quality.”

The following section of this paper describes the case where inverse vehicle dynamics analysis is performed using optimal control and indicates that the analysis method is limited when applied for analyzing the behavior of passengers. Subsequently, technical solutions for overcoming these limitations are described. Lastly, the method for exploring the ride quality of a passenger is presented using transient motion as a case example and by describing the calculations, actual vehicle testing, and evaluations.

2. Ride quality analysis using inverse vehicle dynamics

If the forward vehicle dynamics analysis is considered as “set the control inputs and derive the corresponding vehicle motion,” inverse vehicle dynamics analysis⁽⁷⁾ can be considered as “reverse the cause-and-effect relationship, specify the desired vehicle motion, and derive the control inputs and vehicle motion that satisfy the specified motion.” For the inverse direction, the calculation method will differ depending on what is specified for the desired vehicle motion. In this study, the travel scene was specified as the precondition, the motion comfort of the passengers was explored, and inverse vehicle dynamics analysis was performed using optimal control (the schematic flow of the inverse vehicle dynamics methodology is shown in Fig. 1, and the variable names are provided in Table 1).

Optimal control uses the stage cost function $L(\mathbf{x}(t), \mathbf{u}(t))$, which is described using variables such as the input variables $\mathbf{u}(t)$ and state variables that represent the state of the subject of motion $\mathbf{x}(t)$. The objective is to derive the vehicle motion that yields the minimum value of the function. From a different perspective, the vehicle motion is designed using the stage cost function. The forms of functions that can actually be used for description are limited, such as the quadratic forms of the variables. However, vehicle motion can be designed at least using this function.

The travel scene is specified by setting the initial and terminal values of the state variables and control inputs in the vehicle motion task. In other words, the state of the vehicle motion is fixed at both ends (the analysis becomes a boundary value problem). Therefore, it is possible to derive the control inputs $\mathbf{u}(t)$ that minimize the stage cost function value.

Table.1 Variables and functions for optimal control

Notation	Description
$\mathbf{u}(t)$	Input Variables (1,..., p)
$\mathbf{x}(t)$	State Variables (1,...,m)
t_0 / t_f	Initial / Terminal Time
$\mathbf{u}_0 / \mathbf{u}_f$	Initial / Terminal value of Input Variables (1,..., p)
$\mathbf{x}_0 / \mathbf{x}_f$	Initial / Terminal value of State Variables (1,..., m)
$\mathbf{f}(\mathbf{x}, \mathbf{u})$	State Equation of motion (1,..., m)
$\lambda(t)$	Adjoint Variables (Lagrangian) (1,..., m)
$L(\mathbf{x}, \mathbf{u})$	Stage Cost
$J(\mathbf{u})$	Cost Function

p: Number of Inputs
m: Number of State Variables

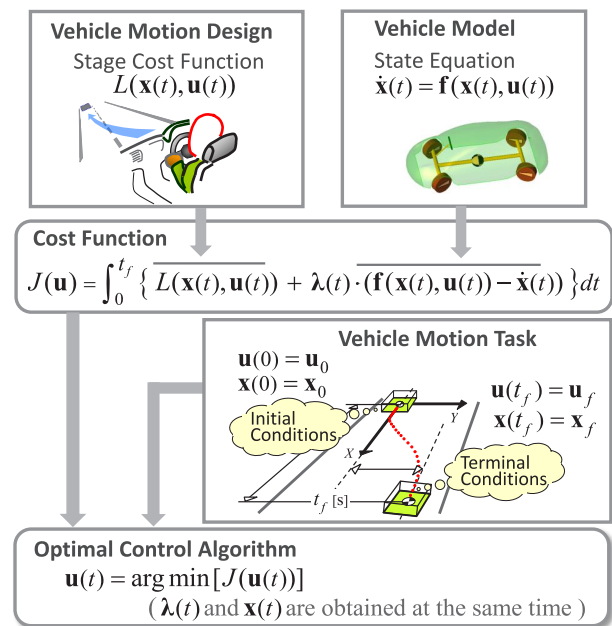


Fig.1 Schematic flow of the inverse vehicle dynamics methodology by optimal control: Ride quality is reflected to stage cost to describe motion design.

To evaluate the ride quality of passengers, in the vehicle model, reproducing the three-dimensional movements of the vehicle body in which the passengers ride is necessary. In addition, when formulating the optimal control using the ordinary variational principle, the vehicle model (in the form of a state equation) is added to the stage cost function using the adjoint variables. However, there are limitations in the model description for the evaluation function, which are related to the time integration of the added values. Specifically, in the description of the state equation, the differential quantities $\dot{\mathbf{x}}(t)$ of the state variable $\mathbf{x}(t)$ needs to be described <Explicitly> using the state variable, as shown in equation (2), and not in the form of equation (1):

$$\dot{\mathbf{x}}(t) = \mathbf{f}(\dot{\mathbf{x}}(t), \mathbf{x}(t), \mathbf{u}(t)) . \tag{1}$$

$$\dot{\mathbf{x}}(t) = \mathbf{f}(\mathbf{x}(t), \mathbf{u}(t)) . \tag{2}$$

In a previous study,⁽⁷⁾ the authors developed a vehicle model to express the vehicle dynamics accurately, including the load transfer among the wheels, while observing the restrictions for describing the equation. Table 2 and Fig. 2 present the vehicle model, including

the vehicle dynamics and state variables. The coordinate system is based on the unsprung position. For the tire characteristics, the response characteristics using the relaxation length were added to the simplified Magic Formula. Refer to the previous research of the authors⁽⁷⁾ for details regarding the vehicle model using equation (2).

Table.2 Variables and input functions of vehicle model

Notation		Description
State Variables $\mathbf{X}(t)$	$X_G(t), Y_G(t), Z_G(t)$	C.G. Position (Ground Coordinate)
	$V_\xi(t), V_\eta(t), V_z(t)$	C.G. Velocity (Vehicle Coordinate)
	$\Omega(t), \omega(t)$	Yaw Angle, Yaw Rate
	$\Phi(t), \phi(t)$	Roll Angle, Roll Rate
	$\Theta(t), \theta(t)$	Pitch Angle, Pitch Rate
Inputs $\mathbf{u}(t)$	$\alpha_i(t)$	Tire Slip Angle
	$\delta(t)$ $Acc(t)$	Front Tire Toe Angle Longitudinal(ξ) Acceleration

Subscript i : Wheel Position [Front $\rightarrow FR, FL$; Rear $\rightarrow RR, RL$]

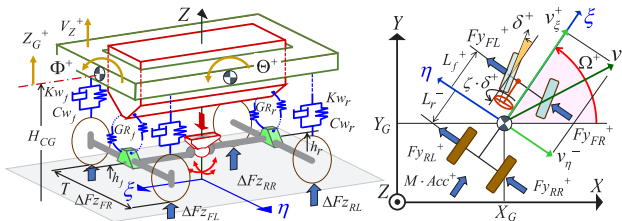


Fig.2 Two track and body motion vehicle model conforms to equation (2): Refer to author's previous research⁽⁷⁾

Using the inverse vehicle dynamics analysis described thus far, passenger ride quality enhancement is discussed. First, the passenger body model must be placed inside the vehicle body model. When doing so, passenger modeling is conducted using the form of equation (2), as in the case of the vehicle model.

Next, to deal with the ride quality in motion design, a value related to the passenger perception of the vehicle motion needs to be provided as a state variable $\mathbf{x}(t)$. For example, the vestibular organ recognizes the translational acceleration and angular velocity. Because, as shown in equation (1), acceleration is not a state variable but is rather the differential $\dot{\mathbf{x}}(t)$ of the state variable, acceleration cannot be incorporated into the stage cost function when creating the motion design policy. Thus, a method of converting acceleration into a state variable is required.

The abovementioned considerations suggest that two issues need to be addressed to apply the inverse vehicle dynamics analysis to passenger ride quality. The resolution of these issues is discussed in the subsequent section.

3. Expansion to passenger ride quality evaluation

3.1 Passenger body behavior modeling

The passenger body motion model was created while observing the restriction of <explicitly> expressing the

state variables, as shown in equation (2). If the inertia force of the passenger motion acts on the vehicle, it will not be possible to make <explicit> expressions using the state variables of the vehicle and passenger. Therefore, only the passive motion due to the inertia force of the vehicle motion is considered, and a model for the motion of the upper body in the lateral direction (roll), without separating the head portion, is proposed.

Table.3 Variables and parameters of passenger model

Notation		Unit	Description
State Variables	$\Phi_B(t), (\dot{\Phi}_B(t))$	[rad], [rad/s]	Upper Body Roll Angle (Angular Velocity) (Vehicle Body-Fixed Coordinate)
Temporal Variables	$X_S(t), Y_S(t), Z_S(t)$	[m]	Seating Pivot Point (Ground Coordinate)
	$F_{y_B}(t), F_{z_B}(t)$	[N]	Applied Force at Upper Body C.G.
Model Parameters	ξ_S, η_S, ζ_S	[m]	Seating Pivot Point (Vehicle Body-Fixed Coordinate)
	h_{BCG}	[m]	Height of Upper Body C.G. from Pivot
	I_B / m_B	[kg·m ²]/[m]	Upper Body Mass / Inertia
	K_B / C_B	[Nm/rad]/[Nm/(rad/s)]	Upper Body Roll Stiffness / Damping

$\Phi(t), \phi(t), \theta(t), \dot{\omega}(t), V_\xi(t), V_\eta(t), V_z(t)$ are the state variables of vehicle model⁽⁷⁾

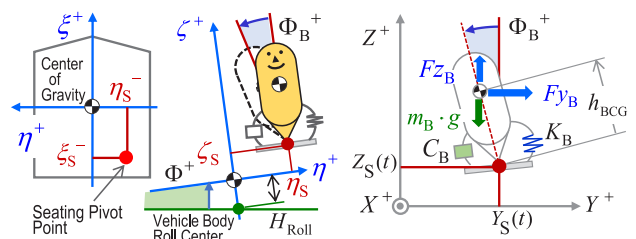


Fig.3 Passenger seating point configuration: Passenger upper body (including head) is simplified to a single inverted pendulum, then affected with vehicle motion.

As the first step, the inertia force of the vehicle motion, which is applied to the passenger, is expressed. The passenger seating point in the fixed coordinate system of the vehicle body as well as the rigid upper body model that has a pivot at that point are presented at the left and center of Fig. 3; the variables and constants that are related to the passenger model described below are listed in Table 3. Owing to the vehicle motion, the three-axis translational acceleration shown in equation (3) is applied to this pivot (terms that have little effect are omitted):

$$\begin{cases} \ddot{X}_S(t) = -V_\eta(t) \cdot \omega(t) + \dot{V}_\xi(t) - \eta_S \cdot \dot{\omega}(t), \\ \ddot{Y}_S(t) = V_\xi(t) \cdot \omega(t) + \dot{V}_\eta(t) + \xi_S \cdot \dot{\omega}(t) - (\zeta_S + H_{Roll}) \cdot \dot{\phi}(t), \\ \ddot{Z}_S(t) = \dot{V}_z(t) + \eta \cdot \dot{\phi}(t) - \xi \cdot \dot{\theta}(t). \end{cases} \quad (3)$$

In the next step, the force acting on the center of gravity (CG) of the upper body is expressed. To this end, it is necessary to derive the acceleration at the CG of the upper body. Here, the acceleration is given by the second-order differentiation of the upper body CG position (pivot point + effect of upper body roll posture angle), which is expressed using the coordinate system based on the ground. The force acting in the lateral and vertical directions, as shown on the right side of Fig. 3, are approximated as the acceleration by multiplying the

mass of the upper body and are expressed in equation (4):

$$\begin{cases} Fy_B(t) = m_B \cdot \frac{d^2}{dt^2} \left(Y_S(t) - h_{BCG} \cdot \sin(\Phi_B(t) + \Phi(t)) \right), \\ Fz_B(t) = m_B \cdot \frac{d^2}{dt^2} \left(Z_S(t) + h_{BCG} \cdot \cos(\Phi_B(t) + \Phi(t)) \right) \\ \quad + m_B \cdot g. \end{cases} \quad (4)$$

The equation of motion of the upper body about the pivot in the roll direction, caused by the forces Fy_B and Fz_B acting on the upper body CG, is expressed as equation (5). For the roll stiffness and damping, the effects of the supporting force acting between the passenger and the seat surface, friction, etc. are included as approximate values:

$$\begin{aligned} I_B \cdot \ddot{\Phi}_B(t) + C_B \cdot \dot{\Phi}_B(t) + K_B \cdot \Phi_B(t) = \\ Fy_B(t) \cdot h_{BCG} \cdot \cos(\Phi_B(t) + \Phi(t)) \\ + Fz_B(t) \cdot h_{BCG} \cdot \sin(\Phi_B(t) + \Phi(t)). \end{aligned} \quad (5)$$

In the last step, equations (3) and (4) are substituted into the equation of motion of the upper body (equation (5)) to determine the roll angle acceleration of the upper body $\ddot{\Phi}_B$ <explicitly>, as shown in equation (6):

$$\begin{aligned} \ddot{\Phi}_B(t) = \frac{1}{I_B + h_{BCG}^2 \cdot m_B} \cdot \\ (g \cdot \sin(\Phi_B(t) + \Phi(t)) \cdot h_{BCG} \cdot m_B \\ - K_B \cdot \Phi_B(t) - C_B \cdot \dot{\Phi}_B(t) \\ + \sin(\Phi_B(t) + \Phi(t)) \cdot h_{BCG} \cdot m_B \cdot \\ (\dot{V}_\zeta(t) + \eta_S \cdot \dot{\phi}(t) - \xi_S \cdot \dot{\theta}(t)) \\ + \cos(\Phi_B(t) + \Phi(t)) \cdot h_{BCG} \cdot m_B \cdot \\ (V_\xi(t) \cdot \omega(t) + \dot{V}_\eta(t) + \xi_S \cdot \dot{\omega}(t) - (\zeta_S + H_{Roll}) \cdot \dot{\phi}(t)) \\ - h_{BCG}^2 \cdot m_B \cdot \dot{\phi}(t)). \end{aligned} \quad (6)$$

The differential quantities of the state variables of the vehicle model, \dot{V}_η , \dot{V}_ζ , $\dot{\phi}$, $\dot{\theta}$, and $\dot{\omega}$, are included in the derived passenger model, as shown in equation (6). However, if equation (6) is converted from the equation of motion to the equation of state and if the converted equation and the vehicle model are considered as a set of simultaneous equations, replacement with the state variables can be performed such that the equation will converge to the form of equation (2). In this manner, the formulation of the optimal control used for the inverse vehicle dynamics analysis was realized.

3.2 Converting motion perceived by passengers into state variables

The physical quantities that can be expected to be related to the ride quality may include the translational and angular accelerations applied to the passenger body. However, as mentioned in the previous section, quantities other than the state and input variables cannot be

incorporated into the evaluation function.

The acceleration can be converted into a state variable by differentiating the equation of motion, which is expressed as a second-order differential equation, once more to a third-order differential equation (and to the fourth order for conversion to the jerk state variable). However, this increases the number of equations that need to be solved, leading to a calculation burden and making this approach unsuitable for inverse vehicle dynamics calculations. To address this problem, a state observer is used to derive the approximate state variables that can be incorporated in the evaluation function.

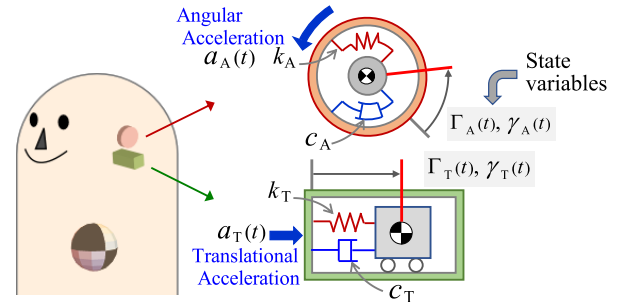


Fig.4 Acceleration and jerk detection with soft sensor (physical image of state observer) : Acceleration and jerk at the attached body are approximated to state variables.

To formulate optimal control by combining the vehicle and passenger models, the state observer is used as a soft sensor, as shown in Fig. 4. Specifically, the state equation described in equation (7) is employed, and the acceleration at the passenger body or at the measurement target position of the vehicle body is used as input $a(t)$. Utilizing this method, the translational acceleration, roll acceleration, and jerk at the mounting position can be observed as approximate state variables $\Gamma(t)$, $\gamma(t)$:

$$\begin{cases} \dot{\gamma}(t) = c \cdot \gamma(t) + k \cdot \Gamma(t) - a(t), \\ \dot{\Gamma}(t) = \gamma(t). \end{cases} \quad (7)$$

The approximation accuracy of the state variables is determined by setting the c and k values in equation (7). Fig. 5 shows the characteristics corresponding to different natural frequencies when the set values are altered. The set values are selected such that the gain, which represents the degree of approximation, is close to 1; this implies that the characteristics will be flat.

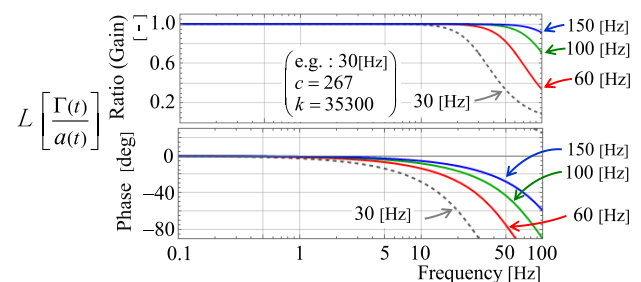


Fig.5 Frequency response characteristic of state observer: Four cases of translational and angular accelerations.

At this point, the effect of the approximation accuracy of the state observer in the inverse vehicle dynamics analysis is reviewed. In the lane change behavior analysis, discussed in the next section, the state observer was mounted at the vehicle body CG position, and calculations were performed such that the lateral acceleration at the vehicle CG was minimized. The calculation results are presented in Fig. 6. With regard to the stage cost function values, it is evident that there exists an appropriate value range within which the approximation accuracy can be increased by increasing the response frequency. In other words, if the response frequency is excessively high, the differential equation of the state observer stiffens the overall system to be solved. Thus, when calculating the values, it is necessary to consider the trade-off between accuracy and the accumulation of calculation errors.

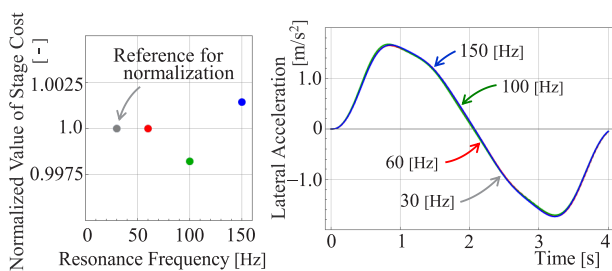


Fig.6 The degree of approximation of state observer (stage cost is quadratic value of lateral acceleration): There is an appropriate value for the resonance frequency of state observer.

Using the state observer described above, it was possible to approximate the values of the acceleration and jerk (which are related to the motion perceived by passengers) and to design the evaluation function by incorporating the approximated values in the evaluation function as state variables.

4. Exploring ride quality factors by designing passive motion of passengers

4.1 Designing motion for ride quality evaluation

Here, the method of exploring the vehicle motion to enhance the ride quality is specified. In this method, it is necessary to consider how to use the inverse vehicle dynamics to derive the minimum value of the evaluation functions, which include the amount of motion perception that occurs due to the body motion of the passengers.

An important aspect in the vehicle evaluation is to maintain identity, that is, “the condition that should be kept the same when making comparisons.” The logic of this matter has been presented in previous reports.⁽⁷⁾ When solving the functions in the inverse vehicle dynamics analysis, identity is ensured by setting the state variables and input variables for the initial and terminal motion conditions for the vehicle motion task shown in Fig. 1. Using this method, a motion design based on the evaluation functions is established.

The design flow can be classified into the following

three phases:

- (i) Set the travel scene to be evaluated (vehicle motion task).
- (ii) Set the ride quality factors in the evaluation function and calculate the optimal solution.
- (iii) Reproduce the optimal solution as the vehicle motion and conduct tests and evaluations.

The characteristics that can be obtained as the optimal solution are the control inputs and motion of the target vehicle. Therefore, when reproducing the vehicle motion in the last phase, the control inputs are provided to the actual vehicle, or the motion is applied to the passenger using equipment that can reproduce the acceleration space (as shown in Fig. 7).

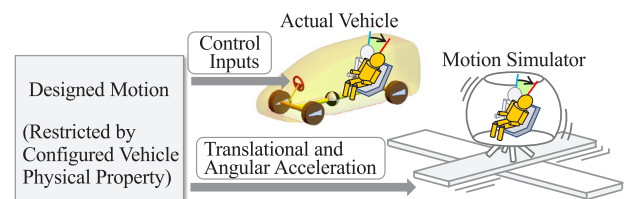


Fig.7 Methodology to construct acceleration space

In the first phase, i.e., setting the travel scene for ride quality evaluation, there will be no significant difference in the results of the evaluation function related to motion perception if the travel scene is the steady driving mode; however, the results may depend on the types of control inputs (such as steering only and the addition of active acceleration/deceleration using the brake/accelerator). Therefore, in this work, transient motion is utilized as the travel scene example because it is easier to obtain the difference in motion perception under this case than in the other situations (Fig. 8).

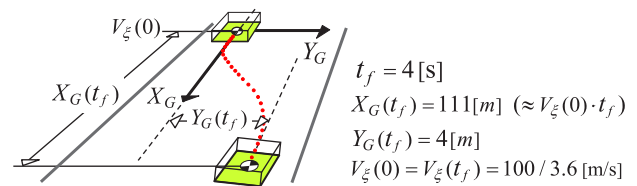


Fig.8 Example of vehicle motion task: Lane change as a typical transient vehicle motion scene.

Next, the design specifications for the vehicle motion in this example are presented in Table 4. In the vehicle motion task, a lane change scene was set, in which the following terminal conditions were returned to straight-line travel (=0): the control inputs and the track angle and yaw angle velocity, which are the state variables for plane motion on the road. Assuming passenger ride quality enhancement, the following specifications were set for the evaluation functions: the steering control input minimizing specification V0, assuming the ride quality of the driver, and the body roll angle acceleration minimizing specification R1. For comparison, specification R2 was also set; R2 represents the body roll angle

acceleration minimization specification added with the conditions for returning the roll angle acceleration and angle velocity to zero at the terminal.

Table.4 Vehicle and passenger motion design specification: Three condition to exemplify design methodology.

Stage Cost *		Terminal Condition (Motion Task)			Symbol
Subject	Roll Angular Acceleration	Vehicle		Passenger	
		Control Input	Plane Motion	Body Roll Motion	
Driver (Vehicle)	Vehicle Body	Steering Angle & Angular Velocity return to 0	Track Angle & Yaw Rate return to 0	Arbitrary State	V0
			Lateral Velocity of C.G. return to 0		
Passenger	Passenger's Body	Same Speed as initial condition	Set C.G. Position	Angular Acceleration & Velocity back to 0	R2

* Applied quadratic form of state and/or input variables

4.2 Calculating passenger acceleration space based on design

The calculations were performed in accordance with the motion design specifications. Here, the characteristics of the passenger body model need to be determined (the settings of the vehicle characteristics are the same as those mentioned in a previous report by the authors⁽⁷⁾). Because the passenger model is simple, the accuracy improvement effect will be small, even if the thoroughness of the model characteristics definition is improved. Therefore, for the characteristic values of the shape and mass, values close to those of the actual vehicle test evaluator, as mentioned in subsection 4.3, are used. The body stiffness, K_B , near a lateral acceleration of 2 m/s^2 was set by referring to the distribution results of the measurements of the test subjects ($n = 15$). Examples of the stiffness measurements are presented in the box-and-whisker plot in Fig. 9. The value when the passenger was facing down and reading text was used for the calculations, and the passenger was considered to be seated on the left side of the rear seat.

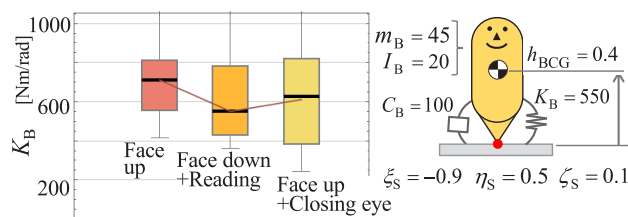


Fig.9 Passenger body roll stiffness (box-and-whisker plot) and other characteristics: Passenger model parameters were fixed from subject measurement ($n=15$) and estimation.

The settings necessary for the calculation were implemented. Thereafter, inverse vehicle dynamics analysis was performed to calculate the control inputs and vehicle motion (Fig. 10 shows the path of the vehicle CG) that minimizes the evaluation functions while satisfying the terminal conditions.

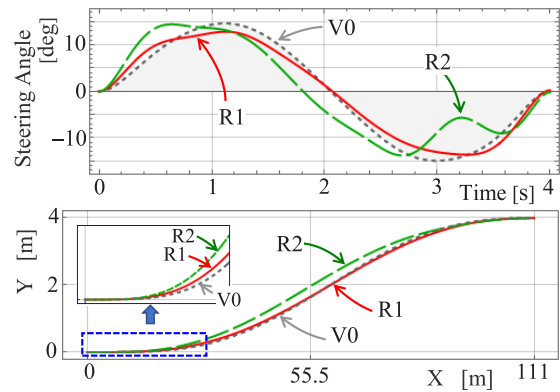


Fig.10 Steering pattern and vehicle C.G. path (with enlarged view) to satisfy design specification of vehicle and passenger motion: Inverse vehicle dynamics analysis fixes both input and state variables simultaneously.

The calculated optimal vehicle motion, lateral acceleration of the vehicle CG, and roll posture angle of the passenger body Φ_B are depicted in Fig. 11. According to the calculation results, the transition of V0 appears as a sine function. Compared to V0, the peak value of the passenger behavior is suppressed for R1 (in which case the passenger behavior is optimized). In R2 (in which case additional terminal constraints are implemented), the posture angle converges to a certain value at the end of the calculation.

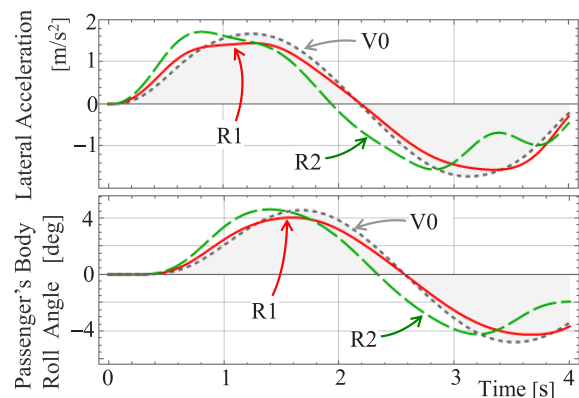


Fig.11 Vehicle and passenger motion to satisfy the design specification: Calculated results.

4.3 Evaluation using the acceleration (vehicle) space

In the test method, a steering robot was mounted on a vehicle to reproduce the calculated steering waveform such that acceleration was applied to the passenger seated on the rear seat. To correspond to the actual environment, a term that represents the effects of slopes was included in the vehicle model when performing the calculations. The test values were compared with the calculated values for the last 4 seconds.

The passenger has a body build close to the average of the measurement results of the passenger characteristics and is an expert in vehicle dynamics evaluation. The passenger can recognize the start of the vehicle motion based on the inevitable driving noise of the steering robot. However, it should not be easy for the passenger to

predict the vehicle motion because the passenger can only view the external environment through the surrounding view. Therefore, the test environment should be similar to that in the passive motion evaluation. The transitions in the passenger posture were estimated using the movement detected by the displacement sensor attached to the rear of the neck.

The test results are presented in Fig. 12 in a manner that corresponds to the calculation examples (Fig. 11). It can be considered that the reproducibility of the acceleration space was ensured. The deviation between the passenger posture transition and the calculated value (the results in the figure were multiplied with a coefficient of 2.0) is attributed to the differences between individual evaluators, as the passenger model characteristic values in Fig. 9 were used for the calculation (the values differ by a factor of approximately 2 for some data within the quartile range). It is judged that the relative relationship between the specifications is in-line with the predictions based on the calculations.

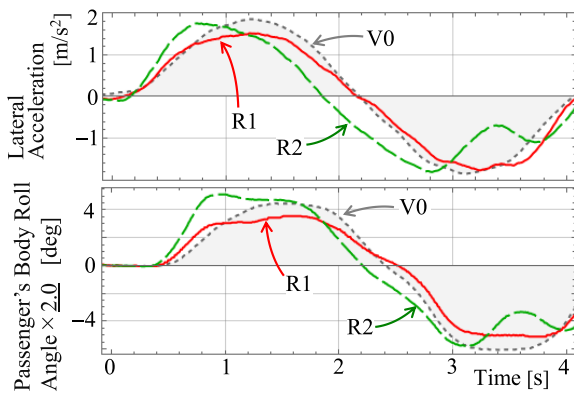


Fig.12 Vehicle and passenger motion of actual vehicle test: Every data curve was averaged ($n=5$).

In the subjective evaluation, it “seems that the motion is smooth while the body posture transition is large” with specification V0, whereas it “seems that the body roll posture transition is small” with specification R1 (in which the body roll angle acceleration is suppressed). In other words, the result that “the body seems to have moved along with the vehicle motion” was obtained. However, in the case of specification R2 (in which additional terminal constraints for the roll posture are implemented), the evaluation “movement at the early stage of the motion was large compared to V0” was obtained. In addition, the evaluation that “while the high-frequency motion was somewhat noticeable, it was possible to feel the load reduction due to the suppressed body motion” was obtained for the “body roll suppression” terminal condition, with the objective of maintaining body posture. In summary, it was possible to parameterize the ride quality in terms of both the measurements and subjective evaluations using the passenger passive motion design.

5. Considerations for exploring ride quality

In the passenger body model, increasing the degree of freedom (such as by separately defining the head portion) is possible. However, this will make it difficult to determine the appropriate model characteristic values, such as the stiffness at the neck portion, even if the scope of the model is limited to passive motion. It is assumed that passengers will perform various activities and be in various states in the vehicle. Therefore, in addition to addressing the complexity of the passenger model, determining the settings of the characteristic values of the model needs to be resolved in future research.

However, the motion perceived by the passenger cannot be mechanically calculated based on the body model. Thus, it may be important to add a model that represents the human inner sensory characteristics such that the evaluation function is configured using the actual perception values. Fig. 13 shows the body behavior (calculated values) under the specifications, where the body roll angle acceleration is used as the evaluation function. R1 does not include terminal constraints, whereas R2 has terminal constraints. Compared to specification R1, specification R2 causes more lateral movements during the intermediate test time. It is clear that the body roll movement must occur early to control the body behavior at the terminal. Although the roll motion is suppressed, the translational acceleration is increased. Therefore, the mechanism of the perceptual recognition of translational and rotational motions must be considered.

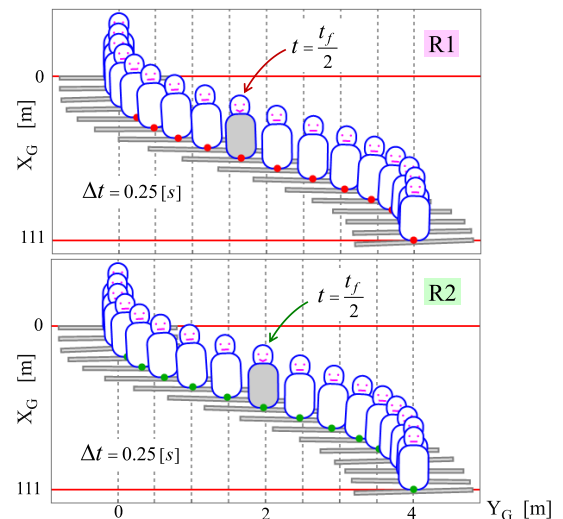


Fig.13 Passenger upper body posture transition: Earlier motion generation is required for terminal posture control, then needs quick initial motion, too.

The degree of freedom of the motion design depends on the limitations in the form of the evaluation function. The variables that can be incorporated are typically limited to a combination of quadratic forms. In addition, in the travel scene expanded to multiple control inputs,

the terms corresponding to each control input must be set in the evaluation functions. Otherwise, simultaneous optimization is not possible (ensuring orthogonality of the terms). To advance research on ride quality, the flexibility of expressing the evaluation functions needs to be improved.

6. Conclusion

In this study, the effects of vehicle dynamics on passengers were considered from the perspective of ride quality, and a <methodology for testing/evaluation> for improving ride quality was presented herein. Passenger ride quality can be improved by determining the vehicle motion if it is assumed that the ride quality depends on the passive motion load applied to the body and on the perception caused by the vehicle motion within the acceleration space.

Therefore, the desirable motion was set as the evaluation function, and motion design was attempted using inverse vehicle dynamics analysis, where the vehicle motion was derived from the optimal control. An observer was established to incorporate a passenger body model which estimate the load, and acceleration which used to estimate the motion perceived by passengers into the evaluation function. In this manner, an inverse dynamics analysis that combines the passenger and the vehicle was realized.

It is necessary to subjectively evaluate whether the form of the evaluation function successfully indicates the improvements in the ride quality of the designed vehicle motion and to also investigate the passengers' perception of vehicle motion. For these purposes, this paper presents an evaluation flow using a specific example. In the first phase, a travel scene is assumed. In the next phase, the vehicle dynamics are designed using a candidate evaluation function setting. In the last phase, evaluation is performed by placing a passenger in the designed acceleration space (the actual vehicle in this study).

This research will be extended such that the "vehicle motion gentle to the passenger" can be incorporated into the technological developments in autonomous driving via control logics and artificial intelligence, among others.

(Addendum): The tests conducted in this study were examined and approved by the Experimentation Ethics Committee of Nissan Motor Co., Ltd. The tests were

conducted after obtaining informed consent from the participants.

References

- (1) Tatsuya Yoshimoto, Takanori Fukao, Yasuyoshi Yokokohji, Hiroshi Inou: Path Generation of Lane Change in Dynamic Environments Considering Characteristics of Driver's Operation, Transactions of the JSAE, Vol.47, No.2, p.633-638 (2016)
- (2) Takahiro Wada: On Motion Sickness in Highly Automated Vehicles, Proceedings of the JSAE Annual Congress (2016), 20165263
- (3) Katsunori Yamada, Harutoshi Motojima, Yuichi Kitagawa, Tsuyoshi Yasuki: Investigation of Relations between Occupant Kinematics and Supporting by the Seat in Lane Change Maneuvers, Proceedings of the JSAE Annual Congress (2016), 20165176
- (4) Makoto Yamamoto, Tadashi Yamamoto, Shuji Nishiyama: Proposal for a Transition Curve with Smoothly Changing Curvature Using Multiple Clothoid Curve, Transactions of the JSME, Vol.83, No.852 (2017)
- (5) Tohru Yoshioka, Masato Abe, Makoto Yamakado, Yoshio Kano, Yusaku Takeda, Kazuhiro Takemura, Takatoshi Tsukano, Fuminori Kato, Daisuke Umetsu: Analyses on Vehicle Dynamics Improvements from Human Aspects with G-Vectoring Control, Proceedings of the JSAE Annual Congress (2016), 20165250
- (6) Alexander Lange, Martin Albert, Karl-Heinz Siedersberger, Klaus Bengler: Ergonomic Design of the Vehicle Motion in an Automated Driving Car, 6th International Conference on Applied Human Factors and Ergonomics (AHFE) (2015)
- (7) Mitsuhiro Makita: A Solution to Apply Load-Transfer Including Vehicle Model to Optimal Control Formulation, Transactions of the JSME, Vol.81, No.826 (2015)

Source

公益社団法人自動車技術会
自動車技術会論文集
Vol.50, No.5 文献番号:20194687

Recipient



Mitsuhiro Makita



Akihiro Matsushita



Yoshinori Kusayanagi



Masahiro Miura

Development of driving assistance system in multi-lane highway

Yohei Taniguchi* Katsuhiko Degawa* Seiji Tokunaga*
Shimpei Nagae** Koji Sasaki**

1. Introduction

A new driving assistance system that guides a vehicle until reaching the specified highway exit and enables hands off under each certain condition has been implemented on a production vehicle. The system can guide a vehicle through a multi-lane highway, working in tandem with the navigation-system-planned route. It also can operate in hands off mode, provided the driver consistently monitors the objects and events and responds immediately to operate the steering wheel in response to the road, traffic and vehicle conditions. The details of this system are described in this paper.

2. Function overview

This system offers navigation linked driving such as merging on to a highway when destination is set in the navigation system. When the navigation linked driving is initiated, system supports driving through interchanges and assists overtaking another vehicle until reaching the relevant exit. Provided that the driver always attends to the road ahead and can operate the steering wheel with certainty and immediately in response to the road, traffic, and vehicle conditions, the system operates with hands off with in the same lane and provides wide range driving maneuver support to the driver. In addition, using the navigation data and information of the surroundings from a 360° degrees sensing, the system determines an appropriate lane-change starting point for branching or overtaking whilst following the planned route, and proposes the relevant actions to the driver. Lane-change assistance is initiated by the driver when both hands are placed on the steering wheel and the switch to approve the proposal is operated. An operational image is shown in Figure 1.

3. Sensor configuration

This system integrates and uses seven cameras, five radars, 12 vehicle-mounted sonars, a global navigation satellite system, and 3D high-definition map data to collect information from the surroundings (i.e., not only from the front but also the right, left, and rear of the

vehicle) and determines the correct position on the road. The 3D high-definition map data include information detailing the road structure, the number of lanes, and the positions of merging points, branching points, and intersections. These information allow system control that foresee the road structure ahead and realize smooth driving as that of an experienced driver. A sensor mounting configuration and a 360° sensing image diagram are presented in Figures 2 and 3.

4. Driving assistance on a multi-lane highway

Acquiring information pertaining to the lanes ahead is one challenge in realizing lane-change assistance.

At the start of the lane change, the camera may not be able to collect comprehensive lane information for the point where the lane change ends. Accordingly, if information is only received from the camera, the appearance of a dividing line forbidding lane changes during the lane change (or other operations) may prevent the lane change. Meanwhile, because the 3D high-definition map data include lane-level data (e.g., curvatures and dividing lines), the acquisition of road shapes beyond the camera's detection range allows lane-change opportunities to be judged by considering the section of any lane between the start and end points.

In this system, lane-level information included in the 3D high-definition map data are used to create the route plan such that the system can propose changing lanes at a suitable timing for the purpose of providing passing assistance and for proceeding along the route recommended by the navigation system.

5. Conclusion

In this development project, the navigation system, 360° sensing, and 3D high-definition map data were combined to realize a driving assistance system for use on multi-lane highways. This technological development helps advance driving assistance technology and also introduces possibilities for further developments.

*AD/ADAS Advanced Technology Engineering Department

**Customer Performance and Test Engineering Methodology Innovation Department

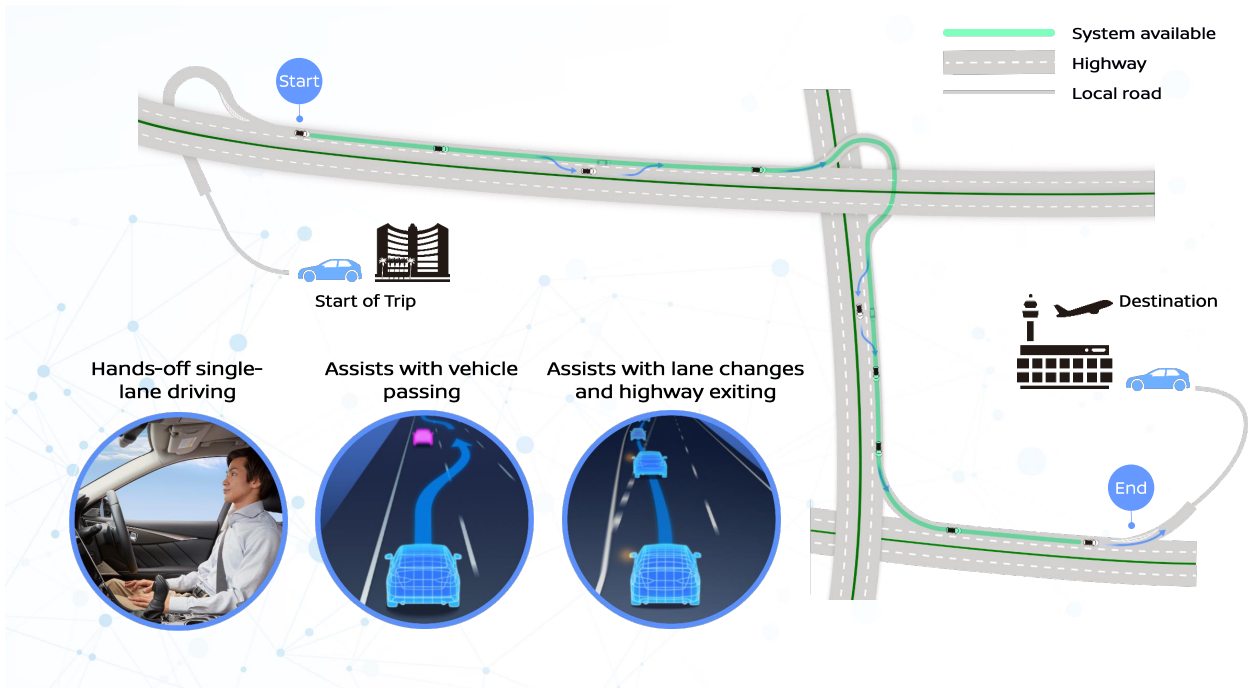


Fig.1 System Overview

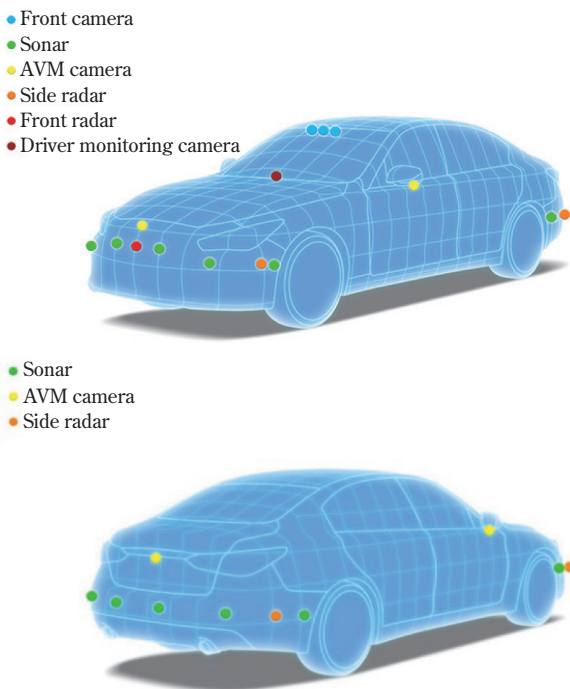


Fig.2 Onboard technology

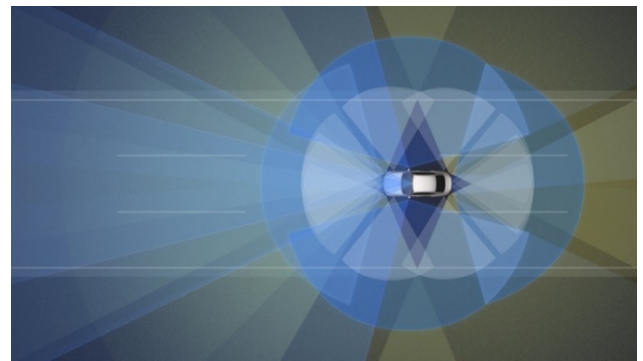


Fig.3 360 degree sensing

Source

公益社団法人自動車技術会
自動車技術
Vol.75 No.06

Recipient



Yohei Taniguchi



Katsuhiko Degawa



Seiji Tokunaga



Shimpei Nagae



Koji Sasaki

Strength evaluation of CFRP tank based on meso-scopic zooming analysis

Shinichiro Takemoto*

Abstract For stringent cost reduction with sufficient safety of a high pressure hydrogen tank made by carbon fiber reinforced plastic (CFRP) installed in a fuel cell vehicle, a method to precisely predict the burst pressure of the tank has been intensely required. CFRP layers in the tank consist of complicated meso-structures with carbon fiber bundles and matrix resin, in which crimps of the bundles are stacked by a filament winding process. We propose a method to predict the burst pressure by zooming analysis of conventional axisymmetric continuum model of the whole tank with the meso-scale model. The proposed method is validated through the burst test of tank with accurate prediction of the burst pressure by means of the carbon fiber rupture in the meso-scale model.

1. Introduction

To promote the widespread use of fuel cell vehicles (Ohnaka, 2009), there are growing demands for reducing the weight and price of high-pressure hydrogen fuel tanks (Council for a Strategy for Hydrogen and Fuel Cells, 2019). To withstand a pressure of 70 MPa, a fuel tank employs a liner, which seals the hydrogen inside an inner aluminum or plastic tank composed of carbon fiber-reinforced plastic (CFRP) laminated using the filament winding (FW) method (Maki et al., 1970). One effective means of reducing the weight and price of these tanks is to minimize the amount of fiber used by optimizing the laminated structure; to this end, a highly accurate method for predicting the tank burst pressure is required.

The fracture strength of tanks laminated using the FW method is governed by the local fracture phenomenon that occurs in the meso-structure composed of carbon fiber bundles and matrix resin. An approach equivalent to a conservative strength evaluation method (High Pressure Gas Safety Association, 2016) based on macro-stress criteria, such as that employed for steel tanks, has not been established thus far; therefore, the safety and reliability are assessed by performing a series of tests (Takehana, and Ota, 1997) or (United Nations, 2013) by spending considerable amounts of time and money to impose loads similar to actual loads on real tanks. Although there exists a strong desire to replace actual tank tests with computer simulations, a method for appropriately predicting the tank damage and fracturing has not been presented thus far.

To date, various studies have focused on the strength evaluations of CFRP tanks. The related reports include the evaluation based on laminate theory in the macroscale

structure of CFRP layers (Iida, 1978), the comparison between laminate theory and FEM analysis of axisymmetric shell model (Hirase et al., 1991), and the evaluation of tank with uniform stress surface in dome part (Liu et al., 1997). In each of these studies, the prediction accuracy for tank rigidity and strength was improved within the framework of continuum mechanics. In addition, the fracture mechanism has been clarified experimentally (Arai et al., 2007). Although these methodologies are effective for evaluating the macroscopic deformation in tanks, it is difficult to accurately evaluate the fracture phenomenon caused by the increase in the local stress and strain that occurs in a meso-structure comprising carbon fiber bundles and resin. Meanwhile, the evaluation for viscoelastic constitutive equation of CFRP laminates using homogenization method have tried the combination of the micro-analysis of CFRP unit cells and the macro-analysis of the entire member (Arai et al., 2008). However, thus far, fracture evaluations for actual-size components, including tanks, have not been achieved.

In the authors' previous study (Takemoto, Yoshikawa, 2019), assuming that the CFRP tank would be destroyed by tensile forces acting in the circumferential and/or axial directions, a biaxial tensile test and finite element analysis were conducted using a test piece with crossed fiber bundles; furthermore, the factors governing the tensile strength development mechanism in the CFRP helical layer were clarified. This current report presents a method for predicting the burst pressure of a high-pressure hydrogen tank designed for fuel cell vehicles by elucidating the factors that control the strength mechanism and using mesoscopic zooming analysis. Hydraulic burst tests were performed on Type 3 small pressure tanks designed for convenient fracture evaluations, and it was demonstrated that this method can predict the test results with high accuracy.

*Advanced Materials and Processing Laboratory

2. Hydraulic burst test on Type 3 small pressure tanks

2.1 Preparation of pressure tank

To verify the strength evaluation method developed in this study, Type 3 small pressure tanks with CFRP laminates were prepared using the FW method and subjected to a hydraulic burst test. The liner, designed to encapsulate hydrogen in the tank, was composed of A6061-T6 aluminum alloy processed through rolling and spinning (Fig. 1). The wall thickness of the tank body (cylindrical part) was $d = 2$ mm, and the thickness of the dome part was increased through the molding process to enhance its strength, such that the burst could easily occur in the cylindrical part; this enabled a convenient evaluation of the CFRP strength. A helical layer (Fig. 2 (a)) and a hoop layer (Fig. 2 (b)) were applied to this liner using the FW method, followed by the application of the thermoset.

The material constants of the members, as presented by the manufacturers, are listed in Table 1. The carbon fiber bundle was T700SC-24000-50C from Toray, with a width of 10 mm and a thickness of 0.5 mm. The matrix resin was prepared by blending the main agent epoxy resin (jER828 from Mitsubishi Chemical) with a curing agent (HN2200 from Hitachi Kasei) and an accelerator (Kaorizer No. 20 from Kao) at a mass ratio of 100:10:1 and adjusting the volume content of the carbon fibers to $V_f = 55\%$. After laminating, thermosetting was performed by arranging the tanks in the horizontal direction in a curing furnace and maintaining them at 80°C for 2 h and then at 110°C for 3 h while rotating.

The CFRP layer structures of the four tanks used in this study are described in Table 2. The CFRP layers are

referred to as the first, second, third, and fourth layers, from the innermost layer on the liner side. The thickness of each layer was 0.5 mm. The helical layer exhibited fiber orientation angles of $\pm 30^\circ$ with respect to the central axis of the tank. Tank No. 1 had a helical layer alone, Tank No. 2 had a hoop layer with a fiber orientation angle of 90° inside the helical layer, Tank No. 3 had a hoop layer on the outside, and Tank No. 4 had an additional hoop layer on the outside. In addition, for each of the tanks, hoop winding reinforcement was applied to the bosses at both ends to prevent water leakage from the threads due to the increased water pressure. Photographs of the tanks are provided in Fig. 3

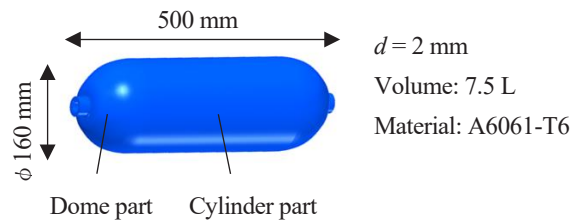
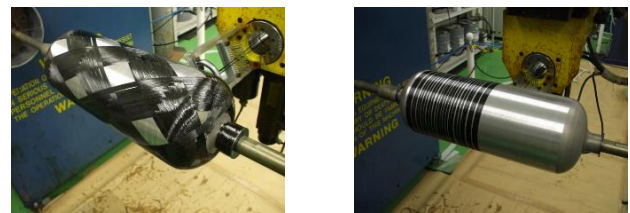


Fig. 1 Aluminum liner.



(a) Helical layer (± 30 degree). (b) Hoop layer.

Fig. 2 CFRP layer manufactured by filament winding.

Table 1 Material properties.

	Carbon fiber	Matrix resin	Aluminum liner	Steel plug
Young's modulus [GPa]	230	3.75	70.0	210
Poisson ratio	0.26	0.41	0.33	0.30
Elongation [%]	2.1	2.6	12	-

Table 2 Variation of CFRP layers of tanks for evaluation.

Tank No.	CFRP 1st layer	CFRP 2nd layer	CFRP 3rd layer	CFRP 4th layer
1	Helical ± 30 degree			
2	Hoop	Helical ± 30 degree		
3	Helical ± 30 degree		Hoop	
4	Helical ± 30 degree		Hoop	Hoop



(a) Tank No.1. (b) Tank No.2. (c) Tank No.3. (d) Tank No.4.

Fig. 3 Type 3 tanks for burst test.

2.2 Hydraulic burst test

The burst test was performed on the prepared tanks as follows. The test pressure was applied as a static load in steps of 0.75 MPa for 4 s or more per step, and the water pressure was increased such that the preset pressure reached ± 0.05 MPa. The fiber-direction strain of the carbon fiber bundle on the tank surface was also measured. The positions at which the strain gauges were attached are depicted in Fig. 4. On one surface, seven gauges were attached at equal intervals on the geodesic at an inclination of 30° with respect to the central axis, which is the orientation angle of the helical layer; on the other surface, seven gauges were also attached at equal intervals on the meridian. The strain gauges (KFG-5-120-C1-11 L5M3R, Kyowa Electronic Instruments) were used for one-way measurements and attached in the direction of the outermost fiber bundle. For Tanks No. 1 and No. 2, the gauges were attached at an inclination of 30° with respect to the central axis along the fiber bundle of the outermost helical layer, whereas for Tanks No. 3 and No. 4, they were attached along the outermost hoop layer in the circumferential direction. A photograph of the strain gauges attached to Tank No. 4 is provided in Fig. 5 as an example

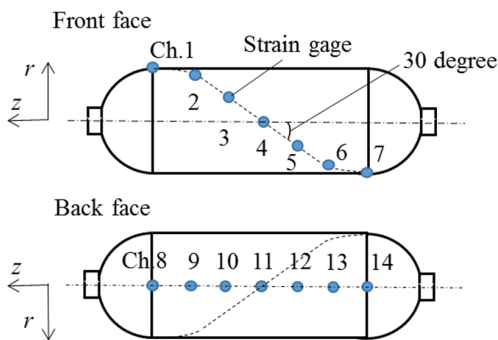


Fig. 4 Locations of strain gages.

The measured burst pressure was 12.0, 26.3, 24.8, and 35.3 MPa for Tanks No. 1, 2, 3, and 4, respectively. The states of the broken tanks after the hydraulic burst test are shown in Fig. 6. As indicated by Fig. 6 (a), both the liner and helical layers of Tank No. 1 were fractured at the center of the body. For Tank No. 2, shown in Fig. 6 (b), the liner was broken at the center of the tank, whereas the damage on the outermost helical layer was limited. When the CFRP layer was disassembled, the hoop layer, which was the innermost layer at the center of the cylinder, was fractured along the axial direction, as presented in Fig. 6 (c). In Tanks No. 3 and No. 4, the hoop layer, which was the outermost layer, was broken along with the liners at the centers of the cylinders. In Tank No. 4, the aluminum liner was considerably deformed as the burst pressure increased.

3. Prediction of burst pressure using axisymmetric continuum model

3.1 Axisymmetric continuum model

The burst pressures of the tanks subjected to the burst test were predicted via macroscale simulations through



Fig. 5 Strain gages on tank No. 4 set up.



(a) Tank No.1.



(b) Tank No.2.



(c) Tank No.2 (Hoop layer from inner side).



(d) Tank No.3.



(e) Tank No.4.

Fig. 6 The tanks listed Table 2 after burst tests are shown. Both CFRP layers and aluminum liner are broken at center of cylindrical part at all the tanks. The CFRP helical layer is broken at tank No.1. The CFRP hoop layer of inner side is broken at tank No.2. The CFRP hoop layer of the most outside is broken at tank No.3 and No.4.

the axisymmetric continuum modeling of the tanks (Kim et al., 2017). The CFRP layer was composed of an orthogonal anisotropic linear elastic material, and its material constants were calculated based on those of the carbon fiber and resin shown in Table 1, according to the law of mixtures (Maki et al., 1970). The helical layer was modeled based on the laminate theory (Vasiliev and Morozov, 2001), assuming that the layers with fiber orientation angles of $+30.0^\circ$ and -30.0° were laminated with the same thickness. The local increase in strain due to the crossing of the fiber bundles caused by the FW method could not be evaluated. The stress-strain constitutive law of the aluminum liner is based on the isotropic elastoplastic solid, as shown in Fig. 7. In addition, because the steel plug did not break even after the burst test and possessed sufficient strength and rigidity, it was selected as an isotropic elastic body, whose material properties are listed in Table 1.

The axisymmetric finite element model used for the analysis and its boundary conditions are depicted in Fig. 8; those related to Tanks No. 1, 2, 3, and 4 are shown in Figs. 8 (a), (b), (c), and (d), respectively. Half of each tank was modeled on the r - z plane, while considering symmetry around the z -axis. At the boss part at the end of the liner, the plug and CFRP hoop layer that reinforced the boss part were completely connected, and the displacement U_r in the radial direction (r -direction) of the tank was constrained by the central axis of the plug. Moreover, each tank was set to be vertically symmetrical with

respect to the central surface, and the displacement U_z in the z -direction was constrained along the central surface. The internal pressure of the tank was increased in increments of 0.750 MPa. In Figs. 8 (a)–(d), the right side presents a magnified view of the layers of the cylindrical part, from the inner aluminum liner to the CFRP first layer, to the second layer (a), to the third layer (b) and (c), up to the fourth layer (d). The aluminum liner, hoop layer, and helical layer were all modeled with triangular primary elements. The CFRP helical layer increases in thickness from the equator to the boss in the dome section. This change was set according to a theoretical formula (Kim et al., 2017). Furthermore, because the fiber orientation angle changes continuously, different material constants were set for the orthogonal anisotropy of each element. Tank No. 1 had 17,842 elements and 9,551 nodes, Tanks No. 2 and No. 3 both had 19,171 elements and 10,216 nodes; and Tank No. 4 had 20,444 elements and 10,853 nodes.

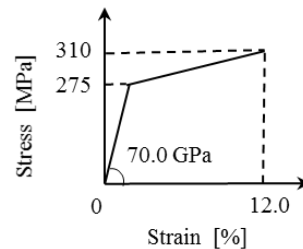


Fig. 7 Constitutive law of aluminum liner.

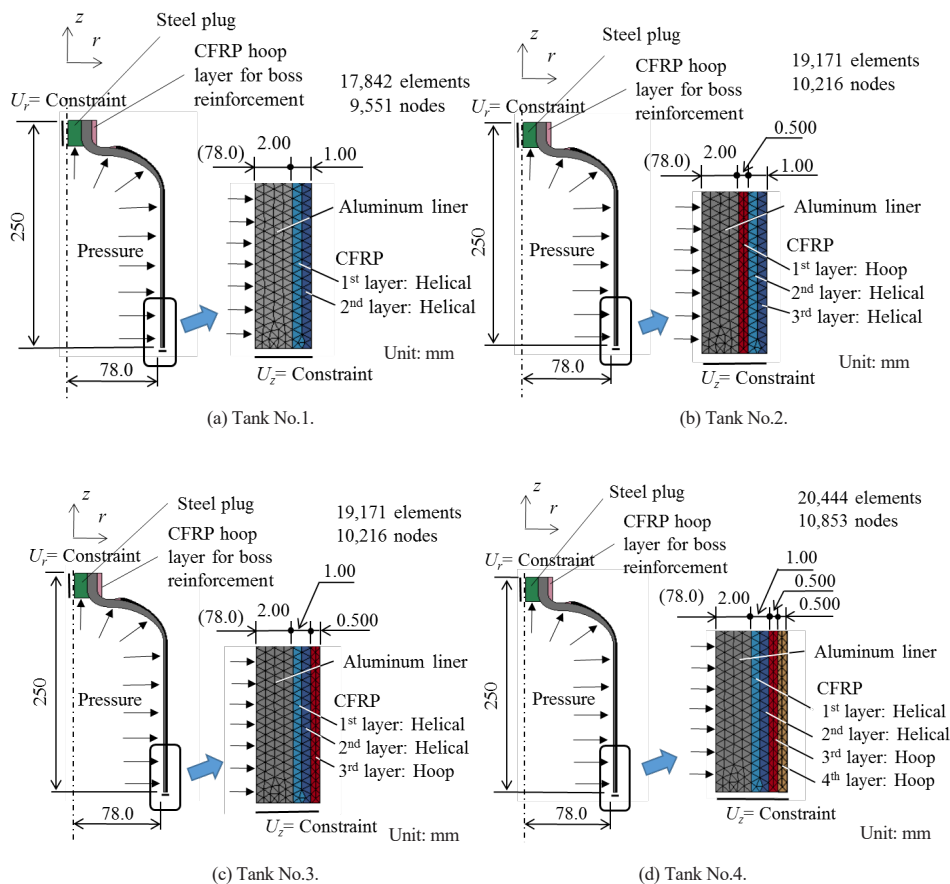


Fig. 8 Axisymmetric analysis models of tank.

3.2 Analysis result

The analysis results for Tanks No. 1, 2, 3, and 4 are presented in Figs. 9 (a), (b), (c), and (d), respectively, along with the experimental results from Section 2. The horizontal axis represents the pressure inside the tank, and the vertical axis represents the strain. The green squares indicate the strain values measured during the tank burst test. Among the measurement positions shown in Fig. 4, the value at the position closest to the burst start point shown in Fig. 6 was plotted up to the burst pressure. The solid line indicates the analysis results obtained using the axisymmetric continuum model. The black, blue, and red lines represent the circumferential strain of the aluminum liner, the fiber-direction strain of the CFRP helical layer, and the fiber-direction strain of the CFRP hoop layer, respectively. The strain is maximized at the innermost surface of each layer near the center of the tank, which is the burst position; the solid line in the figure indicates this value. In addition, as shown in Table 1, when the fiber-direction strain of the CFRP reached 2.10% of the fiber fracture strain, the relevant CFRP layer broke and led to tank fracture. A solid line is drawn up to the burst pressure calculated.

The maximum strain of the aluminum liner did not exceed the fracture strain (12%) in any of the tanks, as shown in Table 1, and it is considered that the aluminum was not the starting point of the fracture. Based on this result, the respective tanks were predicted to burst at the central part of the cylindrical part, sufficiently far from the dome part, starting from the following layers at the corresponding internal pressures: Tank No. 1, from the

CFRP first layer (helical layer) at 17.2 MPa; Tank No. 2, from the CFRP first layer (hoop layer) at 29.6 MPa; Tank No. 3, from the CFRP third layer (hoop layer) at 29.8 MPa; and Tank No. 4, from the CFRP third layer (hoop layer) at 47.4 MPa.

3.3 Comparison of analysis and experimental results

For all the tanks, the measured values of the fiber-direction strain in the outermost CFRP layer, indicated by the green squares in Fig. 9, agree well with the analysis results in the micro-deformation region, where the strain was 0.5% or less. The strain values measured by the strain gauges do not accurately indicate the increments in the local strain in the fiber bundle and the resin, although these gauges were attached to the fiber bundle. To summarize, this is because the gauges simply represent the average strains in the gauge-mounted areas; this is explained in detail based on the meso-scale model analysis in subsequent sections. Therefore, if the average measured strain is low, the strain measurement results agree relatively well with the analysis results obtained using the axisymmetric continuum model. However, if the strain becomes high and the nonlinear behavior of the resin becomes locally remarkable, the analysis results would deviate from the strain measurement results because the influence of the nonlinear behavior was not considered.

For Tank No. 1, the analysis results agree with the measurement results until the plastic deformation of the aluminum liner commences. However, when the plastic deformation progresses beyond an internal pressure of 8 MPa, the nonlinear behavior of the resin in the CFRP

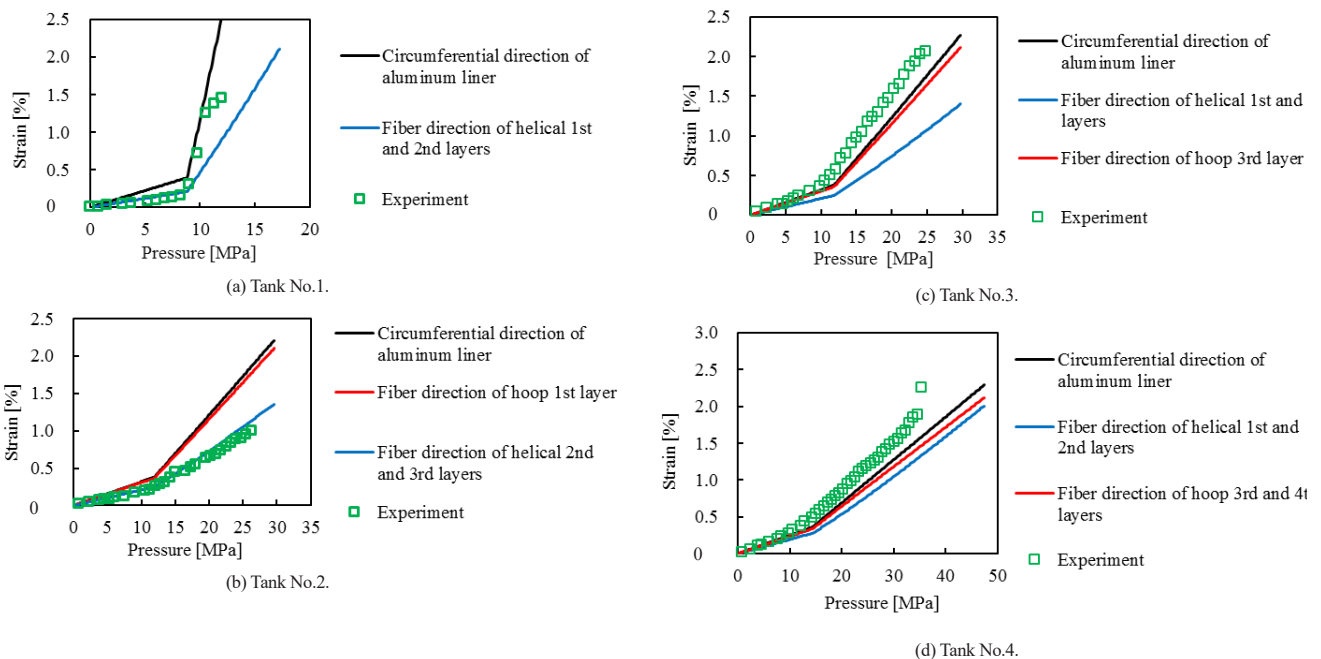


Fig. 9 Pressure-strain curves of axisymmetric analyses and experiments at the tanks are shown. The slopes are identical for experiment and analyses in small strain region before nonlinear behavior of resin becomes prominent. They deviate in large strain region where nonlinear behavior of resin affects much, since the nonlinear behavior of resin is not taken into account in axisymmetric analyses. Predicted burst pressure by the analyses exceed the experimental results by 30 % because of inadequate handling of nonlinear behavior of resin.

layer becomes remarkable; hence, the analysis results deviate from the measurement results. In Tank No. 2, the fiber-direction strain of the outermost helical layer is relatively low; therefore, the analysis results agree well with the measurement results over the entire pressure range. In Tanks No. 3 and No. 4, the analysis results and the measurement results agree well in the low strain region; however, the analysis results gradually deviate from the measurement results as the inelastic deformation of the resin progresses.

The fracture positions predicted by the analysis, including those in the thickness direction of the CFRP layer, agree well with the experimental results. However, the burst pressures of Tanks No. 1, 2, 3, and 4 predicted by the analysis, which are 17.2, 29.6, 29.8, and 47.4 MPa, respectively, are approximately 30% higher than the corresponding experimental results of 12.0, 26.3, 24.8, and 35.3 MPa. In other words, using the axisymmetric continuum model affords predictions on the overestimation side. If the results are to be utilized for design purposes, an appropriate safety margin should be set considering the differences. The methodology of repeating design, manufacturing, and burst tests to set the safety margins according to an empirical rule is often adopted; however, in many cases, a large safety margin is set conservatively, resulting in an unnecessary increase in the tank weight. To address this and realize a rational minimum weight design, analyses based on a meso-scale model are required.

4. Burst pressure predicted by zooming analysis using meso-scale model

4.1 Meso-scale model

This work attempted to predict the burst pressure of the pressure tanks with high accuracy by performing zooming analysis using a meso-scale model (Takemoto and Yoshikawa, 2019), which separates the carbon fiber bundles and matrix resin. According to the test results discussed in Section 2 and the analysis results described in Section 3, the burst evaluation target was narrowed down to the straight cylindrical portion near the center of the tank body, because this region was the starting point of the burst. A meso-scale model was set in the x - y - z Cartesian coordinate system by approximating a part of the side surface of the cylinder as a plane. The x -axis coincides with the circumferential direction (θ -direction) of the cylinder, the y -axis coincides with the radial direction (r -direction), and the z -axis coincides with the central axis direction.

A meso-scale model of a CFRP bundle featuring a columnar body with an elliptical cross-section, which is a single carbon fiber bundle (blue), and a strip-shaped region with a width of 10.0 mm and a thickness of 0.500 mm, which is the matrix resin (yellow) and serves as a basic unit, is shown in Fig. 10 (a). With the major axis of the ellipse set to 3.84 mm and the minor axis set to 0.230 mm, the effect of stress concentration at the major axis end is minimized. The carbon fiber bundle was designed to possess orthogonal anisotropy with a carbon fiber

volume content V_f of 95.0%, in order to ensure that V_f of the entire meso-scale model reaches 55.0%. The helical layer meso-scale model shown in Fig. 10 (b) has a length of 80.0 mm in the z -direction, width of 46.2 mm in the x -direction, and thickness of 1.00 mm in the y -direction. In this region, four carbon fiber bundles were arranged, with the upper layer inclined at $+30.0^\circ$ and the lower layer inclined at -30.0° with respect to the z -axis, thus enabling the bundles to intersect at the center of the z -direction length such that the bends appeared in steps. Only the carbon fiber bundles are shown in Fig. 10 (b). Similar to the helical layer meso-scale model, the hoop layer meso-scale model was arranged at equal intervals along the z -direction within a region with a length of 80.0 mm in the z -direction, width of 46.2 mm in the x -direction, and thickness of 0.500 mm in the y -direction; eight fiber bundles were included in the z -direction. Only the fiber bundle is depicted in Fig. 10 (c).

The meso-scale model used for the analysis was constructed by combining the helical and hoop layer models to appropriately represent the meso-structure of the relevant part. The nodes were shared and bonded between the layers and between the fiber bundle and resin. As the analysis target was the center of the cylindrical part, which is the fracture position of the tanks shown in Fig. 6, it is not necessary to consider the effect of the bending deformation that occurs in the dome part. Consequently, the macroscopic deformation field of the internal tank pressure can be evaluated using the membrane theory. According to the membrane theory, the curvature of the cylindrical part affects only the equilibrium equations of the internal pressure and the in-plane stress. In this analysis method, the displacement field that satisfies the equilibrium equation is evaluated through axisymmetric model-based analysis, and the boundary conditions of the meso-scale model are determined based on the results. Therefore, the influence of the curvature should be neglected.

The meso-scale model of Tank No. 1 is depicted in Fig. 11 (a). This model only has a helical layer, that is, the helical layer meso-scale model shown in Fig. 10 (b). It was discretized with 10-node tetrahedral quadratic elements, resulting in 1,033,956 elements and 1,480,278 nodes. A meso-scale model of Tank No. 2 is illustrated in Fig. 11 (b). This model has a two-layer structure consisting of a hoop layer (lower layer in the y -direction) and a helical layer, with 1,530,251 elements and 2,149,325 nodes. A meso-scale model of Tank No. 3 is provided in Fig. 11 (c). In this model, the order of the layers is the opposite of that in the model of Tank No. 2, with the lower layer being the helical layer, followed by the hoop layer. The numbers of elements and nodes were the same as those of Tank No. 2. A meso-scale model of Tank No. 4 is depicted in Fig. 11 (d). This model has a three-layer structure with two hoop layers and one helical layer (lowest layer), comprising 2,034,346 elements and 2,827,060 nodes.

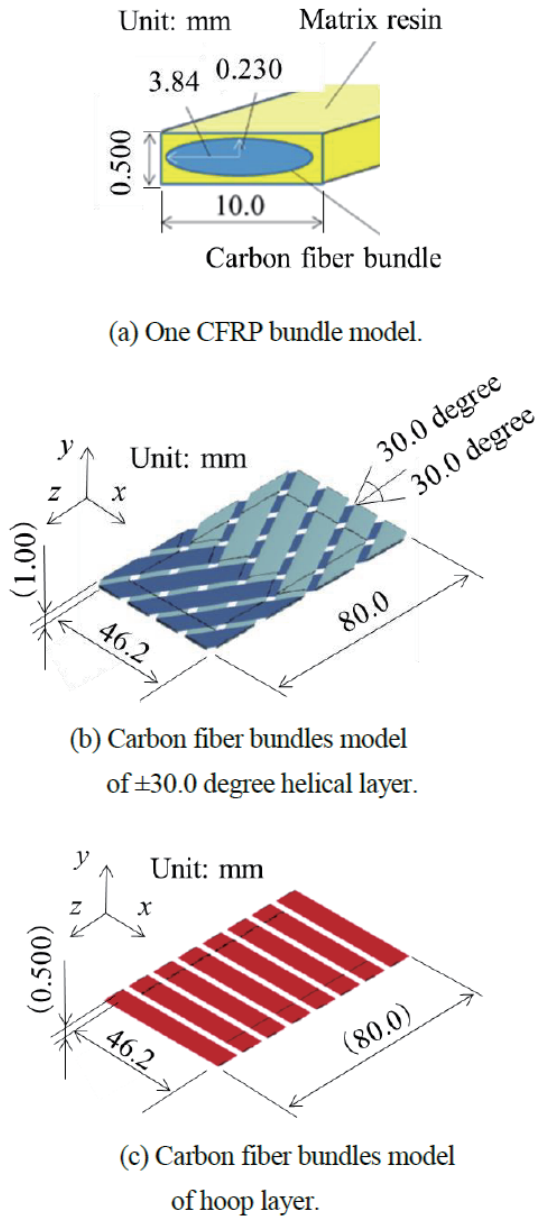


Fig. 10 Meso-scale model for zooming analysis.

4.2 Strength model setting

Epoxy resins used as the CFRP matrix resins generally exhibit strain-rate-dependent properties (Littell et al., 2008). In our previous report (Takemoto and Yoshikawa, 2019), it was clarified that the following three factors are appropriate for reflecting the dependence and constructing the tensile strength expression mechanism of the CFRP helical layer:

- 1) Dependence of resin tensile strength on strain rate: When the resin and fibers break, elastic energy is released in the resin near the fractured part, and the strain rate increases locally. The dependence on the strain rate of the resin increases the resin strength to control the fracture.
- 2) Tension/compression asymmetry of resin strength:

Even if cracks occur during resin fracture, the resin does not disappear and the compressive force perpendicular to the fracture surface is maintained. In other words, the compressive stress is retained after the fracture, although the tensile stress is not retained (LSTC, 2015).

- 3) Anisotropic fracture law of carbon fiber bundle: The fracture in the orthogonal direction of the fiber is governed by the fracture strain of the resin and not by the fracture strain of the fiber.

Even in the model that accurately reproduces the meso-structure of the carbon fiber bundle, the stress field generated in the thin plate test piece owing to the in-plane tensile load is similar to the plane stress field, and the locality in the test piece thickness direction is limited. By contrast, the stress field generated near the boundary between the helical and hoop layers of the tank changes considerably along the thickness direction, and it is

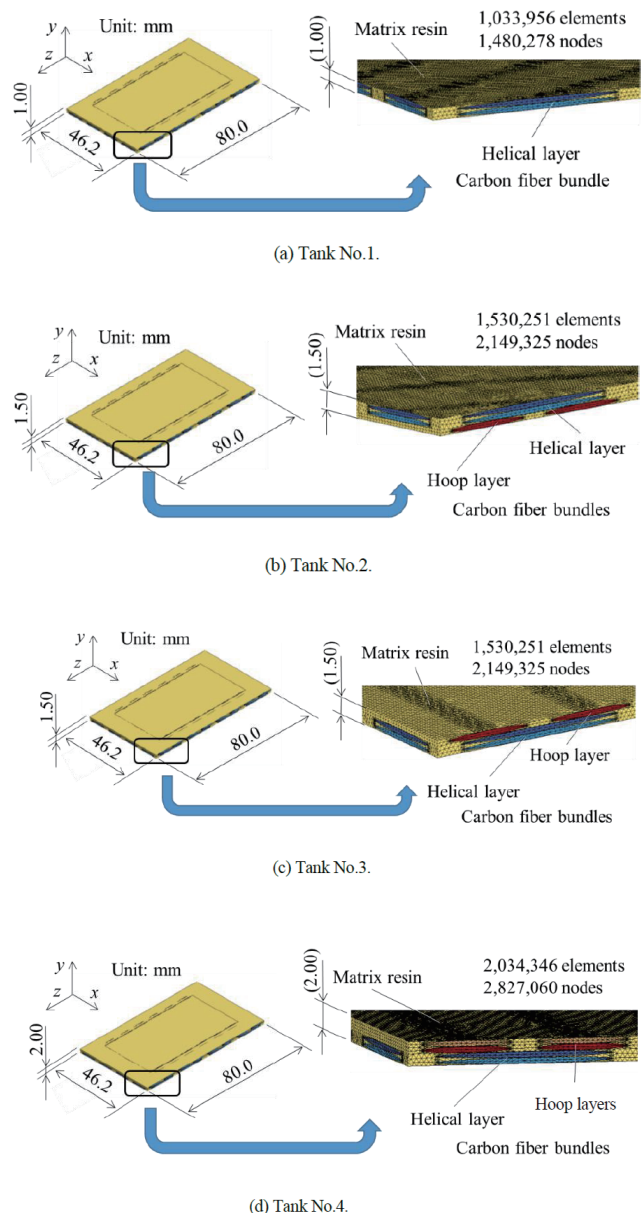


Fig. 11 Meso-scale model of tank.

necessary to consider the influence of the normal stress in the thickness direction. To increase the generality of the strength model considering the abovementioned aspects, the following two constituent factors were added to the aforementioned three constituent factors in order to create the strength model:

- 4) Dependence of resin rigidity on strain rate: Young's modulus increases as the strain rate increases under compressive and tensile stresses.
- 5) Dependence of resin compressive strength on strain rate: The compressive strength increases as the strain rate increases, under both tensile and compressive stresses.

A stress–strain diagram of the matrix resin that embodies the above strength model is provided in Fig. 12. The horizontal and vertical axes represent the equivalent strain and stress, respectively. The resin was formed into an isotropic elastoplastic body, and when the equivalent strain of the resin exceeded 2.60% (based on Table 1) of the fracture strain under tensile stress, it was judged that the resin had broken and that the stress had been released. Even if the resin breaks, it can bear the compressive stress generated during the stress redistribution caused by the failure; hence, it was designed without removing any elements to enable the yield stress to be maintained after being reached under the compressive stress, regardless of the increase in compressive strain. Tension or compression was judged based on whether the volumetric strain was positive or negative. Based on the permanent strain for the yield point strain and the fracture strain, the following strain rate dependence characteristics were applied over the entire stress range from tension to compression, according to the Cooper–Simmons formula (Dietenberger et al., 2005), which expresses the strain rate dependence of the yield stress:

$$\left(\frac{d\sigma_m}{d\varepsilon_m}\right)' = \left\{1 + \left(\frac{\dot{\varepsilon}_m}{C}\right)^{\frac{1}{P}}\right\} \frac{d\sigma_m}{d\varepsilon_m} \quad (1)$$

where σ_m is the equivalent stress of the resin, ε_m is the equivalent strain of the resin, $\dot{\varepsilon}_m$ is the strain rate of the resin, ()' indicates the changes in the resin due to strain-rate-dependent characteristics, and C and P are constants of the Cooper–Simmons formula. According to the results of the dynamic tensile test on the resin test piece described in our previous report (Takemoto and Yoshikawa, 2019), $C = 24.1$ and $P = 1.00$ were identified for the resin with a curing temperature of 80/110°C. As only measurement results corresponding to a strain rate of 43.4/s, indicated by the red line in Fig. 12, were obtained, the stress–strain relationship was applied to the strain rates exceeding this value.

By contrast, for the strength model of the carbon fiber bundle, the anisotropic linear elastic fracture model

(Takemoto, Yoshikawa, 2019) shown in Fig. 13 was set to represent the fracture mode due to the transverse cracks. The vertical axis represents the stress, the horizontal axis represents the strain, the black line indicates the fiber direction, and the blue line shows the fiber orthogonal direction. The fracture strain of the carbon fiber was set to 2.10% in the fiber direction, based on Table 1, whereas the fracture strain in the orthogonal direction of the fiber, in which resin fracture seemed to be dominant, was set to 2.60%. It was assumed that the fiber bundle did not break under compressive stress.

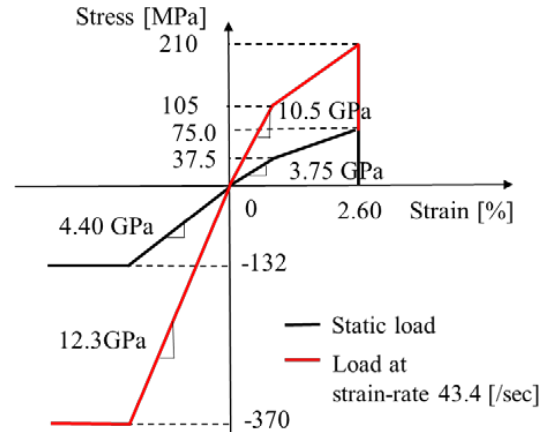


Fig. 12 Asymmetric fracture model of matrix resin for meso-scale analysis.

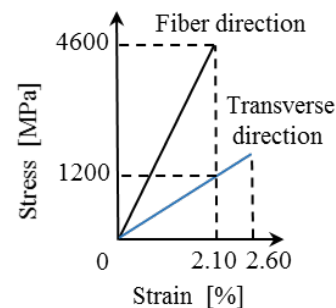


Fig. 13 Anisotropic fracture model of carbon fiber bundle for meso-scale analysis.

4.3 Zooming analysis

The displacement field near the center of the cylindrical part, which is the starting point of the fracture, as indicated by the analysis based on the axisymmetric continuum model described in Section 3, was set as the boundary condition of the meso-scale model, and zooming analysis was conducted. Considering the issues associated with the application to design, the following approximate analysis method was adopted to reduce the calculation load:

- 1) In the axisymmetric continuum model analysis for the tank, the CFRP is considered as a linear elastic body; however, in the meso-scale model, the nonlinear behavior and fracture model of the resin and the orthogonal anisotropic linear elastic body

fracture model of the carbon fiber bundle were incorporated into the analysis.

- 2) According to the homogenization method (Arai et al., 2008), the nonlinear analysis results of the meso-scale model should be fed back to the axisymmetric continuum model to proceed with the sequential analysis. However, this step was not performed in this study; instead, a one-way procedure from the axisymmetric continuum model analysis to the meso-scale model zooming analysis was employed.

Based on the analysis results in Section 3, the displacement field corresponding to the average vertical strain in the central axis direction and the average circumferential strain of each element with respect to the position of 40.0 mm on the central axis direction from the central surface of the tank body were obtained at each internal pressure; furthermore, the prescribed displacements U_z , $-U_z$, U_x , and $-U_x$ with respect to the meso-scale model edge, shown in Fig. 14, were calculated. To suppress the out-of-plane deformation caused by the structural asymmetry of the meso-scale model, the edges that yielded the prescribed displacement were constrained along the y-direction. As the increases in local stress or strain occurred near the edges, it was determined that no fracture checks would be performed in an area equivalent to the size of one fiber bundle from the edge (outside the area, 60.0 mm in the z-direction and 34.7 mm in the x-direction, surrounded by the blue line shown in Fig. 14). The pressurization rate for the analysis was set to 1.50×10^{-4} s/MPa to shorten the calculation time as much as possible within the range where there was no difference in the analysis results.

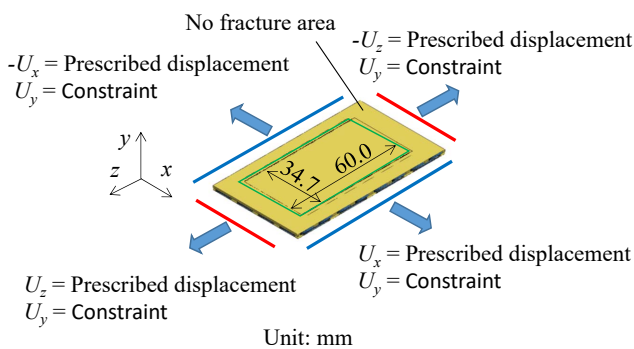


Fig. 14 Boundary condition of meso-scale model for zooming analysis.

4.4 Analysis results

The first-principles strain distributions of the carbon fiber bundle surfaces, obtained from the analysis results based on the meso-scale models of Tanks No. 1, 2, 3, and 4, are presented in Figs. 15, 16, 17, and 18, respectively. The region depicted in each case is that surrounded by the blue lines in Fig. 14. In Figs. 15–17, the distributions immediately before and after fracture are shown in (a) and (b), respectively.

According to the results for Tank No. 1 in Fig. 15, a

local increase of approximately 2.1% in the fiber fracture strain occurred at the crimp (bending) part of the helical layer intersection, and the fracture commenced from this point. Mesoscopic zooming analysis enabled the prediction of the burst mechanism at the meso-scale, which was not captured by the axisymmetric continuum model. According to the results for Tank No. 2 in Fig. 16, the increase in local strain due to the crossing of fiber bundles in the upper helical layer induces a fiber-direction strain similar to the fracture strain in the lower hoop layer fiber bundles, which was the starting point of the fracture. The predicted fracture from the lower hoop layer matches the experimental results presented in Section 2. According to the results for Tank No. 3 in Fig. 17, although the layer order is reversed compared to that of Tank No. 2, the strain increases according to the same mechanism, and the fracture commences at the hoop layer fiber bundle near the intersection with the helical layer fiber bundle. The predicted fracture starting position also agrees with the experimental results.

The results for Tank No. 4 immediately before fracturing are presented in Figs. 18 (a), (b), and (c), and those immediately after fracturing are depicted in Fig. 18 (d). The distribution maps for all fiber bundles from the outermost layer side are provided in Figs. 18 (a) and (d); the internal view of the hoop layer fiber bundles is shown in Fig. 18 (b), and the view from the innermost layer is provided in Fig. 18 (c). Fig. 18 (b) indicates that the local strain inside the hoop layer increases. Moreover, Fig. 18 (c) shows that the local increase in strain due to the crossed fiber bundle in the helical layer resulted in an increase in the strain up to approximately the fracture strain in the hoop layer fiber bundle, which was the starting point of the fracture shown in Fig. 18 (d), similar to the cases of Tanks No. 2 and No. 3. These results are also consistent with the fracture test results. The main strain distribution of the matrix resin for Tank No. 4 is presented in Fig. 19. Internal views of the hoop layer are provided, where (a) and (b) correspond to the first and third principal strains, respectively. The maximum value of the first principal strain exceeds the static fracture strain of the resin (2.6%), as shown in Table 1, and the minimum value of the third principal strain is approximately -5% . If the proposed strength model that depends on the strain rate is not used, it is expected that the fracture progress would be accelerated and the burst pressure would be lower than that obtained in the burst test. The prediction of a low burst pressure is safe and desirable for ensuring tank reliability; however, a conservative design is not economical. The proposed method enables more accurate predictions, affording both high reliability and economy.

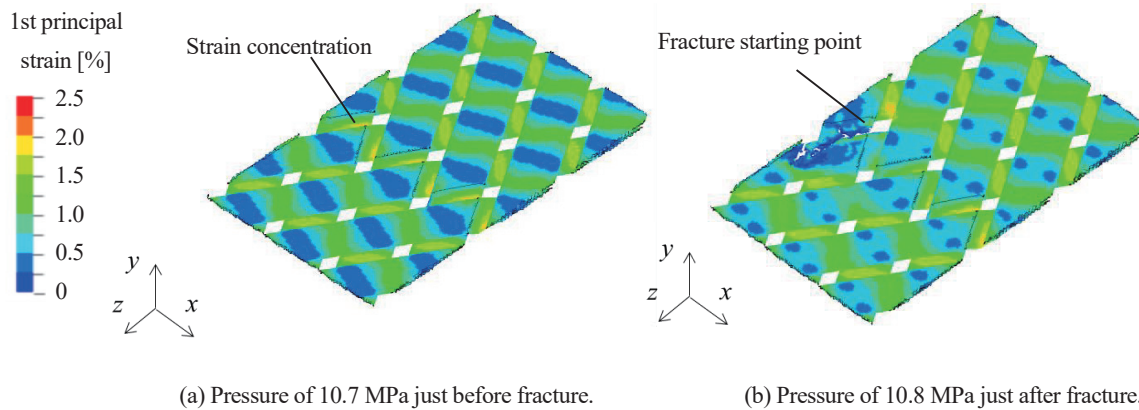


Fig. 15 1st principal strain distributions of carbon fiber bundles obtained by zooming analysis of tank No.1 are shown for just before (a) and after (b) fracture. Local strain concentration occurs to raise the maximum first principal strain in the vicinity of crimp part of the helical layer. The fracture initiates at the point of the strain concentration, when it reaches to 2.1 %, that is, fracture elongation of carbon fiber.

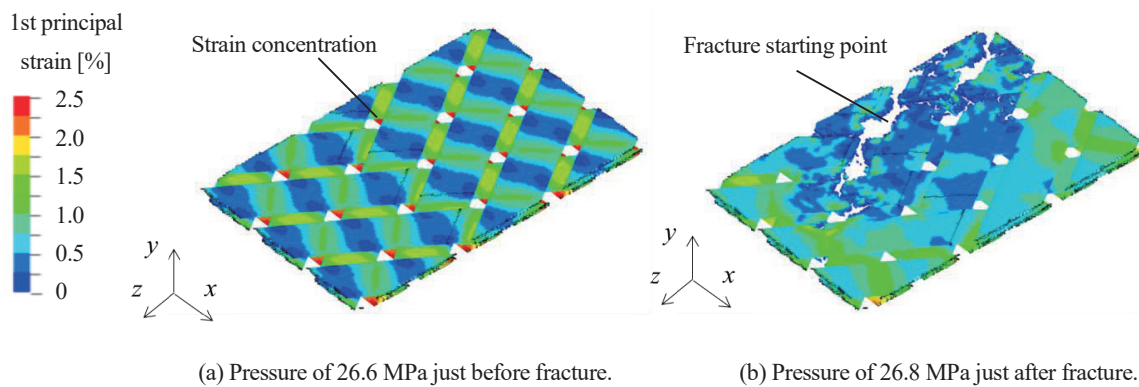


Fig. 16 1st principal strain distributions of carbon fiber bundles obtained by zooming analysis of tank No.2 are shown for just before (a) and after (b) fracture. The local strain concentration of the crimp part in the upper helical layer causes increases of the local strain of the lower hoop layer. The strain reaches to 2.1 % at the moment of fracture.

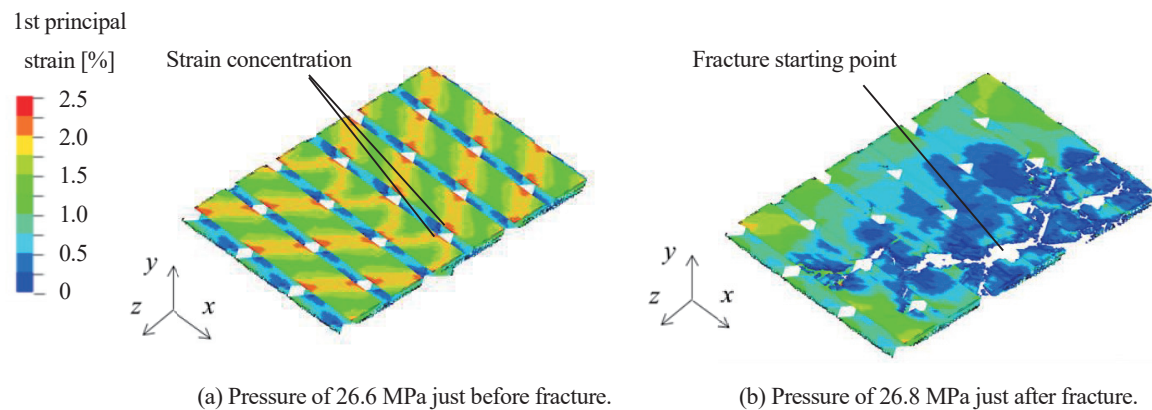


Fig. 17 1st principal strain distributions of carbon fiber bundles obtained by zooming analysis of tank No.3 are shown for just before (a) and after (b) fracture. By the similar mechanism of tank No.2, the local strain enhancement at the crimp part of the lower helical layer causes increase of the local strain of the upper hoop layer.

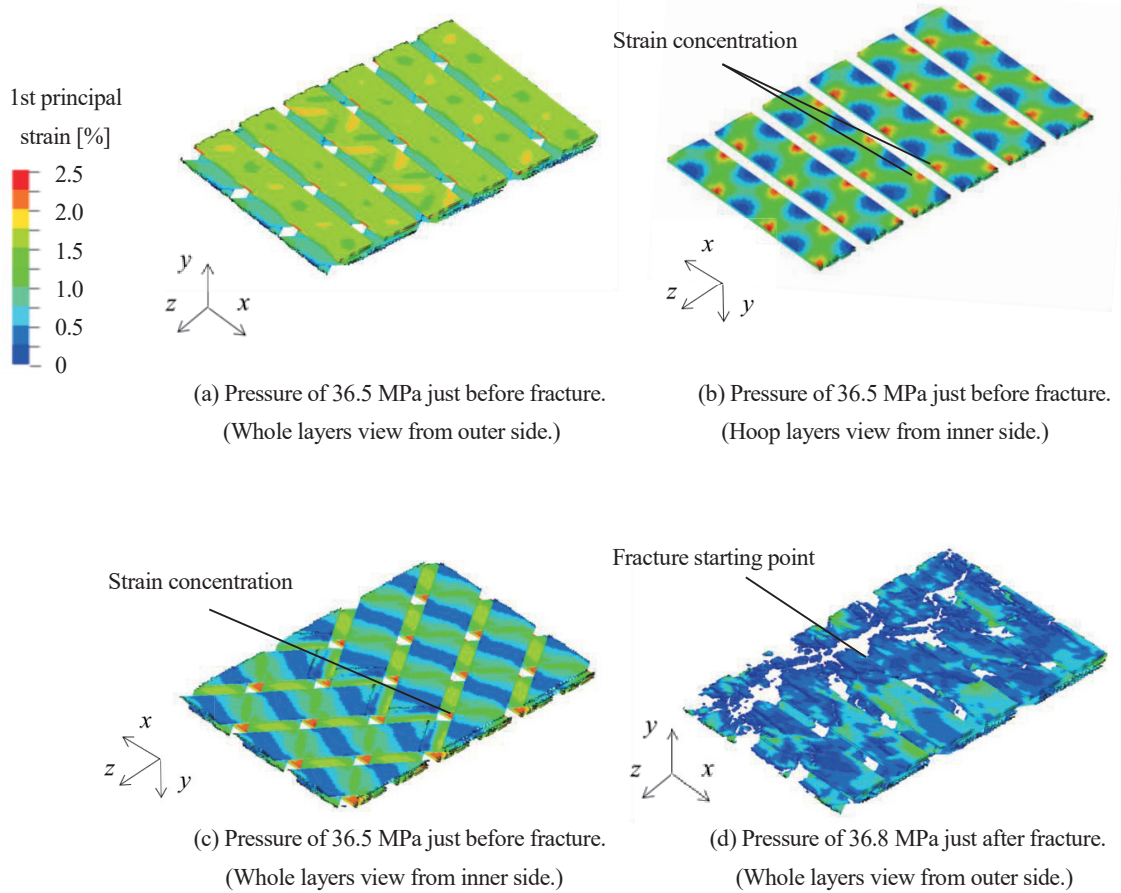


Fig. 18 1st principal strain distributions of carbon fiber bundles obtained by zooming analysis of tank No.4 are shown for just before (a), (b), (c) and after (d) fracture. Both (a) and (d) illustrate by the view from outer side for whole layers. (b) is inner side view for hoop layer. (c) is inner side view for whole layers. The local strain concentration occurs in the hoop layer caused by the crimp in helical layer. The fracture of hoop layer fiber bundle starts when its local strain reaches to 2.1 %.

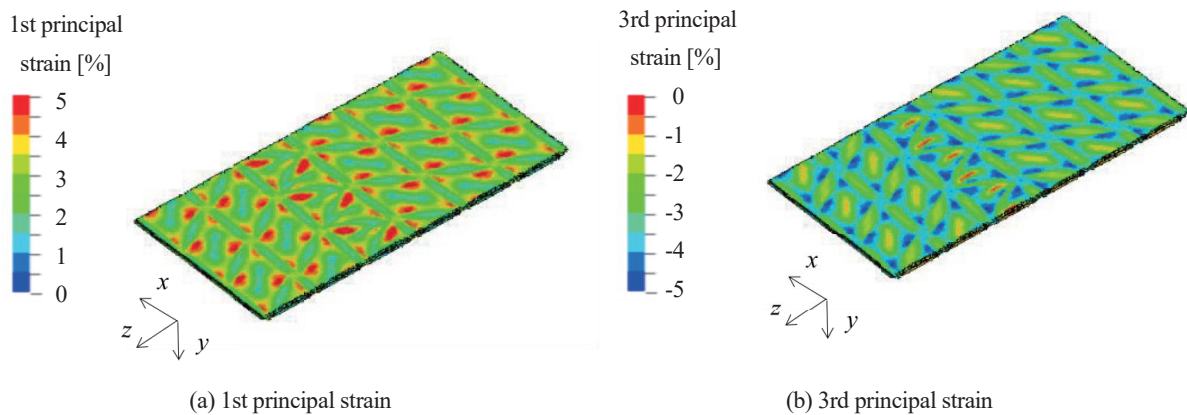


Fig. 19 Distributions of 1st principal strain (a) and 3rd principal strain (b) of matrix resin obtained by zooming analysis of tank No.4 are shown by the view from inner side at internal pressure of 36.5 MPa, that is, just before the fracture. The maximum value of the 1st principal strain exceeds 2.6 %, that is, fracture elongation of matrix resin. The minimum value of the 3rd principal strain is about -5 %.

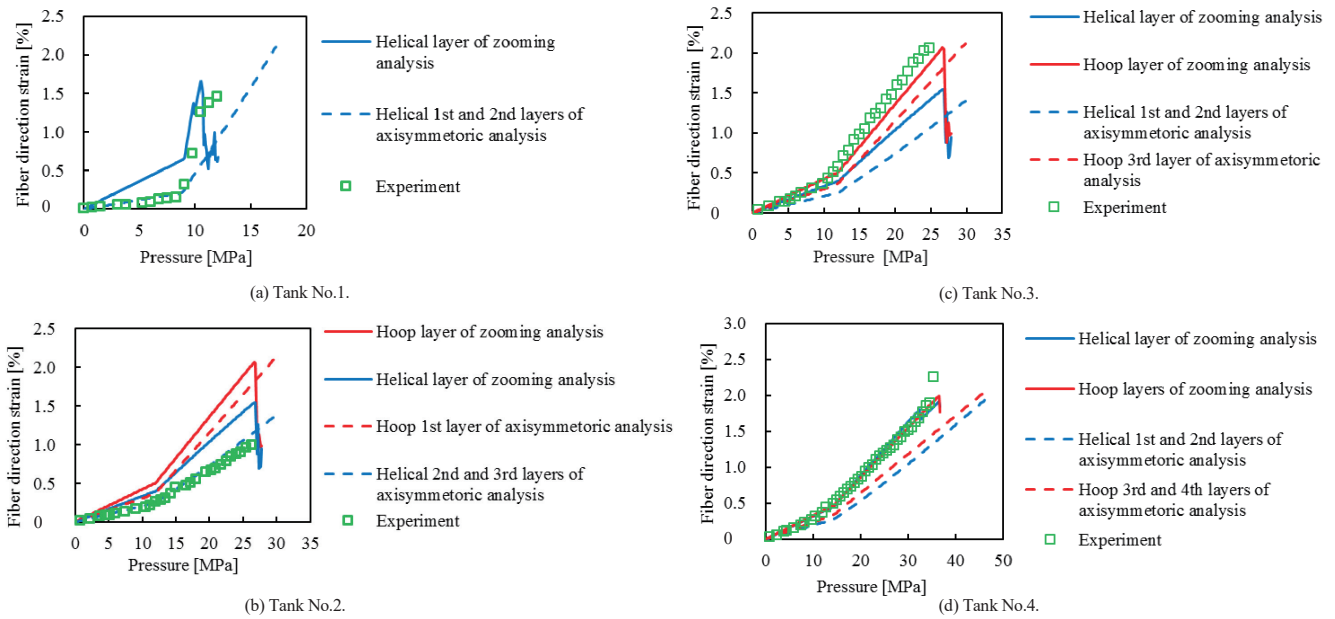


Fig. 20 Pressure-strain curves of analyses and experiments for the tanks are shown. The zooming analyses predict the burst pressure precisely. The analyses yield higher strain than axisymmetric analyses for all the tanks because of precise evaluation of local strain enhancement caused by the mesoscopic structure of fiber bundles and resin. The strains of zooming analyses exceed the experimental one at tank No.1 and 2, since effect of fiber bundle crimp in helical layer cannot be measured by strain gage. The strains of zooming analyses become closer to those of experimental measurements at tank No.3 and 4 since the strain enhancement caused by nonlinear behavior of resin is taken into account in zooming analyses.

4.5 Comparison of zooming analysis and burst test results

The relationship between the strain and internal pressure of the carbon fiber bundle obtained via zooming analysis using the meso-scale model is presented in Figs. 20 (a), (b), (c), and (d) for Tanks No. 1, 2, 3, and 4, respectively. The vertical and horizontal axes represent the fiber-direction strain of the carbon fiber bundle and the pressure inside the tank, respectively. The maximum values evaluated for each layer are indicated by the solid blue and red lines for the helical and hoop layers, respectively. The green squares indicate the fiber-direction strain in the outermost CFRP layer measured during the burst test, the blue dashed line represents the maximum value of the carbon fiber-direction strain in the helical layer evaluated using the axisymmetric continuum model, and the red dashed line denotes the maximum strain in the hoop layer.

As described in Section 3.3, the values measured by the strain gauges can be regarded as the average values for the gauge-mounted areas; in the low strain area, these values agree well with the results of the axisymmetric continuum model analysis. The maximum strain obtained from the zooming analysis exceeds that determined by the axisymmetric analysis, accurately expressing the influence of the crossing of the fiber bundles and the nonlinear deformation behavior of the resin. For Tanks No. 1 and No. 2, whose outermost layers are the helical layers, the local strain increase caused by the crossing of fiber bundles is remarkable. It is impossible to measure this local strain accurately by using strain gauges, and the maximum strain in the helical layer obtained from the zooming analysis exceeds the gauge

measurement result. For Tanks No. 3 and No. 4, whose outermost layers are the hoop layers, the measured fiber-direction strains of the hoop layer are almost identical to the maximum strain values obtained from the zooming analysis. As there is no crossing of the fiber bundles in the hoop layer and the nonlinear behavior of the resin that occurs prior to fiber fracture is accurately expressed in the zooming analysis, the zooming analysis results are closer to the measurement results than the axisymmetric analysis results.

The burst pressures predicted by the zooming analysis were 10.8, 26.8, 26.8, and 36.8 MPa for Tanks No. 1, 2, 3, and 4, respectively, whereas the actual burst pressures obtained from the burst test were 12.0, 26.3, 24.8, and 35.3 MPa, respectively, indicating a difference of less than 10%. Thus, the zooming analysis achieved a significant improvement in prediction accuracy, as compared to the axisymmetric continuum model described in Section 3; the layers that triggered the bursts, as identified by the zooming analysis, were also consistent with the burst test results. Thus, the proposed method was validated.

5. Conclusion

The proposed method based on a meso-scale model that divides the CFRP layer into carbon fiber bundles and the matrix resin is effective for evaluating the burst pressures of high-pressure hydrogen tanks manufactured using the FW method. In constructing the meso-scale model, the following five factors were selected to build the strength model:

- 1) Dependence of resin tensile strength on strain the rate

- 2) Tension/compression asymmetry of resin strength
- 3) Anisotropic fracture law of carbon fiber bundle
- 4) Dependence of resin rigidity on strain rate
- 5) Dependence of resin compressive strength on strain rate

For the demonstration, four types of Type 3 small pressure tanks with different CFRP layer configurations were prototyped and subjected to burst tests. Results of the burst pressure test predicted based on the conventional axisymmetric continuum model were approximately 30% higher than the actual results, even when the layer structures were faithfully modeled; this indicates the overestimation by the model. Meanwhile, the zooming analysis could accurately predict the burst pressures by representing a part of the central cylinder of the tank using a plate-shaped meso-scale model and by setting the displacement field obtained from the axisymmetric continuum model analysis as the boundary condition. Accurate predictions of the burst pressures by using this approach are expected to help manufacturers in designing more reliable and economical products, without being overly conservative.

In this research, the zooming analysis was focused on the cylindrical part of the tank; nevertheless, we believe that the strength model presented herein is a realistic model that includes the tension and compression asymmetry. Therefore, we will continue to verify this methodology by applying it to the CFRP layer in the dome part of the tank, where complicated bending deformation occurs.

References

- Arai, M., Kaku, K., Fushimi, Y., and Matsuda, T., Evaluation for viscoelastic constitutive equation of CFRP laminates using homogenization method, *Journal of Japan Society for Computational Methods in Engineering*, Vol.8, No.10-081128 (2008).
- Arai, Y., Otsuka, T., Suzuki, H., Shibata, S., Obuchi, T., and Iijima, T. Evaluation of fatigue fracture mechanisms of Al alloy liner/FW-CFRP composite pressure vessel, *Transactions of the Japan Society of Mechanical Engineers, Series A*, Vol.73, No.736 (2007), pp.1388-1394.
- Dietenberger, M., Buyuk, M., and Kan, C. D., Development of a high strain rate development vehicle model, *LS-DYNA Anwenderforum Bamberg 2005* (2005).
- High Pressure Gas Safety Association, *KHKS0220 Standards for ultra high pressure gas equipment* (2016).
- Hirase, Y., Mori, T., Ishihara, T., Katoh, A., and Kawahara, M., An investigation of stress analysis of a FRP vessel by using the netting theory, laminar theory, and FEM, *Transactions of the Japan Society of Mechanical Engineers, Series A*, Vol.57, No.535 (1991), pp.550-555.
- Iida, H., Mechanical characteristics of filament-wound pressure vessel, *Journal of the Japan Society for Composite Materials*, Vol.4, No.4 (1978), pp.163-167.
- Kim, S. W., Yoshikawa, N., Tojo, S., and Suzuki, J., Optimization of dome shape for type3 accumulators, *Journal of High Pressure Institute of Japan*, Vol. 55, No.1 (2017), pp.3-11.
- Littell, J. D., Ruggeri, C. R., Goldberg, R. K., Roberts, G. D., Arnold, W. A., and Binienda, W. K., Measurement of epoxy resin tension, compression and shear stress-strain curves over a wide range using small test specimens, *Journal of Aerospace Engineering*, Vol.21, No.3 (2008), pp.162-173.
- Liu, J., Yamada, K., Hosomi, M., Ikeda, T., Hirano, T., Structural design and analysis of fiber reinforced plastic pressure vessels with load-carrying metallic liners, *Transactions of the Japan Society of Mechanical Engineers, Series A*, Vol.63, No.612 (1997), pp.1758-1765.
- LSTC, *LS-DYNA R8.0 keyword user's manual*, Vol.2 (2015), pp.127-129.
- Maki H, Shimamura S, Tabei K, and Oishi S, *Filament winding*, The Nikkan Kogyo Shimbun Ltd. (1970).
- Onaka, H., Development status of fuel cell, *Journal of High Temperature Society*, Vol.35, No.5 (2009), pp.231-238.
- Takehana, T., and Ota, H., Estimation of safety and standard for fiber reinforced plastic composite cylinders, *Journal of High Pressure Institute of Japan*, Vol.35, No.1 (1997), pp.15-20.
- Takemoto, T., and Yoshikawa, N., Advanced nonlinear material model of resin for meso-scale tensile strength evaluation of CFRP structure of high pressure hydrogen tank, *Transactions of the JSME*, Vol.85, No.869 (2019), DOI:10.1299/transjsme.18-00304.
- The Council for a Strategy for Hydrogen and Fuel Cells, *Strategic Roadmap for Hydrogen and Fuel Cells, 16th Meeting of the Council for a Strategy for Hydrogen and Fuel Cells, METI* (2019).
- United Nations, *Global Technical Regulation on Hydrogen and Fuel Cell Vehicle, Global Technical Regulations No.13* (2013).
- Vasiliev, V., and Morozov, V., *Mechanics and Analysis of Composite Materials*, Elsevier (2001), pp.236-237.

Source

一般社団法人日本機械学会
 日本機械学会論文集
 Vol.86, No.8832

Recipient



Shinichiro Takemoto

Editorial Postscript

Thank you for regularly reading the Nissan Technical Review. Globally, there are large transitions toward meeting the carbon neutrality goals of 2050; therefore, we highlight two topics that represent the major transformations undertaken by Nissan as special features in No. 88. The first topic is on ARIYA, Nissan's next-generation EV, and the second is on the Nissan Intelligent Factory, which produces future vehicles that have undergone significant evolutions triggered by ARIYA's production.

The Nissan Intelligent Factory aims to achieve carbon-neutral production as well as allow flexibility and strength for handling various environmental changes. This is an important topic along with promotion of the widespread use of EVs. The other topic, ARIYA, is the next-generation EV model of Nissan, who launched their first EV LEAF in December 2010. This special feature describes the renovated technologies that we have confidence in, including the new EV-specific platform, newly developed powertrain and four-wheeler chassis control technology, and vehicle interface and connectedness.

The contributors to these articles are experts working at Nissan in fields ranging from technological development to production. I would like to take this opportunity to thank all the contributors and editors who wish to make Nissan's technologies known widely.

I sincerely hope that the advanced technologies developed in accordance with "Nissan Ambition 2030," the long-term vision announced by Nissan in November 2021, will be accessible to our readers.

Tomohiro Yamamura,
Research Planning Department,
Nissan Research Center

NISSAN TECHNICAL REVIEW 2022 No.88

Published	September,2022
Publishing office	NISSAN MOTOR CO., LTD. Research Division Research Planning Department Address: 1-1, Morinosatoaoyama, Atsugi-shi, Kanagawa 243-0123
Publisher	Research Division Research Planning Department General Manager TOMOHIRO YAMAMURA
Editorial office	NISSAN CREATIVE SERVICES CO., LTD. Development Information Service Division 560-2 Okatsu.Koku Atsugi Kanagawa 243-0192 C/O Nissan Technical Center

